

# Strangeness Production close to Threshold in Proton - Nucleus and Heavy-Ion Collisions

Christoph Hartnack<sup>1</sup>, Helmut Oeschler<sup>2</sup>, Yvonne Leifels<sup>3</sup>,  
Elena L. Bratkovskaya<sup>4,5</sup>, Jörg Aichelin<sup>1</sup>

<sup>1</sup> SUBATECH, Laboratoire de Physique Subatomique et des Technologies Associées  
UMR 6457, University of Nantes - IN2P3/CNRS - Ecole des Mines de Nantes  
4 rue Alfred Kastler, F-44072 Nantes, Cedex 03, France

<sup>2</sup> Institut für Kernphysik, Darmstadt University of Technology, 64289 Darmstadt, Germany

<sup>3</sup> GSI Helmholtzzentrum für Schwerionenforschung GmbH, 64291 Darmstadt, Germany

<sup>4</sup> Institute for Theoretical Physics, Frankfurt University, 60438 Frankfurt-am-Main,  
Germany

<sup>5</sup> Frankfurt Institut for Advanced Studies, Frankfurt University, 60438 Frankfurt-am-Main,  
Germany

We discuss strangeness production close to threshold in p+A and A+A collision. Comparing the body of available  $K^+$ ,  $K^0$ ,  $K^-$ , and  $\Lambda$  data with the IQMD transport code and for some key observables as well with the HSD transport code, we find good agreement for the large majority of the observables. The investigation of the reaction with help of these codes reveals the complicated interaction of the strange particles with hadronic matter which makes strangeness production in heavy-ion collisions very different from that in elementary interactions. We show how different strange particle observables can be used to study the different facets of this interaction (production, rescattering and potential interaction) which finally merge into a comprehensive understanding of these interactions. We identify those observables which allow for studying (almost) exclusively one of these processes to show how future high precision experiments can improve our quantitative understanding. Finally, we discuss how the  $K^+$  multiplicity can be used to study the hadronic equation of state.

## Contents

<b>I. Introduction</b>	4
A. Introduction	4
<b>II. Theory</b>	7
A. Experimental information on Kaon properties in matter	7
B. Strange particles in infinite matter - theoretical approaches	9
1. $K^+$ mesons	12
2. $K^-$ mesons	12
3. Approach by Ramos et al.	16
4. Approach by Lutz et al.	19
5. Kaonic Atoms	21
6. Deeply bound kaonic states in nuclei	23
C. Strange baryons in matter	24
<b>III. Microscopic Description within IQMD</b>	25
A. Nucleon-nucleon-potentials in IQMD	26
B. Kaon-nucleon potentials	29
C. Collisions	32
D. Virtual particles	32
E. Elementary production of $K^+$	35
F. Elementary production of $K^-$	40
G. Nucleon scattering of $K^+$ and $K^-$	40
H. The standard set of our IQMD and HSD calculations	41
I. Dynamics of heavy-ion collisions	42
J. Pion production in heavy-ion collisions	44
<b>IV. Production of <math>K^+</math> mesons</b>	48
A. $K^+$ production in p+A collisions	48
B. The major production channels in A+A collisions	51
C. $K^+$ production via the $N\Delta$ channel	54
D. The $K^+$ nucleus optical potential	55
E. Reaction Dynamics	57
F. Excitation functions	60
G. Kaon spectra	62
H. Rapidity distribution	73
I. Polar distribution	75
J. Azimuthal distribution	76
1. In-plane flow $p_x(y)$ and $v_1$	76
2. Out-of-plane flow $v_2$	80

K. $\Lambda$ production	83
L. In-plane and azimuthal distribution of the $\Lambda$	85
<b>V. Production of <math>K^-</math> mesons</b>	91
A. Subthreshold $K^-$ production	91
B. Dynamics of $K^-$ production and emission	92
C. Influence of the $K^-$ N potential	93
D. Uncertainties in the input quantities	95
E. $K^-$ multiplicity	96
F. Are data compatible with a strong $K^-$ potential?	96
G. $K^-$ spectra	97
H. Rapidity distribution	104
I. Polar distributions	104
J. Azimuthal distribution	106
1. In-plane flow $p_x(y)$ and $v_1$	106
2. Out-of-plane flow $v_2$	106
<b>VI. Discussion and Summary</b>	111
A. Differences and similarities of $K^+$ and $K^-$ emission	111
B. Sensitivity of the observables on properties of the system	118
C. The nuclear equation of state (EoS)	119
<b>VII. Summary</b>	124
<b>References</b>	129

## I. INTRODUCTION

### A. Introduction

More than a quarter of a century ago, the first strange particles have been observed in heavy-ion collisions at relativistic energies [1, 2] and since then, strangeness production has become one of the major research fields in this domain. In the beginning, the experiments had been performed by different groups at the Bevalac at the Lawrence Berkeley Laboratory (LBL). This search was limited to light ions and only with the advent of the SIS accelerator at the Gesellschaft für Schwerionenforschung (GSI) in Germany it became possible to extend the experimental programs to heavy systems. Two groups, the KaoS and the FOPI Collaborations, performed experiments on different aspects of the physics of strange particles over the last 15 years. Very recently, the HADES Collaboration has joined the efforts and their first results on strangeness production in heavy-ion collisions are appearing. In parallel, at the COSY accelerator in Jülich, a research program on close-to-threshold production of strange particles in proton-proton and proton-nucleus collisions has been launched with the intention to bridge the gap between the production of strange particles in elementary (pp) and in heavy-ion collisions. Heavy-ion collisions are of special interest as strange particles can be produced below the corresponding threshold in NN collisions, yet with quite small cross sections. Their yields and their emission behavior test fundamental properties of hot and dense nuclear matter. In the meantime the field has matured and a broad body of data from the present generation of detectors is available.

In the  $K^+$  sector the start was difficult despite of many efforts of different groups. The first measured  $K^+$  spectrum from a heavy-ion collisions below threshold (being at 1.58 A GeV) was far from theoretical predictions, and therefore the production mechanism remained unclear. Later, after the original data had been superseded by new data from the KaoS Collaboration which came close to the original theoretical prediction, it became clear that strange baryons and  $K^+$  are created in binary collisions of baryons and mesons, even below threshold. The Fermi motion can provide necessary additional energy in the center-of-mass system. Thus, strange particle production tests the momentum distribution of the nucleons inside the nucleus. In addition, the unexpectedly large production yield of  $K^+$  mesons in heavy-ion reactions could be explained by a new mechanism which is not available in elementary collisions, the production via an intermediate nuclear resonance, which acts as an energy reservoir. Thus production of strange particles is sensitive to the behavior of nuclear resonances inside the nucleus. Moreover, because  $K^+$  production competes with the decay of the resonance, a shorter mean free path, in other words a higher density, enhances the  $K^+$  production via resonances and  $K^+$  production became a tool to study nuclear matter properties, especially at the high compression which occurs during the heavy-ion reaction.

Strange particles interact with the hadronic environment not only by collisions but also by potential interaction. At finite densities, this interaction has been investigated by extending

the chiral perturbation theory to the SU(3) sector. This procedure allowed to predict how the  $K^+$  mesons are modified in matter but failed for the description of the  $K^-$  properties, where more sophisticated methods are required, as will be discussed later. Heavy-ion collisions are the only possibility to confront these predictions with nature. This added another interesting aspect to the strangeness production in heavy-ion collisions.

For the  $K^-$  sector already the first measured spectrum in heavy-ion reactions suggested that  $K^-$  production in heavy-ion collisions has little in common with  $K^-$  production in elementary or even in proton-heavy ion (pA) collisions. Indeed, the interpretation of the data identified the strangeness-exchange reaction  $Y\pi \rightarrow K^- N$  ( $Y = \Lambda, \Sigma$ ) as the main source of  $K^-$ , a channel which is absent in pA collisions due to the lack of  $\pi$ 's. The large cross section of the inverse reaction and its energy dependence has the consequence that most of the produced  $K^-$  are, however, reabsorbed. Those which are finally observed are created close to the surface as will be demonstrated. The  $K^-$  spectra carry a very complex information on the system which to reproduce is a challenge for every theoretical approach. What makes the situation even more complicated is the very complex potential interaction with the hadronic environment. In contradistinction to the  $K^+$  mesons, the  $K^-$  can produce baryonic resonances in the nuclear medium which render mean field approaches invalid and require self-consistent multi-channel Brückner G-matrix calculations. These calculations have not reached stable conclusions yet and the depth of the  $K^- N$  potential as a function of the nuclear density is still very much debated. If the interaction were strong enough, a kaon condensate could be created whose existence has also implications for the stability of neutron stars. Also here heavy-ion reactions are the only possibility to test the existence of such condensates because kaonic atoms, the other source for the determination of the  $K^-$ -nucleon interaction probe this potential at very low densities only. In Section V.F it is shown that the existence of a  $K^-$  condensate is not compatible with present heavy-ion data.

This complexity of the physics of strange particles in matter is not easy to assess. The high-density zone, created in heavy-ion reactions has a lifetime of a couple of fm/c. Then the system expands rapidly. The time scale of this fast expansion requires to study the system with help of transport theories in which the above discussed physics is embedded. Transport theories have been developed in the eighties and early nineties and have been continuously improved since then. They simulate the whole reaction, from the initial separation of projectile and target until the formation of the finally observed particles, and use as input the elementary cross sections and the interactions among the different particles. By comparing the results for different input quantities (and it will turn out later that uncertainties in the available input quantities limit in some cases the possibility to draw definite conclusions) with experimental data one is therefore able to test the different theories. These transport theories have proven to be the essential tool to interpret heavy-ion reaction data and many results of such comparisons have been published. They are also a link between many-body calculations, usually performed for infinite matter, and experiment.

It is the purpose of this review

- to review the body of data on strange particle production at threshold energies ( $E_{\text{beam}} \leq 2 A \text{ GeV}$ ) which is available by now and which will not increase much in near future.
- to compare the body of data with the results of one version of one selected transport theory, in order to assess whether the present data can be reproduced consistently in terms of the physics which is embedded in these transport approaches. For this purpose we employ the Isospin Quantum Molecular Dynamics (IQMD) approach [3]. For some key observables we compare data as well with the most advanced version of another transport approach, the Hadron String Dynamics (HSD), which has been developed over the years by Bratkovskaya and Cassing [4]. This allows us to assess possible uncertainties of the theoretical approaches and the consequences of different ingredients. Transport theories have been developed in parallel with the experiments. Therefore, the results published in the literature are not always comparable among each other as they are coming from different program versions.
- to study systematically the dependence of the experimental observables on the input of these transport approaches and to identify those observables which carry the key information on debated physics topics. It includes the  $K^+ N$  and the  $K^- N$  potential and the (experimentally unknown) cross sections.
- to assess whether the present body of data allows for conclusions on the underlying physics like the in-medium modifications of strange meson properties, rescattering of strange hadrons and creation of a local statistical equilibrium.
- to study whether strangeness production in heavy-ion reactions can contribute to the answer of two of the most exciting questions debated presently in many-body and heavy-ion physics:
  - Will there be a  $K^-$  condensate if matter is sufficiently compressed?
  - Can the nuclear equation of state be determined experimentally?

Recently two review articles on kaon production in this energy domain have been published which are complementary to our approach.

The review by Fuchs [5] puts the emphasis on comparing published results of different transport models employed to describe the heavy ion data. The study concentrates on the possibility to explore the nuclear equation of state by  $K^+$  production, a subject which has seen a large progress since then, as we will discuss later.

Dohrmann [6] investigates kaon production via different entrance channels including leptons and photons and limits the study of heavy-ion collisions to a comparison of the spectra with theory without studying in detail how the surrounding matter influences the production of strangeness.

Our report is organized as follows. In Chapter II we present results from the different theoretical groups which study the properties of kaons in infinite matter. This includes a discussion on the role of the  $\Lambda(1405)$  and on the information one may obtain by studying kaonic atoms. This will allow to elucidate the mean-field approach which we employ in the calculation. In Chapter III we outline the IQMD transport theory which is employed to interpret the data. We discuss the input quantities which are experimentally known like the measured cross sections, and comment the different parameterizations for the yet unknown ones (which can be found in the literature). We explain as well the virtual particle concept which allow to study strangeness production despite of the very small production cross section in this energy domain. Section IV is devoted to the discussion of  $K^+$  ( $K^0$ ) and  $\Lambda$  production in matter. We begin with the excitation function of the multiplicity followed by a discussion of the spectra and the information obtained from their slopes. A study of the information which one may obtain from polar, in-plane and azimuthal distributions continues this section. We conclude this section by a discussion of the information on the nuclear reaction mechanism which one may obtain from the  $\Lambda(\Sigma^0)$  observables. In Chapter V we discuss the  $K^-$  observables in the same sequence as the  $K^+$  observables in Chapter IV and in Chapter VI we confront the mechanism of  $K^+$  and of  $K^-$  production and outline similarities and differences. We demonstrate that the two strange mesons are sensitive to different stages of the heavy-ion reaction and discuss the consequences for the study of the KN potential in heavy-ion reactions. In the last part of this section, we study to which extent measurements of  $K^+$  production allow to extract information on the hadronic equation of state. We conclude the report by a summary.

## II. THEORY

### A. Experimental information on Kaon properties in matter

There are several ways to obtain information on the properties of kaons in matter. First of all one can scatter kaons elastically with nucleons to obtain experimentally the scattering length. Its knowledge allows — as we will see — to determine unambiguously the change of the mass of the  $K^+$  even for moderate densities. However, for  $K^-$  the knowledge of the scattering length alone is not sufficient to determine the in medium properties because in  $K^-$  reactions strange baryonic resonances can be created whose properties are density dependent. Using inelastic  $K^-$  N data in coupled-channel calculations allows for exploring the properties of  $K^-$  in matter. This analysis may be complemented by that of kaonic atoms, which are bound  $K^-$ -nucleus systems in which the low-density  $K^-$ -nucleon interaction is tested. The binding energy of kaonic atoms gives a direct information on the  $K^-$  potential at low densities. Finally,  $K^-$  nucleus cluster states have been suggested to determine the depth of the  $K^-$  N potential. We will discuss the information obtained from these approaches in

turn. However, we first show which properties can be directly inferred from experiments in a model-independent way.

Knowing the kaon-nucleon scattering amplitude, the KN potential for low densities of nuclear matter,  $\rho$ , can be obtained in a simple  $t\rho$  approximation [7–11]. Employing

$$\Pi_K = -4\pi t_{\text{KN}} \cdot \rho \quad (1)$$

where  $t_{\text{KN}}$  is the (known) free elementary KN scattering amplitude, and  $\Pi_K = 2EU_{\text{opt}}$  is the self energy of the  $K$  meson. Using the scattering length given below, we obtain for the  $K^+$  a repulsive optical potential and a corresponding mass shift of

$$U_{\text{opt}}^{\text{K}^+}(\mathbf{q} = \mathbf{0}, \rho) = +\mathbf{30} \text{ MeV} \cdot \rho/\rho_0. \quad (2)$$

$\rho_0$  is the saturation density of nuclear matter. This value is compatible with the experimental results [12].

Later it has been realized that at low density  $\rho < \rho_0$  the in-medium kaon self-energies can be obtained by a systematic expansion of the chiral Lagrangian. All phenomenological approaches should therefore be consistent with this result. In this approach a low-density theorem [13] can be formulated which relates the change of the kaon mass squared to the kaon-nucleon scattering amplitude  $a_{\text{KN}}$  [14, 15] as

$$\begin{aligned} \Delta m_K^2 &= -\pi (1+x) \left( a_{\text{KN}}^{(I=0)} + 3 a_{\text{KN}}^{(I=1)} \right) \rho \\ &+ \alpha \left( \left( a_{\text{KN}}^{(I=0)} \right)^2 + 3 \left( a_{\text{KN}}^{(I=1)} \right)^2 \right) k_F^4 + \mathcal{O}(k_F^5), \end{aligned} \quad (3)$$

where

$$\alpha = \frac{1 - x^2 + x^2 \log(x^2)}{\pi^2 (1-x)^2} \simeq 0.166, \quad x = \frac{m_K}{m_N}, \quad \rho = \frac{2 k_F^3}{3 \pi^2}. \quad (4)$$

The KN scattering lengths,  $a_{\text{KN}}^{(I=0)}$  and  $a_{\text{KN}}^{(I=1)}$ , have been measured in the eighties and the results of the different experiments are summarized in Refs. [16, 17]. They are  $a_{\text{K}^+\text{N}}^{(I=0)} \approx 0.02$  fm and  $a_{\text{K}^+\text{N}}^{(I=1)} \approx -0.32$  fm for the  $K^+$  and  $a_{\text{K}^-\text{N}}^{(I=0)} \approx (-1.70 + i0.68)$  fm and  $a_{\text{K}^-\text{N}}^{(I=1)} \approx (0.37 + i0.60)$  fm for the  $K^-$ . With these values the result of Eq. (1) is compatible with Eq. (2).

For the  $K^+$  meson, the term  $\propto k_F^4$  modifies only slightly the leading term (the mass shift changes from 28 MeV to 35 MeV [18] at normal nuclear matter density). Thus this expansion in  $\rho$  or  $k_F$  seems to converges quite well even at moderate densities. Consequently, the increase of the  $K^+$  mass with density is theoretically well under control and a simple  $t\rho$  approximation gives already quantitatively good results.

For the  $K^-$  meson, on the contrary, the situation is considerably more complicated. At saturation density  $\rho_0$ , the  $k_F^4$  term is larger than the term proportional to  $k_F^3$  and hence the expansion does not converge. Thus already at moderate densities the low-density theorem - although still valid at very low densities - is of little use. In addition, according to Eq. (3),



the interaction is repulsive whereas the results in kaonic atoms [19] indicate that already at quite low densities the interaction becomes attractive. Koch [20] and later Waas *et al.* [21–23] found that this change of sign of the potential can be explained by the influence of the  $\Lambda(1405)$  state, a resonance 27 MeV below the KN threshold. They showed that the Pauli blocking of intermediate KN states at finite density shifts the mass of this resonance above threshold and renders the potential attractive. Later, it has been realized that the situation becomes even more complex: When the  $K^-$  potential is calculated self-consistently the attractive self-energy of the  $K^-$  counteracts the Pauli blocking and pushes the  $\Lambda(1405)$  mass again to lower values but leaving it moderately attractive, as we will see.

## B. Strange particles in infinite matter - theoretical approaches

The theoretical study of kaon properties in dense matter goes back to Kaplan and Nelson [24, 25]. The degrees of freedom are the baryon octet  $B$  with a degenerate mass  $m_B$  and the pseudoscalar meson octet giving rise to the non-linear Sigma field  $\Sigma$

$$\Sigma = \exp(2i\pi/f) \quad (5)$$

with  $\pi = \pi_\alpha \tau_\alpha$  ( $\text{Tr} \tau_\alpha \tau_\beta = \frac{1}{2} \delta_{\alpha\beta}$ ). The pseudoscalar meson decay constants  $f$  are all equal in the  $SU(3)_V$  limit and are denoted by  $f = f_\pi \simeq 93$  MeV. Using

$$\xi = \sqrt{\Sigma} = \exp(i\pi/f) \quad (6)$$

the meson vector  $V_\mu$  and axial vector  $A_\mu$  currents are defined as

$$V_\mu = \frac{1}{2}(\xi^+ \partial_\mu \xi + \xi \partial_\mu \xi^+) \quad \text{and} \quad A_\mu = \frac{i}{2}(\xi^+ \partial_\mu \xi - \xi \partial_\mu \xi^+), \quad (7)$$

respectively. In chiral perturbation theory the meson - baryon Lagrangian is formulated in terms of operators which are invariant under  $SU(3)_L \times SU(3)_R$ . Expanding this Lagrangian in powers of  $\frac{m_\pi}{\Lambda}$  and  $\frac{\partial}{\Lambda}$  is the chiral symmetry breaking scale which is of the order of 1 GeV and neglecting terms with four or more baryon fields as well as terms of the order  $\frac{m_\pi}{\Lambda}$  and  $\frac{\partial}{\Lambda}$  and higher one obtains the nonlinear chiral Lagrangian

$$\begin{aligned} \mathcal{L} = & \frac{1}{4} f^2 \text{Tr} \partial^\mu \Sigma \partial_\mu \Sigma^+ + \frac{1}{2} f^2 \Lambda [\text{Tr} M_q (\Sigma - 1) + \text{h.c.}] + \text{Tr} \bar{B} (i\gamma^\mu \partial_\mu - m_B) B \\ & + i \text{Tr} \bar{B} \gamma^\mu [V_\mu, B] + D \text{Tr} \bar{B} \gamma^\mu \gamma^5 \{A_\mu, B\} + F \text{Tr} \bar{B} \gamma^\mu \gamma^5 [A_\mu, B] \\ & + a_1 \text{Tr} \bar{B} (\xi M_q \xi + \text{h.c.}) B + a_2 \text{Tr} \bar{B} B (\xi M_q \xi + \text{h.c.}) \\ & + a_3 [\text{Tr} M_q \Sigma + \text{h.c.}] \text{Tr} \bar{B} B + \mathcal{O}(\frac{m_\pi}{\Lambda}) + \mathcal{O}(\frac{\partial}{\Lambda}). \end{aligned} \quad (8)$$

The current quark mass matrix is given by  $M_q = \text{diag}\{m_q, m_q, m_s\}$ , neglecting the small difference between the up and down quark masses. For the reduction of the different terms to the kaon-nucleon problem we follow here the very clear and straightforward presentation

by Ko and Li [26]. For a more detailed discussion of the effective field theory treatment of the kaon nucleon interaction we refer to [27, 28]. Terms involving the axial vector current can be ignored as they have no effects on the kaon mass. Expanding  $\Sigma$  to order of  $1/f^2$  and keeping explicitly only the kaon field, the first two terms in Eq. (8) can be written as

$$\partial^\mu \bar{K} \partial_\mu K - \Lambda(m_q + m_s) \bar{K} K, \quad (9)$$

where

$$K = \begin{pmatrix} K^+ \\ K^0 \end{pmatrix} \quad \text{and} \quad \bar{K} = (K^- \quad \bar{K}^0). \quad (10)$$

Keeping explicitly only the nucleon and kaon, the third and fourth terms in Eq. (8) become

$$\bar{N}(i\gamma^\mu \partial_\mu - m_B)N - \frac{3i}{8f^2} \bar{N} \gamma^0 N \bar{K} \overset{\leftrightarrow}{\partial}_t K, \quad (11)$$

where

$$N = \begin{pmatrix} p \\ n \end{pmatrix} \quad \text{and} \quad \bar{N} = (\bar{p} \quad \bar{n}). \quad (12)$$

The last three terms in Eq. (8) can be similarly worked out, and the results are

$$\begin{aligned} \text{Tr} \bar{B}(\xi M_q \xi + \text{h.c.})B &= 2m_q \bar{N} N - \frac{\bar{N} N}{2f^2} (m_q + m_s) \bar{K} K, \\ \text{Tr} \bar{B}B(\xi M_q \xi + \text{h.c.}) &= 2m_s \bar{N} N - \frac{\bar{N} N}{f^2} (m_q + m_s) \bar{K} K, \\ [\text{Tr} M_q \Sigma + \text{h.c.}] \text{Tr} \bar{B}B &= 2(2m_q + m_s) \bar{N} N - \frac{2\bar{N} N}{f^2} (m_q + m_s) \bar{K} K. \end{aligned} \quad (13)$$

Combining the above expressions, one arrives at the Lagrangian,

$$\begin{aligned} \mathcal{L} &= \bar{N}(i\gamma^\mu \partial_\mu - m_B)N + \partial^\mu \bar{K} \partial_\mu K - \Lambda(m_q + m_s) \bar{K} K \\ &\quad - \frac{3i}{8f_K^2} \bar{N} \gamma^0 N \bar{K} \overset{\leftrightarrow}{\partial}_t K + [2a_1 m_q + 2a_2 m_s + 2a_3(2m_q + m_s)] \bar{N} N \\ &\quad - \frac{\bar{N} N \bar{K} K}{2f_K^2} (m_q + m_s) (a_1 + 2a_2 + 4a_3) \end{aligned} \quad (14)$$

where one can identify the kaon mass as

$$m_K^2 = \Lambda(m_q + m_s) \quad (15)$$

and the nucleon mass as

$$m_N = m_B - 2[a_1 m_q + a_2 m_s + a_3(2m_q + m_s)]. \quad (16)$$

The KN sigma term is given as

$$\begin{aligned} \Sigma_{\text{KN}} &\equiv \frac{1}{2} (m_q + m_s) \langle N | \bar{u}u + \bar{s}s | N \rangle \\ &= \frac{1}{2} (m_q + m_s) \left[ \frac{1}{2} \frac{\partial m_N}{\partial m_q} + \frac{\partial m_N}{\partial m_s} \right] \\ &= -\frac{1}{2} (m_q + m_s) (a_1 + 2a_2 + 4a_3). \end{aligned} \quad (17)$$

The second line in the above equation follows from explicit chiral symmetry breaking in the QCD Lagrangian, and the last step is obtained using Eq. (16). Then Eq. (14) can be rewritten as

$$\begin{aligned} \mathcal{L} = & \bar{N}(i\gamma^\mu\partial_\mu - m_N)N + \partial^\mu\bar{K}\partial_\mu K - (m_K^2 - \frac{\Sigma_{KN}}{f_K^2}\bar{N}N)\bar{K}K \\ & - \frac{3i}{8f_K^2}\bar{N}\gamma^0 N\bar{K} \overset{\leftrightarrow}{\partial}_t K. \end{aligned} \quad (18)$$

From the Euler-Lagrange equation and using the mean-field approximation for the nucleon field, i.e. the factorization of products of four or more field operators into products of bilinear terms over which one averages independently and the replacement of  $\langle\bar{N}\gamma^0 N\rangle$  by the nuclear density  $\rho_N$  and of  $\langle\bar{N}N\rangle$  by the scalar density  $\rho_S$ , one obtains the following Klein-Gordon equation for a kaon in the nuclear medium,

$$\left[\partial_\mu\partial^\mu + \frac{3i}{4f_K^2}\rho_N\partial_t + (m_K^2 - \frac{\Sigma_{KN}}{f_K^2}\rho_S)\right]K = 0. \quad (19)$$

The kaon dispersion relation in nuclear matter is then given by

$$\omega^2(\mathbf{k}, \rho_N) = m_K^2 + \mathbf{k}^2 - \frac{\Sigma_{KN}}{f_K^2}\rho_S \pm \frac{3}{4}\frac{\omega}{f_K^2}\rho_N, \quad (20)$$

where  $\mathbf{k}$  is the three-momentum of the kaon and the upper(lower) sign refers to  $K^+(K^-)$ . The third term in the above equation results from the attractive scalar interaction due to explicit chiral symmetry breaking and depends on the kaon-nucleon sigma term  $\Sigma_{KN}$ . With a strangeness content of the nucleon, normally taken as  $y = 2\langle N|\bar{s}s|N\rangle/\langle N|\bar{u}u + \bar{d}d|N\rangle \approx 0.1 - 0.2$ , its value is  $350 < \Sigma_{KN} < 405$  MeV taking the strange to light quark mass ratio to be  $m_s/m_q \approx 29$ . On the other hand, recent lattice gauge calculations [29, 30] show that  $y \approx 0.33$  which would give  $\Sigma_{KN} \approx 450$  MeV. The last term in Eq. (20) is due to the repulsive vector interaction and is proportional to the nuclear density  $\rho_N$ . For a  $K^-$  meson, this term becomes attractive due to G parity.

From the dispersion relation, the in-medium kaon energy can be obtained

$$E(\mathbf{k}, \rho_N) = \left[ m_K^2 + \mathbf{k}^2 - \frac{\Sigma_{KN}}{f_K^2}\rho_S + \left( \frac{3}{8}\frac{\rho_N}{f_K^2} \right)^2 \right]^{1/2} \pm \frac{3}{8}\frac{\rho_N}{f_K^2}. \quad (21)$$

The in medium mass, defined as

$$E(\mathbf{k} \rightarrow 0, \rho_N), \quad (22)$$

is the central quantity for the discussion of the experimental observables which follows in the next chapters. Using the KFSR relation ( $m_\rho = 2\sqrt{2}fg_\rho$ ) and the SU(3) relation ( $g_\omega = 3g_\rho$ ) [31], the kaon vector potential in the last term can be written as  $(1/3)(g_\omega/m_\omega)^2\rho_N$  which is just 1/3 of the nucleon vector potential. This can be understood in the constituent quark model since the kaon contains only one light quark as compared to three in a nucleon. Since

an antikaon has one light antiquark, its vector potential becomes attractive, leading to a reduction of its in-medium energy.

In their original papers, Kaplan and Nelson [24, 25] obtained for both,  $K^+$  and  $K^-$ , only the mass correction term

$$\Delta m_K^2(\rho) = -\frac{\Sigma_{KN}}{f_K^2}\rho_S \quad (23)$$

with  $\Sigma_{KN}$  as defined in Eq. (17), which reflects the Pauli blocking of the light quarks in matter. With this approximation, with  $f_K = 106$  MeV and  $\Sigma_{KN} \approx 350$  MeV and with the assumption that the only medium modifications are those of Eq. (23), Eq. (20) predicts a kaon condensation around  $3 \rho_0$  which would have enormous consequences for supernovae explosions as well as for heavy-ion collisions. Employing a Nambu Jona-Lasinio (NJL) Lagrangian, Lutz *et al.* [15] showed later that there are additional correction terms

$$\Delta m_K^2(\rho) = -\frac{\Sigma_{KN}}{f_K^2}\rho_S - \frac{m_K^2 \Delta f_K^2}{f_K^2} \pm \frac{m_K(\rho_u - \rho_s)}{4f_K^2} + \mathcal{O}(m_u^0, s). \quad (24)$$

which are not at all negligible.  $\Delta f_K^2$  is the change of the kaon decay constant in matter which reflects the change of the intrinsic wave function and  $\rho_u(\rho_s)$  are the  $u$  and  $s$  quark densities, respectively. Calculations in the framework of the NJL model showed that these two terms dominate the first term and that therefore the mass of the  $K^+$  increases in matter as predicted by the low-density theorem. These correction terms are very close to the terms of the chiral Lagrangian which have been neglected by Kaplan and Nelson. Assuming that  $\omega \approx m_K$  and  $\rho_s = 0$ , the last terms of Eqs. (20) and (24) differ only by the decay constants  $f_K$  and  $f = f_\pi$ . Their numerical values differ by 10 % only.

### 1. $K^+$ mesons

The results for the in-medium properties of the  $K^+$  obtained in the chiral perturbation theory, in the NJL approach or in self-consistent calculations [32] agree among each other and at low density also with those obtained by analyzing the scattering length. Figure ii.1 shows the mass shift calculated by Korpa and Lutz [32] in comparison with that from the scattering length analysis. Figure ii.2 shows the spectral function of the  $K^+$  at  $\rho_0$  and at  $2\rho_0$  [32] demonstrating that the  $K^+$  is a good quasi-particle. Therefore it is a good approximation to propagate it as stable particle in the simulation programs.

### 2. $K^-$ mesons

As discussed above, the  $K^-$  mesons can easily form resonances with baryons and its coupling to these resonances modifies its medium properties. The repulsive free-space scattering of  $K^-$  mesons is dominated by the presence of the zero isospin  $\Lambda(1405)$  resonance. At zero density the interaction is repulsive but already at very moderate densities the potential

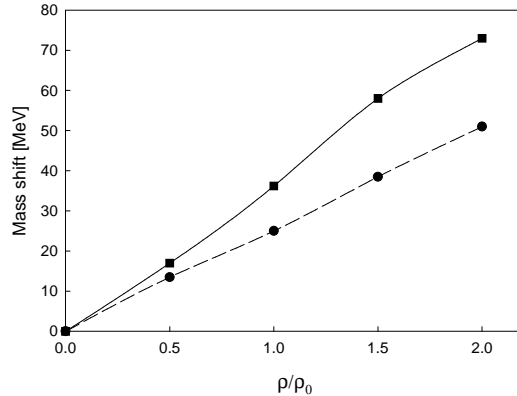


FIG. ii.1: The  $K^+$  mass shift as a function of the nucleon density, with  $\rho_0$  denoting the saturation density. The circles show the results based on the vacuum kaon-nucleon scattering amplitude, while the squares correspond to the self-consistent result [32].

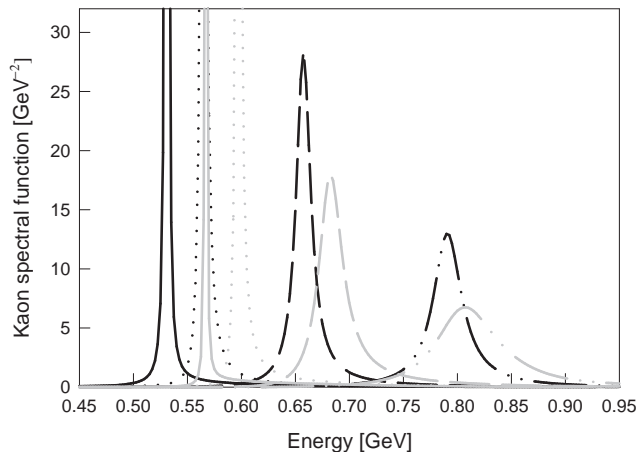


FIG. ii.2: The kaon spectral function for different momenta: 0 (solid line), 200 MeV (dotted line), 400 MeV (dashed line), and 600 MeV (dash-dot-dot line). Black lines show the result at saturation density, gray lines, at twice saturation density. [32].

becomes attractive. The rapid change in sign cannot be understood in the framework of a simple  $t\rho$  approximation (Eq. (3)). Also an expansion in the chiral parameter  $\Lambda$  is not sufficient to understand the properties of  $K^-$  mesons in matter.

Motivated by the  $K^-$  data obtained at the SIS facility at GSI in Darmstadt, many efforts have been advanced to understand the  $K^-$  properties in matter as we will discuss now. All present-day calculations use a self-consistent approach for the calculation the  $K^-$  properties. The starting point of these renewed efforts is the on-shell scattering amplitude

$$\begin{aligned}
\langle M^i(\bar{q}) B^k(\bar{p}) | T | M^j(q) B^l(p) \rangle &= (2\pi)^4 \delta^4(p + q - \bar{p} - \bar{q}) \\
&\times \bar{u}_B^k(\bar{p}) T_{M^i B^k \rightarrow M^j B^l}^{ij}(\bar{q}, \bar{p}; q, p) u_B^l(p) \quad (25)
\end{aligned}$$

where  $M$  and  $B$  represent the different mesons ( $K^-, \pi, \eta$ ) and baryons ( $N, \Lambda, \Sigma, \Xi$ ), respectively, including their corresponding quantum numbers. The term  $\delta^4(\dots)$  guarantees energy-momentum conservation and  $u_B(p)$  is the nucleon isospin-doublet spinor. In quantum field theory the free space scattering amplitude  $T_{MB \rightarrow MB}$  is obtained by solving the Bethe-Salpeter matrix equations

$$\begin{aligned} T(K, k; w) &= K(K, k; w) + \int \frac{d^4l}{(2\pi)^4} K(K, l; w) G(l; w) T(l, k; w), \\ G(l; w) &= -i S_B(\frac{1}{2}w + l) D_M(\frac{1}{2}w - l), \end{aligned} \quad (26)$$

defined in terms of the elementary MB  $\rightarrow$  MB scattering kernel  $K(K, k; w)$ , the baryon propagator  $S_N(p) = 1/(\not{p} - m_B + i\epsilon)$ , and the pion propagator  $D_\pi(q) = 1/(q^2 - m_M^2 + i\epsilon)$ . In Eq. (26) convenient kinematical variables are used:

$$w = p + q = \bar{p} + \bar{q}, \quad k = \frac{1}{2}(p - q), \quad K = \frac{1}{2}(\bar{p} - \bar{q}). \quad (27)$$

The  $K^-N$  channel has isospin  $I = 0$  or  $I = 1$ . Neglecting the  $\eta$  and  $\Xi$  (which due to their mass do not play an important role but have to be taken into account for a quantitative comparison with data [33]), it can only couple to the  $\pi\Sigma$  channel and the corresponding  $I=0$  matrix has the following structure

$$\begin{pmatrix} T_{\bar{K}N \rightarrow \bar{K}N} & T_{\bar{K}N \rightarrow \pi\Sigma} \\ T_{\pi\Sigma \rightarrow \bar{K}N} & T_{\pi\Sigma \rightarrow \pi\Sigma} \end{pmatrix},$$

whereas for  $I = 1$  it can couple to both, the  $\pi\Sigma$  and the  $\pi\Lambda$  channel,

$$\begin{pmatrix} T_{\bar{K}N \rightarrow \bar{K}N} & T_{\bar{K}N \rightarrow \pi\Sigma} & T_{\bar{K}N \rightarrow \pi\Lambda} \\ T_{\pi\Sigma \rightarrow \bar{K}N} & T_{\pi\Sigma \rightarrow \pi\Sigma} & T_{\pi\Sigma \rightarrow \pi\Lambda} \\ T_{\pi\Lambda \rightarrow \bar{K}N} & T_{\pi\Lambda \rightarrow \pi\Sigma} & T_{\pi\Lambda \rightarrow \pi\Lambda} \end{pmatrix}.$$

The free scattering amplitude, Eq. (25), is used to determine the elementary interaction vertices  $K$  by comparing the calculation with the available  $KN \rightarrow MB$  differential cross sections in a partial wave expansion.

In the medium, the Bethe-Salpeter equation takes the form

$$\mathcal{T} = \mathcal{K} + \mathcal{K} \cdot \mathcal{G} \cdot \mathcal{T} \quad (28)$$

with  $\mathcal{K}$  and  $\mathcal{G}$  being the in-medium interaction and propagator, respectively.

This equation is only formal because  $\mathcal{K}$  is not known. Working with effective meson-baryon theories, in which  $\mathcal{K}$  cannot be derived from a more fundamental QCD approach, approximations are required. Making the assumption that the interaction does not change in a hadronic environment by identifying  $\mathcal{K}$  with  $K$  one can proceed to quantitative results.

Particles feel the hadronic environment in different ways as studied in Refs. [14, 34]. First of all, the Pauli principle prevents scattering into intermediate nucleon states below

the Fermi momentum. Thus, the free nucleon propagator  $S_B^0$  is replaced by an in-medium propagator which projects on the available states. The consequences of the Pauli blocking of the states below the Fermi surface is shown in Fig. ii.3 (top), taken from Ref. [34]. At a moderate density a double-hump structure is seen. The left hump is the kaon pole whereas the right one corresponds to the  $\Lambda(1405)$  - hole state which at this density is located above the  $K^-$  mass. With increasing density the right hump disappears and at  $\rho_0$  the strength of the  $K^-$  is concentrated around a peak value which is 80 MeV lower than the mass of the free  $K^-$  and hence the potential is attractive. There remains, however, a long tail toward higher energies. The phase-space restriction of the Pauli principle has shifted the center of the  $\Lambda(1405)$  resonance above the  $K^-N$  threshold.

The second medium modification of the free propagators is due to the interaction of the  $K^-$  with the hadronic environment which is encoded in the self-energies  $\Pi_i(\omega, \mathbf{q}, \rho)$ . For the  $K^-$  the free propagator  $D_0^{-1}$  has to be replaced by the dressed propagator  $D^{-1}$

$$D_0^{-1} \propto \omega^2 - \mathbf{q}^2 - m_K^2 \rightarrow D^{-1} \propto \omega^2 - \mathbf{q}^2 - m_K^2 - \Pi_{K^-}(\omega, \mathbf{q}, \rho) . \quad (29)$$

The middle part of Fig. ii.3 shows the spectral function if we use both, the Pauli principle and the dressed  $K^-$  propagator. The spectral function broadens and the energy of the  $\Lambda(1405)$  is lowered because the attractive  $K^-N$  interaction counteracts the increase of the energy of the  $\Lambda(1405)$  - hole state [14] due to the Pauli principle. Consequently, the two separate peaks merge into one. In addition, the strength in the  $K^-$  channel is lowered.

Finally one also has to dress the pion propagator. The result of this is shown in the bottom part of Fig. ii.3. For the choice of the dressing of Ref. [34] the spectral function becomes very broad which raises the question whether the  $K^-$  can still be treated as a quasi particle, i.e. with a fixed relation  $\omega^2 = m^{*2} + \mathbf{q}^2$ . The way how the pion dressing has to be done is currently very much debated and different suggestions gave different results for the spectral function [14, 35, 36].

The other particles which appear in Eq. (26) have large masses. Therefore, their dressing does not influence the results in the  $K^-$  sector.

Limiting the discussion to those theories in which the in-medium modification of the  $K^-$  propagators are calculated self-consistently, one finds essentially two different approaches, that of the group of Ramos, Oset and Tolos [34, 35, 37–39] and that of Lutz and Korpa [14, 18, 40]. Both of them became more and more refined over the years. Sometimes the calculations are limited to s-wave scattering whereas others include p-waves in order to have a wider dynamical range for constraining the parameters. Both use the same strategy to determine the parameters of the  $K^-N$  interaction in fitting the available free scattering data and both use this interaction subsequently in a Bethe-Salpeter equation. The models differ in the form of the interaction as well as in the dressing of the propagators and in the regularization of the loop integrals of Eq. (26).

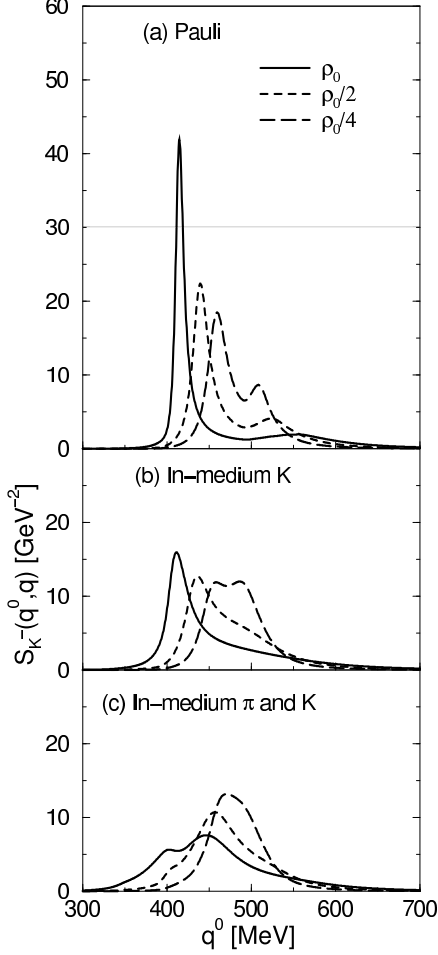


FIG. ii.3:  $K^-$  spectral density for zero momentum as a function of energy at several densities:  $\rho_0$  (solid line),  $\rho_0/2$  (short-dashed line) and  $\rho_0/4$  (long-dashed line). Results are shown for the three approximations discussed in the text: a) Pauli blocking (top panel), b) Pauli blocking and in-medium kaons (middle panel) and c) Pauli blocking and in-medium pions and kaons (bottom panel). The figure is taken from Ramos *et al.* (Ref. [34]).

### 3. Approach by Ramos *et al.*

Ramos, Oset and Tolos [35, 37] start from the chiral Lagrangian in lowest order in momentum and with the complete set of the pseudoscalar mesons and the baryon  $1/2^+$  octet including s- and p- waves. Later Tolos *et al.* [41] added self-consistency in the  $K^-$  propagator. Projecting onto positive-energy states in the Dirac equation for the nucleons they obtained a three-dimensional equation of the Brückner-Goldstone type

$$\langle M_1 B_1 | T(\Omega) | M_2 B_2 \rangle = \langle M_1 B_1 | V(\sqrt{s}) | M_2 B_2 \rangle$$



$$+ \sum_{M_3 B_3} \langle M_1 B_1 | V(\sqrt{s}) | M_3 B_3 \rangle \frac{Q_{M_3 B_3}}{\Omega - E_{M_3} - E_{B_3} + i\eta} \langle M_3 B_3 | T(\Omega) | M_2 B_2 \rangle \quad (30)$$

with

$$E_{M_i(B_i)}(k, \omega) = \sqrt{k^2 + m_{M_i(B_i)}^2} + \Pi_{M_i(B_i)}(k, \omega) . \quad (31)$$

$Q_{M_3 B_3}$  is the Pauli operator. Due to the possible decay into the  $\pi$ -hyperon channel the self-energies  $\Pi_{M_i(B_i)}(k, \omega)$  become complex. The optical  $K^-N$  potential  $U_{\text{opt}}(k, \rho)$  is obtained via the relation

$$U_{\text{opt}}(k, \rho) = \frac{\Pi_{K^-}(k, \omega = \sqrt{k^2 + m_k^2})}{2\sqrt{k^2 + m_k^2}} . \quad (32)$$

The baryon potential is parameterized in different ways with values of about -70 MeV for nucleons and -30 MeV for hyperons at  $\rho_0$ . The  $K^-$  self-energy is calculated self-consistently on the quasi-particle level using

$$\Pi_{K^-}(k, \omega) = \sum_{N \leq F} \langle K^- N | T_{K^- N \rightarrow K^- N}(\Omega = E_N + E_{K^-}) | K^- N \rangle, \quad (33)$$

where  $T$  is defined in Eq. (30). An extension to self-consistency on the level of the spectral function has been given in Ref. [37]. The self-energy of the pion is taken from Ref. [35].

Given the self-energies of the  $K^-$  and of the  $\pi$ , we can write their propagators as

$$D_i(q^0, \mathbf{q}, \rho) = \frac{1}{(q^0)^2 - \mathbf{q}^2 - m_i^2 - \Pi_i(q^0, \mathbf{q}, \rho)} \quad (34)$$

( $i = K^-, \pi$ ) with the corresponding spectral densities

$$S_i(\omega, \mathbf{q}, \rho) = -\frac{1}{\pi} \text{Im} D_i(\omega, \mathbf{q}, \rho) = -\frac{1}{\pi} \frac{\text{Im} \Pi_i(\omega, \mathbf{q}, \rho)}{|\omega^2 - \mathbf{q}^2 - m_i^2 - \Pi_i(\omega, \mathbf{q}, \rho)|^2} . \quad (35)$$

The spectral density obtained in this approach for the  $K^-$  has already been shown in Fig. ii.3. The effective mass of the  $K^-$ , the solution of the dispersion relation

$$\omega^2 = \mathbf{q}^2 + m_K^2 + \text{Re} \Pi_{K^-}(\omega, \mathbf{q}, \rho) \quad (36)$$

for  $\mathbf{q} = \mathbf{0}$ , is displayed as a function of density in Fig. ii.4. The effective mass of the  $K^-$  is reduced but by far not as much as shown in the original paper of Kaplan and Nelson.

Tolos *et al.* [39] use the same equation (Eq. 30) but with two important changes: For the interaction  $V(\sqrt{s})$  they use the  $K^-N$  potential of the Jülich group [42] which is based on meson-exchange and which describes the available scattering data also quite reasonably. To simplify the calculation they limit the self-consistent calculation of the self-energy  $\Pi_{K^-}(\omega, \mathbf{q}, \rho)$  to the quasi-particle branch  $\Pi_{K^-}^{qp}(\omega = \sqrt{m_k^2 + k^2}, \mathbf{q}, \rho)$ . In addition they use a different parametrization of the baryon potentials

$$U_{\Lambda, \Sigma} = -30 \frac{\rho}{\rho_0}, \quad (37)$$

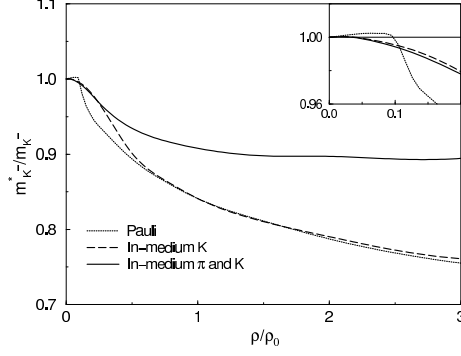


FIG. ii.4: Effective mass of the  $K^-$  meson in nuclear matter as a function of density for the three approximations shown in Fig. ii.3 and discussed in the text: *Pauli blocking* (dotted lines), *Pauli blocking and in-medium kaons* (dashed lines) and *Pauli blocking and in-medium pions and kaons* (solid lines). The inset shows details at low densities. The figure is taken from Ref. [34]

and

$$U_N(\rho, k) = \alpha(\rho) + \frac{\beta(\rho)}{1 + \left[ \frac{k}{\gamma(\rho)} \right]^2} \quad (38)$$

with density-dependent functions  $\alpha, \beta, \gamma$ . From the self-consistent on-shell self-energy  $\Pi_{K^-}(k_{K^-}, E_{K^-}^{qp})$  one obtains via dispersion relation the complete energy dependence of the self-energy,  $\Pi_{K^-}(k_{K^-}, \omega)$ , which can be used to determine the  $K^-$  single-particle propagator in the medium,

$$D_{K^-}(k_{K^-}, \omega) = \frac{1}{\omega^2 - k_{K^-}^2 - m_{K^-}^2 - 2m_{K^-}\Pi_{K^-}(k_{K^-}, \omega)}, \quad (39)$$

and the corresponding spectral density

$$S_{K^-}(k_{K^-}, \omega) = -\frac{1}{\pi} \text{Im} D_{K^-}(k_{K^-}, \omega). \quad (40)$$

The  $K^-N$  potential of this approach is displayed in Fig. ii.5 and the spectral function in Fig. ii.6. The influence of the  $K^-$  momentum dependence of the optical potential on the observables in heavy-ion collisions will be discussed in the *K^- chapter*. Later this model has been extended to finite temperatures [35]. The results, displayed in Fig. ii.7, show that at  $\rho_0$  and a temperature of 70 MeV, which we encounter in reactions with beam energies around  $E_{\text{beam}} = 1 - 2A$  GeV, the general behavior does not change but the double-hump structure of the spectral function has disappeared. In heavy-ion collisions the  $K^-$  therefore behaves as a quasi particle albeit with a large width of about 150 MeV.

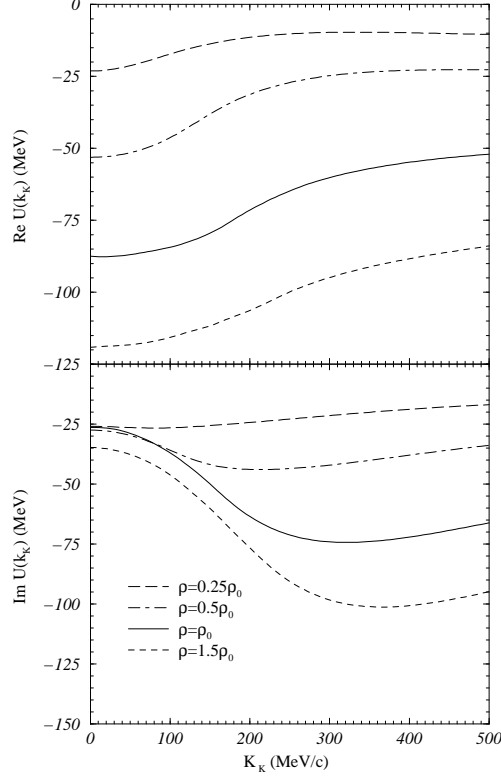


FIG. ii.5: Real and imaginary parts of the  $K^-$  optical potential as functions of the  $K^-$  momentum for various densities. The figure is taken from Ref.[39].

#### 4. Approach by Lutz *et al.*

The work of Lutz *et al.* [18, 32] starts out as well from the Bethe-Salpeter equation (Eq.( 28)). It uses, however, a different reduction to the three-dimensional Brückner-Goldstone equation. Assuming also that the interaction vertices do not change in the medium,  $\mathcal{K} = K$ , the in-medium reaction amplitude  $\mathcal{T}$  can be expressed in terms of the on-shell  $T$  matrices and propagator modifications  $\Delta G \equiv \mathcal{G} - G$ . In the case of the  $I = 0$  channel [32] (denoting the channel  $K^-N$  by the index “1” and  $\pi\Sigma$  by “2”) we write out the [11]-component of the matrix Bethe-Salpeter equation:

$$\mathcal{T}_{11} = T_{11} + T_{11} \Delta G_1 \mathcal{T}_{11} + T_{12} \Delta G_2 \mathcal{T}_{21}. \quad (41)$$

Similarly, the [21]-component allows to solve for the  $\mathcal{T}_{21}$  in terms of  $\mathcal{T}_{11}$  and  $\mathcal{T}_{22}$ :

$$\mathcal{T}_{21} = (1 - T_{22} \Delta G_2)^{-1} [T_{21} + T_{21} \Delta G_1 \mathcal{T}_{11}]. \quad (42)$$

Substituting Eq. (42) into (41) we obtain:

$$\mathcal{T}_{11} = \hat{T}_{11} + \hat{T}_{11} \Delta G_1 \mathcal{T}_{11}, \quad (43)$$

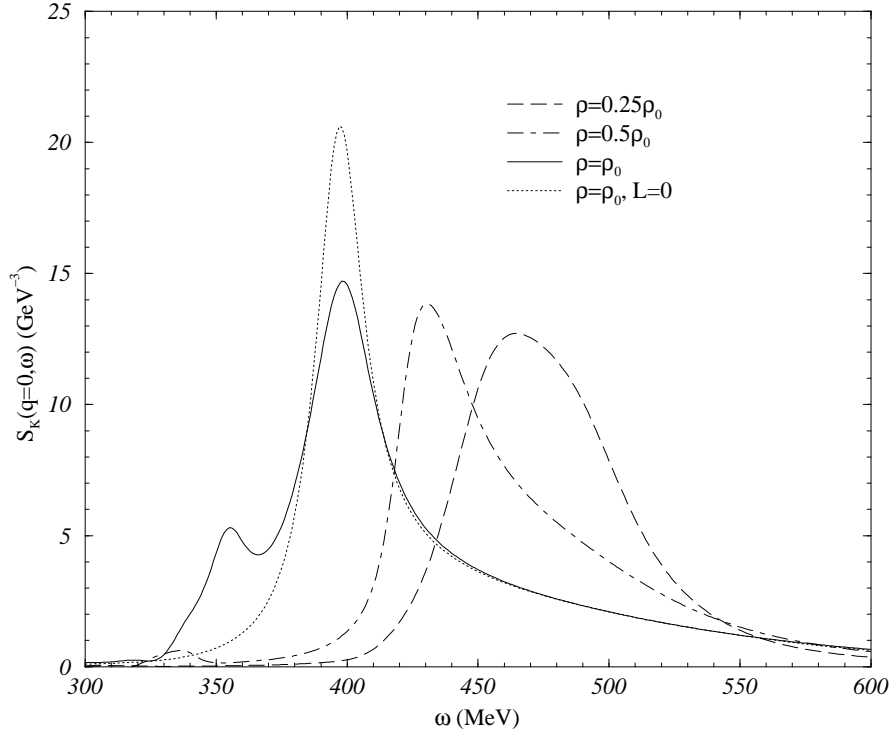


FIG. ii.6:  $\bar{K}$  spectral density at  $k_{\bar{K}} = 0$  as a function of energy for various densities. The curve  $L=0$  includes s-wave only. The figure is taken from Ref.[39].

where we introduced

$$\hat{T}_{11} \equiv T_{11} + T_{12} \Delta G_2 (1 - T_{22} \Delta G_2)^{-1} T_{21}. \quad (44)$$

In the approach of Lutz *et al.* [40] neither nucleons nor  $\pi$  are dressed. The form of the Bethe-Salpeter equation with and without self-energy of the pions is formally identical but the propagators are different. These pion propagators are input quantities and not self-consistently obtained by the solution of the Bethe-Salpeter equation. The interaction vertices are determined by an extensive comparison of the available KN scattering data with a relativistic chiral Lagrangian in the large  $N_c$  limit which allows to reduce the number of parameters to be adjusted. This comparison is made using s- and p-waves in the partial-wave expansion. The  $K^-$  nucleon potential which is obtained in this approach is displayed in Fig. ii.8, the spectral function in Fig. ii.9.

Comparing the three spectral functions (Figs. ii.3, ii.6 and ii.9) one finds that their general structure is quite similar in the three approaches. In absolute magnitude as well as in detail they differ by factors up to two whereas the models agree in the description of the  $K^+$  in dense matter. Therefore, one has to conclude that the  $K^-$  properties in matter are much less known than those of the  $K^+$ . More important for our numerical simulations is the fact that the extracted optical potentials (Figs. ii.5 and ii.8) differ by about a factor of three at normal nuclear matter density. Consequently, in the case of the  $K^-$ , the predictive power of the results of the simulation programs is strongly limited by the uncertainty of the  $K^-$

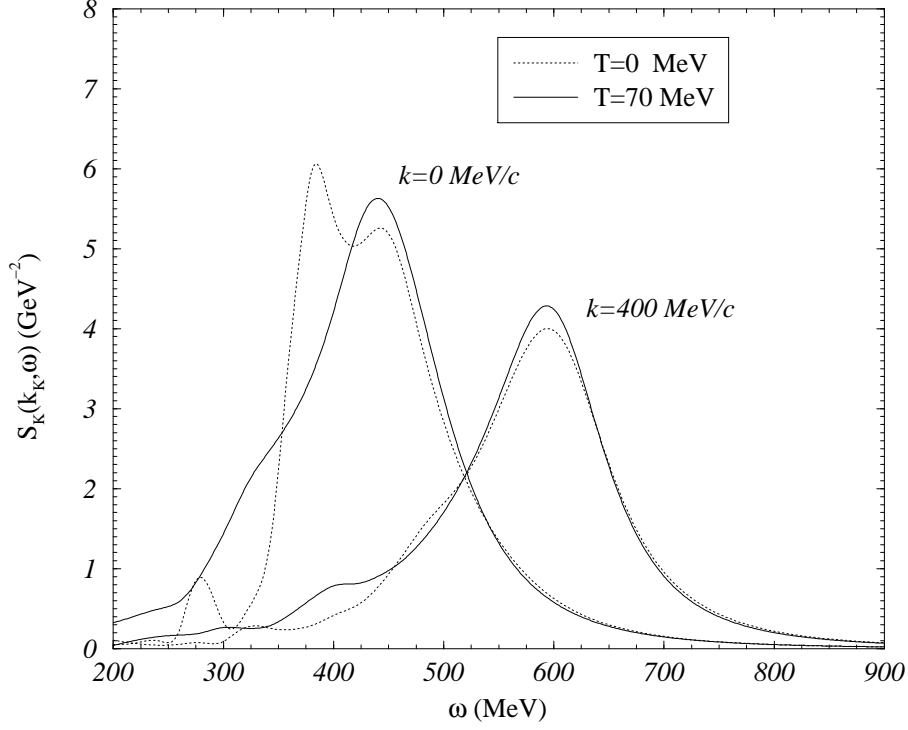


FIG. ii.7: Spectral density of the  $K^-$  at  $\rho_0 = 0.17 \text{ fm}^{-3}$  as a function of energy for  $K^-$  momenta  $k_{\bar{K}} = 0$  and  $k_{\bar{K}} = 400 \text{ MeV}/c$ , and for  $T = 0 \text{ MeV}$  and  $T = 70 \text{ MeV}$ . The figure is taken from Tolos et al. [35].

properties the nuclear matter.

### 5. Kaonic Atoms

Another source of information of the behavior of  $K^-$  mesons in matter are kaonic atoms. In kaonic atoms an electron is replaced by a  $K^-$  which, due to its larger mass, has a finite probability to be in the tail region of the nucleus. Therefore, these systems test the  $K^-N$  potential at very low densities. Both, the fits of phenomenological density-dependent optical potential to the kaonic atom data [36, 43] and relativistic mean field (RMF) calculations by Friedman *et al.* [44], which describe the data quantitatively very well, lead to a deeply attractive potential ( $-\text{Re } V_{\text{opt}}(\rho_0) \approx 150 - 200 \text{ MeV}$ ). Thus, the potential values fitted to kaonic atoms are in conflict with the results of the self-consistent approaches mentioned above which give values of less or about 80 MeV at  $\rho_0$  (see Figs. ii.5 and ii.8). Cieply *et al.* [45] were the first who tried to fit kaonic atom data, low-energy  $K^-N$  and  $K^-$  nucleus scattering data simultaneously using a self-consistent coupled-channels approach, similar to the one of Ref. [34], for  $K^-$  in matter and assuming a Klein-Gordon equation of the form

$$\left[ \nabla^2 - 2\mu(B + V_{\text{opt}} + V_{\text{Coul}}) + (V_{\text{Coul}} + B)^2 \right] \psi = 0 \quad (45)$$

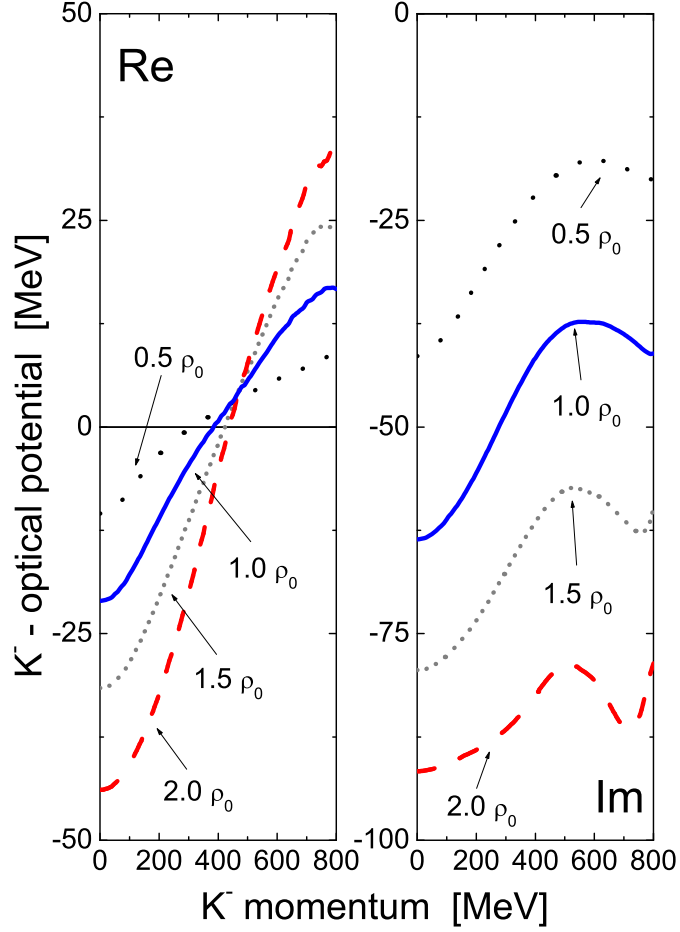


FIG. ii.8: Real and imaginary parts of the  $K^-$  optical potential as functions of the  $K^-$  momentum for various densities from Ref. [15].

for the kaonic atoms.  $B$  is the complex binding energy and  $V_{\text{Coul}}$  is the Coulomb interaction of the hadron with the finite-size nucleus, including vacuum-polarization terms. Equation (45) assumes that the optical potential  $V_{\text{opt}}$  and also  $V_c$  behave as a Lorentz scalars.  $V_{\text{opt}}$  is given by a  $t(\rho)\rho$  form (see Eq. 3)

$$2\mu V_{\text{opt}}(r) = -4\pi\left(1 + \frac{\mu}{M}\right)[a_{K^-p}(\rho)\rho_p(r) + a_{K^-n}(\rho)\rho_n(r)], \quad (46)$$

where  $M$  is the nucleon mass,  $\mu$  is the reduced mass of the  $K^-$  and the nucleus,  $a_{K^-p}$  and  $a_{K^-n}$  are the  $K^-p$  and  $K^-n$  threshold scattering amplitudes evaluated at nuclear matter density  $\rho = \rho_p + \rho_n$ , and  $\rho_p(r)$  and  $\rho_n(r)$  are the proton and neutron density distributions.

These calculations confirmed that a slight modification of the chiral meson-baryon interaction of Ref. [7, 8] yields a relatively shallow attractive real part of the potential ( $\approx 55$  MeV), which is of about the same size as obtained from the  $K^-N$  scattering data if analyzed in the same chirally motivated coupled channel approach. They confirm in addition that

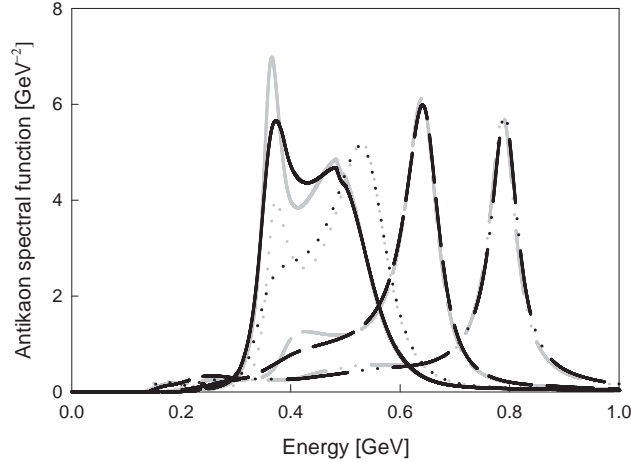


FIG. ii.9: The  $K^-$  spectral function for different momenta: 0 (solid line), 200 MeV (dotted line), 400 MeV (dashed line), and 600 MeV (dash-dot-dot line). Black lines show the result if both, pion and  $K^-$ , are dressed [32], gray lines previous results without pion dressing [40], in the nuclear matter at saturation density.

such a potential can also fit well kaonic atoms with a  $\chi^2$  value which is very close to the value obtained for the deep attractive potential of 180 MeV of Refs. [44, 46]. The authors conclude that kaonic atom data cannot distinguish between shallow and deep potentials and new experiments have to be designed to clarify the depth of the  $K^-N$  potential. For the present status of this discussion we refer to Ref. [46].

### 6. Deeply bound kaonic states in nuclei

Motivated by the conjecture that a very strong  $K^-$  nucleon potential could form a deeply bound  $K^-ppn$  state [47] a systematic experimental search has been launched at the KEK facility. The first results by Suzuki *et al.* [48] showed a structure in the missing-mass spectra in the  ${}^4\text{He}(K^-_{\text{stopped}}, p)$  reaction which — due to kinematic reasons — cannot be due to hypernucleus formation  $(K^- + {}^4\text{He})_{\text{atomic}} \rightarrow \pi^- + {}^4_{\Lambda}\text{He}$ ,  ${}^4_{\Lambda}\text{He} \rightarrow p + {}^3_{\Lambda}\text{H}$ . This structure has been identified with two deeply bound  $\bar{K}NNN$  states

$$(K^- + {}^4\text{He})_{\text{atomic}} \rightarrow S^0(3115) + p \quad (47)$$

and

$$(K^- + {}^4\text{He})_{\text{atomic}} \rightarrow S^+(3140) + n. \quad (48)$$

The properties of these states, however, and especially their binding energies are far from the values predicted in Ref. [47] as seen in Fig. ii.10. More recently in the FINUDA

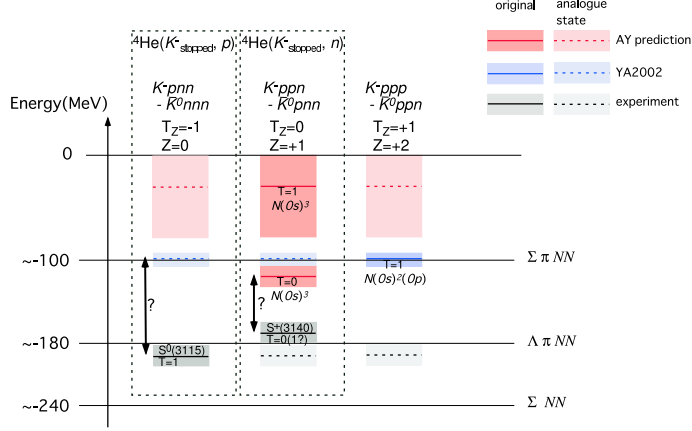


FIG. ii.10: A comparison between non-relativistic calculations of deeply bound kaonic nuclear states and experimental results. The original [47], subsequent [51, 52] predictions, and experimental results are represented by red, blue and grey, respectively.

experiment [49] a proton peak at a very similar proton momentum has been observed in a reaction in which the  ${}^4\text{He}$  has been replaced by a  ${}^6\text{Li}$ . It is not expected that for the two nuclei the binding energy of the  $\text{K}^-$  is identical. Hence this observation has reinforced the interpretation of these structures as a  $\text{K}^-$  absorption on a quasi-deuteron. For the details of this interpretation of deeply bound  $\text{K}^-$  states we refer to Ref. [50] which also concludes that from deeply bound  $\text{K}^-$  states there is presently little experimental evidence for a strong  $\bar{K}\text{N}$  potential. Recently it has been argued [53–55] that there is presently no experimental evidence for deeply bound kaonic clusters.

### C. Strange baryons in matter

The many-body scheme based on the Brückner-Goldstone equation which has been successfully applied to the description of kaons in matter, was recently extended to the hyperonic sector [56–58]. It starts with the construction of all the baryon-baryon (i.e., NN, YN and YY)  $G$ -matrices, which describe in an effective way the interactions between baryons in the presence of a surrounding baryonic medium

$$G(\omega)_{B_1 B_2, B_3 B_4} = V_{B_1 B_2, B_3 B_4} + \sum_{B_5 B_6} V_{B_1 B_2, B_5 B_6} \frac{Q_{B_5 B_6}}{\omega - E_{B_5} - E_{B_6} + i\eta} G(\omega)_{B_5 B_6, B_3 B_4} . \quad (49)$$

In the above expression the first (last) two sub-indices indicate the initial (final) two-baryon states compatible with a given value  $S$  of the strangeness, namely NN for  $S = 0$ , YN for  $S = -1, -2$ , and YY for  $S = -2, -3, -4$ ,  $V$  is the bare baryon-baryon interaction,  $Q_{B_5 B_6}$  is the Pauli operator which prevents the intermediate baryons  $B_5$  and  $B_6$  from being scattered to states below their respective Fermi momenta, and  $\omega$ , the so-called starting energy, corresponds to the sum of non-relativistic single-particle energies of the interacting



baryons (see Ref. [58] for details). The single-particle energy of a baryon  $B_i$  is given by

$$E_{B_i} = M_{B_i} + \frac{k^2}{2M_{B_i}} + \text{Re}[U_{B_i}(k)] , \quad (50)$$

where  $M_{B_i}$  denotes the rest mass of the baryon and the real part of the single-particle potential  $U_{B_i}(k)$  is the averaged field “felt” by the baryon due to its interaction with the other baryons of the medium. In the BHF approximation,  $U_{B_i}(k)$  is given by (see Eq. 33)

$$U_{B_i}(k) = \sum_{B_j} \sum_{k'} n_{B_j}(k') \langle \mathbf{k}\mathbf{k}' | G_{B_i B_j, B_i B_j}(\omega = E_{B_i} + E_{B_j}) | \mathbf{k}\mathbf{k}' \rangle , \quad (51)$$

where

$$n_{B_j}(k) = \begin{cases} 1, & \text{if } k \leq k_{F_{B_j}} \\ 0, & \text{otherwise} \end{cases} \quad (52)$$

is the corresponding occupation number of the species  $B_j$ . A sum over all the different baryon species is performed and the matrix elements are anti-symmetrized when baryons  $B_i$  and  $B_j$  belong to the same isomultiplet.

The result of this calculation is shown in Fig. ii.11. The potential of strange baryons is considerably shallower than that of protons and neutrons and can even get repulsive for the multi-strange baryons. These findings are in agreement with measured  $a_{\Lambda N}$  scattering length of about 2 fm [59].

In the simulation of heavy-ion collisions, discussed in the following, this reduction of the single-particle potential of strange baryons is taken into account by assuming that the strange quark is inert with respect to the hadronic mean field and therefore  $U_{\Lambda, \Sigma} = 2/3 U_{\text{p,n}}$ .

### III. MICROSCOPIC DESCRIPTION WITHIN IQMD

The detailed analysis of strangeness production presented in this article was performed using the Isospin Quantum Molecular Dynamics model (IQMD) [3, 60–63], which is a semi-classical model simulating heavy-ion collisions on an event-by-event basis. We briefly sketch the model here and refer for a detailed description to Refs. [3, 61, 62]. Furthermore the derivation of the basic transport equations, the description in terms of Skyrme potentials, and the considerations for exploring the nuclear equation of state in heavy-ion collisions can be found in Ref. [64]. General information on microscopic models of heavy-ion collisions and on different numerical realizations are given in Refs. [5, 65–67]. In order to have a comparison with other transport models, some of the results presented in this report are as well calculated using the Hadron-String-Dynamics model (HSD) [4, 68, 69] in the version as presented in Ref. [70]. This microscopic model includes higher resonances in the baryonic and mesonic sector and is therefore also applicable in the range of several tens of GeV. The results for antikaons [69] in HSD have been obtained in a version which includes off-shell propagation of resonances.

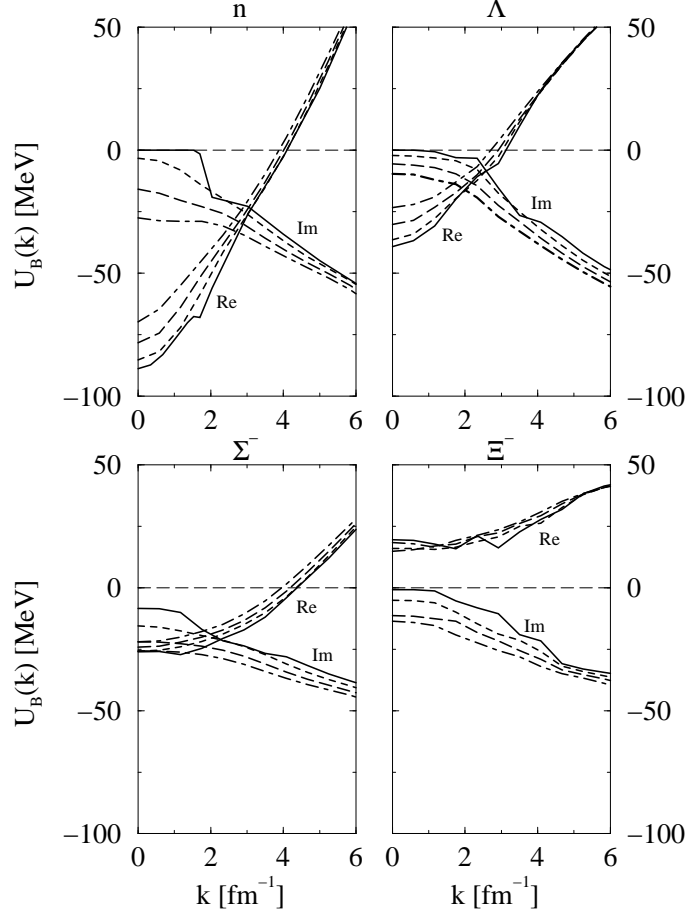


FIG. ii.11: Single-particle potential of the octet baryons at  $\rho_0$  as a function of momentum for various temperatures:  $T = 0$  (solid lines), 20 MeV (short-dashed lines), 40 MeV (long-dashed lines) and 60 MeV (dot-dashed lines). The figure is from Ref. [58].

### A. Nucleon-nucleon-potentials in IQMD

In IQMD a particle is represented by the single-particle Wigner density

$$f_i(\mathbf{r}, \mathbf{p}, t) = \frac{1}{\pi^3 \hbar^3} e^{-\frac{2}{L}(\mathbf{r}-\mathbf{r}_i(t))^2} e^{-\frac{L}{2\hbar^2}(\mathbf{p}-\mathbf{p}_i(t))^2} . \quad (53)$$

The total one-body Wigner density is the sum of the Wigner densities of all nucleons. The particles move according to Hamiltonian equations of motion

$$\dot{r}_i = \frac{\partial \langle H \rangle}{\partial p_i} \quad \dot{p}_i = -\frac{\partial \langle H \rangle}{\partial r_i} , \quad (54)$$

where the expectation value of the total Hamiltonian is

$$\begin{aligned} \langle H \rangle &= \langle T \rangle + \langle V \rangle \\ &= \sum_i \frac{p_i^2}{2m_i} + \sum_i \sum_{j>i} \int f_i(\mathbf{r}, \mathbf{p}, t) V(\mathbf{r}, \mathbf{r}', \mathbf{p}, \mathbf{p}') f_j(\mathbf{r}', \mathbf{p}', t) d\mathbf{r} d\mathbf{r}' d\mathbf{p} d\mathbf{p}' . \end{aligned} \quad (55)$$

The in-medium nucleon-nucleon potential interaction consists of the real part of the Brückner  $G$ -Matrix [71] with an additional Coulomb interaction between the charged particles. The former is modelled here by a sum of several terms: A contact interaction of Skyrme-type, a finite-range Yukawa term, a momentum-dependent interaction, and a symmetry contact interaction that distinguishes between protons and neutrons

$$\begin{aligned}
V(\mathbf{r}_i, \mathbf{r}_j, \mathbf{p}_i, \mathbf{p}_j) &= G + V_{\text{Coul}} \\
&= V_{\text{Skyrme}} + V_{\text{Yuk}} + V_{\text{mdi}} + V_{\text{sym}} + V_{\text{Coul}} \\
&= t_1 \delta(\mathbf{r}_i - \mathbf{r}_j) + t_2 \delta(\mathbf{r}_i - \mathbf{r}_j) \rho^{\gamma-1}(\mathbf{r}_i) + \\
&\quad t_3 \frac{\exp\{-|\mathbf{r}_i - \mathbf{r}_j|/\mu\}}{|\mathbf{r}_i - \mathbf{r}_j|/\mu} + \\
&\quad t_4 \ln^2(1 + t_5(\mathbf{p}_i - \mathbf{p}_j)^2) \delta(\mathbf{r}_i - \mathbf{r}_j) + \\
&\quad t_6 \frac{1}{\rho_0} T_3^i T_3^j \delta(\mathbf{r}_i - \mathbf{r}_j) + \frac{Z_i Z_j e^2}{|\mathbf{r}_i - \mathbf{r}_j|}.
\end{aligned} \tag{56}$$

The local Skyrme term contains an attractive term linear in the baryonic density  $\rho$  and a repulsive term yielding a power law dependence  $\rho^\gamma$  which also simulates effectively many-particle correlations; for more details see e.g. Ref. [64]. The finite-range Yukawa term (with  $t_3 = -6.7$  MeV and  $\mu = 1.5$  fm) is important to stabilize the surface of a finite nucleus. The momentum dependence  $V_{\text{mdi}}$  of the NN interaction, which may optionally be used in IQMD, is fitted to experimental data [72–74] on the real part of the nucleon optical potential [75–77]. This yields the parameters  $t_4 = 1.57$  MeV and  $t_5 = 5 \cdot 10^{-4}$  MeV $^{-2}$ . The very simplified asymmetry term, where  $T_3^i$  and  $T_3^j$  denote the isospin projection  $T_3$  of the nucleons  $i$  and  $j$  (i.e.  $1/2$  for protons and  $-1/2$  for neutrons) with a strength of  $t_6 = 100$  MeV gives a symmetry energy which is linear in the density difference of protons and neutrons.

For a nucleus in its ground state, the expectation value of the total Hamiltonian has to correspond to its total binding energy. When comparing to the Bethe-Weizsäcker mass formula the kinetic energy, the Skyrme interaction, and the momentum-dependent interaction contribute to the volume energy, the Yukawa interaction to the surface and the volume energy, and the symmetry interactions to the volume symmetry energy. There is no term corresponding to the pairing energy since it corresponds to a global property of the nucleus which would be difficult to model by microscopic local forces. Besides protons and neutrons the IQMD model includes the  $\Delta$  resonance as degree of freedom. Concerning the Skyrme-, Yukawa- and momentum-dependent interactions the  $\Delta$ 's are treated like “heavy nucleons”, i.e. they interact with the same coupling constants as nucleons. Coulomb interactions are performed with their real charges. However, no symmetry interaction is assumed for the  $\Delta$ .

The nuclear equation of state (EoS), on the other hand, describes the properties of infinite nuclear matter (without Coulomb interactions) and is therefore given by the volume energy only. The EoS describes the variation of the energy  $E(T = 0, \rho/\rho_0)$  when changing the nuclear density to values different from the saturation density  $\rho_0$  for zero temperature. Often

nuclear matter is assumed to be isospin saturated, but we also consider asymmetric nuclear matter, where the symmetry energy term contributes. In fact, the density dependence of the symmetry energy has recently been of great interest [78].

The single-particle potential resulting from the convolution of the distribution functions  $f_i$  and  $f_j$  with the interactions  $V_{\text{Skyme}} + V_{\text{Yuk}} + V_{\text{mdi}}$  (local interactions including their momentum dependence) is for symmetric nuclear matter

$$U_i(\mathbf{r}_i, t) = \alpha \left( \frac{\rho_{int}}{\rho_0} \right) + \beta \left( \frac{\rho_{int}}{\rho_0} \right)^\gamma + \delta \ln^2 \left( \varepsilon (\Delta \mathbf{p})^2 + 1 \right) \left( \frac{\rho_{int}}{\rho_0} \right), \quad (57)$$

where  $\rho_{int}$  is the interaction density obtained by convoluting the distribution function of a particle with the distribution functions of all other particles of the surrounding medium.  $\Delta \mathbf{p}$  is the relative momentum of a particle with respect to the surrounding medium.

The parameters  $t_1 \dots t_5$  in Eq. (56) are uniquely related to the coefficients  $\alpha, \beta, \gamma, \delta$ , and  $\varepsilon$  in Eq. (57). Values of these parameters for the different model choices can be found in Tab. I.

	$\alpha$ (MeV)	$\beta$ (MeV)	$\gamma$	$\delta$ (MeV)	$\varepsilon \left( \frac{c^2}{\text{GeV}^2} \right)$	$K$ (MeV)
S	-356	303	1.17	—	—	200
SM	-390	320	1.14	1.57	500	200
H	-124	71	2.00	—	—	376
HM	-130	59	2.09	1.57	500	376

TABLE I: Parameter sets for the nuclear equation of state used in the IQMD model

The parameters  $\varepsilon$  and  $\delta$  are given by fits to the experimentally measured optical potential.  $E/A = -16$  MeV at the ground-state density  $\rho_0$  and  $\rho_0 = 0.16 \text{ fm}^{-3}$  are two constants for the three parameters  $\alpha, \beta, \gamma$ . The remaining degree of freedom is related to the compression modulus  $K$  of the nucleus, which corresponds to the curvature of the volume energy at  $\rho = \rho_0$  (for  $T = 0$ ) and is also given in Tab. I

$$K = -V \frac{dp}{dV} = 9\rho^2 \frac{d^2 E/A(\rho)}{(d\rho)^2} \Big|_{\rho=\rho_0}. \quad (58)$$

An equation of state with a rather low value of the compression modulus  $K$  yields a weak repulsion of compressed nuclear matter and thus describes "soft" matter (denoted by "S"). A high value of  $K$  causes a strong repulsion of nuclear matter under compression (called a "hard EoS", H). The parameters of the momentum-dependent interactions  $\delta$  and  $\varepsilon$  can optionally be switched on (denoted "with mdi", parametrization HM and SM) or off (denoted "no mdi").

In the calculations presented in this article the standard parametrization is SM. It was shown to describe best many observables of intermediate energy heavy-ion collisions, (see e.g. [79–81]) as will also be seen for the kaon production in the later sections of this article.

## B. Kaon-nucleon potentials

The kaons and antikaons interact with the nuclear medium via a Schrödinger-type potential of the form

$$U_{\text{opt}} = \omega(\mathbf{k}, \rho) - \sqrt{\mathbf{k}^2 + m^2} \quad (59)$$

where  $\omega$  and  $\mathbf{k}$  are the energies and momenta of the (anti)kaon.

For the calculation of the energy  $\omega$  we consider the  $K^-$  as stable quasi particles. This allows us using the relativistic mean field (RMF) calculations of Schaffner-Bielich et al. [10, 82]. For a comparison of this approach with chiral perturbation theory we refer to [82]:

$$\omega(\mathbf{k}, \rho) = \sqrt{(\mathbf{k} - \boldsymbol{\Sigma}_{\mathbf{v}})^2 + m^2 + m\Sigma_s} \pm \Sigma_v^0 \quad (60)$$

with a scalar self energy  $\Sigma_s$  and a vector self energy  $(\Sigma_v^0, \boldsymbol{\Sigma}_{\mathbf{v}})$ , where the sign of the vector term  $\pm \Sigma_v^0$  is positive for kaons and negative for antikaons. This leads to different energies of kaons and antikaons as it is seen in Fig. iii.1. The terms of the scalar potential  $\Sigma_s$  are related to the field of the  $\sigma$  which itself is related in a non-linear way to the scalar density  $\rho_s$

$$\Sigma_s = g_{\sigma K} \sigma ; \quad -g_{\sigma N} \rho_s = m_\sigma + b\sigma^2 + c\sigma^3. \quad (61)$$

For the coupling constants we use the parametrization TM1 of [82] :

$$g_{\sigma K} = 1.93 \quad g_{\sigma N} = 10.0289 \quad (62)$$

and for the description of the  $\sigma$ -field we use

$$m_\sigma = 511.198 \text{ MeV} \quad b = -7.2325 \text{ fm}^{-1} \quad c = 0.6183. \quad (63)$$

The vector potential is related to the baryon density  $\rho_B$  by

$$\Sigma_v^0 = g_{\omega K} V_0 \quad \boldsymbol{\Sigma}_{\mathbf{v}} = g_{\omega K} V_0 \boldsymbol{\beta}_{KN} \quad V_0 = \frac{g_{\omega N}}{m_\omega^2} \rho_B \quad (64)$$

where  $\boldsymbol{\beta}_{KN}$  is the relative velocity of the kaon to the nuclear medium. Again, the coupling constants are taken from the TM1 set of [82] :

$$g_{\omega K} = 3.02 \quad g_{\omega N} = 12.6139 \quad m_\omega = 783 \text{ MeV}. \quad (65)$$

In order to compare our approach with other models, we can approximate  $\omega(\mathbf{k} = 0, \rho) = m_{K^\pm}(\rho)$  by the linear relations

$$m_{K^+}(\rho) = m_{K^+}(\rho = 0) \left(1 + \alpha_{K^+} \frac{\rho}{\rho_0}\right) \quad (66)$$

$$m_{K^-}(\rho) = m_{K^-}(\rho = 0) \left(1 + \alpha_{K^-} \frac{\rho}{\rho_0}\right). \quad (67)$$

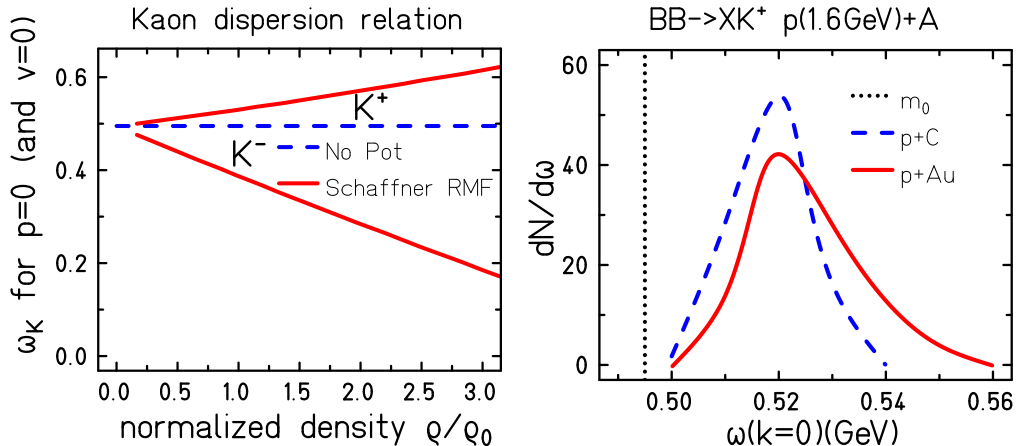


FIG. iii.1: Left: The function of the kaon rest energy  $\omega(\mathbf{k} = \mathbf{0})$  as function of the baryonic density. Right: Distribution of the rest energies of  $K^+$  produced in BB-BYK collisions in a p+A reaction.

A value of  $\alpha_{K^+} = 0.08$  reproduces the calculations of [32]. The HSD model, advanced before detailed calculations became available, uses  $\alpha_{K^+} = 0.04$ . For  $\alpha_{K^-}$  we obtain  $-0.21$ .

In later sections we may modify the strength of our potential in order to study its significance. This will be done by applying a factor  $\alpha$  to the scalar and vector potentials:

$$\omega_\alpha(\mathbf{k}, \rho) = \sqrt{(\mathbf{k} - \alpha \Sigma_v)^2 + m^2 + m\alpha \Sigma_s \pm \alpha \Sigma_v^0} \quad (68)$$

A value of  $\alpha = 0$  corresponds to a calculation without KN-potentials, while  $\alpha = 1$  corresponds to our standard potential described above. Note that we assume  $\alpha = 1$  as default, if not explicitly stated to have a different value.

Figure iii.1, left, shows the dependence of  $\omega(\mathbf{k} = \mathbf{0}, \rho)$  of  $K^+$  and  $K^-$  (eq.60) as a function of the density of the nuclear medium. The nuclear medium is assumed to be at rest, otherwise an additional contribution from the vector potential will show up. The energy rises with density if we consider a kaon, but it falls for the antikaons. Since this energy is the minimum energy needed to create a (anti)kaon in the medium, it follows that the KN potential enhances the threshold for kaon production but reduces it for antikaons.

The right panel of Fig. iii.1 shows the effect of the kaon potential on the distribution of the kaon rest energy  $\omega(\mathbf{k} = \mathbf{0}, \rho)$  of  $K^+$  in p+A collisions at 1.6 GeV incident energy. For this analysis we selected both production channels,  $NN \rightarrow YNK^+$  and  $NN \rightarrow N NK^+ K^-$ . The former is energetically more favorable (and thus more probable). The kaons produced in p+Au collisions (red full line) reach higher values of  $\omega$  than the kaons produced in p+C collisions (blue dashed line). The density profile of carbon and gold nuclei are quite different and the gold nucleus allows a better study of the effect of the nuclear medium. For most of the kaons the rest energy is enhanced by about 20-30 MeV with respect to the free case (black dotted line) corresponding to a density at production between  $1/2\rho_0$  and  $3/4\rho_0$ .

For antikaons the situation is different. The optical potential lowers their production threshold as shown in Fig. iii.2 which displays the distribution of the rest energies  $\omega(\mathbf{k} = \mathbf{0}, \rho)$

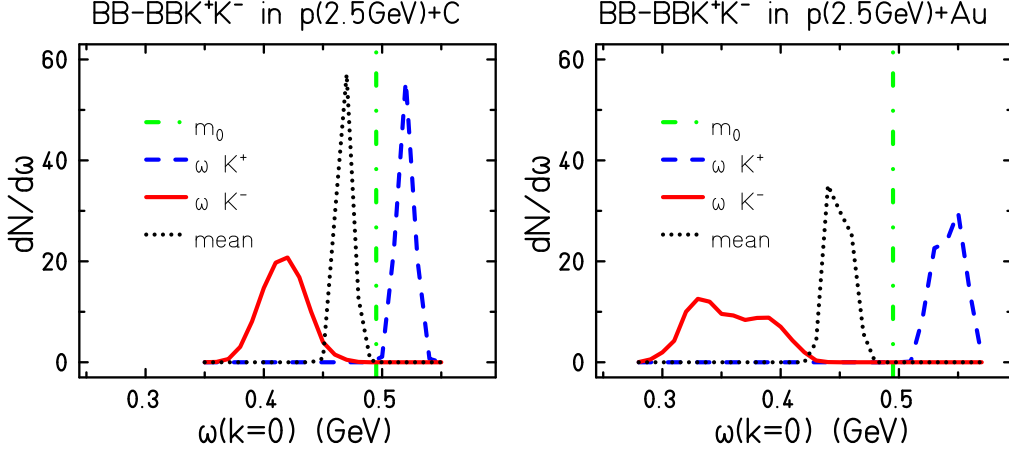


FIG. iii.2: Energies of kaons and antikaons produced in pair production reactions of p+C (left) and p+Au (right)

of  $K^-$  (red full line) and  $K^+$  (dashed blue line) produced in a p+C collisions (left) resp. p+Au collision (right) at 2.5 GeV incident energy. Again the effects are stronger in the case of p+Au than for p+C. It should be noted that due to strangeness conservation the  $K^-$  have to be produced together with a  $K^+$ . The decrease of the rest energy of the antikaon is not compensated by the increase of the rest energy of the kaon. On the average the change of the both rest energies (black dotted line) is negative and therefore the threshold for the reaction  $NN \rightarrow NNK^+ K^-$  is lowered in the medium as compared to a production in free space.

It should be noted that for the production of a kaon in matter, the determination of the threshold has to include the potential contributions of all particles (nucleons, hyperons, kaons) in the ingoing and in the outgoing channels. For instance, the momentum-dependent potential of an out-coming nucleon has to be consistent with the total available energy. Similarly the momentum dependence of the produced kaon depends on its relative momentum with respect to the nuclear medium. This requires an iteration procedure, since the available momentum of the nucleon and the kaon are themselves dependent on the available energy. However, it is found that the shift of the threshold (and thus also the production yield of the kaon) depends on the application of a momentum dependence of the nucleons but not on the application of a momentum dependence of the kaons. This is due to the effect that normally the center of mass of a high energy collision has a low relative velocity with respect to the total nuclear medium. When a collision takes place at an energy nearby the threshold, the kaon will obtain a small relative velocity with respect to the center of mass of the system and thus a small relative velocity with respect to the nuclear medium. The incoming nucleons, however, had to show a high relative velocity to the medium in order to obtain the required high energy.

### C. Collisions

In addition to the propagation of particles in the simulation, collisions can take place. We use the common description that two particles collide, if their minimum distance  $d$  in their c.m.-frame, i.e. the minimum distance of the centroids of the Gaussians, fulfills the requirement

$$d \leq d_0 = \sqrt{\frac{\sigma_{\text{tot}}}{\pi}}, \quad \sigma_{\text{tot}} = \sigma(\sqrt{s}, \text{type}), \quad (69)$$

where "type" denotes the collision type considered (e.g. NN,  $N\Delta$ , ...). The total cross section is the sum of the elastic and all inelastic cross sections

$$\sigma_{\text{tot}} = \sigma_{\text{el}} + \sigma_{\text{inel}} = \sigma_{\text{el}} + \sum_{\text{channels}} \sigma_i \quad . \quad (70)$$

For instance, for a pp collision the important contributions are

$$\sigma_{\text{tot}} = \sigma_{\text{el}} + \sigma(\text{pp} \rightarrow \text{p}\Delta^+) + \sigma(\text{pp} \rightarrow \text{n}\Delta^{++}) \quad . \quad (71)$$

We use systematically free cross sections as given by experiments with the exception of the  $\text{NN} \rightarrow \text{K}^+ \Lambda\text{N}$  channel, where experiments have revealed a strong final state interaction which is not present in matter. Different isospin channels are weighted by isospin coefficients, e.g. for a pp collision we have

$$\sigma(\text{pp} \rightarrow \text{n}\Delta^{++}) = 3\sigma(\text{pp} \rightarrow \text{p}\Delta^+) = \frac{3}{4}\sigma_{\text{inelastic}}. \quad (72)$$

Experimentally inaccessible cross sections like  $\Delta\text{N} \rightarrow \text{NN}$  are calculated from their reverse reactions (here  $\text{NN} \rightarrow \Delta\text{N}$ ) using detailed balance. For reactions involving unstable particles with a finite width the form derived in Ref. [84] is used.

The probability that a collision leads to a particular channel is given by the contribution of this channel to the total cross section

$$P_{\text{channel}} = \frac{\sigma_{\text{channel}}}{\sigma_{\text{tot}}} ; \quad \text{e.g.} \quad P_{\text{pp} \rightarrow \text{p}\Delta^+} = \frac{1}{4} \frac{\sigma_{\text{tot}} - \sigma_{\text{el}}}{\sigma_{\text{tot}}} \quad . \quad (73)$$

For the example we used Eqs. (70,71,72). In the numerical simulation the channel is chosen randomly according to the probability of the channel, e.g. in the above case, there will be a 25% chance to obtain a  $\Delta^+$  in an inelastic pp-collision.

### D. Virtual particles

The production of kaons in this energy domain is a very rare process with a production cross section of only a few nanobarns, in comparison to the total NN cross section of about 20-40 mb. The probability of producing strangeness is thus very small. Then, the method presented above will lead to severe limitations in statistics for the investigation of kaon



production. Nevertheless, simulation codes oriented toward higher collision energies, like UrQMD [67, 85] apply successfully this method for reactions above the threshold. Results of such calculations (without a mean field) on global kaon spectra and rapidity distributions in Ni+Ni collisions at 1.93 A GeV are quite comparable to IQMD results [86]. However, detailed investigations of triple differential cross sections and differential flow patterns (like  $v_2(p_t, y_{c.m.})$ ) cannot be addressed in those approaches.

A way to overcome this problem is the method of “perturbative production” of kaons, which was used in Ref. [87]. In this method one determines the probability for producing a kaon in a collision from Eq. (73). The production probability  $P$ , the c.m.-momentum  $\mathbf{p}$  and the invariant mass  $\sqrt{s}$  of the collisions are stored but the strangeness production is not executed (the momenta of the incoming particles are not changed). Instead, the collision branches into another collision channel which is then executed. At the end the stored data are analyzed to calculate the production of kaons in these elementary collisions by summing up the probabilities.

However, this method has the disadvantage that further interactions of the perturbatively produced particles can only roughly be estimated. To overcome this we use the method of virtual particles:

- With each particle  $i$  we associate a probability  $P_i$ . Protons, neutrons, deltas and pions initially have  $P_i = 1$ .
- After a collision which takes place with the probability  $P_r = \frac{\sigma(i,j \rightarrow k+X)}{\sigma_{tot}}$  according to Eq. (73), the particle  $k$  carries the probability

$$P_k = P_i \cdot P_j \cdot P_r. \quad (74)$$

If this collision is not executed (because  $k$  is a virtual particle) the parents continue undisturbed and after the collision have the probabilities

$$P'_i(\text{undisturbed}) = P_i(1 - P_r \cdot P_j) \quad P'_j(\text{undisturbed}) = P_j(1 - P_r \cdot P_i).$$

- The interaction potential felt by particle  $i$  is the sum of the interaction potentials of the free particles multiplied by the probabilities of the interacting particles.

$$V_i = \sum_k P_k V_{ik} \quad (75)$$

For the production of strangeness we have  $P_r \ll 1$  and therefore  $1 - P_r \cdot P_i \approx 1$  and  $1 - P_r \cdot P_j \approx 1$ , we can simplify the above scheme in the following way, which is illustrated in Fig. iii.3:

- Nucleons, deltas and pions are *real* particles with  $P = 1$ . Strange particles are *virtual* particles who have a very small probability  $P_i$ .

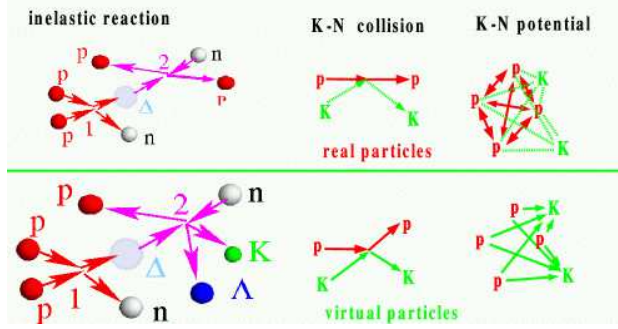


FIG. iii.3: Example for the differences in the treatment of “real” and “virtual” particles (see text).

- In a collision virtual particles are produced with a reaction probability  $P_r = \sigma(BB \rightarrow KX)/\sigma(tot)$ . The parent particles do not change their properties and follow another channel of the collision according to its probability. (Fig. iii.3 , top-left, e.g.  $\Delta^{++}n \rightarrow pp$ ).

The produced strange particles proceed as if the production reaction had taken place and carry a probability of  $P_r$  (Fig. iii.3 , bottom-left, e.g.  $\Delta^{++}n \rightarrow p\Lambda K$ ).

- In a collision of a real and a virtual particle, the momentum of the real particle remains unchanged (Fig. iii.3 , top-middle). The virtual particle acts, as if this collision had taken place (Fig. iii.3 , bottom-middle).
- The real particles do not see a potential interaction with the virtual particles (Fig. iii.3, top-right). The virtual particles feel a potential with the nuclear matter. (Fig. iii.3, bottom-right).

This method has the advantage to allow for high-statistics calculation of kaon one-body observables including all effects of the medium like potential propagation, rescattering, absorption etc. However, there are also some drawbacks of this method:

1. The strange particles do not appear in the energy balance. Therefore including strange particles violates the energy conservation, perfectly assured for the real particles. The real particle do not ‘feel’ whether strange particles are produced or not.

Questions like ‘*Do events with kaons produce less highly energetic pions than other events*’ (which would be interesting for analogies between kaons and high energy pions) cannot be addressed.

2. KN- correlations cannot be calculated.
3. Higher-order processes might be described incorrectly. To give an example:
  - (a) An NN collision produces virtually  $NAK^+$ . In the ‘real world’ it produces a  $N\Delta$ -pair.

- (b) The virtual  $\Lambda$  rescatters with another nucleon while the real  $\Delta$  decays into  $N \pi$ .
- (c) The virtual  $\Lambda$  and the real  $\pi$  resulting from the real  $\Delta$ -decay scatter and produce an  $N K^-$ -pair.

The latter process should not be allowed because after a real production of the  $\Lambda$  the  $\Delta$ -production could not take place and therefore the  $\pi$  would not exist. In our simulations such processes are explicitly forbidden (by checking for different parents of the collision partners), but if the  $\pi$  in between has been reabsorbed by a nucleon  $\pi N \rightarrow \Delta \rightarrow \pi N$  we cannot trace back its origin. However, the probability of such a process is low.

It should be noted that in IQMD kaons and antikaons are propagating under the influence of an optical potential as described in subsection III B. Thus the particles have effective masses as seen in Fig. iii.1. These effective masses enter in the time evolution equations. Contrary to HSD [69] there is no propagation of the finite width of the spectral functions of antikaons in IQMD.

### E. Elementary production of $K^+$

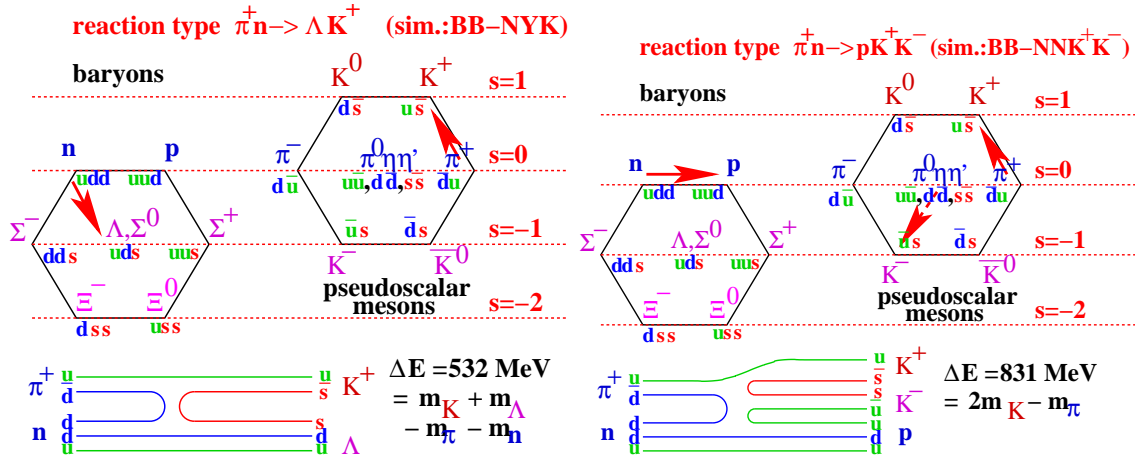


FIG. iii.4: Representation of the major elementary production channels of  $K^+$  mesons in a  $\pi^+ n$  collision in the quark language and the SU(3) scheme.

The elementary production of  $K^+$  is governed by the conservation of strangeness. The initial net strangeness is zero, thus strange quarks can only be produced together with strange anti-quarks. In Fig. iii.4 we show the main production processes for  $K^+$  mesons schematically together with the baryon and pseudoscalar meson octets. The arrow indicates the transit in each octet. In this scheme the sum of the red arrows have to be zero. The most economic way to do this is to create an  $s$ -quark which remains in a baryon (and thus transforms the nucleon into a hyperon) together with a  $\bar{s}$ -quark which becomes part of a

kaon. An example of such a process is given on the l.h.s. of Fig. iii.4, where the reaction  $\pi n \rightarrow \Lambda K^+$  is shown. In this reaction a  $d\bar{d}$ -pair annihilates to form an  $s\bar{s}$  pair. This reaction requires less energy than the production via  $NN \rightarrow NNK^+ K^-$  (r.h.s. of Fig. iii.4) (see also Eq. (80)). From the quark diagrams at the bottom of Fig. iii.4 we see that the latter process creates an additional  $u\bar{u}$  pair and should thus be suppressed by the OZI rule [88].

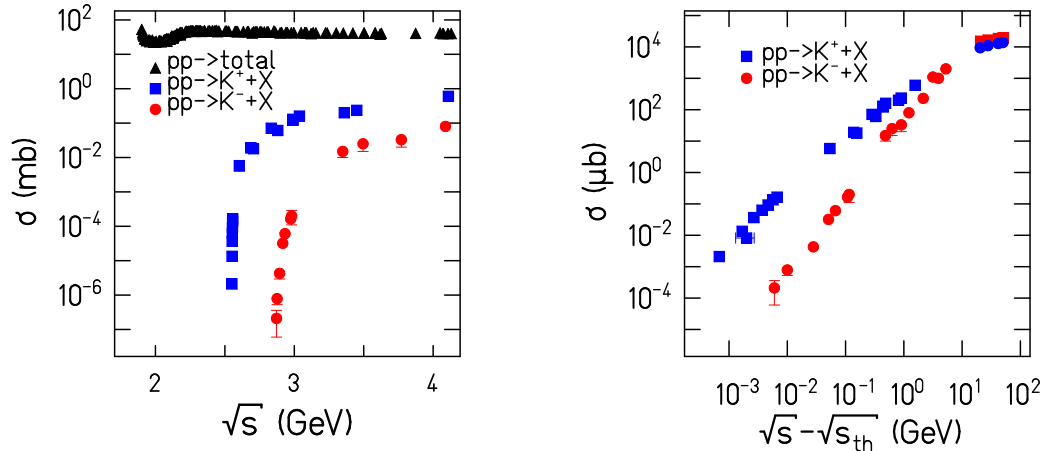


FIG. iii.5: Left: Comparison of the total cross section and of the production cross section of  $K^+$  and  $K^-$  as function of  $\sqrt{s}$ . Right: Near threshold energy dependence of cross sections of the  $K^+$  and  $K^-$  production channels in proton-proton collisions.

For proton-proton reactions there are experimental data on strangeness production available. Figure iii.5 shows on the left hand side a comparison of the cross sections for the production of a  $K^+$  (blue squares) and the production of a  $K^-$  (red circles) together with the total reaction cross section (black triangles) as a function of the c.m.-energy  $\sqrt{s}$  in proton-proton collisions. We see a steep rise of the cross sections after passing the kaon production threshold. However, the cross sections of strangeness production are very small in comparison to the total cross section, which motivates the description of strangeness in the framework of virtual particles (see Fig. iii.3). The threshold is lowest in reactions in which the associate particle is a  $\Lambda$ . Thus this channel gives the strongest contribution to the proton-proton induced  $K^+$  production at low energies. Channels with the production of a  $\Sigma$  or of a  $K^+K^-$  pair contribute only at higher energies due to their higher thresholds.

The right hand side of Fig. iii.5 demonstrates the behavior of the production of  $K^+$  and  $K^-$  near the threshold. Note that the abscissa gives the excess energy in the c.m.-frame and both axes are in a logarithmic scale. Both processes strongly rise with the available excess-energy. However, the rise of the production cross section of the  $K^-$  is stronger than that of the  $K^+$  when we are in the range of several MeV to several hundred MeV. This is the dominant range contributing to the production of kaons and antikaons in the energy domain we are studying.

The cross section for the production of strangeness in neutron-induced reactions is still a subject of investigation. In the One-Boson-Exchange model the isospin factor which has to be employed when calculating the np cross section from the known pp cross section depends on the nature of the exchanged particle. It varies between 1 for a pion and 5/2 for a kaon exchange. In IQMD the latter choice of 5/2 is used which leads to an isospin averaged cross section of

$$\sigma(\text{NN} \rightarrow \text{NYK}^+) = \frac{1}{4}(\sigma_{\text{pp}} + 2\sigma_{\text{pn}} + \sigma_{\text{nn}}) = \frac{1 + 5 + 0}{4}\sigma_{\text{pp}} = \frac{3}{2}\sigma(\text{pp} \rightarrow \text{NYK}^+). \quad (76)$$

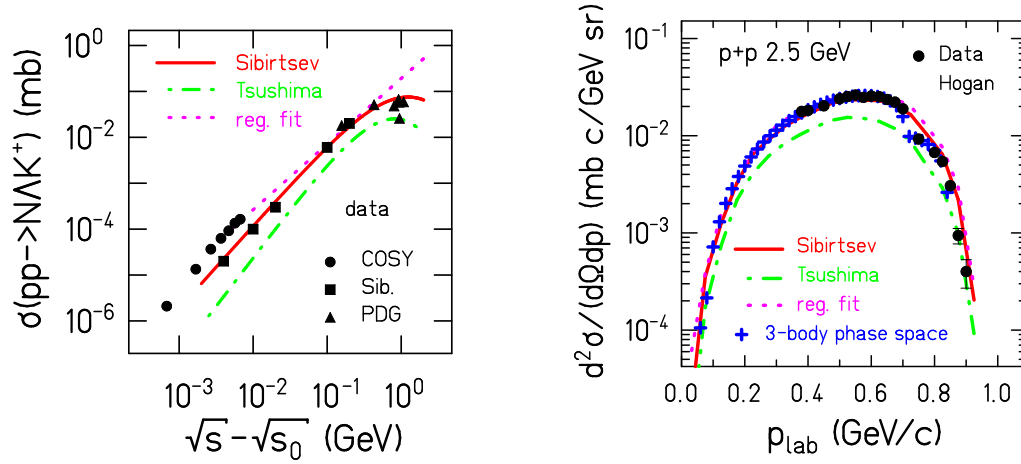


FIG. iii.6: Different parameterizations of the  $\text{pp} \rightarrow \text{p} \Lambda \text{K}^+$  cross section (left) and comparison of IQMD results using these parameterizations with experimental pp-data at 2.5 GeV measured at  $\theta_{\text{lab}} = 40^\circ$  from [89](right).

There exist different microscopic models for describing the production of kaons and corresponding parameterizations of these cross sections. Figure iii.6 on the l.h.s. shows several parameterizations of the  $\text{pp} \rightarrow \text{p} \Lambda \text{K}^+$  channel used in our simulations. The parameterization of Sibirtsev are obtained by correcting the experimental data for the final state interaction [90]. We use this set and its parametrization (red full line)

$$\sigma(\text{NN} \rightarrow \text{NAK}^+) = 1.098 \text{ mb} \cdot \left(1 - \frac{s_{\text{thres}}}{s}\right)^{1.8} \cdot \left(\frac{s_{\text{thres}}}{s}\right)^{1.5} \quad (77)$$

as our standard input. Tsushima et al.[91] have calculated the production cross section in a resonance model. They obtain

$$\sigma(\text{NN} \rightarrow \text{NAK}^+) = 1.165 \mu\text{b} \cdot \left(\frac{s}{s_{\text{thres}}} - 1\right)^{2.14} \cdot \left(\frac{s_{\text{thres}}}{s}\right)^{5.024} \quad (78)$$

shown as green dash-dotted line. Another simple parametrization is a linear regression fit in a log-log representation (magenta dotted line) of recent COSY data [92] with reads

$$\sigma(\text{pp} \rightarrow \text{p}\Lambda\text{K}^+) = 191 \mu\text{b} \cdot \left(\sqrt{s} - \sqrt{s_{\text{thres}}}\right)^{1.43}. \quad (79)$$

This parametrization is valid for energies below 3 GeV, which is above the high energy limit of IQMD because high mass baryon resonances are not included.

The right hand side of Fig. iii.6 compares results of experimental pp-data of Hogan et al. [89] (black full circles) with IQMD calculations (full red line) using the cross section [90] of Eq. (77). At this energy, the COSY data and the Sibirtsev parametrization agree and we do not expect a difference. The agreement shows that in the energy range where data are available our parametrization of the cross section works well. Changing to the  $\sigma(\text{NN} \rightarrow \text{N}\Lambda\text{K}^+)$  cross section by Tsushima [91, 93], (green dash-dotted line) results in a too low yield. The regression-fit parametrization (magenta dotted line, Eq. (79)) shows again a spectrum quite comparable to that using the Sibirtsev parametrization. The blue crosses indicate the results of a fit using a 3-body phase-space distribution. The agreement shows that at this energy the production of a kaon proportional to the 3-body phase-space decay is compatible with the data. We adopt this 3 body phase space production in our simulations for all baryon-baryon channels. Other models, like UrQMD [67], generate the kaon via a two-step process producing first a resonance (e.g. the  $N^*(1650)$ ) which decays then into a hyperon-kaon pair. As said, results are reported to be compatible to experimental data as well [86].

In heavy-ion collisions kaons may be produced in baryon-baryon collisions in which at least one of the reaction partners is a baryonic resonance. As already discussed for pp collisions,  $\text{B}_1\text{B}_2 \rightarrow \text{B}_3\text{YK}^+$  reactions have lower thresholds than the channel  $\text{B}_1\text{B}_2 \rightarrow \text{B}_3\text{B}_4\text{K}^+\text{K}^-$ . Here B may be a nucleon N or a  $\Delta$ , and Y a  $\Lambda$  or a  $\Sigma$ .

Whereas the cross sections for  $\text{K}^+$  production in the pp and  $\pi$  N channel are known, the production cross section for the  $\Delta$  N channel is experimentally not directly accessible. One has to rely on theoretical calculations which have produced quite different results. As far as the predictive power of transport calculations is concerned (where these elementary cross section are input quantities) these uncertainties add to those due to the unknown cross section in the pn channel.

For the  $\text{NN} \rightarrow \text{K}^+ \Lambda \text{N}$  channel, both IQMD and HSD use a parametrization of the experimental pp data from Sibirtsev [90], discussed above, applying only the mentioned isospin corrections to the np channels. For the  $\text{N}\Delta \rightarrow \text{K}^+ \Lambda \text{N}$  cross section two approaches have been advanced which differ substantially, as may be seen in Fig. iii.7. Randrup-Ko [94] proposed to scale the NN cross section by the appropriate isospin factor:  $\sigma(\text{N}\Delta \rightarrow \text{K}^+\text{N}\Lambda) = 0.75 \sigma(\text{NN} \rightarrow \text{K}^+\text{N}\Lambda)$  whereas Tsushima calculates this cross section in a resonance model [91, 93]. The latter is used in present-day simulation programs, especially in the actual version of the HSD approach. Former HSD calculations used, however, the cross section of Randrup and Ko and therefore a comparison of the present results with the former ones has

to be done with care. As can be seen in Fig. iii.7 for  $\sqrt{s}$  values above 2.7 GeV, corresponding to beam energies above 2 GeV in pp collisions, there is quite a difference between the two parameterizations.

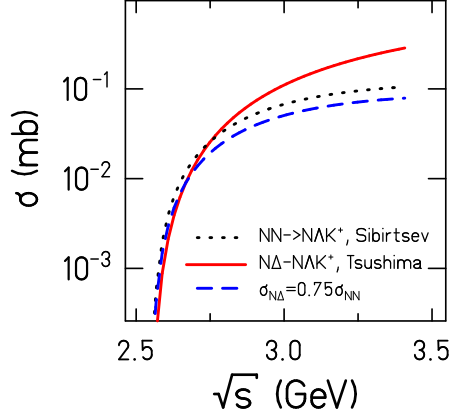


FIG. iii.7: Different parameterizations of the  $N\Delta \rightarrow N\Lambda K^+$  cross section as compared to the  $NN \rightarrow N\Lambda K^+$  cross section (see text).

Furthermore, kaons may also be produced in pion-induced reactions. Table II presents all channels in IQMD which contribute to the  $K^+$  production.

$NN \rightarrow N\Lambda K^+$	$NN \rightarrow N\Sigma K^+$	$NN \rightarrow \Delta\Lambda K^+$	$NN \rightarrow \Delta\Sigma K^+$
$N\Delta \rightarrow N\Lambda K^+$	$N\Delta \rightarrow N\Sigma K^+$	$N\Delta \rightarrow \Delta\Lambda K^+$	$N\Delta \rightarrow \Delta\Sigma K^+$
$\Delta\Delta \rightarrow N\Lambda K^+$	$\Delta\Delta \rightarrow N\Sigma K^+$	$\Delta\Delta \rightarrow \Delta\Lambda K^+$	$\Delta\Delta \rightarrow \Delta\Sigma K^+$
$\pi N \rightarrow \Lambda K^+$	$\pi N \rightarrow \Sigma K^+$	$\pi\Delta \rightarrow \Lambda K^+$	$\pi\Delta \rightarrow \Sigma K^+$
$NN \rightarrow NNK^+K^-$	$N\Delta \rightarrow NNK^+K^-$	$N\Delta \rightarrow N\Delta K^+K^-$	$\Delta\Delta \rightarrow NNK^+K^-$
$\Delta\Delta \rightarrow \Delta\Delta K^+K^-$	$\pi N \rightarrow NK^+K^-$	$\pi\Delta \rightarrow NK^+K^-$	

TABLE II: List of the  $K^+$  producing reactions parameterized in IQMD.

In these channels different isospin combinations for  $N, \Delta, \pi$  are possible which lead to a further subdivision of these channels. Note that we only use the  $\Delta(1232)$  resonance which is the dominant resonance channel in the interesting energy domain. For each channel the production threshold is given by the sum of the outgoing masses. In free space we find

$$\begin{aligned}
\sqrt{s_{\text{thres}}}(NN \rightarrow N\Lambda K) &= m_N + M_\Lambda + m_K = 2.55 \text{ GeV}, \\
\sqrt{s_{\text{thres}}}(NN \rightarrow N\Sigma K) &= m_N + M_\Lambda + m_K = 2.62 \text{ GeV}, \\
\sqrt{s_{\text{thres}}}(NN \rightarrow NNK\bar{K}) &= 2m_N + 2m_K = 2.87 \text{ GeV}
\end{aligned}
\tag{80}$$

where we use isospin averaged masses  $m_N = 938$  MeV,  $m_\Lambda = 1115$  MeV,  $m_\Sigma = 1189$  MeV,  $m_K = 495$  MeV,  $m_\pi = 138$  MeV,  $m_\Delta^{\text{pole}} = 1232$  MeV. Note that for channels having a  $\Delta$

in the outgoing channel we set its mass to its pole mass. However, these channels do not contribute significantly. In the medium the free masses are replaced by the effective masses at the production density.

For the channels with an incoming  $\Delta$  no information from experiment exists which leads to uncertainties in the interpretation of heavy ion data. This was already mentioned above for the  $N\Delta \rightarrow N\Lambda K$  cross section. We will discuss this point later.

### F. Elementary production of $K^-$

As mentioned above in proton-proton collisions near threshold a  $K^-$  is always produced together with a  $K^+$  via  $NN \rightarrow NNK^- K^+$ . Only a few experimental points are available for this reaction as can be seen in Fig. iii.5. We parameterize the production cross section by

$$\sigma = 63\mu\text{b}(\sqrt{s} - \sqrt{s_{\text{thres}}})^{1.6}, \quad (81)$$

with  $\sqrt{s}$  given in GeV.

Similar to the  $K^+$  also the  $K^-$  may be produced in reactions with resonances or pions in the entrance channel. For the resonance-induced channels we use the same cross sections as for the corresponding NN induced channel with isospin factors of 0.75 for  $N\Delta$  and 0.5 for  $\Delta\Delta$ . The fact that some combinations (like  $\Delta^-\Delta^-$ ) have no or only restricted outgoing channels is taken into account by the appropriate isospin factors. For the pion-induced reaction  $\pi N \rightarrow NK^+K^-$  we use the cross section parametrization of Sibirtsev [95].

In heavy-ion collisions, discussed later in detail, the major contributions to the  $K^-$  production are strangeness exchange reactions of the type  $\pi Y \rightarrow NK^-$  and  $BY \rightarrow NNK^-$ . The cross section for the pion-induced strangeness exchange is deduced from the kaon absorption cross section via detailed balance. For the baryon-induced strangeness exchange channel we use the parametrization of Ko et al.:  $\sigma(N\Lambda) = 0.8\text{mb}(E - E_{\text{thres}})$  where the energies are taken in GeV in the hyperon rest frame. For  $N\Sigma$  this cross section is scaled by a factor of 1.5. For  $\Delta Y$  reactions we assume the same energy dependence of the cross section, but apply an isospin factor of 0.75, taking also into account that several combinations (like  $\Delta^{++}\Lambda$ ) have restricted outgoing channels.

### G. Nucleon scattering of $K^+$ and $K^-$

The produced kaons may scatter in the nuclear medium. For the scattering of kaons on protons experimental data exist, as shown in Fig. iii.8. The red bullets show experimental cross sections of elastic scattering with a proton. The left hand side presents data of elastic scattering of the  $K^+$  with a proton, the right hand side elastic scattering of the  $K^-$  with a proton.



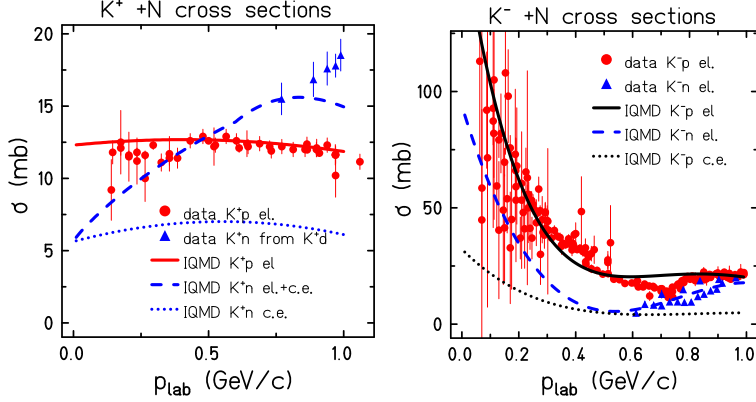


FIG. iii.8: Total cross section for  $K^\pm p$  and  $K^\pm n$  elastic scattering and charge exchange (c.e.) reactions [96] and the parameterizations used in IQMD calculations (see text).

We parameterize these cross sections as  $\sigma(K^+p)/\text{mb} = 12.3 + 1.88p - 2.32p^2$  (red solid line, left hand side) and  $\sigma(K^-p)/\text{mb} = 169 - 809p + 1657p^2 - 1585p^3 + 706p^4 - 118p^5$  (black solid line, right hand side) where  $p$  is the kaon momentum in the nucleon rest frame in  $\text{GeV}/c$ . For  $p > 2 \text{ GeV}$  we set  $\sigma(K^-p) = 2.5 \text{ mb}$ .

Similarly there exist cross sections for the scattering with neutrons (blue triangles). The left hand side shows the total scattering cross section of a  $K^+$  with a neutron. The data (blue triangles) are deduced from scattering with deuterons. The total cross section includes elastic scattering  $K^+n \leftrightarrow K^+n$  and the charge exchange  $K^+n \leftrightarrow K^0p$ . The IQMD parameterizations for the total cross section are given by the blue dashed lines, those of the charge exchange by the blue dotted lines. The difference of both curves corresponds to the elastic cross section.

The right hand side of Fig. iii.8 presents the data of elastic scattering of  $K^-$  with neutrons (blue triangles). The IQMD parametrization is shown as blue dashed line on the right hand side. The black dotted line shows the parametrization of the charge-exchange reaction  $K^-p \leftrightarrow \bar{K}^0n$ .

Finally antikaons may be absorbed by a nucleon, producing a pion and a hyperon.

## H. The standard set of our IQMD and HSD calculations

If not referenced explicitly the calculations performed with IQMD are using a soft equation of state with momentum dependent interactions (SM, see Table I). For the HSD a semi-soft equation of state is used with an incompressibility  $K \simeq 250 \text{ MeV}$ . For the  $K^+$  nucleus potentials we use in both models the parametrization discussed in subsection III B, assuming  $\alpha = 1$  in Eq.68. Please note that this potential differs from that originally used in the HSD calculations [4]. For the  $K^-$  nuclear potential in IQMD we use as well the parametrization of subsection III B, assuming  $\alpha = 1$  in Eq. (68) whereas in HSD a G-matrix approach [69] is employed. The nucleons collide with free nucleon-nucleon cross sections without any medium

modification. The kaons are produced using the parametrization of Sibirtsev (Eq. 77) for pp-NYK collisions and those of Tsushima et al. [91, 93] for the  $\Delta$ -induced collisions. For pn-collisions we apply a factor of 5/2 to the pp-cross section. Therefore the parameterizations of the dominant  $K^+$  production cross sections ( $BB \rightarrow BYK$  and  $\pi B \rightarrow YK$  are identical for both models.

When comparing IQMD and HSD calculations the following main features should be taken into account:

### KN elastic scattering:

The elastic scattering of (anti)kaons with nucleons in IQMD treats the collision partners as free on-shell particles while HSD performs the collision with effective masses.

### Production of $K^-$ :

- In IQMD there is no propagation of the finite width of the spectral function of the  $K^-$ , as it is done in HSD. IQMD assumes the  $K^-$  to be on shell.
- In HSD the treatment of off-shell effects also influences the production processes, e.g.  $\pi Y \rightarrow NK^-$ . Resonances below the threshold of the free production (like the  $\Lambda(1405)$ ) may change the production cross section in the medium. This is incorporated in HSD. In IQMD the production process is assumed to be the free production cross section taken at  $\sqrt{s}$  modified by the in-medium mass of the  $K^-$ .

## I. Dynamics of heavy-ion collisions

As an introduction to the dynamics of kaon production we briefly sketch the evolution of a heavy-ion collision in this energy range, in which the production and propagation of strange particles is embedded.

We describe the reaction of Au+Au at 1.5 A GeV incident beam energy at an impact parameter of  $b = 0$  fm. The time of the whole reaction is less than  $10^{-22}$  seconds and we describe the time evolution in units of fm/c:  $1 \text{ fm}/c = \frac{10^{-15} \text{ m}}{3 \cdot 10^8 \text{ m/s}} \approx 3.3 \cdot 10^{-24} \text{ s}$

The time  $t = 0$  fm/c is chosen such that projectile and target have first contact. The first nucleon-nucleon collisions take place and first resonances are produced. The nuclear matter starts to decelerate by collisions between projectile and target nucleons.

Figure iii.9 shows, on the left hand side, the time evolution of the densities of N,  $\Delta$ , and  $\pi$  in the central region (top), the mean kinetic and transverse energies in the central region (mid) and the number of deltas and pions (bottom). The nucleon density (top, red full line) grows rapidly, reaches a maximum of about 2.5 times saturation density at about 8 fm/c and falls afterwards. The density of  $\Delta$ 's (black dotted line) begins to rise later, reaching a maximum of nearly half saturation density at about 9 fm/c and falls rapidly afterwards. The pion density (multiplied by 10, blue dashed line) starts to rise even later and reaches a maximum of around one sixth of the saturation density at about 10 fm/c.

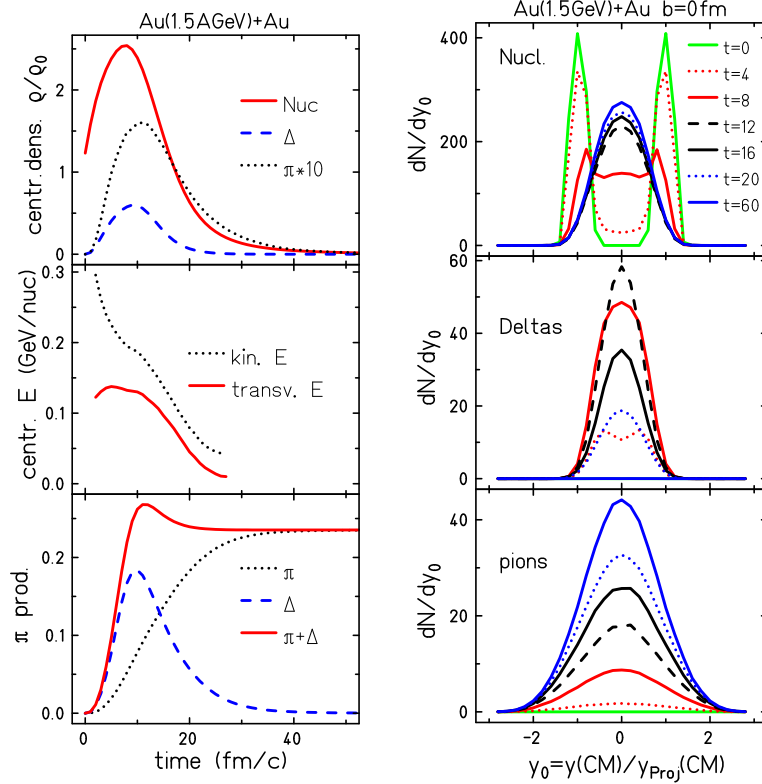


FIG. iii.9: Time evolution of a Au+Au collision at 1.5 A GeV and at  $b=0$  fm. Left: Evolution of central density, central energy, pion and Delta multiplicities as a function of time. Right: Rapidity distributions for nucleons, Deltas, and pions for different times of the evolution (in fm/c).

In the central region the kinetic energy (left hand side, middle, black dotted line) drops rapidly. In the center-of-mass frame the incident energy leads to a large initial longitudinal momentum. This energy is partly consumed by the creation of resonances ( $\Delta$ 's), but another part of it is redirected by nuclear collisions into the transverse direction. Therefore, the transverse energy (red full line) is built up rapidly in the central region. Equilibrium is not obtained, as will be discussed in section VI. In the final expansion phase the fast (high energy) particles are leaving the central region very rapidly, leaving the slower particles behind. Thus, the energies are falling. Finally, the particles are leaving the central region.

The fast decrease of the energy is accompanied by a fast increase of the number of deltas (bottom, blue dashed line). As already noted, the production of resonances consumes a large share of this energy, which will be released later in the form of pions (black dotted line). Their number is continuously increasing to reach the final value at about 30-40 fm/c. Pions are strongly interacting with nucleons. Therefore, pions propagating in the dense medium have a high chance to be reabsorbed and to feed the number of deltas. This effect explains the slow increase of the pion yield when the density is high. The deltas themselves are also reabsorbed by the nuclear matter in  $N\Delta \rightarrow NN$  collisions. This effect can be seen looking at the total number of deltas and pions (full red line). It shows a maximum at about 10-12

fm/c and decreases slightly afterwards. From 20 fm/c on it stays roughly constant. Now only the relative contribution of deltas and pions to the total yield is changing.

The right hand side of Fig. iii.9 shows the time evolution of the rapidity distribution of nucleons (top), deltas (middle) and pions (bottom) at different times. The rapidity has been scaled to the projectile rapidity in the center-of-mass. Thus, a value of 1 corresponds to projectile rapidity, -1 to target rapidity.

At  $t = 0$  fm/c (green full line) projectile and target show their incident momentum distribution as peaks at projectile and target rapidity. The width of the peaks is due to the momentum distribution of the nucleons in the nuclei. Deltas and pions do not exist at this time. At  $t = 4$  fm/c (red dotted line) first nucleons have been stopped to mid-rapidity, and first deltas have been produced. The stopped nucleons collide with incoming nucleons of the projectile and target causing a slight double peak in the delta rapidity distribution about halfway between the cm-rapidity (0) and the projectile (1) resp. target rapidity (-1). There are almost no pions.

At  $t = 8$  fm/c (red full line) when maximum density is reached, the nuclei still have not been completely stopped. There are remnants of the peaks at projectile and target rapidities. The number of deltas has strongly increased, their distribution is now peaked around mid-rapidity. The rather narrow width is due to the high mass of the delta which takes up a big part of the energy available in the first collisions. In the decay of deltas a large amount of momentum is given to the light pions. Therefore, the rapidity distribution of the pions becomes rather broad.

At  $t = 12$  fm/c (black dashed line) the rapidity distribution of nucleons is peaked at mid-rapidity. The delta distribution shows its maximum values while the pion distribution rises continuously. At  $t = 16$  fm/c (full black line) and  $t = 20$  fm/c (blue dotted line) the nucleon rapidity distribution is slightly growing in the center. This is due to the feeding by the decay of the deltas whose yield is continuously falling. For kinematic reasons in the  $\Delta$ -decay the nucleon receives only little energy while most of the energy is given to the light pion whose broad rapidity distribution is still rising. At  $t = 60$  fm/c (full blue line) the reaction is in the final state. There are no more deltas. The system is expanding and the particles are directed outwards and will finally hit the detectors.

## J. Pion production in heavy-ion collisions

As we have seen, the production of deltas and their decay into pions is very important for the understanding of the dynamics of heavy-ion collisions. Thus we briefly report on comparisons of experimental pion observables with IQMD calculations. For more details of the description of pions in IQMD we refer to Ref. [63]. Details on experimental observations of pions at these energies can be found in [80, 97, 98]. For more detailed comparisons of experiment and theory concerning the production of pions we refer to [99].

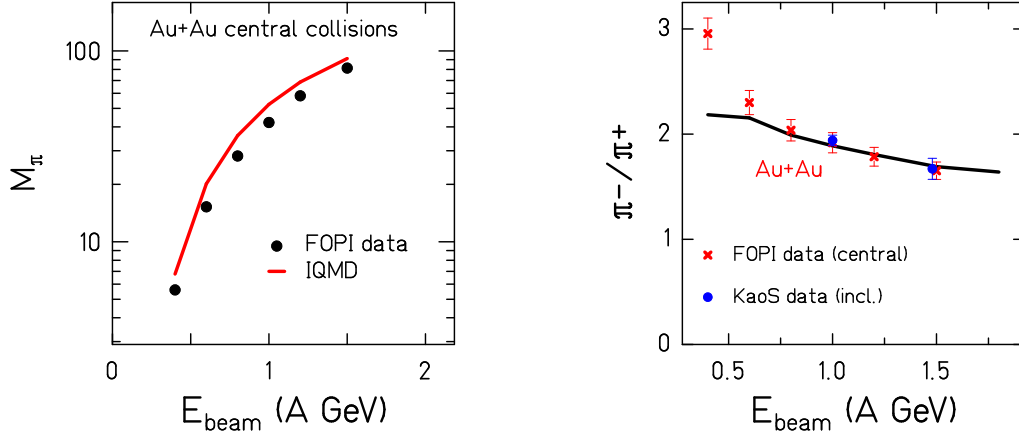


FIG. iii.10: Comparison of the experimental [99] excitation function of the pion yield (left) and of the  $\pi^-/\pi^+$  ratio (right) [97, 100] with IQMD calculations (full line) for central Au+Au collisions.

Figure iii.10 shows on the left side the comparison of the excitation function of the pion yield in central Au+Au collisions, measured by the FOPI collaboration [99], with calculations performed by IQMD (red full line). The calculated pion yield exceeds the experimental one which is found to be mainly due to description of the reabsorption of the delta in the dense medium. The right side compares to the ratio of the multiplicities of negatively and positively charged pions (full line) to experimental data of Au+Au collisions at different energies from the FOPI Collaboration (crosses, central collisions) and from the KaoS Collaboration (circles, inclusive data from [97, 100]). For energies above 500 A MeV a good agreement between data and calculations is observed.

Figure iii.11 compares the spectra of  $\pi^+$  from inclusive collisions of C+C, Ni+Ni and Au+Au at 1.0 A GeV incident energy (left side) and of  $\pi^+$  and  $\pi^-$  in central collisions (370 mb most central) of Au+Au at 1.5 A GeV incident energy (right side) of IQMD calculations (lines) with KaoS data (symbols) [100]. The absolute yields at kinetic center of mass energies above 0.1 GeV as well as the slopes are well described. It should be noted that subthreshold kaon production is influenced by the behavior of high-energy pions. Furthermore, it should be kept in mind that the pions are strongly interacting with the nucleons. Thus, the pion spectra are influenced by rescattering and their shape is determined mainly at times later than the time of the production of kaons. The rapidity distribution of pions is also reasonably well reproduced as can be seen in Fig. iii.12. All transport theories have problems to reproduce low energy  $\pi$ 's at mid-rapidity (see Fig. iii.11). These do not play, however, an important role, neither for the strangeness multiplicity nor for the strangeness dynamics.

Last but not least we present in Fig. iii.13 the rapidity distribution of free participant protons. It is obtained by subtracting from the total yield of participants those which are

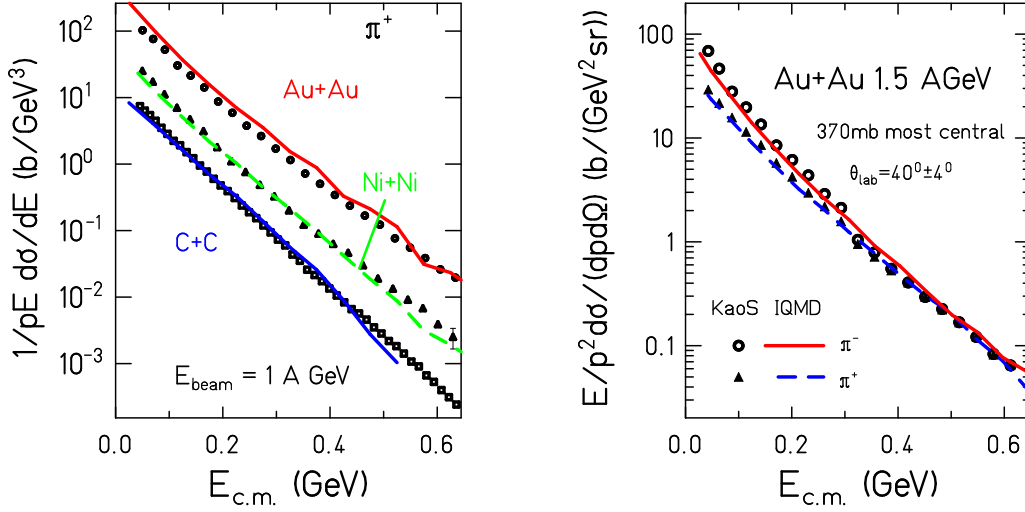


FIG. iii.11:  $\pi^+$  spectra of KaoS at 1.0 A GeV [101, 102] compared with IQMD calculations (left). Comparison of the  $\pi^\pm$  spectra at 1.5 A GeV beam energy [100] with IQMD calculations (right).

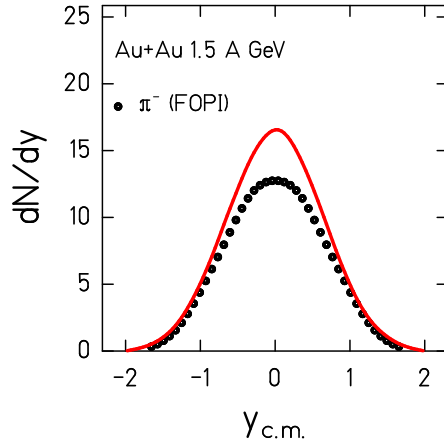


FIG. iii.12: Comparison of the  $dN/dy$  distribution of  $\pi^-$  of central Au+Au collisions ( $b < 2$  fm) at 1.5 A GeV from the FOPI Collaboration [99] with IQMD calculations.

bound in fragments. It should be stressed that for this analysis the results of IQMD have undergone the same treatment as the experimental data concerning filtering, triggering, event selection, etc. The width of the distribution is well reproduced. Around mid-rapidity one observes slightly more protons in the IQMD simulations as compared to experiment. This is due to the underprediction of the yield of light composites like  $t$ ,  ${}^3\text{He}$ ,  $\alpha$ , which are difficult to model in semiclassical approaches. The difference is less than 10% and therefore does not essentially perturb our conclusions.

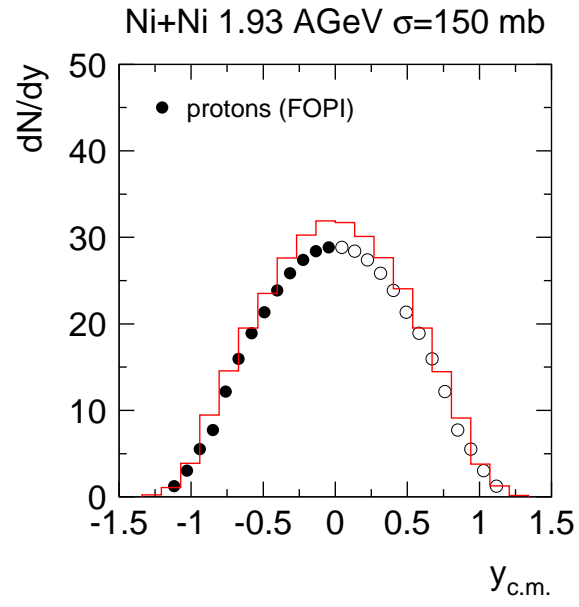


FIG. iii.13: Comparison of the  $dN/dy$  distribution of free participant protons of Ni+Ni collisions at 1.93 A GeV measured by the FOPI collaboration [103] with IQMD calculations (red histogram).

## IV. PRODUCTION OF $K^+$ MESONS

### A. $K^+$ production in p+A collisions

At first glance, p+A collisions seem to be a nice intermediate step from p+p to A+A studies. Indeed, they offer the opportunity to investigate the kaon properties in a well-defined environment as the charge distribution of the nucleons in nuclei is known from electron scattering. However, in going from p+p to p+A collisions, several changes happen simultaneously:

1. Strange particles can be created at sub-threshold energy, i.e. at an incident energy at which a production in a free p+p collision is not possible due to energy-momentum conservation. The  $K^+$ -production threshold is constrained by the conservation of strangeness. The lowest threshold in p+p reactions is given by the channel  $p + p \rightarrow p + \Lambda + K^+$  with the threshold

$$\sqrt{s} = \sqrt{\sum P_\mu P^\mu} \geq m_p + m_\Lambda + m_{K^+} = 2.55 \text{ GeV}; \quad P = p_1 + p_2 \quad (82)$$

where  $p_1$  and  $p_2$  are the four-momenta of the colliding particles. This implies a minimum incident kinetic energy of 1.58 GeV for the proton projectile. In p+A collisions a  $K^+$  can in principle be produced starting from a beam energy of

$$E_p = \frac{s_{\text{thres}} - m_p^2 - m_A^2}{2m_A}; \quad \sqrt{s_{\text{thres}}} = m_A + m_\Lambda + m_{K^+} \quad (83)$$

where  $m_A$  is the mass of the target nucleus. At the absolute threshold,  $K^+$  creation is very improbable because the available energy and momentum has to be transferred in one single nucleon nucleon collision producing a  $K^+$ . Therefore, the cross section decreases rapidly at energies below the nucleon-nucleon threshold.

2. Due to the Fermi momentum of the nucleons in the target nucleus, the effective c.m. energy in a p+A collision may be higher than that in a p+p collision at the same beam energy. This reduces the threshold incident energy in single NN collisions down to a beam energy of around 1 GeV.
3. Resonances may serve as an energy storage since they transform kinetic energy into mass. The projectile proton which collides with a target nucleon may create a  $\Delta$ . Subsequently, the  $\Delta$  may collide with another target nucleon producing a  $K^+$ .
4. There is a potential interaction between the  $K^+$  and the surrounding nucleons which modifies the  $K^+$  properties in matter.

Figure iv.1 shows the  $K^+$  momentum distribution in the laboratory system in p+p and p+A collisions at 1.6 GeV incident energy, i.e. slightly above the threshold. In the p+p case (black



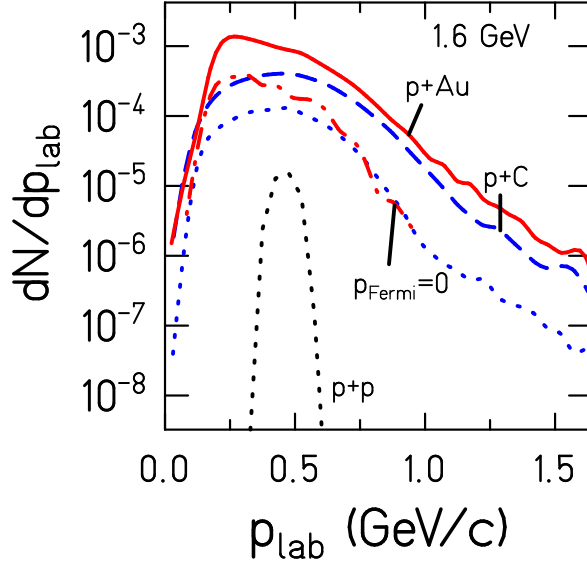


FIG. iv.1: Inclusive momentum spectra of  $K^+$  mesons produced in p+p, p+C and p+Au collisions at 1.6 GeV. We compare calculations for p+C and p+Au, including (solid and dashed lines) and excluding (dotted and dash-dotted lines) the Fermi motion, with p+p calculations.

dotted line) the emitted  $K^+$  mesons are limited to a very small momentum range in the c.m. system and therefore the kinematically allowed region in the laboratory is also a quite narrow and centered around  $p_{\text{lab}} = 0.5$  GeV. Already in the p+C collision (blue dashed line) there is a much wider distribution which is also peaked around  $p_{\text{lab}} = 0.5$  GeV. Surprisingly, this widening is only in part due to the Fermi momentum of the nucleons in the carbon target where the projectile may collide with a nucleon with a Fermi momentum in the opposite direction of its momentum and thus enhance the available energy of the  $K^+$ . This can be seen when comparing the p+p curve (black dotted line) with a calculation for p+C without Fermi momentum ( $p_{\text{Fermi}} = 0$ , blue dotted curve). The Fermi motion enhances the cross section but does not change the form of the momentum distribution obtained in calculations which include the Fermi motion (blue dashed line).

The major part of the difference between p+p and p+C stems from the opening of additional channels due to multi-step processes:  $N_1N_2 \rightarrow N\Delta$ ,  $N_3\Delta \rightarrow NYK$  ( $N\Delta$  channel) and  $N_1N_2 \rightarrow N\Delta$ ,  $\Delta \rightarrow N\pi$   $\pi N_3 \rightarrow YK$  ( $N\pi$  channel) which in the case of p+C contribute 30% or 15% to the total kaon multiplicity at  $E_{\text{lab}} = 1.6$  GeV with zero or with full Fermi momentum, respectively. The relative contributions of these channels are strongly beam energy dependent: At energies below  $E_{\text{lab}} = 1.3$  GeV, the  $N\pi$  channel dominates as illustrated by Fig. iv.2.

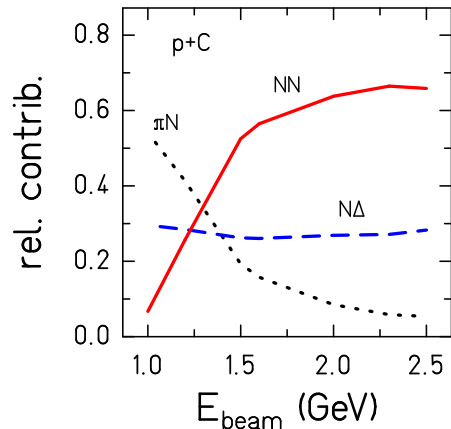


FIG. iv.2: Contribution of different production channels to the  $K^+$  production in p+C collisions as a function of the incident beam energy.

Because the cross section increases strongly close to the threshold (see Fig. iv.2) the Fermi motion allows for a strong enhancement of the  $K^+$  production due to collisions in which the Fermi motion of the target nucleon points toward the projectile. Finally, if the first collision is elastic (the cross section at these energies is strongly forward-backward peaked) there is a chance for producing a  $K^+$  in a second or even third collision of the projectile with a target nucleon. All these effects enhance the  $K^+$  production cross section with respect to p+p collisions and explain the huge increase of the  $K^+$  multiplicity when going from p+p to p+C collisions. When going from p+C (blue dashed line) to p+Au (red full line) Fig. iv.1 shows an additional increase at low laboratory momenta. This is due to  $K^+$  production in second or third collisions of the projectile after it had already lost a part of its energy. It may still produce a  $K^+$  if the Fermi momentum of the hit target nucleon supports this. In the Au case there is a much higher chance to find such a particle. The  $K^+$  is then not anymore produced in the p+p c.m. system but in the c.m. of the slowed-down projectile with a target nucleon. This explains the shift toward lower momenta which can be seen in calculations with (red full line) and without (red dash-dotted line) Fermi momentum.

In Fig. iv.3 we compare the simulations in the standard version with experimental p+C  $\rightarrow K^+$  data measured at COSY by the ANKE Collaboration [104, 105] at very small laboratory angles ( $0^\circ \leq \theta \leq 6^\circ$ ), and at energies around threshold ( $E_{\text{beam}} = 1.2, 1.5, 2.0$  and  $2.3$  GeV). There is an uncertainty in the absolute values of about 20% due to the ANKE cross section determination [106]. Simulations of spectra measured under almost zero degree in the laboratory are very sensitive to the rescattering of the kaons. Isotropic KN collision will deplete the yield in forward direction and rescattering into this region is rare. This depletion is directly proportional to the cross section. Changes of the density distribution of the target nucleons, the  $K^+$  nucleus potential or differences of the momentum distribution of the

nucleons which all have influence on the c.m. energy of the scattering partners show visible changes of the  $K^+$  spectra because the cross section increases very strongly as a function of  $\sqrt{s}$ . The influence of the Coulomb potential is negligible. The calculations have been filtered to respect the experimental acceptance. The simulated spectra show the same form as the experimental ones but over-predict slightly the experimental values for the standard (Sibirtsev [90])  $NN \rightarrow K^+$  cross section. As seen for the  $E_{\text{beam}} = 1.5$  GeV data the other available  $NN \rightarrow K^+$  cross section parameterization (Tsushima [91, 93]) brings the simulation closer to the data. Besides for high  $p_{\text{lab}}$  values, the  $K^+$  production in p+C collisions is a superposition of elementary p+p  $\rightarrow K$  collisions (dotted magenta line,  $E_{\text{beam}} = 2.0$  GeV). Fermi motion of the nucleons and multiple NN collisions tend to increase the  $K^+$  yield, the  $K^+$  nucleus potential has to opposite effect. At high beam energies the influence of the Fermi motion is visible at large momenta only. At the two lower energies the influence of the  $K^+$  nucleus potential is almost compensated by the Fermi motion. Consequently, at low momentum the  $K^+$  spectrum in p+C collision is very close to a superposition of p+p collisions with a scaled isospin averaged p+p cross section ( $\sigma(NN \rightarrow K^+ \Lambda N) = 1.5 \sigma(p + p \rightarrow K^+ \Lambda p)$ ). Due to poorly known  $pn \rightarrow K^+ Y$  nn cross section and due to the uncertainty of the in-matter modification of the  $pp \rightarrow K^+ Y$  pn cross section which are different in the parameterizations of Sibirtsev and Tsushima it is presently difficult to interpret the p+A data. If we switch off the Fermi momentum (green dashed-dotted line) the cross section drops by a factor of 2 (10) for the reaction at 1.5 (1.2) GeV. This demonstrates another time the importance of the Fermi motion for the total yield of the sub-threshold particle production.

Spectra at larger laboratory angles are much less sensitive to these details. Here rescattering plays already an important role. In Fig. iv.4 we compare IQMD calculations with the only other data set which is available for  $K^+$  production in p+A collisions. The KaoS Collaboration has measured  $K^+$  at laboratory angles of  $\theta_{\text{lab}} = 32^\circ$  and  $40^\circ$  [107]. These values correspond to an emission close to  $90^\circ$  in the center of mass of the p+p system. We present results using two different  $NN \rightarrow K^+$  cross-section parameterization (Tsushima [91, 93], Sibirtsev[90]) to demonstrate the uncertainty of the result due to the limited knowledge of this input quantity.

The standard IQMD simulation reproduces these data quite well, both the shape as well as the absolute value, a pre-requisite to apply the model to A+A collisions.

## B. The major production channels in A+A collisions

By going from p+A to A+A collisions the importance of the different production channels changes. Whereas in p+A collisions NN interactions are the most important ones for the  $K^+$  production (Fig. iv.2), in A+A collisions the channels which involve a  $\Delta$  dominate, as seen in Fig. iv.5, left. In heavy-ion reactions the chance increases that a  $\Delta$ , produced in a collision between a projectile and a target nucleon, hits a second projectile or target

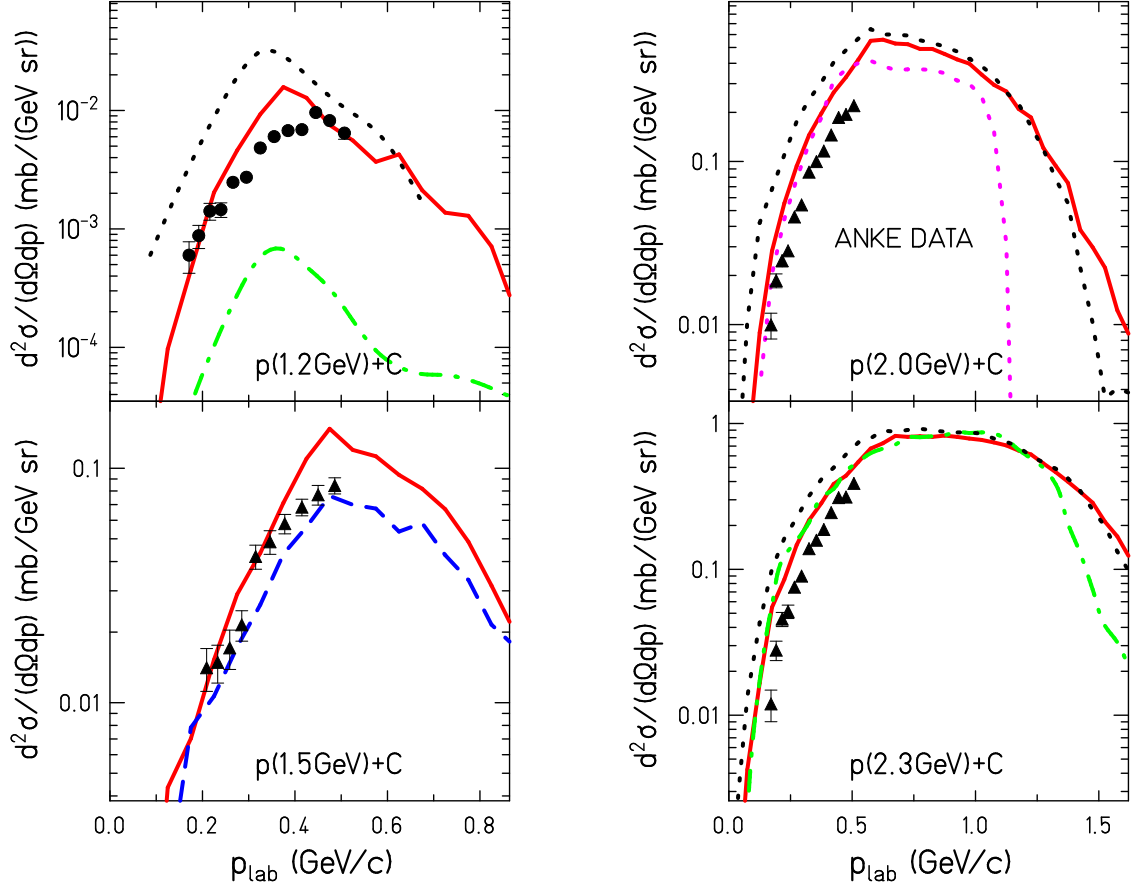


FIG. iv.3: Calculated p+C spectra at energies below and above the threshold as compared with the experimental results of the ANKE Collaboration [104, 105]. Full red line: Standard version, dotted black line: Standard without  $K^+$  nucleus potential, green dashed-dotted: Standard without Fermi motion, blue dashed: Standard but Tsushima parametrization of the  $NN \rightarrow K^+$  cross section, dotted magenta: Superposition of p+p cross section.

nucleon. In such a collision the available c.m. energy,  $\sqrt{s}$ , is quite high due to the large momentum of the nucleon on the one side and due to the high mass of the  $\Delta$  on the other side. Because all cross sections increase with  $\sqrt{s}$ , we expect a high production yield in this channel. Figure iv.5 shows on the left hand side the excitation function of the contributions of the different channels to the  $K^+$  yield in central Au+Au collisions. The right hand side displays the excitation function of  $K^+$  production via all channels and via  $NN \rightarrow K^+ \Lambda N$  alone for central Au+Au and C+C collisions. We observe that for both systems the NN channel represents only a small fraction.

The  $N\Delta$  channel is dominating even well above the NN threshold at 1.58 GeV incident energy. Contributions from the  $\Delta\Delta$  channel cannot be neglected at the rather low beam energies. The relative channel decomposition of the  $K^+$  production as a function of the

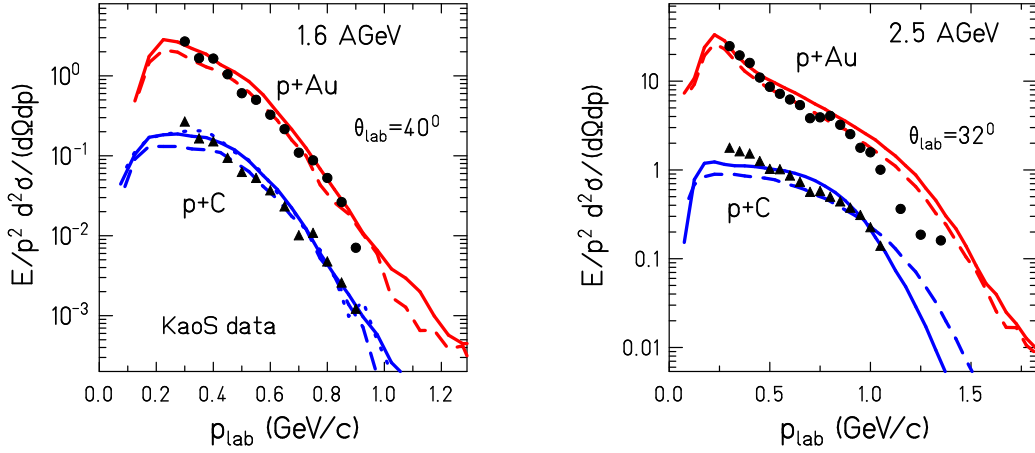


FIG. iv.4: Comparison of p+C and p+Au momentum spectra of the KaoS Collaboration [107] with calculations. The solid lines refer to the cross section parametrization of Sibirtsev et al. [90] and the dashed ones to that of Tsushima et al. [91, 93].

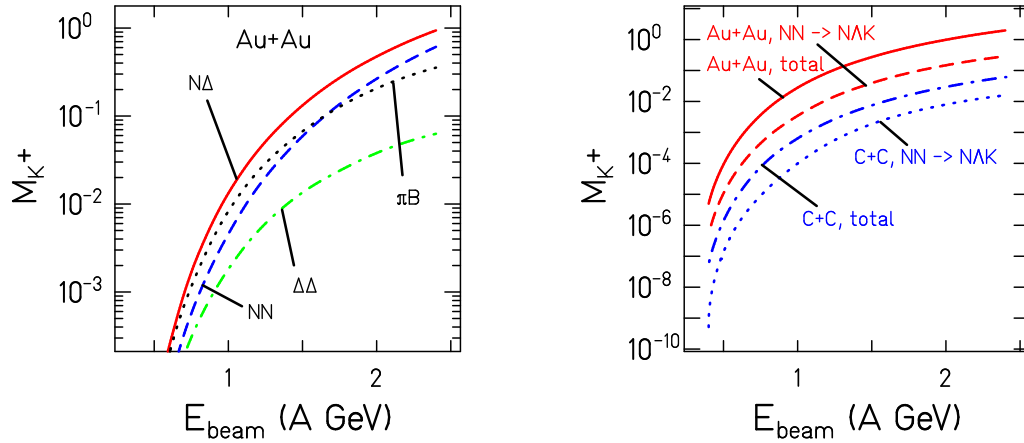


FIG. iv.5: Excitation function of  $K^+$  meson production in central ( $b=0$ ) collisions. Left: Excitation function of the different channels for Au+Au collisions. Right: Comparison of the total yield of Au+Au and of C+C collisions with the contribution of the elementary channel  $NN \rightarrow NAK$ .

beam energy (for  $b=0$  events in Au+Au collisions), as a function of the impact parameter (for Au+Au collisions at 1.5 A GeV) and as a function of the system size (for  $b=0$  at 1.5 A GeV beam energy) are shown in Fig. iv.6. The excitation functions, shown on the left, demonstrate that at different energies the importance of the different channels varies substantially as already visible in Fig. iv.5. At low beam energies a  $K^+$  can hardly be produced in NN collision, the Fermi momentum does not provide sufficient energy. Even in

$\Delta N$  collisions the c.m. energy is usually not sufficient. In  $\Delta\Delta$  collisions the available c.m. energy is larger and - although these collisions are rare - their contribution (as well as the  $\pi B$  cross section) gets significant at the lowest beam energy. This means as well that the prediction of the  $K^+$  yield at this energy depends on the quality of the theoretical prediction of the  $\Delta\Delta$  cross section which is experimentally not accessible. At higher energies, the  $N\Delta$  cross section dominates more and more until the direct production in a  $NN$  collision takes over, yet only very much above the threshold.

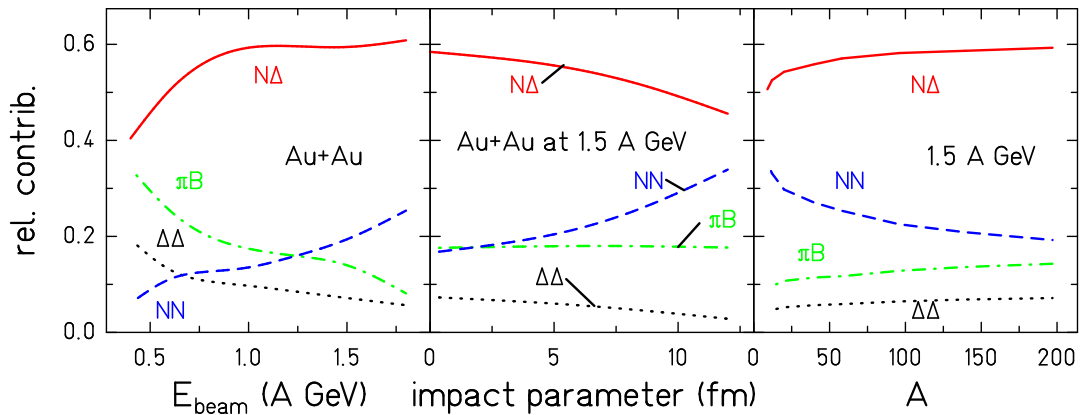


FIG. iv.6: The contribution of different production channels. Left: As a function of the beam energy in Au+Au reactions at  $b=0$ . Middle: As a function of the impact parameter in Au+Au reactions at 1.5 A GeV. Right: As a function of the system size for  $b=0$  at 1.5 A GeV.

### C. $K^+$ production via the $N\Delta$ channel

As shown in Fig. iii.7, for  $\sqrt{s}$  values above 2.7 GeV, corresponding to beam energies above 2 GeV in p+p collisions, there is quite a difference between the two parameterizations for the  $N\Delta \rightarrow K^+$  channel. In heavy-ion collisions well below 2 A GeV this difference is even amplified because the most energetic collisions contribute most to the yield. In non-peripheral collisions the  $\Delta$  channels are dominant and hence this difference to the elementary cross section transforms directly into a difference of the  $K^+$  yield in A+A collisions which increases with increasing system size (Fig. iv.7, right) as expected from the relative importance of the  $\Delta$  channels. As the difference between the various parameterizations increases with incident energy (Fig. iv.7, left), the excitation functions of the  $K^+$  production in Au+Au collisions exhibit an increasing difference with beam energy.

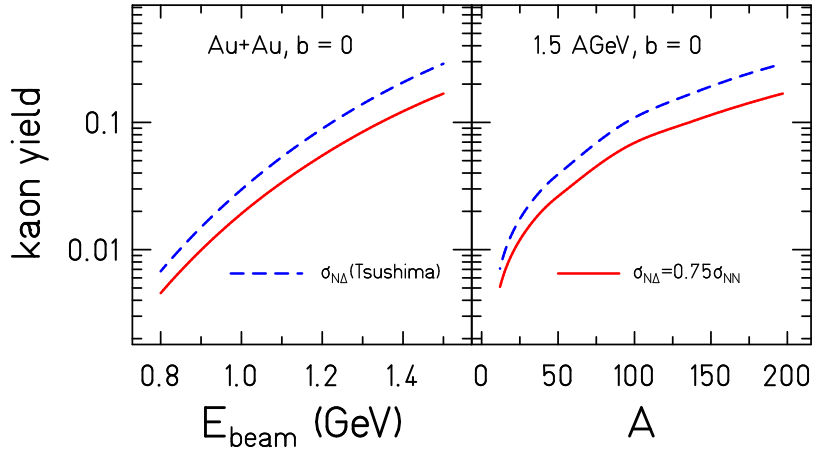


FIG. iv.7: The influence of the various parameterizations of the elementary  $N\Delta \rightarrow N\Lambda K^+$  cross section (see Fig. iii.7) on the kaon yield in A+A collisions. Left we display the excitation function, right the system-size dependence.

#### D. The $K^+$ nucleus optical potential

As discussed in section II,  $K^+$  mesons interact with the nuclear environment. The resulting IQMD distribution of  $K^+$  rest energy,  $\omega(\mathbf{k} = 0)$ , at the moment of their production in a central Au+Au reaction at 1.5 A GeV is shown in Fig. iv.8. An average mass shift of about 57 MeV is seen, corresponding to an average baryonic density at creation of around  $2\rho_0$  (see Fig. iii.1). A larger mass means a larger threshold and therefore the  $K^+$  nucleus potential lowers the  $K^+$  yield. This is demonstrated in Fig. iv.9, left, where in central Au+Au reactions the yield at the lowest beam energy is suppressed by a factor of three whereas at the highest energy the suppression is only 40%. The system-size dependence is rather weak as shown in Fig. iv.9, right. Light systems become less compressed during the reaction and consequently the influence of the  $K^+$  nucleus potential decreases.

Please note that the modification of the yield due to the different parameterizations of the  $N\Delta \rightarrow K^+ N\Lambda$  cross section (Fig. iv.7) is of the same order of magnitude as that of the  $K^+$  nucleus potential (Fig. iv.9). Hence, a smaller  $K^+$  production cross section has the same influence on the  $K^+$  multiplicity as a larger  $K^+$  nucleus potential. Also the Fermi motion of the nucleons modifies the production yield considerably, as seen in Fig. iv.9. Both graphs show as well the importance of the Fermi motion for the  $K^+$  yield.

These compensatory effects make it highly questionable if not impossible to use the absolute  $K^+$  yield to separate cross-section parametrization and potential effects. Initially this problem has not been realized. Different groups advanced calculations using different cross sections ([94], [91, 93]) and came to different conclusions, especially about the importance

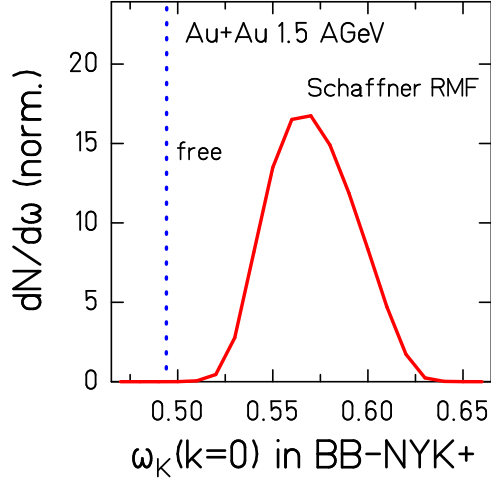


FIG. iv.8: Mass ( $\omega(\mathbf{k} = 0)$ ) distribution of the  $K^+$  at production in central ( $b = 0$  fm) Au+Au collisions at 1.5 A GeV as compared to the free  $K^+$  mass.

of the  $K^+$  nucleus potential for the explanation of the experimentally measured  $K^+$  yield in A+A collisions. In the meantime this has been solved [108].

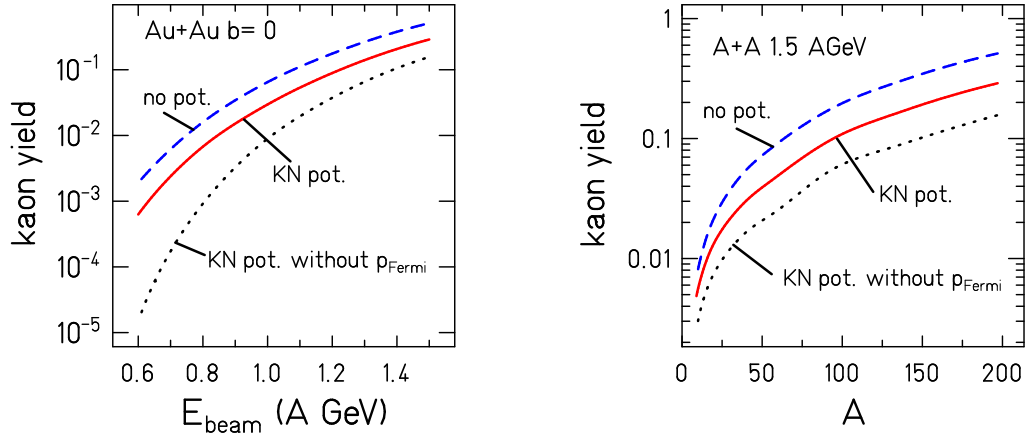


FIG. iv.9: Excitation function (left) and system-size dependence (right) of the  $K^+$  yield with and without  $K^+$  nucleus potential and with  $K^+$  nucleus potential but no Fermi momentum.

Despite of their relatively small cross section with nucleons of about 13 mb (the sum of elastic and charge-exchange collisions) most of the  $K^+$  rescatter with nucleons. We add in passing that we have not considered the details of the charge-exchange reactions  $K^+ n \rightarrow K^0 p$  in this calculation. We have parameterized this cross section, as it is shown in Fig.iii.8, but we do not apply the charge exchange itself. We simply treat these collisions like elastic ones



without changing the charge of the kaon. This may cause an uncertainty on the  $K^+$  yield of at most 10% in the Au case. These collisions do not change the total yield because all other particles which contain an  $\bar{s}$  quark are beyond reach.

Figure iv.10, left, shows the density at the time when the  $K^+$  mesons are created, and the mean free path of the  $K^+$  as a function of the distance of the production point from the center of the reaction. On the right hand side we display the distribution of the radial position at which  $K^+$  mesons are produced (upper part) and at which the  $K^+$  have their last interaction (lower part), selected according to the number of rescatterings  $N_C$ . (Note that  $N_{\text{coll}}$  refers to the number of NN collisions prior to  $K^+$  production, while  $N_C$  gives the number of KN collisions.) Those with many rescattering interactions originate more from the interior; those without collision ( $N_C = 0$ , corresponding to 18% of the produced  $K^+$ ) more from the outer region but not from the surface. This can easily be understood from the mean free path, shown left. Due to the high density in the center, the mean free path is there about 2 fm and  $K^+$ , which are created there, scatter quite frequently.

Dividing the time by the system size, one can see that the scaled time evolution of the  $K^+$  production in a C+C collision is similar to that of a Au+Au collision as shown in Fig. iv.11, left. The corresponding distributions of densities (Fig. iv.11, right) at which  $K^+$  mesons are produced and at which the last collision between a  $K^+$  and a nucleon takes place, differ strongly. This reflects the much larger stopping (and consequently the higher baryon density) in Au+Au as compared to C+C collisions.

## E. Reaction Dynamics

Close to threshold  $K^+$  are rarely produced in a first collision between a projectile and a target nucleon. Figure iv.12, left, shows the probability distribution of the number of collisions prior to the  $K^+$  production of those nucleons which produce finally a  $K^+$  meson. Its production in first-chance collisions is a negligible process even at a beam energy of 1.5 A GeV. In order to gain sufficient energy the nucleons have to collide before, usually quite often. These collisions start to thermalize the momentum distribution, as is seen from the average  $Q_{zz} = 3p_z^2 - p^2 = 2p_z^2 - p_t^2$  value for protons, shown on the mid part of Fig. iv.12 which approaches the value of zero, expected for a system with an isotropic momentum distribution.

The average number of collisions prior to  $K^+$  creation depends on the reaction channel and it increases with the number of  $\Delta$  in the entrance channel because these particles have to be produced first. These collisions modify the momentum distribution of the nucleons or - in other words - these nucleons carry information on their environment which they can communicate to the  $K^+$ . However, different  $K^+$  momenta are not selective to a different number of prior collisions of the parents as demonstrated in Fig. iv.12, right. The inverse slope parameters of  $K^+$  mesons from the various channels are very similar. We note, however,

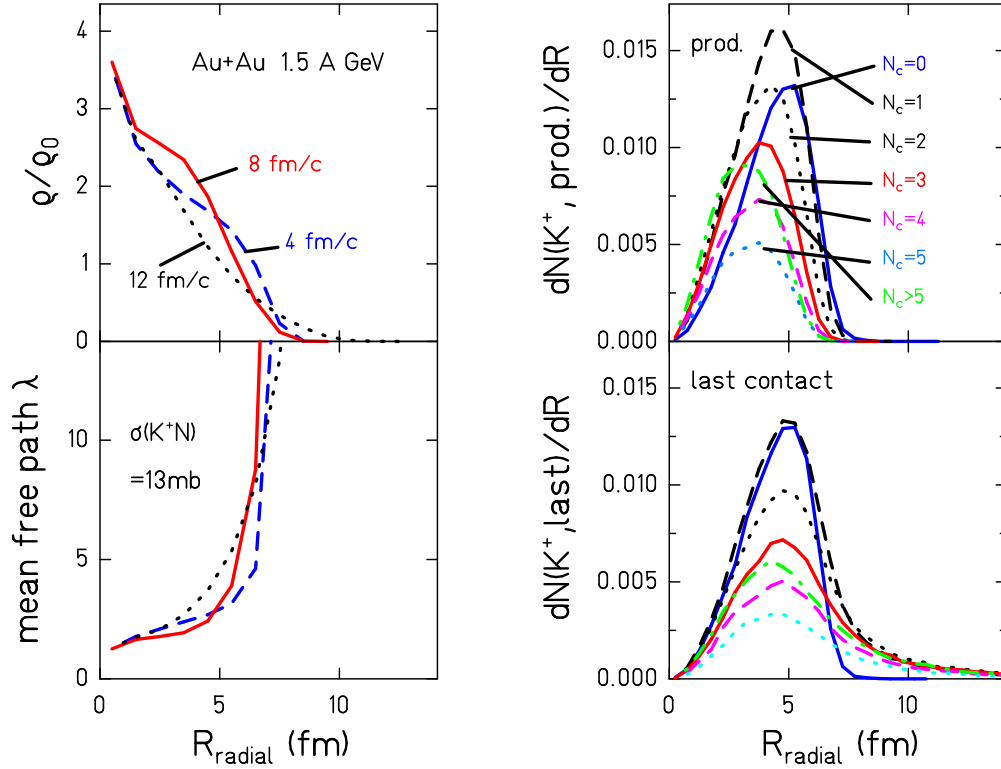


FIG. iv.10: Left: Density of nucleons and the mean free path of the  $K^+$  as a function of the distance of the production point from the center of the reaction for various time steps. Right: Density profiles for production and last contact selected according to the number of rescattering collisions  $N_C$ .

that first-chance NN collisions show a steeper slope than the average over all collisions as will be discussed later.

The  $K^+$  mesons are produced quite early ( $\approx 7$  fm/c) in the Au+Au reaction (Fig. iv.13, left). The difference between the different channels reflects how many collisions the parents have to have before a  $K^+$  meson is created giving a sequence starting with NN, then  $\Delta N$ ,  $\pi B$  and  $\Delta\Delta$  collision. The average baryon density at the production of the  $K^+$  is around  $\rho = 2\rho_0$  (Fig. iv.13, right) as observed already in Fig. iv.8. As expected,  $K^+$  with a  $\Delta$  in the entrance channel a) are produced later because the  $\Delta$  has to be created first and b) are produced at a higher density because the lower the density the higher is the chance that the  $\Delta$  decays before producing a  $K^+$ . This density dependence is of great importance for our later discussion on the nuclear equation of state, section VIA.

In Fig. iv.6, middle, we have shown that with increasing impact parameter, this means with decreasing number of participants, the importance of the two-step channels implying a  $\Delta$  decreases. Whereas in central collisions the two-step reactions dominate, in peripheral

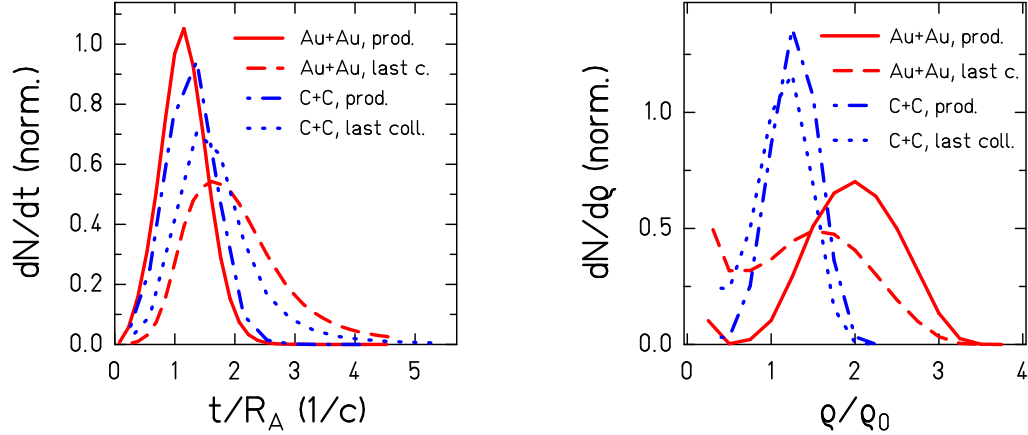


FIG. iv.11: Comparison of central ( $b = 0$ ) collisions of C+C and Au+Au at 1.5 A GeV . On the left hand side the yields are shown as a function of the production/emission time divided by the radius  $R_A$  of the respective nuclei. The right hand side exhibits the respective densities at production and at the last collision.

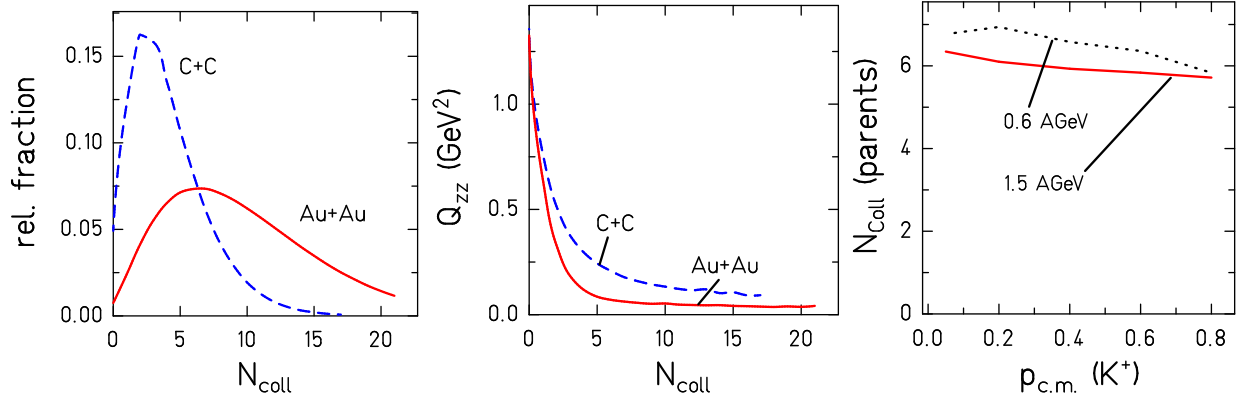


FIG. iv.12: Properties of the parent baryons which create a  $K^+$  for Au+Au and C+C at  $b=0$  fm and for 1.5 A GeV. Left: Distribution of the number of collisions prior to the  $K^+$  production. Middle: Sphericity  $Q_{zz}$  as a function of the collision number. Right: Average number of collisions prior to the creation of a  $K^+$  with a given momentum  $p_{c.m.}$  in central AuAu collisions.

collisions the NN channel becomes almost as important. Studying the contributions as a function of the system size (right hand side) a very similar behavior is seen: The smaller the system the less important becomes the two-step  $N\Delta$  or three-step  $\Delta\Delta$  channel. In conclusion,  $K^+$  production in A+A collisions is very different from that in p+A collisions. The in-medium modification of the  $K^+$  properties change, due to different densities. Furthermore the dominant production channels are different and rescattering is an important issue if we want to understand the spectra. The influence of these effects depends on the size of the

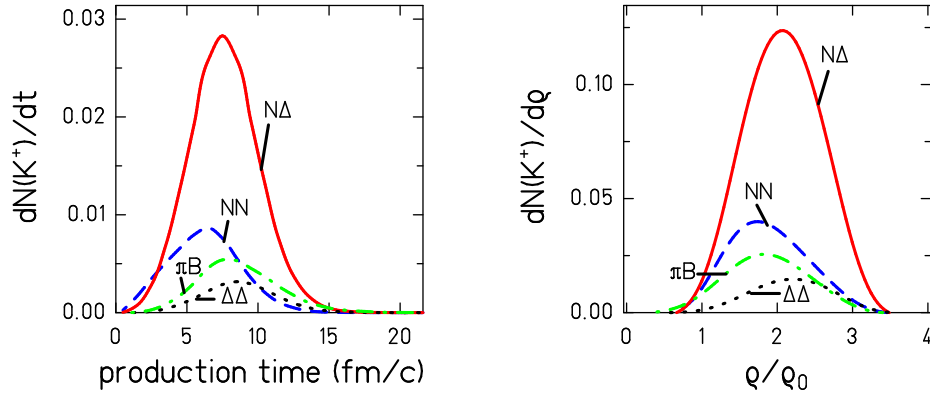


FIG. iv.13: Evolution of the  $K^+$  yield for the various production channels as a function of the time (left) and in respect to the density at which they are produced (right) for central Au+Au collisions at 1.5 A GeV.

system. Consequently, the  $K^+$  observables allow to study many features of the heavy-ion reaction which are not accessible by non-strange particle observables. We continue with a detailed study of these observables and — by comparing the experimental results with IQMD calculation — with the interpretation of these observations.

### F. Excitation functions

The excitation function of the  $K^+$  yield in experiment [109] and in theory for inclusive Au+Au and C+C reactions is shown in Fig. iv.14, top left. The dashed lines present the theoretical results assuming a vanishing  $K^+$  nucleus potential, the full ones include the  $K^+$  nucleus potential. In order to demonstrate the high collectivity of the  $K^+$  production, the cross sections in this figure are divided by  $A^{5/3}$ . If the  $K^+$  multiplicities are proportional to the system size, i.e. to the number of participating nucleons,  $\sigma/A^{5/3}$  is constant and the results of both systems coincide. The top and bottom left figure shows that for the heavier system  $\sigma/A^{5/3}$  is up to 5 times higher than for the lighter one. The origin of this enhancement is the higher compression which leads to a smaller mean free path and, as a consequence, to more many-step processes as will be discussed in the next section. The influence of the  $K^+$  nucleus potential depends on the system size and on the beam energy, Fig. iv.14, top right. While a considerable change is observed as a function of the beam energy, the influence of the system size is rather small.

Including the  $K^+$  nucleus potential brings the calculation close to the experimental data (top left). One may ask whether one can turn this argument around and claims that the experimental data are a “smoking gun” for the mass change of the  $K^+$  mesons in the medium. As discussed in the last section, at high beam energies a smaller  $\sigma_{\Delta N \rightarrow K^+}$  cross section leads

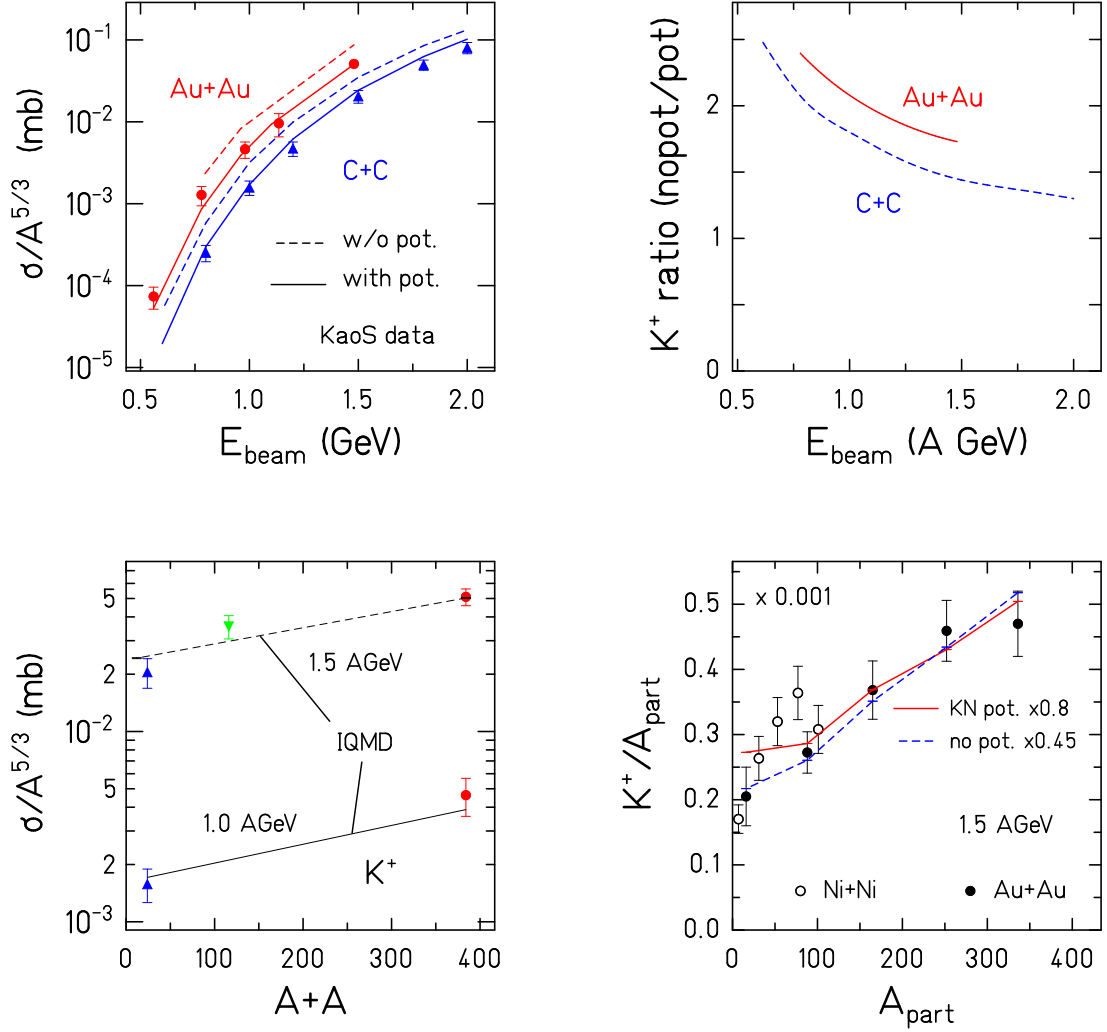


FIG. iv.14: Upper left: Excitation function of the inclusive  $K^+$  cross section in C+C and Au+Au collisions divided by  $A^{5/3}$  with and without the  $K^+$  nucleus potential. The symbols represent experimental results of the KaoS Collaboration [109]. Upper right: Influence of the  $K^+$  nucleus potential demonstrated by the ratio of the  $K^+$  yields without potential divided by those with potential for two collision systems. Lower left: Production cross section divided by  $A^{5/3}$  as a function of the system size  $A + A$ . The symbols represent data from the KaoS Collaboration [109], the lines connect the calculations for C+C and Au+Au. Lower right: Multiplicity per  $A_{\text{part}}$  of  $K^+$  mesons as a function of  $A_{\text{part}}$  for Au+Au and Ni+Ni collisions at 1.5 A GeV [109] as compared to IQMD simulations. The calculations are scaled by factors of 0.8 and 0.45, respectively.

to a similar increase of the yield as a smaller  $K^+$  nucleus potential. This is, however, not true any more for the excitation function. The influence of the  $K^+$  nucleus potential on the  $K^+$  yield increases with decreasing energy (top right) whereas the contribution of the  $N\Delta$  channel stays rather constant down to a beam energy of 750  $A$  MeV, see Fig. iv.6. On the basis of the present calculation one can identify the  $K^+$  nucleus potential as the reason for the agreement of the experimental and theoretical excitation function of the cross sections of C+C and Au+Au systems, although for a confirmation data at lower incident energies and for different system sizes are necessary.

The collectivity of the  $K^+$  production is quantified in Fig. iv.14, bottom. The left side shows the scaling with system size. If the cross section would be proportional to the number of participating nucleons, i.e. the nucleons which are located in the overlap zone between projectile and target, we would expect a cross section  $\propto A^{5/3}$ . For an easy comparison in this presentation we have divided the inclusive cross section by  $A^{5/3}$ . Both, the data and the calculation (dashed and full lines), show an increase of this quantity with the system size  $A + A$ . A similar comparison is presented in the bottom right figure where for reactions at 1.5  $A$  GeV the multiplicity per  $A_{\text{part}}$  for the different centrality bins are displayed and compared with theory. IQMD calculations reproduce quite well the trend but over-predict the data by 20%. Without  $K^+$  nucleus potential the over-prediction is more than a factor of 2.

## G. Kaon spectra

The  $K^+$  momenta at production are modified by two processes before they are registered in the detectors: Elastic rescattering off the nucleons and potential interactions. Both effects are demonstrated in Fig. iv.15. The spectra are displayed as  $E/p^2 dN/dp$  and can be described by an exponential function  $\exp(-E_{\text{c.m.}}/T)$ . The fitted inverse slope parameters  $T$  are given in this figure. At production the shape of the spectra is determined by the three-body phase space, which is not exponential. Averaging over the distribution of  $\sqrt{s}$  and of the center of mass velocities of all collisions which produce a  $K^+$  the distribution becomes almost exponential. Due to the (in the average) lower c.m.-energy the slope of the  $K^+$  is slightly steeper if two nucleons are in the entrance channel ( $T = 70$  MeV) as compared to a  $\Delta N$  combination ( $T = 78$  MeV). As the  $\Delta N$  channels dominates, the inverse slope parameter at production is  $T = 75$  MeV. This value is lower than that of the final baryons and subsequent  $KN$  rescattering causes the slope of the  $K^+$  mesons to be shallower as seen in Fig. iv.15, left. The fitted inverse slope parameter for central Au+Au reactions at 1.5  $A$  GeV is initially  $T = 73$  MeV for  $K^+$  with more than two rescattering collisions and increases to 113 MeV (Fig. iv.15, left). In more detail, we find that the slope of the  $K^+$  spectra increases with the number of rescattering collisions ( $T = 88, 99, 121, 113$  MeV for  $N_C = 0, 1, 2, > 2$ ).

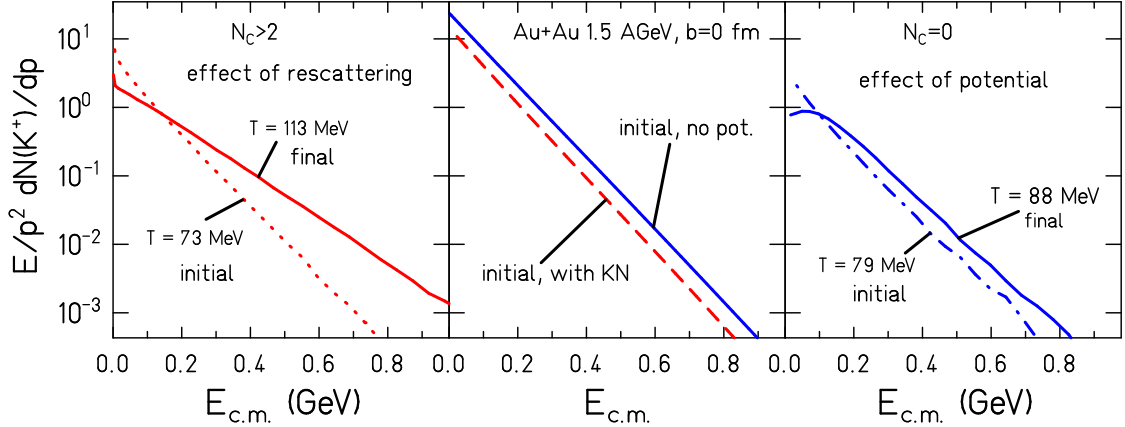


FIG. iv.15: Influence of rescattering and of the  $K^+$  nucleus potential demonstrated for central Au+Au collisions at 1.5 A GeV. Left: Influence of the rescattering of  $K^+$  mesons by selecting kaons which have scattered twice or more, showing their initial and final distribution. Middle: Influence of the  $K^+$  nucleus potential on the spectra at production. Right: Influence of the  $K^+$  nucleus potential on the spectral shape demonstrated by selecting kaons which never scattered ( $N_C = 0$ ) and comparing the initial and final spectra.

The  $K^+$  nucleus potential lowers the  $K^+$  yield, as we have discussed. It has, however, little influence on the shape of the  $K^+$  spectrum as shown in Fig. iv.15, middle. Between production and registration in the detector the  $K^+$  mesons have to lose their excess mass and this leads — due to the inherent momentum and energy conservation — to an acceleration of the  $K^+$ . This acceleration shifts the spectrum to higher momenta and distorts it only for small momenta as can be seen in Fig. iv.15, right, where events with  $N_C = 0$  are selected. At higher momenta we observe a marginal increase of the slope.

Figure iv.16, left, displays the distribution of the number of rescatterings ( $N_C$ ) the  $K^+$  suffers before leaving the collision zone. The distribution is quite independent on the  $K^+$  nucleus potential. Only about 17.5% do not suffer a rescattering collision. Thus, it is evident that the scattering of the  $K^+$  with the environment determines the slope of its spectra. This is demonstrated on the right hand side where we display the influence of the  $K^+$  nucleus potential and of the  $K^+$  rescattering on the shape of the  $K^+$  energy spectra. The inverse slope parameters of the  $K^+$  at production (dotted line), at last contact (last  $K^+$  N collision or production if  $N_C = 0$ , solid line) and after the  $K^+$  is out of range of the  $K^+$  nucleus potential (dashed line) are shown with respect to the number of KN scatterings for Au+Au collisions at 1.5 A GeV. The values at production vary with  $N_C$  as different densities are selected by this way. This figure demonstrates that in this heavy system the influence of scattering on the slope is huge as compared to the acceleration by the potential and that after two collisions the inverse slope parameter of the  $K^+$  mesons reaches a

saturation value. Even an artificial increase of the cross section for rescattering does not cause higher values. Thus two collisions bring the  $K^+$  into a kinetic equilibrium with its environment.

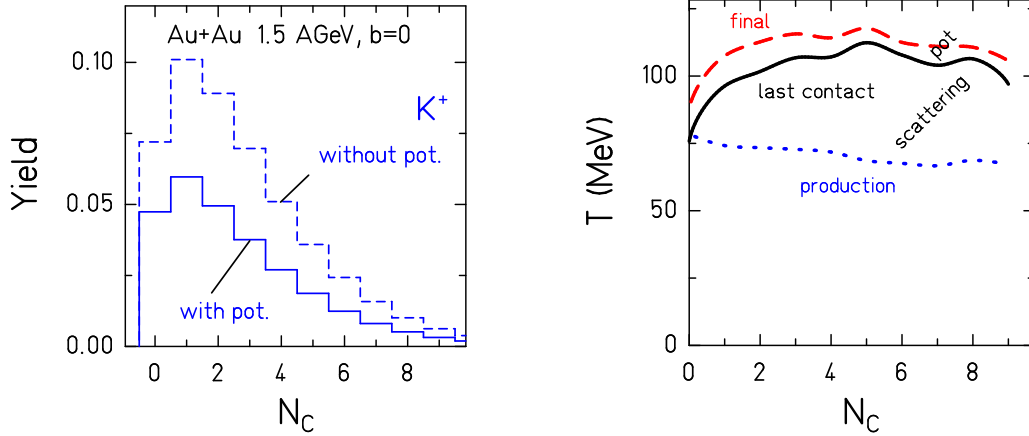


FIG. iv.16: Left: Number of  $K^+$  rescattering Right: Change of the inverse slope parameters due to the different processes discussed in the text as a function of the number of rescatterings  $N_C$ .

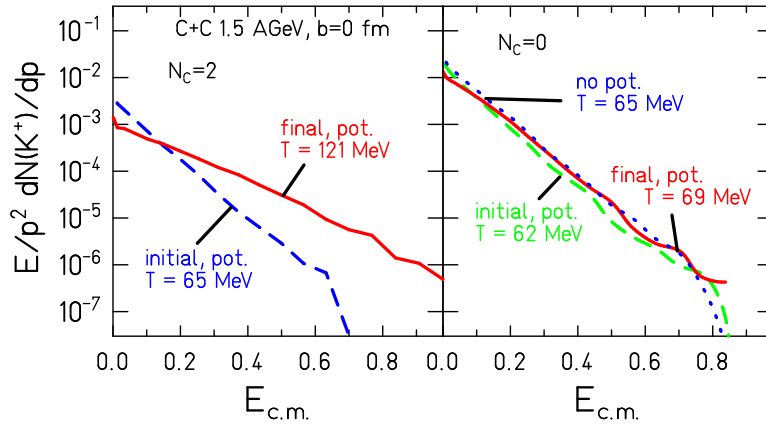


FIG. iv.17: Influence of rescattering and of the  $K^+$  nucleus potential demonstrated for central C+C collisions at 1.5 A GeV. Left: Influence of the rescattering of  $K^+$  mesons by selecting kaons which have scattered twice, showing their initial and final distribution. Right: Influence of the  $K^+$  nucleus potential on the  $K^+$  spectrum for  $K^+$  which do not rescatter. Without  $K^+$  nucleus potential initial and final distribution is identical.

For the lighter C+C system we expect that rescattering is less important. Consequently, in C+C collisions the slope of the energy spectra should be steeper. Indeed, as shown in



Fig. iv.17, the slope at production of the  $K^+$  is around 65 MeV and thus about 10 MeV lower than in the Au+Au reaction (Fig. iv.15) because in a gold nucleus the fraction of NN collisions as compared to those with a  $\Delta$  in the entrance channel is lower (see Fig. iv.6), 20% as compared to 35% in the C+C system. In the right panel of Fig. iv.17 the effect of the potential is demonstrated by selecting  $N_C = 0$ . That effect is marginal. Rescattering increases the slope to a value of 121 MeV for  $N_C = 2$  as it can be seen from the left part of the figure. In the discussion of Fig. iv.15 we found in the Au case a similar slope value for the final momenta for the same  $N_C = 2$  selection.

Due to the lower density the  $K^+$  mass shift is smaller and hence the influence of the  $K^+$  nucleus potential on the spectra is, especially at low energies, weaker as compared to Au + Au reactions. Consequently, for the same number of rescattering collisions the spectra in Au+Au and C+C collisions are rather similar. Thus a different slope of the spectra in C+C as compared to Au+Au is predominantly due to the much smaller number of rescattering collisions in the former case. We have also to take into account, that - as we will see in Fig. iv.28 - kaons show a strong polar anisotropy, preferring an emission towards the beam axis. This may indicate that kaons may not only have rescattered with "thermalized matter" but also with spectators. This might explain the high values of the slope especially for the C+C case.

As already indicated in Eqs. (59) and (60) the  $K^+$  nucleus potential contains a part depending on the relative velocity  $\beta_{rmKN}$  of the kaon with respect to the nuclear medium. One might thus question whether the influence of that momentum dependence might show a significant effect on the spectra. Indeed the deactivation of those momentum-dependent interactions would yield a slight increase at high energies for the Au+Au case and thus enhance the temperature by about 1-2 MeV. For the C+C no significant effect is visible. The reason for that moderate influence is related to several aspects: the momentum dependence shows only strong effects for large  $\beta_{KN}$ . These kaons should be dominantly seen at the high-energy part of the spectra. However, these kaons are dominated by a (late) rescattering of the kaons with the nucleons which takes place at quite moderate densities. Furthermore, rescattering normally reduces the relative momenta with respect to the nuclear medium. Therefore, the effect of the momentum dependence becomes quite small.

After these theoretical considerations we now compare our results with data. Figure iv.18 shows the experimental inclusive momentum distributions for 1.5 A GeV Au+Au by the KaoS Collaboration [109] at various angles in the laboratory system in comparison with calculations, including and excluding the  $K^+$  nucleus potential. The influence of the potential is visible and gives a suppression by about a factor of 1.5 as compared to the calculation without potential. As expected the influence of the potential is largest at low momenta. The theory reproduces the data quantitatively at all emission angles but the measured angular distributions exhibit a somewhat stronger asymmetry than the calculated ones.

The inclusive spectra at mid-rapidity for different symmetric systems and at various incident energies as measured by the KaoS Collaboration [109] are compared in Fig. iv.19 with

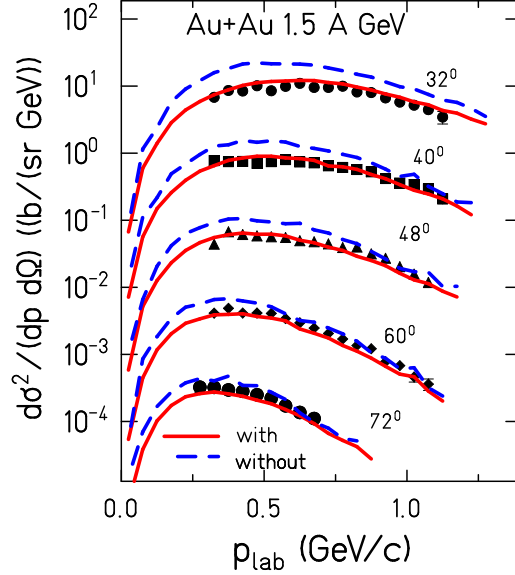


FIG. iv.18: Comparison of experimental laboratory momentum spectra with IQMD calculations including and excluding the  $K^+$  nucleus potential. The data are from the KaoS Collaboration [109].

IQMD calculations (top) and with HSD calculations [70] (bottom), both in their standard version. All these spectra are well reproduced by an exponential function with one inverse slope parameter  $T$ .

The KaoS Collaboration has also analyzed the  $K^+$  spectra at  $\theta_{\text{lab}} = 40^\circ$  for different centrality classes and in Fig. iv.20 we compare these data with IQMD calculations. The slopes are increasing towards central collisions both in theory as well as in experiment. This is expected due to the increasing number of  $K^+$  which have scattered. A very good agreement between theory and experiment for all centrality classes can be seen.

These spectra can be well described by an exponential function with an inverse slope parameter  $T$ . These values, both from experiment and from IQMD calculations (lines), are displayed in Fig. iv.21, on the upper left hand side as excitation function for three different systems. The inverse slope parameters increase both with system size and with increasing incident energy. This trend can be explained by the increasing fraction of  $K^+$  mesons which rescatter. Increasing energy means more available energy in the elementary production but also increasing density and therefore more rescattering. It is interesting to compare the results for  $K^+$  with the corresponding values for high-energy pions [102](upper right panel). Both exhibit a remarkable resemblance.

On the bottom part of Fig. iv.21, the centrality dependence of the inverse slope parameters is given for Au+Au collisions at 1.5 A GeV. This figure also elucidates the influence of both, the  $K^+$  nucleus potential and rescattering, on the final slopes. The effect of rescattering is important, yet only if both are present the slope of the experiment can be reproduced. For

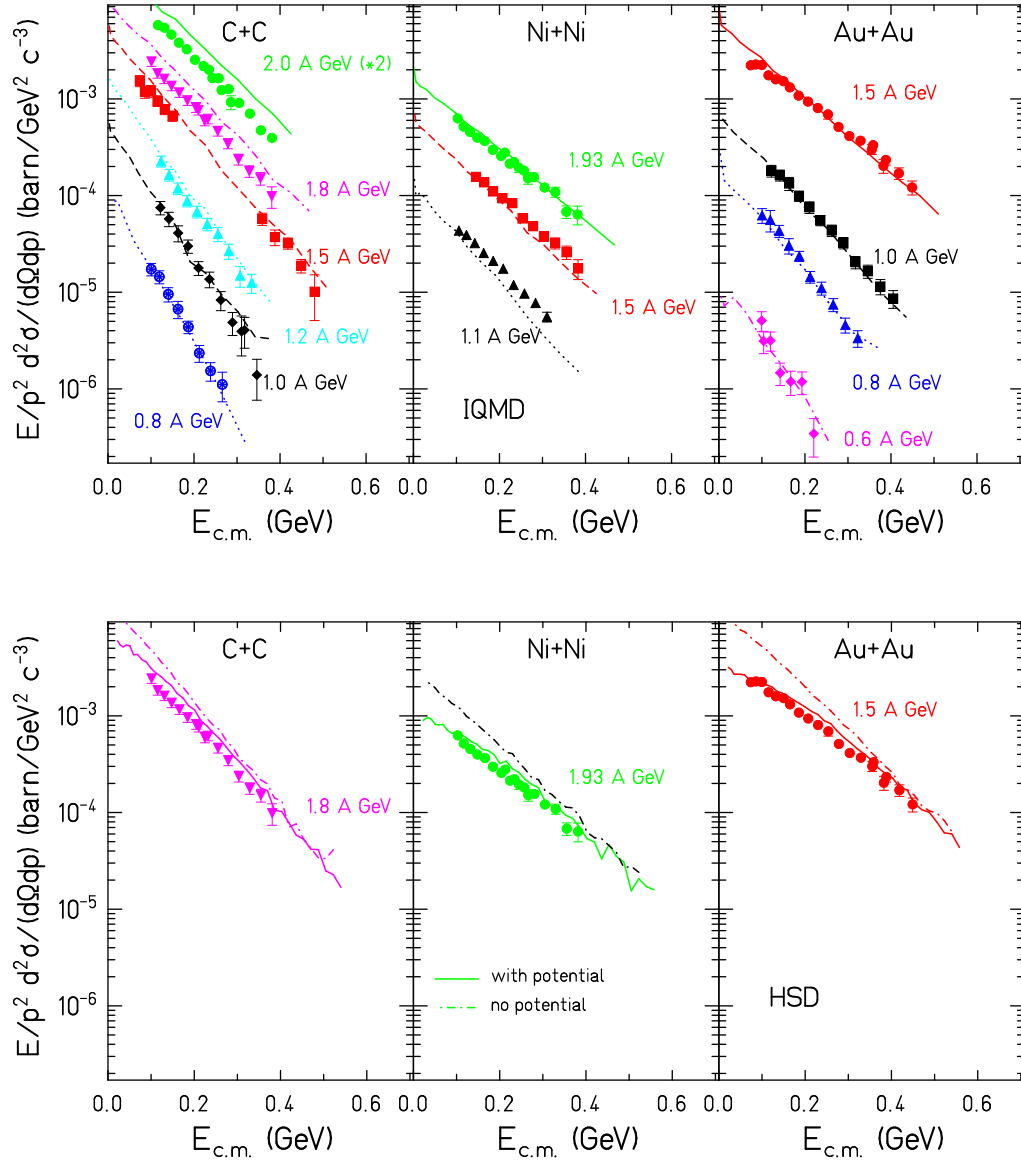


FIG. iv.19: Top: Measured (symbols) and calculated (IQMD, lines) inclusive invariant cross sections of  $K^+$  at mid-rapidity as a function of the kinetic energy  $E_{c.m.}$  for C+C (left), Ni+Ni (middle) and Au+Au (right) reactions at various beam energies. The mid-rapidity condition is a selection of  $\theta_{c.m.} = 90^\circ \pm 10^\circ$  both for the data and the calculations. The data are from the KaoS Collaboration [109], the lines represent calculations with  $K^+$  nucleus potential included. Bottom: The same data compared to HSD calculations [70]. Here the dashed lines refer to the option without  $K^+$  nucleus potential, the solid ones to that with  $K^+$  nucleus potential.

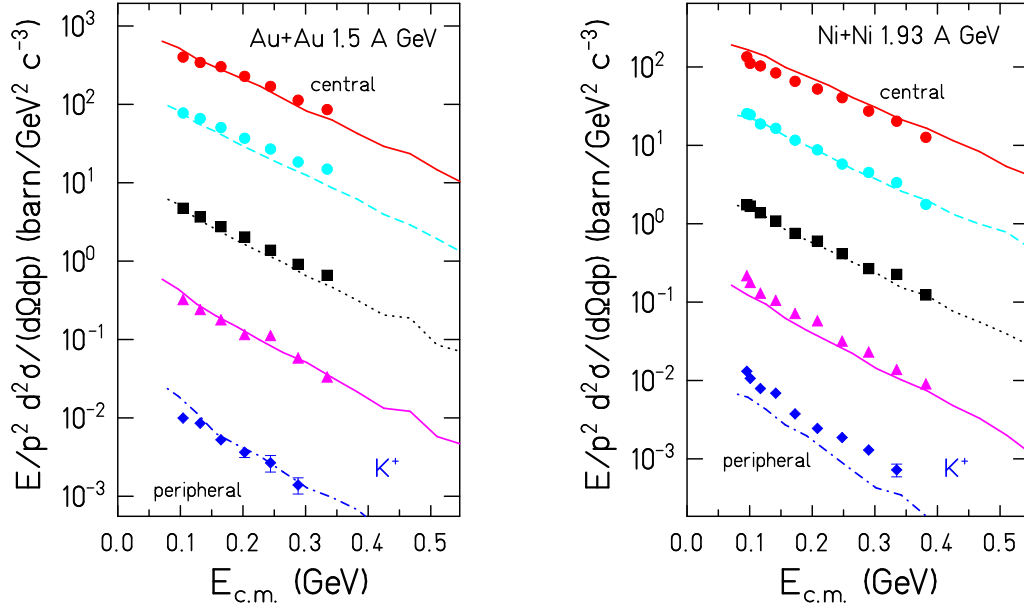


FIG. iv.20: Centrality selected energy spectra for Au+Au at 1.5 A GeV and for Ni+Ni at 1.93 A GeV both at  $\theta_{\text{lab}} = 40^\circ$  (right) as compared with IQMD calculations.

the Ni+Ni case (not shown) the theoretical (experimental) slope parameters (going from the most central to the most peripheral reactions) are 106.1 (109.1), 101.8(96.4), 97.8(91.7), 91.4(81.0), 79.2(69.3) MeV, reflecting as well the decreasing number of rescattering collisions. The uncertainty of the fitted inverse slope parameters is of the order of 10%. In passing we would like to mention that also the magnitude of the nucleon-nucleon cross section has a mild influence on the  $K^+$  slope. If we assume that the in-medium nucleon-nucleon cross section is only half of the free cross section the  $K^+$  yield decreases by 5%.

The FOPI Collaboration has measured the  $m_t - m_0$  spectra of  $K^0$  mesons for central Ni+Ni collisions ( $\sigma \approx 350$  mb, this value equates to an impact parameter in a sharp cut-off model of  $b=3.2$  fm) at 1.93 A GeV. The spectra for different rapidity bins are shown in Fig. iv.22 and compared with IQMD and HSD calculations. In the experiment central events are selected by requiring high charged-particle multiplicity in the forward hemisphere of the detector setup. The IQMD output was used as an event generator for a detector simulation based on the GEANT package to obtain a realistic impact-parameter distribution for the multiplicity selection cut [110] which was then used for the comparisons between data and model predictions.

More recently the HADES Collaboration has obtained  $m_t - m_0$  spectra of  $K^0$  for the lighter Ar+KCl system at a slightly lower beam energy of 1.75 A GeV. These results are compared with IQMD and HSD calculations in Fig. iv.23, upper panel. In the calculation we have chosen a sharp cut-off of  $b = 6$  fm. This gives  $\langle b \rangle = 4$  fm, a value which is

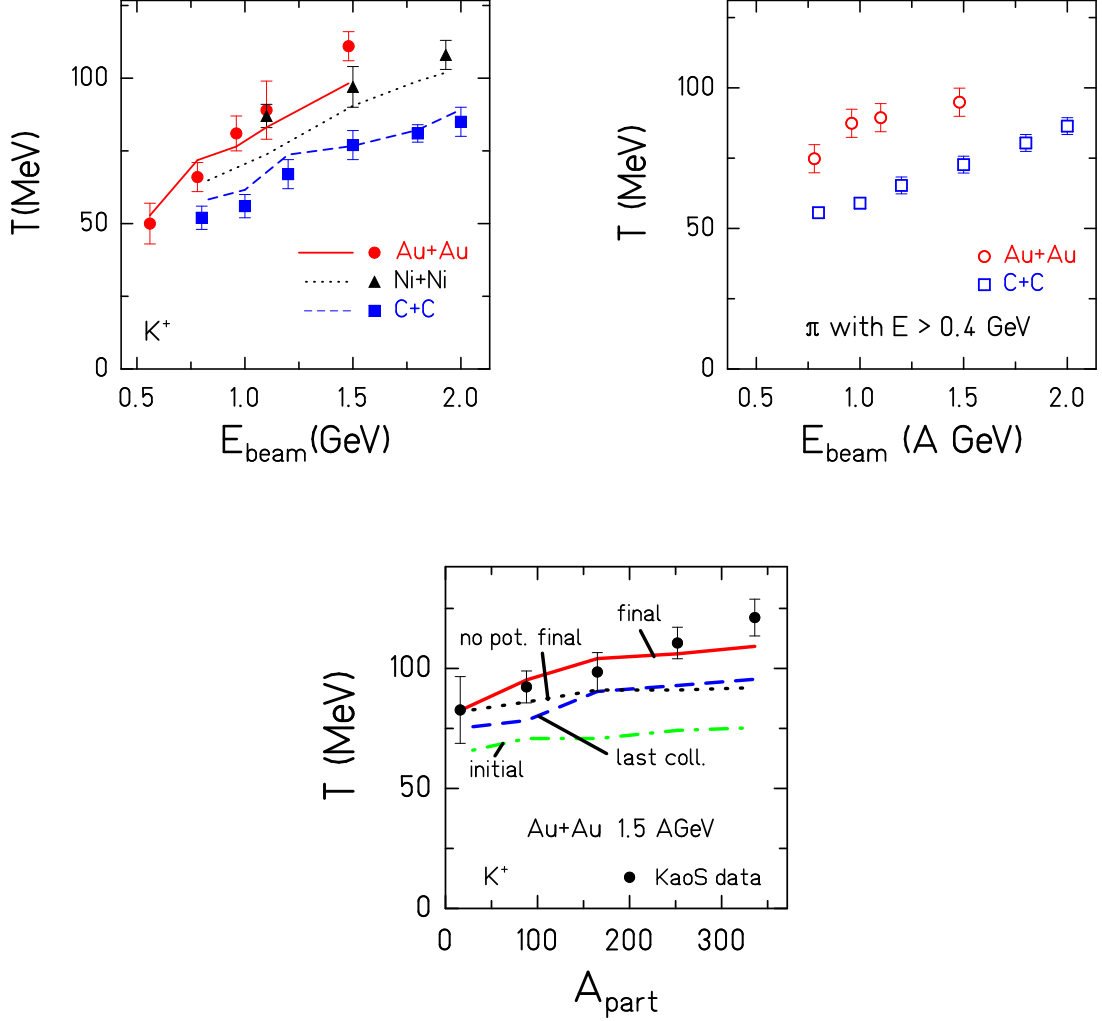


FIG. iv.21: Dependence of the inverse slope parameter on incident energy (top) and on centrality (bottom). All results are for inclusive collisions and at mid-rapidity ( $\theta_{c.m.} = 90^\circ \pm 10^\circ$ ). The upper left panel displays the  $K^+$  inverse slope parameter which can be compared to those of the high-energetic pions (upper right). The IQMD results for  $K^+$  are given as lines. The data (symbols) are from the KaoS Collaboration [102, 109]. at mid-rapidity. Bottom: Dependence of the slope parameter on the centrality for Au+Au at 1.5 A GeV.

compatible with  $\langle b \rangle = 3.5$  fm, the value reported by the HADES collaboration using a rather soft central trigger.

In the top panel the measured  $m_t - m_0$  spectra are depicted in comparison to the predictions of the IQMD and of the HSD model, with and without a  $K^+$  nucleus potential. In the lower panel the ratio of IQMD model predictions and the experimental data is shown. Calculations incorporating an  $K^+$  nucleus potential are better describing the experimental

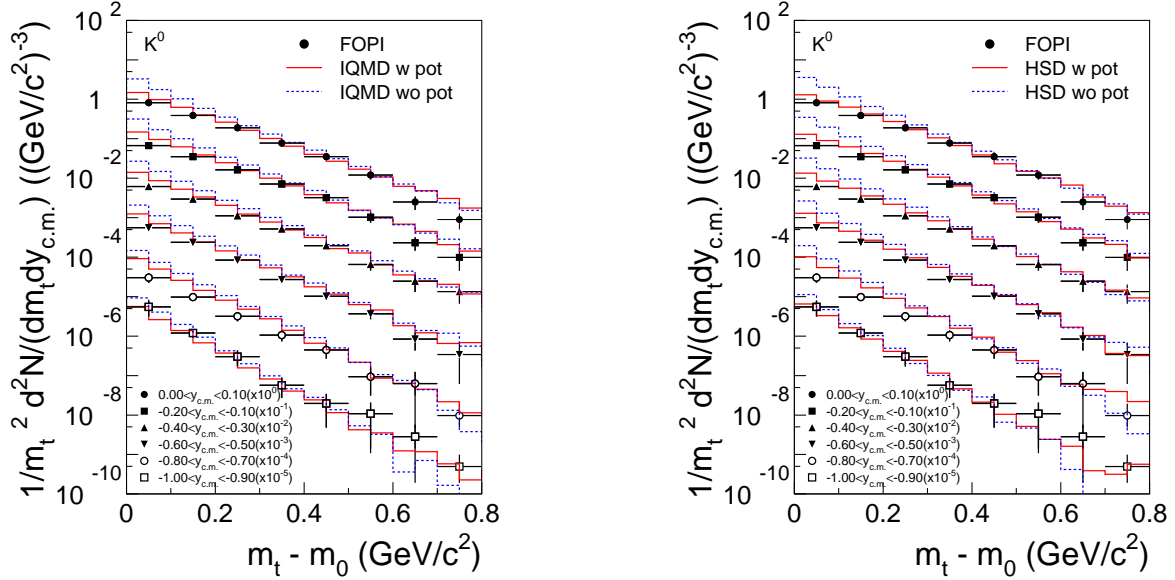


FIG. iv.22:  $m_t - m_0$  spectra of  $K^0$  measured by the FOPI Collaboration for central Ni+Ni at 1.93 A GeV [110] in comparison with IQMD (left) and HSD (right) calculations (histogram) for different values of the rapidity  $y_{c.m.}$ . We present calculations with and without  $K^+$  nucleus potential.

data.

Fitting the measured and the calculated  $m_t - m_0$  spectra of  $K^0$  of Fig. iv.22 and Fig. iv.23 with an exponential function and extrapolating towards vanishing  $m_t - m_0$  values allows for the determination of the rapidity dependence of the slopes and of the total yield  $dN/dy$ . As seen in Fig. iv.22 the spectra of  $K^0$  are not really exponential and therefore the extrapolation depends on the range of  $m_t$  which is used for this fit. It was taken care that the fit ranges for the experimental data and the theoretical distributions are the same. Therefore the theoretical and experimental inverse slope parameters can be compared but neither the slope nor the  $dN/dy$  are free from the uncertainty of the fit. For the HADES data Fig. iv.23 the situation is different. Here theory as well as experiment show an exponential form of the spectrum. Because the HADES acceptance is close to mid-rapidity we expect more thermalization.

Figure iv.24 displays the experimental inverse slope parameters measured by FOPI (top) and by HADES (bottom) as a function of the rapidity in comparison with the two model predictions. The Ni+Ni data at 1.93 A GeV as well as the Ar+KCl data at 1.75 A GeV are well described by both models approaches.

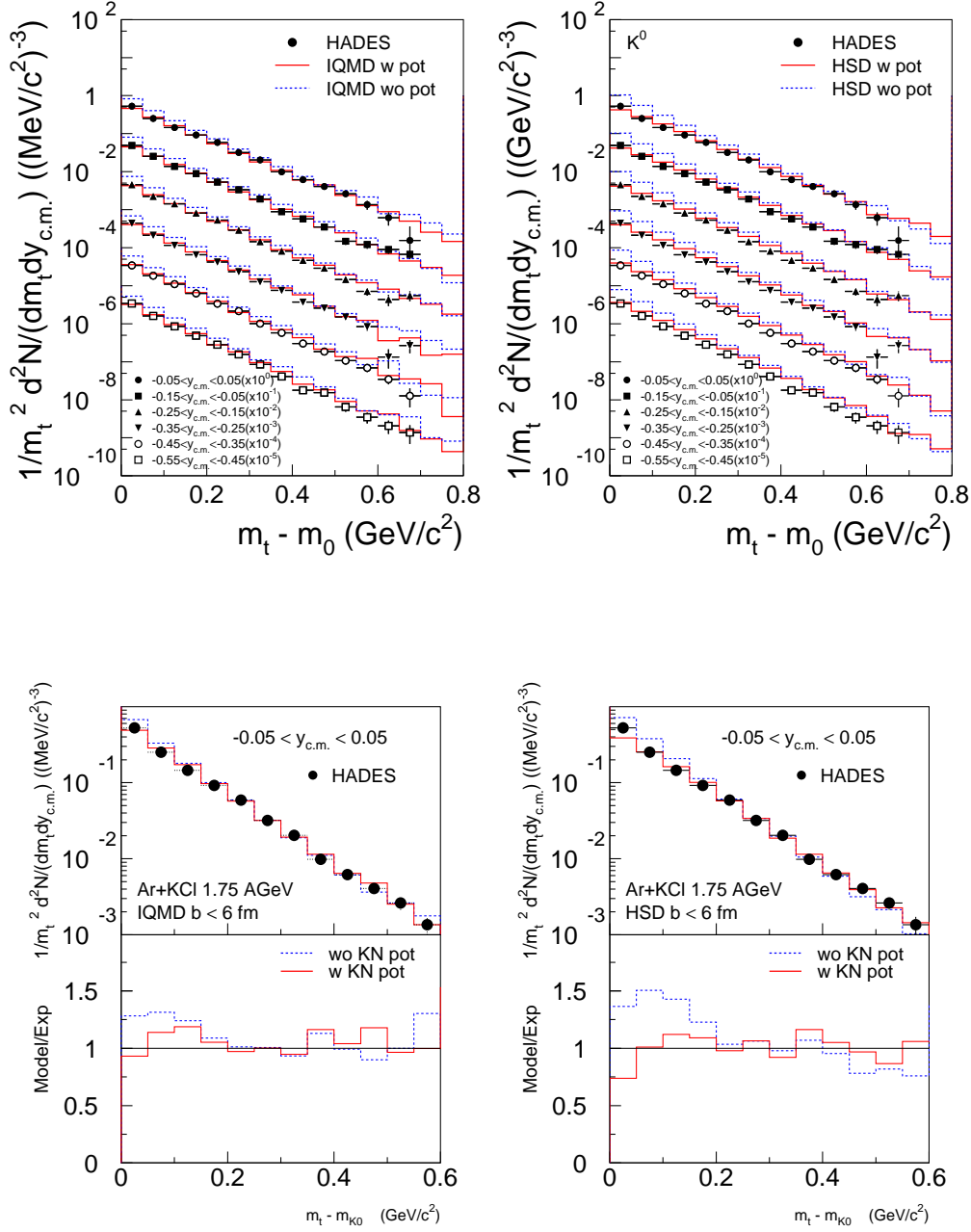


FIG. iv.23: Upper panel:  $m_t - m_0$  spectra of  $K^0$  measured by the HADES Collaboration for Ar+KCl at 1.75 A GeV [112] in comparison with IQMD and HSD calculations for different values of the rapidity. Lower panel: Top: Comparison of measured  $K^0$  spectrum at mid-rapidity with IQMD and HSD calculations with and without  $K^+$  nucleus potential. Bottom: Ratio of the calculations divided by the measured spectrum, enhancing the sensitivity. The model calculations are normalized to the experimental data beyond  $m_t - m_0 > 0.3$  GeV/c<sup>2</sup>.

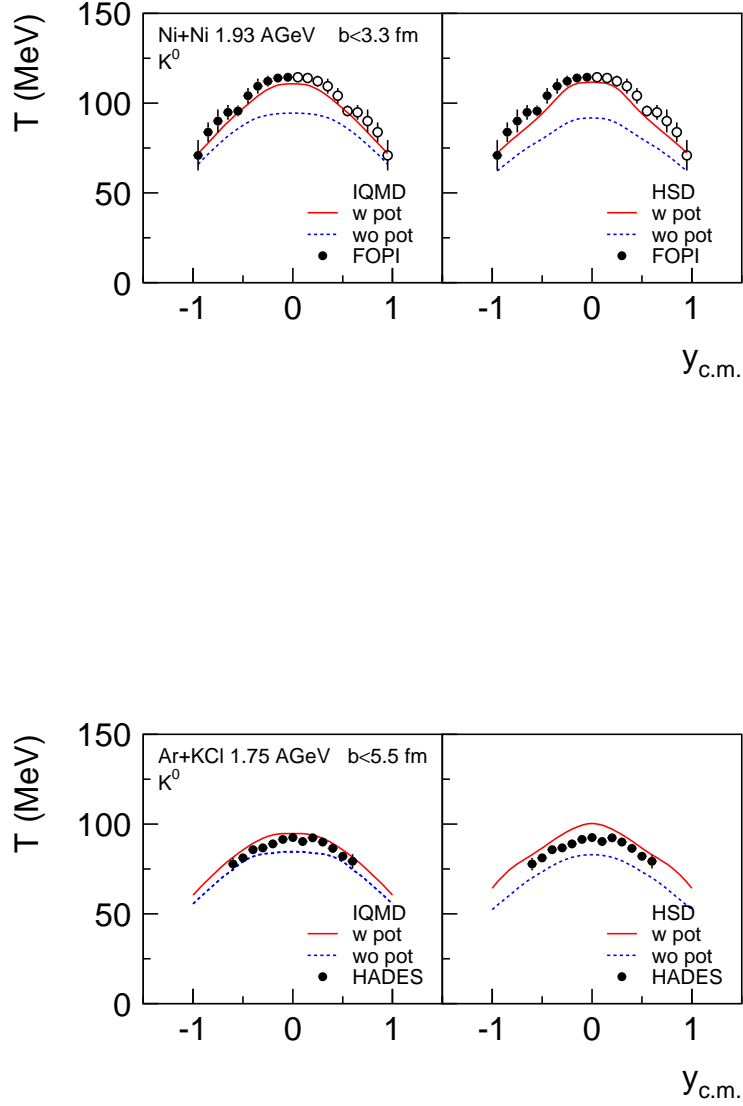


FIG. iv.24: Inverse slope parameter  $T$  of the spectra figs. iv.22 and iv.23. Upper part: For central ( $b < 3.3$  fm) Ni+Ni collisions at 1.93 A GeV as measured (and extrapolated to  $4\pi$ ) by the FOPI collaboration in comparison with those obtained in IQMD (left) and HSD (right) calculations. The error bars contain only the statistical error. Lower part: Same for central Ar+KCl collisions at 1.75 A GeV as measured by the HADES collaboration [112].



## H. Rapidity distribution

The rapidity of the center of mass of the two baryons, which create a  $K^+$ , is centered around  $y_{c.m.} = 0$ , as shown in Fig. iv.25, left. When  $K^+$  and  $\Lambda$  are created according to the three-body phase space the rapidity distribution of the  $\Lambda$  is broader than that of the sources and that of the  $K^+$  becomes quite wide. This will have consequences for the in-plane flow discussed in Section J.  $K^+$  mesons produced in  $\pi$ -induced reactions exhibit a similar width as if produced in BB collisions, Fig. iv.25, right. The center of mass rapidity of these collisions is not centered around mid-rapidity because the  $\pi$  are decay products of  $\Delta$  resonances.

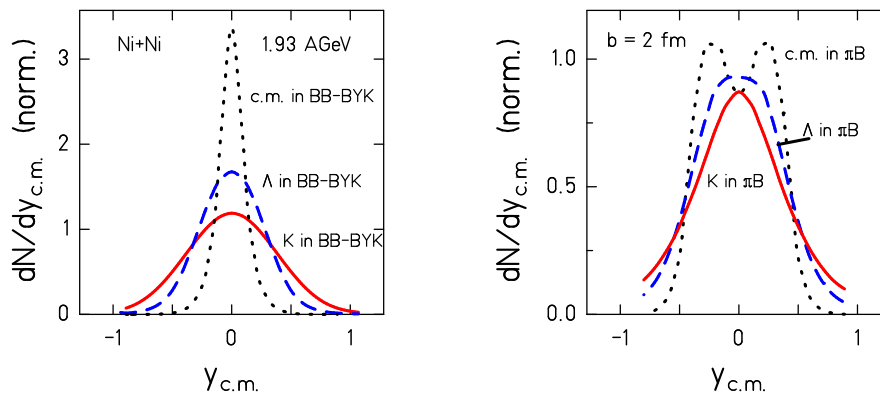


FIG. iv.25: Initial rapidity distribution  $dN/dy$  of  $K^+$  and  $\Lambda$  separated for the two principal  $K^+$  production processes for Ni+Ni at 1.93 A GeV .

Figure iv.26 displays the experimental  $dN/dy$  distributions of  $K^0$  (which should be - besides isospin effects - identical to that of the  $K^+$ ), in comparison with IQMD as well as with HSD calculations. The free  $dN/dy$  is larger in IQMD due to different isospin assumptions. The agreement between the experiments and IQMD calculations is reasonable if the  $K^+$  nucleus potential is employed. Without the  $K^+$  nucleus potential IQMD over-predicts the yield by a factor of two. As discussed, in HSD calculations the density dependence of the  $K^+$  nucleus potential is weaker. Therefore the difference between calculations with and without potential is smaller. HSD calculations also reproduce quite well the data when employing an  $K^+$  nucleus potential for the kaons.

Figure iv.27 compares the experimental results of the FOPI [115] and the KaoS Collaboration for the  $K^+$  rapidity distribution. The results from the FOPI Collaboration, measured at  $b < 3.3$  fm, have been scaled with a factor of 1.22 to match with the central bin of the KaoS Collaboration measured at  $b < 4.5$  fm. This factor has been obtained by comparing IQMD calculations with the two impact parameter ranges. As for the  $K^0$  a good agreement between the experiments and IQMD calculations is found if the  $K^+$  nucleus potential is employed.

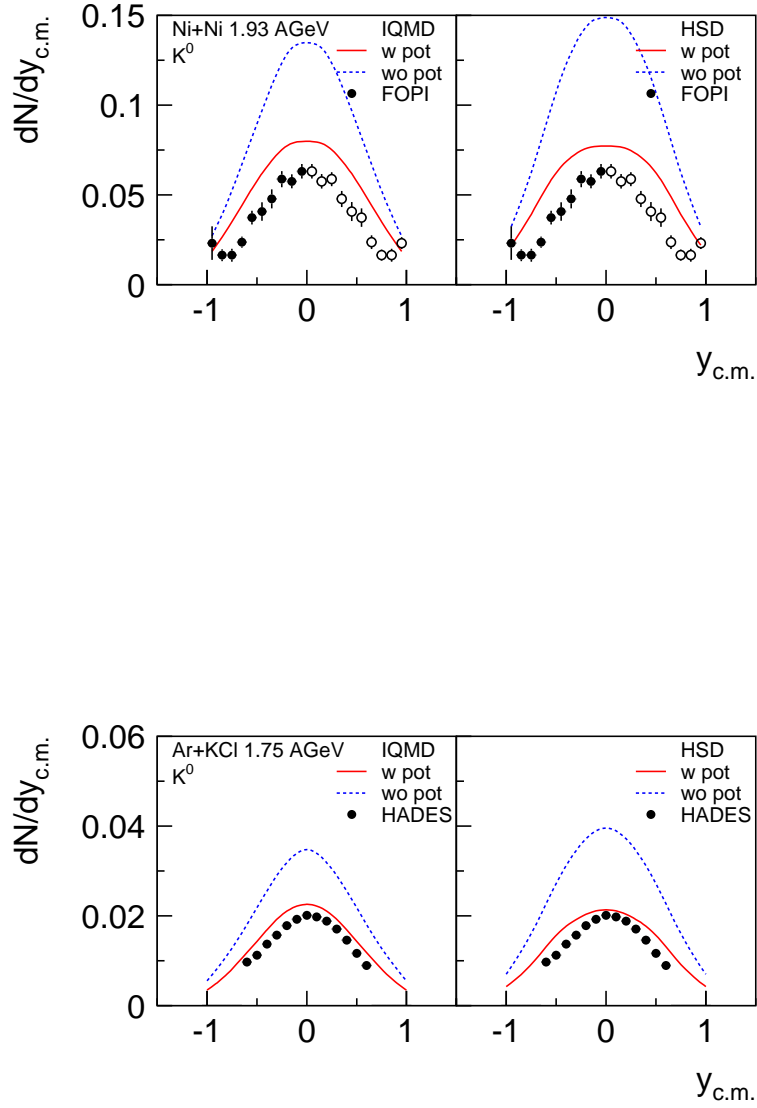


FIG. iv.26: Rapidity distributions  $dN/dy$  of  $K^0$ . Upper part: For central ( $b < 3.3$  fm) Ni+Ni collisions at 1.93 A GeV as measured (and extrapolated to  $4\pi$ ) by the FOPI collaboration in comparison with those obtained in IQMD (left) and HSD (right) calculations. The error bars contain only the statistical error. Lower part: Same for central Ar+KCl collisions at 1.75 A GeV as measured by the HADES collaboration [112].

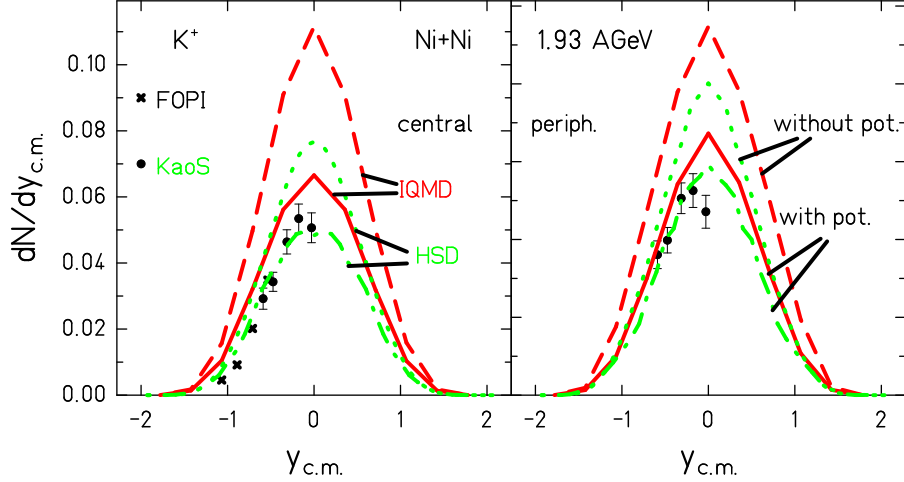


FIG. iv.27:  $4\pi$  extrapolated rapidity distribution of the  $K^+$  in Ni+Ni reactions at 1.93 A GeV as measured by the FOPI and KaoS Collaborations for central ( $b < 4.5$  fm) and peripheral ( $4.5 \text{ fm} < b < 7.5$  fm) collisions. Only the statistical errors are shown.

### I. Polar distribution

IQMD predicts that at creation the polar distribution of  $K^+$  mesons in central collisions is rather flat. This is a consequence of the dominance of the BB channel and of the creation of the  $K^+$  according to phase space.

Figure iv.28 addresses the question of how this distribution is modified later by KN collisions and by the  $K^+$  nucleus potential. In central collisions Au+Au collisions ( $b < 5.9$  fm) the polar distribution is almost flat at creation. The  $K^+$  nucleus potential causes a forward-backward enhancement demonstrated by selecting  $K^+$  that did not rescatter ( $N_C = 0$ , right panel of Fig. iv.28). It is important to note that rescattering ( $N_C > 2$ ) alone creates the same or an even stronger forward-backward enhancement as can be seen from the left hand side of Fig. iv.28. If we combine both effects by switching on the  $K^+$  nucleus potential for  $N_C > 2$  the enhancement does not change as shown in the center panel.

Figure iv.29 compares the model predictions with data for central and peripheral impact parameters for Au+Au at 1.5 A GeV and for Ni+Ni at 1.93 A GeV. In theory as well as in experiment [116] peripheral collisions yield a stronger asymmetry due to collision of the  $K^+$  with less stopped (spectator) target or projectile baryons. For central collisions theory and experiment agree. For the peripheral collisions the experimental distribution is slightly more forward/backward peaked than theory predicts.

In conclusion, the anisotropy of the polar distribution is a consequence of the interaction of the  $K^+$  with nucleons. At production the distribution is rather flat. If one switches off the  $K^+$  nucleus potential the anisotropy does not change considerably but for heavier

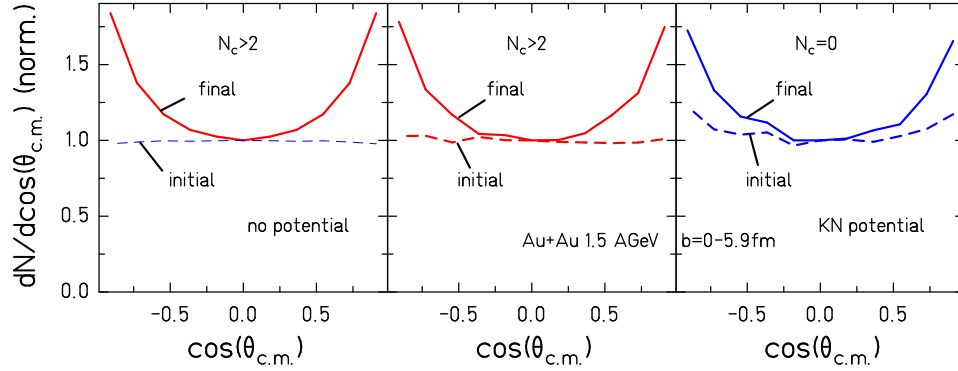


FIG. iv.28: Influence of rescattering and of the  $K^+$  nucleus potential on the polar distribution for central ( $b < 5.9$  fm) Au+Au reactions at 1.5 A GeV in IQMD calculations.

systems the  $K^+$  nucleus potential alone creates a similar asymmetry. Because the effects of rescattering and  $K^+$  nucleus potential do not add linearly polar distributions are of little help to disentangle both.

## J. Azimuthal distribution

The azimuthal distribution of the emitted particles is often parameterized in a Fourier series

$$\frac{dN(y)}{d\phi} = C [1 + 2v_1(y) \cos(\phi) + 2v_2(y) \cos(2\phi) + \dots], \quad (84)$$

with  $y$  being the rapidity and  $v_1$  and  $v_2$  the parameters to be determined.

### 1. In-plane flow $p_x(y)$ and $v_1$

The  $K^+$  are created according to the three-body phase space. We therefore expect that their in-plane  $v_1(y) = \langle p_x/p_t \rangle$  or  $\langle p_x(y) \rangle$  distribution is that of the sources, i.e. that of the producing baryons. In the calculations this is not the case. Directly after creation we see a much smaller  $\langle p_x(y) \rangle$  of the  $K^+$  as compared to the sources. This is shown in Fig. iv.30 and is a consequence of the large rapidity shift of the  $K^+$  with respect to the source rapidity (see Fig. iv.25). Therefore, at a given  $K^+$  rapidity bin, the positive and negative  $v_1(y)$  values from the different source rapidity bins cancel each other almost. The repulsive  $K^+$  nucleus potential accelerates the  $K^+$  to the side opposite to that of the projectile/target remnant and  $\langle p_x(y) \rangle$  changes its sign. Rescattering collisions have the opposite effect by aligning the  $K^+$  to the flow of the nucleons. The final  $\langle p_x(y) \rangle$  distribution is hence a combination of both effects and is sensitive to the number of rescattering collisions as well as to the  $K^+$  nucleus potential.

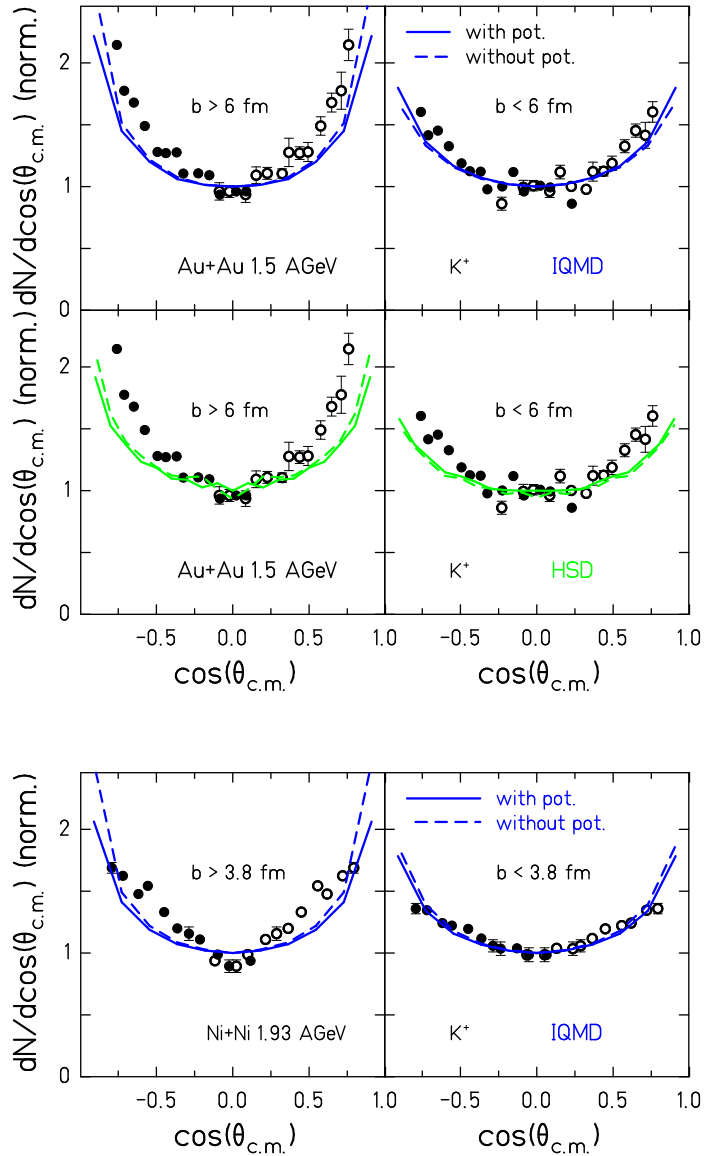


FIG. iv.29: The measured polar angle distribution for Au+Au reaction at 1.5 A GeV (upper part) and for Ni+Ni reactions at 1.93 A GeV (lower part) for two impact parameter ranges are compared to calculation using IQMD and HSD [70] (only for Au+Au). The data are from the KaoS [109]. The solid lines refer to calculations with and the dashed ones to those without  $K^+$  nucleus potential. The distributions are normalized to 1 for  $\cos \theta_{c.m.} = 0$ .

The experimental distributions of the directed transverse momentum  $\langle p_x \rangle$  as a function of the center of mass rapidity  $y_{c.m.}$  from the FOPI collaboration for central Ni+Ni collisions are shown in Fig. iv.31 for  $K^+$  mesons in comparison to protons [117]. The data points tend to an almost vanishing flow which is reproduced by the IQMD as well as by the HSD model when employing a  $K^+$  nucleus potential. The sensitivity of this particular observable

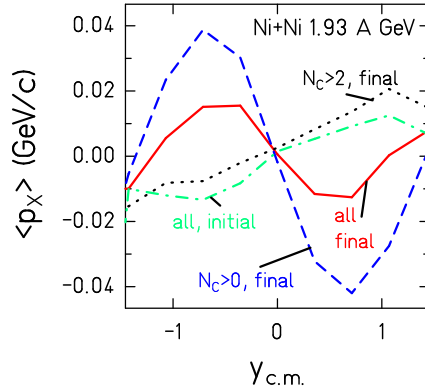


FIG. iv.30:  $\langle p_x \rangle$  of  $K^+$  as a function of the rapidity  $y_{c.m.}$ . We compare the distribution at creation with the final distribution, separated according to the number of collisions. All calculations are performed with  $K^+$  nucleus potential included.

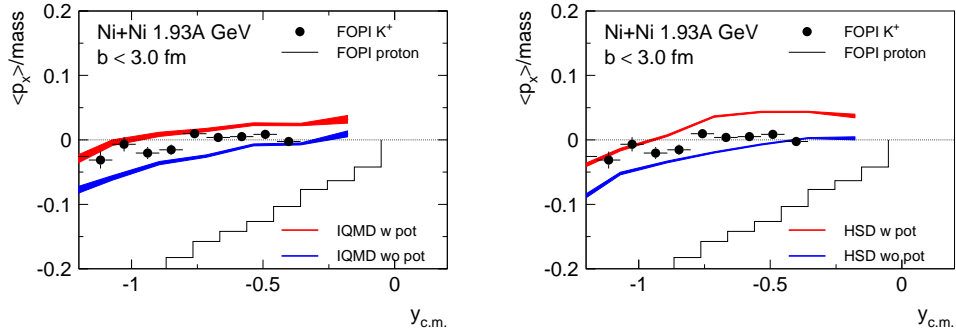


FIG. iv.31: Experimental data for  $\langle p_x \rangle$  as a function of rapidity in central Ni+Ni collisions in comparison to IQMD (left) and HSD (right) calculations. Data points are for  $K^+$ , full black histogram for protons. Both distributions were generated with a transverse momentum cut of  $0.5 p_t/m$ . The data are from the FOPI collaboration [117].

to the  $K^+$  nucleus potential is, however, weak. The situation is different if studying the  $p_t$  differential distribution.

The FOPI Collaboration has measured  $v_1$  as a function of the transverse momentum  $p_t$  of the  $K^+$  mesons at target rapidities for two systems [118]. In addition, the impact-parameter dependence was studied in the intermediate heavy system Ru+Ru. The overall magnitude of the experimental data is quite well described by the IQMD model (Fig. iv.32). The strong variation of the  $v_1$  as a function of transverse momentum  $p_t$  is not reproduced by the calculations. The strength  $K^+$  nucleus potential changes the absolute value but not

the form of the distribution, neither do different choices of the rescattering cross section. Within the IQMD model the difference between theory and experiment cannot be related to either potential or rescattering and is not understood yet. Employing the HSD model and using a similar approach for treating the in-medium properties of  $K^+$  mesons, the strong  $p_t$  dependence of  $v_1$  is described using a repulsive  $K^+$  nucleus potential of  $\approx 20$  MeV (half of the standard value of 40 MeV) see Fig. iv.33. The data are from Ref. [118], note that in that paper BUU calculation have been shown.

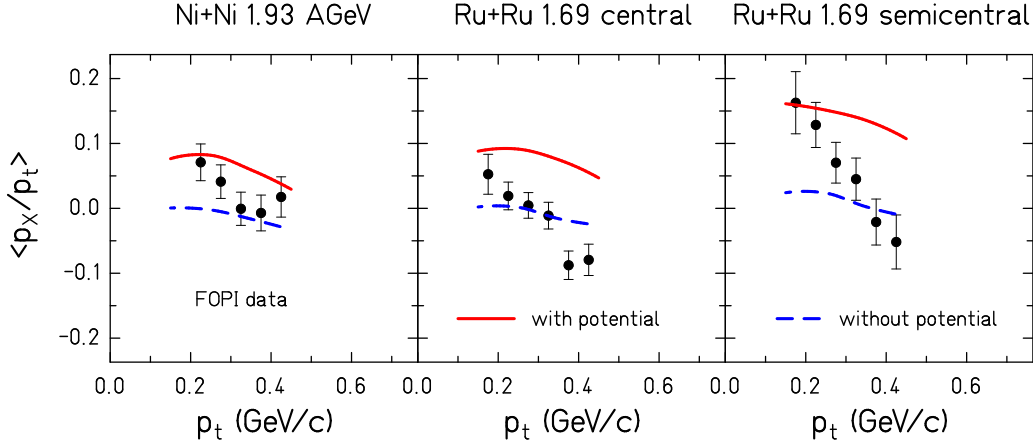


FIG. iv.32:  $v_1 = \langle \frac{p_x}{p_t} \rangle$  of the  $K^+$  as a function of the transverse momentum,  $p_t$ , for Ni+Ni (left) and Ru+Ru (middle and right). The experimental data of the FOPI Collaboration [118] are compared with IQMD calculations.

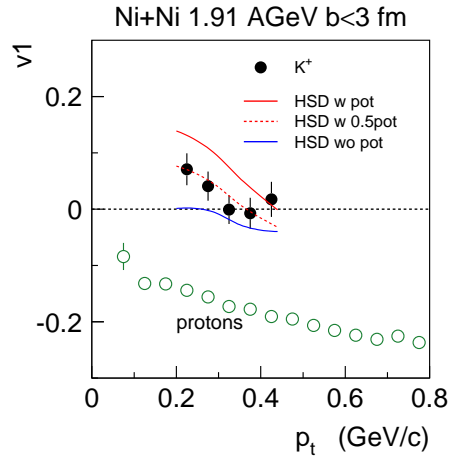


FIG. iv.33:  $v_1$  of the  $K^+$  as a function of the transverse momentum,  $p_t$ , for Ni+Ni. The experimental data of the FOPI Collaboration [118] are compared with HSD calculations.

## 2. Out-of-plane flow $v_2$

The out-of-plane distribution is best studied at mid-rapidity, when in symmetric systems the contribution of the in-plane flow  $v_1$  is zero by definition and therefore the problem to separate  $v_1$  from  $v_2$  is not given.

Geometry is an important factor for the  $K^+$  out-of-plane distribution, as demonstrated in Fig. iv.34. The  $K^+$  are produced in the participant zone. If they have to pass spectator matter (lying by definition in-plane) they suffer in the average from more collisions than those emitted under  $90^\circ$  with respect to the reaction plane. Therefore, by selecting  $K^+$  with  $N_C = 0$  preference is given to those emitted perpendicular to the reaction plane (dotted line in Fig. iv.34, left). The  $K^+$  nucleus potential (dashed line) enhances the out-of-plane flow. This class represents only 17.5% of all  $K^+$ . For  $N_C > 2$  the initial distribution is slightly in-plane enhanced. By rescattering the positive  $v_2$  value of the baryons is transferred to the  $K^+$ . By this mechanism rescattering contributes to an increase of the out-of-plane enhancement.

In Fig. iv.35, left, we display the influence of rescattering and of the  $K^+$  nucleus potential on the azimuthal distribution  $dN/d\phi$  at mid-rapidity for Au+Au collisions at 1.5 A GeV (left) and for Ni+Ni collisions at 1.93 A GeV (right) (data from [119]). Without  $K^+$  nucleus potential and rescattering (sources, purple dash-dotted line) the distribution is quite flat. Rescattering without the  $K^+$  nucleus potential (no pot., resc., green dotted line) causes an enhancement of the out-of-plane emission ( $v_2 = -0.092$ ). If we switch on the  $K^+$  nucleus potential but ignore the rescattering (pot., no resc., blue dashed line) the enhancement is of a similar strength ( $v_2 = -0.117$ ). Combining the two contributions (pot., resc., red full line) results in an enhancement of  $v_2$  by about only 30% ( $v_2 = -0.1408$ ). Both, rescattering and  $K^+$  nucleus potential cause an asymmetry, yet combining both sources results only in a hardly visible stronger asymmetry, similar to what has been observed for the polar distribution.

For central Ni+Ni collisions at 1.93 A GeV the FOPI Collaboration has measured  $v_2$  as a function of the rapidity and compared with IQMD calculations (Fig. iv.36). This distribution is rather flat and the sensitivity on the  $K^+$  nucleus potential which we have seen for the large Au system (Fig. iv.35), has disappeared. IQMD as well as HSD calculations reproduce the experimental findings.

The excitation function of  $v_2$  around mid-rapidity for different options and for the Au+Au system is shown in Fig. iv.37. Without rescattering and without  $K^+$  nucleus potential  $v_2$  is around zero. At all energies the azimuthal anisotropy of the  $K^+$  is not created in their production process but by rescattering and by the  $K^+$  nucleus potential. A significant out-of-plane enhancement is already caused by rescattering. The  $K^+$  nucleus potential alone creates as well a significant out-of-plane enhancement. The combined effect of rescattering and of the  $K^+$  nucleus potential interaction enhances, however, only slightly that created by the  $K^+$  nucleus potential only. The  $b = 7$  fm calculations are compared with experimental



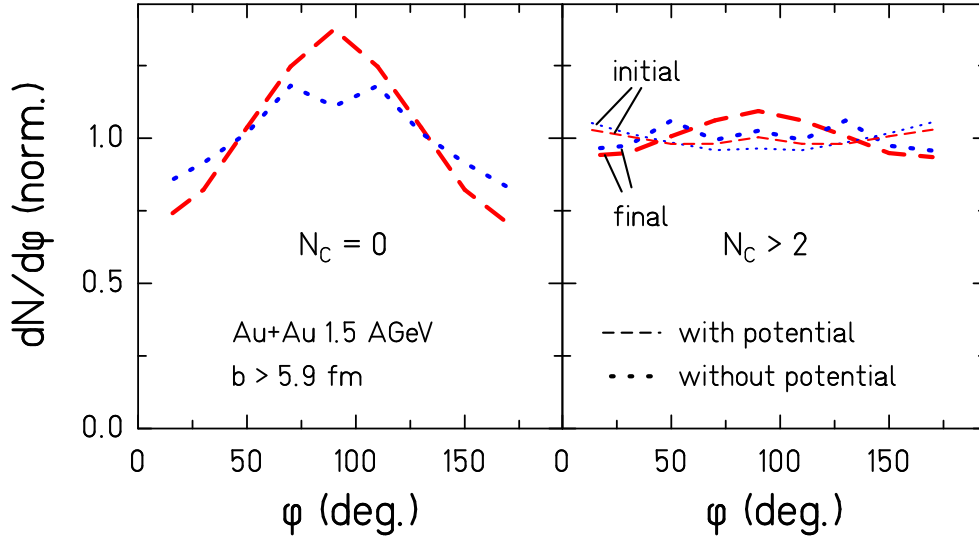


FIG. iv.34: Initial and final out-of-plane distribution of the  $K^+$  selected according to the number of rescattering collisions,  $N_C$  after production. For  $N_C = 0$  and no potential the initial and final distributions are identical and similar to the initial with potential.

data [119–121]. The two results at 1.5 A GeV agree within error bars.

The origin of the  $v_2$ , created by the  $K^+$  nucleus potential, is visible in Fig. iv.38 where we study  $v_2$  as a function of the last contact time (equal to the production time if the  $K^+$  do not rescatter, otherwise equal to the time of the last collision). The early produced  $K^+$  which do not rescatter ( $N_c = 0$ ) have initially a moderate negative  $v_2$  (dashed dotted line) but finally a very strong  $v_2$  (dashed line). The difference originates from the potential interaction. Thus early created  $K^+$  show a squeeze out perpendicular to the reaction plane created by the presence of the (in-plane) spectator matter. Rescattering weakens this squeeze by randomizing the  $K^+$  direction (full line). Late emitted  $K^+$  show an opposite trend because they cannot interact with the fast moving spectator matter any more. They follow the  $v_2$  of the sources. In contradistinction to  $v_1$  (Fig. iv.32) the value of  $v_2$  depends (in theory as well as in experiment) only slightly on the momentum of the  $K^+$  as seen in Fig. iv.38, right [121]. As already seen for the integrated value (Fig. iv.37) IQMD calculations with  $K^+$  nucleus potential give a larger negative  $v_2$  value for this reaction. The present error bars are too large to allow for conclusions on the  $K^+$  nucleus potential from the excitation function of  $v_2$  at mid-rapidity and hence also from the momentum dependence.

Thus we can conclude that the  $K^+$  mesons at creation have a flat in-plane and out-of-plane distribution, i.e.  $v_1 = v_2 = 0$ . The experimentally observed finite values of these coefficients are due to rescattering and due to the repulsive  $K^+$  nucleus potential which add in a non linear way. This shows that  $K^+$  interact with the medium after production but this implies

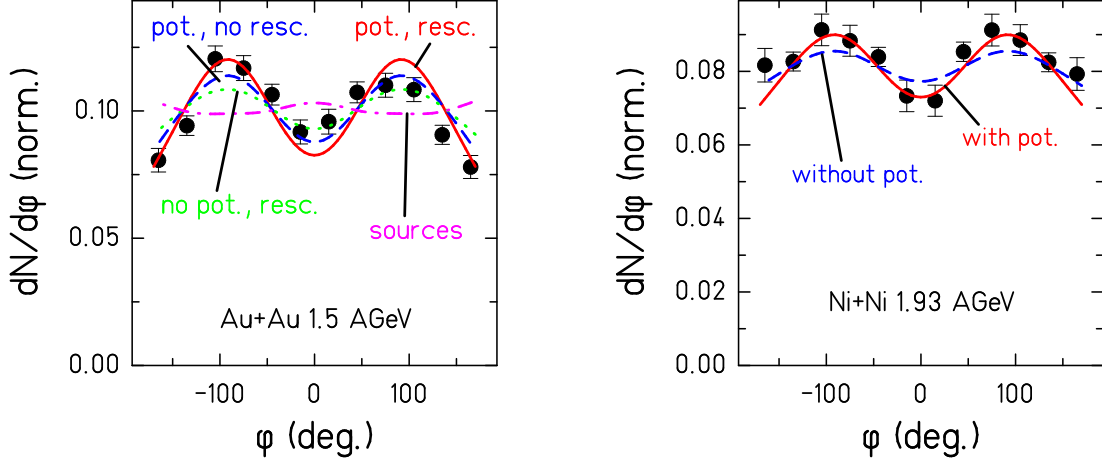


FIG. iv.35: The influence of the  $K^+$  nucleus potential and the KN rescattering on the azimuthal distribution of the  $K^+$  in the experimental acceptance region for Au+Au collisions at 1.5 A GeV with impact parameter  $b > 7.8$  fm (left) and for Ni+Ni at 1.93 A GeV with impact parameter  $b > 3.8$  fm (right). Data from [119].

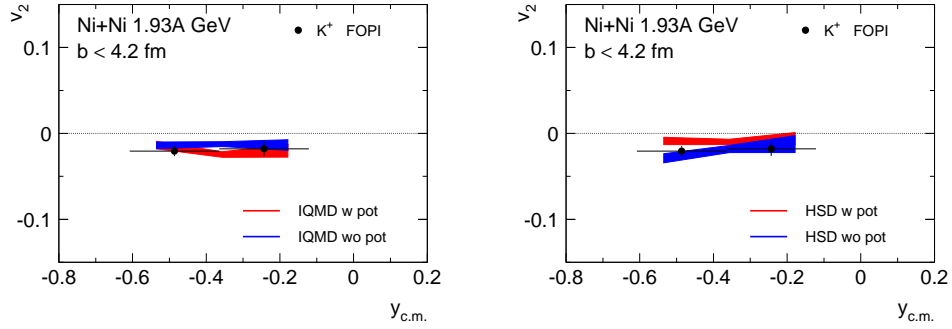


FIG. iv.36: Comparison of  $v_2$  of  $K^+$  as a function of the rapidity between preliminary FOPI data and IQMD (left) as well as HSD (right) calculations.

as well that these observables reflect the complex reaction dynamics. Therefore, to use these data to gain additional information on either of them is difficult and not possible without including other observables. Besides the dependence of  $v_1$  on  $p_t$  the measured coefficients are quantitatively reproduced by theory.

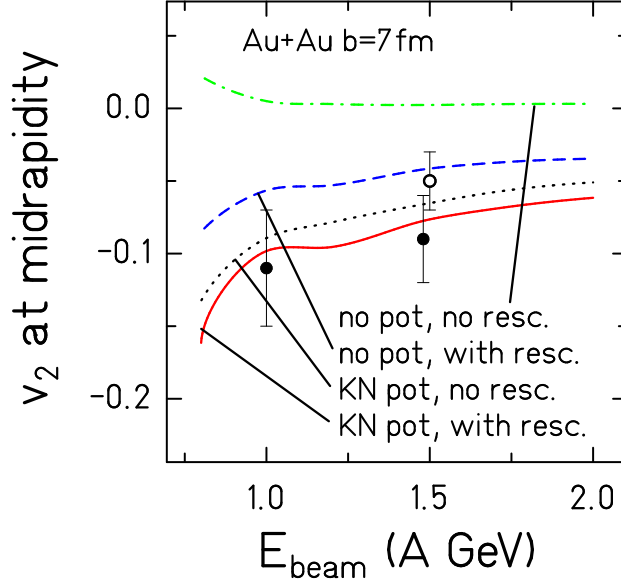


FIG. iv.37: Excitation function of the  $v_2$  coefficient at mid-rapidity for Au+Au reactions and with different options for the simulation. We compare here IQMD calculations at  $b = 7$  fm with peripheral KaoS data (points [119, 120], open circles [121])

### K. $\Lambda$ production

Being unstable, strange baryons are more difficult to detect. Therefore there are much less data on  $\Lambda$  and  $\Sigma$  production than on strange meson production. Their multiplicity corresponds to that of the  $K^+$  and  $K^0$ , the associated particles, and is therefore of little importance. The understanding of the dynamics of the  $\Lambda$  in matter is important for the understanding of the  $K^-$  mesons which at these energies are almost exclusively created by a strangeness-exchange reaction between a strange baryon and a pion. The  $\Lambda N$  cross section is larger than the  $K^+ N$  cross section and therefore the  $\Lambda$  adopt rapidly the properties of their environment. It is expected that their final distribution differs substantially from that at production.

Figure iv.39 shows the experimental  $m_t$  spectra for different rapidity bins for Ni+Ni at 1.93 A GeV [110] and Fig. iv.40 the same distribution for Ar+KCl at 1.75 A GeV [113]. Both sets of spectra have an exponential form. The experimental data are compared to IQMD (left) and HSD (right) calculations, presented by the histograms. The FOPI data are filtered using the FOPI filter, the HADES data have the same normalization as the  $K^0$  shown in Fig. iv.23. For the 1.93 A GeV ( $b \leq 3.3$  fm) data of the FOPI Collaboration we see at low- $m_t$  values a quantitative agreement between calculations and the data for almost all rapidity bins. At high values of  $m_t$  differences between simulations and data appear,

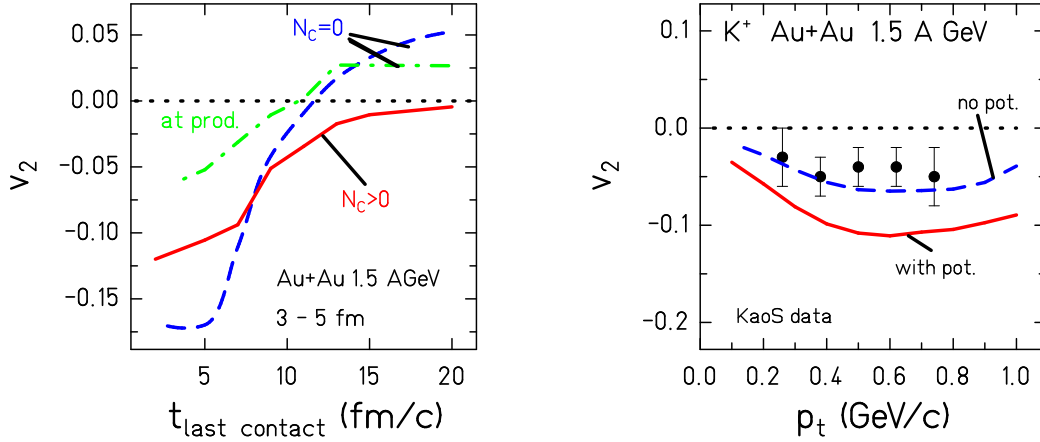


FIG. iv.38: Left:  $v_2$  as a function of the time when the  $K^+$  had its last contact with the system for Au+Au at 1.5 A GeV . Dashed dotted line:  $v_2$  of  $K^+$  which do not rescatter ( $N_c = 0$ ) at production, dashed line  $v_2$  of the same  $K^+$  at the end of the reaction, full line:  $v_2$  of  $K^+$  with  $N_c > 0$  at the time point of their last collision. Right: Comparison of the theoretical and experimental [121]  $v_2$  values as a function of the  $K^+$  transverse momentum,  $p_t$ , for Au+Au reactions at 1.5 A GeV .

especially close to mid-rapidity. These differences are more pronounced in HSD calculations than in IQMD calculations. For the Ar+KCl at 1.75 A GeV the agreement between theory and experiment is good even for large  $m_t$  values.

The influence of the  $K^+$  nucleus potential is visible. It increases the threshold and reduces therefore the number of  $\Lambda$  which are created together with the  $K^{+0}$  in  $BB \rightarrow YNK^{+0}$  reactions.

At production the slope is determined (as that of the  $K^+$  which is well described) by the three body phase space. Due to the large  $N\Lambda$  elastic scattering cross section [123, 124] the final slope differs quite substantially from that at production and is therefore sensitive to the  $\Lambda N$  dynamics during the reaction. Assuming an exponential form, the fitted inverse slope parameters  $T$  as a function of the rapidity for 1.93 A GeV Ni+Ni and 1.75 A GeV Ar+KCl are displayed in Fig. iv.41 and compared with theory. The  $K^+$  nucleus potential does not change the slope of the distribution. We see quite a discrepancy between both models and the data. The FOPI collaboration measured inverse slope parameters of  $\Lambda$  are typically higher than those predicted by the models as can be inferred already from fig. iv.39. Hyperon rescattering is treated in a similar way in both models.

For the Ar+KCl data at 1.75 A GeV the experimental slopes are quite well reproduced by theory, although at mid-rapidity the fit to the experimental spectra yields slightly higher inverse slope parameter than predicted by the simulations.

Extrapolating the  $m_t$  spectra to  $m_t - m_0 = 0$  one obtains the  $\Lambda$  rapidity distribution  $dN/dy$  which is displayed for the same data in Fig. iv.42. We compare the experimental

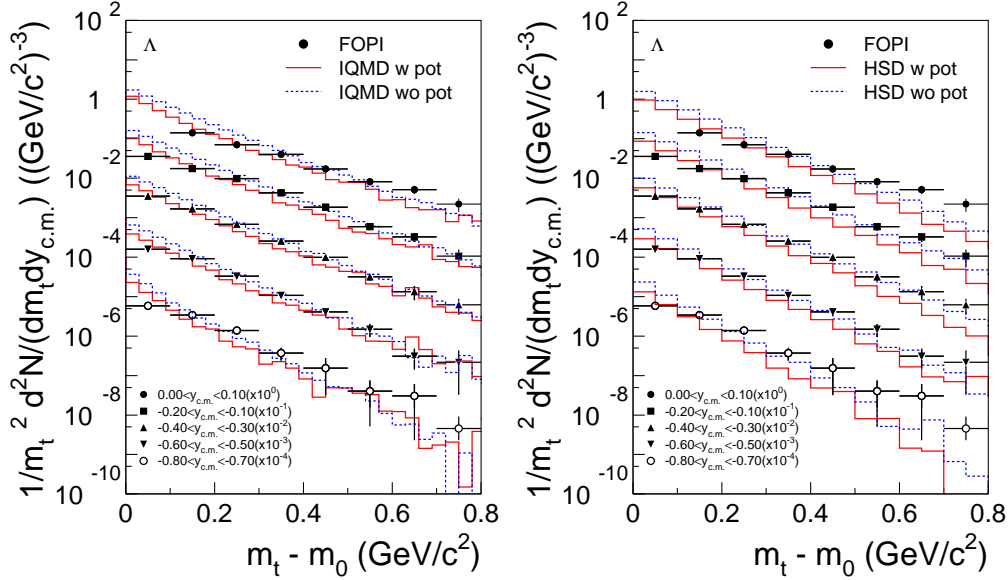


FIG. iv.39: Central Ni+Ni collisions at 1.93 A GeV :  $m_t$  spectra of  $\Lambda$  for different rapidity bins. The experimental results are compared with IQMD calculations (left) and with HSD calculations (right).

result, Ni+Ni at 1.93 A GeV (measured by FOPI) with IQMD and HSD calculations, as well as and Ar+KCl at 1.75 A GeV (measured by HADES), including and excluding the  $K^+$  nucleus potential. Due to a stronger  $K^+$  nucleus potential the IQMD model comes only close to the experimental data when this potential is included, whereas for the HSD calculations are close to experiment with and without this potential.

It is not understood why both theories under-predict the  $\Lambda$  slope of the Ni+Ni data set of the FOPI Collaboration by at least 20% but come close to that observed in the Ar+KCl experiment from the HADES collaboration. The relatively little known elastic rescattering cross section can not be the origin of this difference because it is sufficiently large to bring the  $\Lambda$  to equilibrium with their local environment, as has been tested with IQMD calculations.

### L. In-plane and azimuthal distribution of the $\Lambda$

The  $v_1$  and  $v_2$  values of the  $\Lambda$  for  $p_t/m_0 > 0.5$  have been measured and have been compared with theory by the FOPI Collaboration. In Fig. iv.43 we display  $v_1$  as a function of the  $\Lambda$  rapidity as compared to IQMD calculations. In this acceptance region the model predicts that  $v_1(y)$  of proton and of  $\Lambda$  are identical for  $y_{c.m.} > -0.4$  and deviate slightly for  $y$ -values, close to target rapidity. This corresponds quantitatively to the experimental

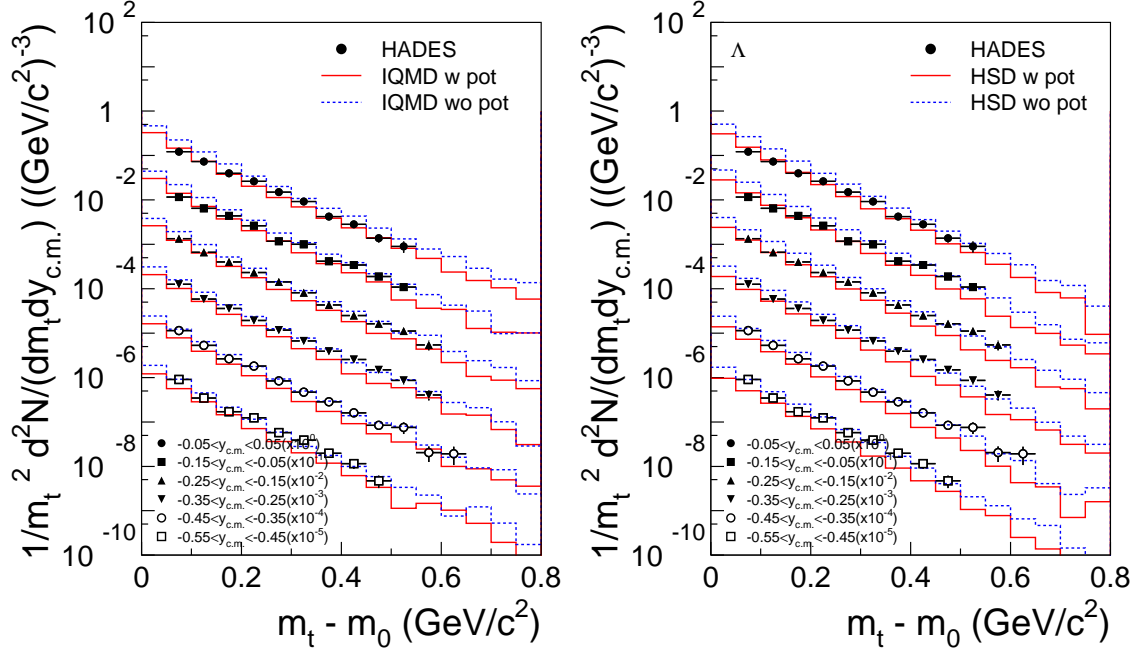


FIG. iv.40:  $m_t$  spectra of  $\Lambda$  at different rapidity bins for the reaction Ar+KCl at 1.75 A GeV . The experimental results of the HADES Collaboration [113] are compared with predictions of IQMD and HSD calculations with (red full line) and without (blue dashed line)  $K^+$  nucleus potential.

findings. At production  $\Lambda$  do not show flow, they acquire it by rescattering with protons. Figure iv.43 show that  $\Lambda$  with a high  $p_t$  have sufficient rescattering collisions to have the same flow as the scattering partners. A large rescattering cross section would not increase the  $v_1$  value further.

It is interesting to study the in-plane flow of the  $\Lambda$  without the above mentioned cut in  $p_t$  . This is presented in Fig. iv.44. There we display the rapidity distribution and the in-plane flow of p and  $\Lambda$  as a function of rapidity. We see that at mid-rapidity the in-plane flow of both baryons agree whereas at beam and target rapidity a substantial difference can be observed. The  $\Lambda$  are located at mid-rapidity whereas the protons show a rather flat distribution. If one weights the in-plane flow by the distribution of the particles it is evident that the rapidity integrated in-plane flow of protons ( $p_x^{dir} = (\sum_{\text{all particles}} \text{sign}(y_i) p_x(y_i))/N_{\text{all particles}}$ ) is rather large as compared to that of the  $\Lambda$ .

Fig. iv.45 shows this from another point of view. Here we present [125] the in-plane flow averaged over all transverse momenta and rapidities as a function of time. We see quite a different behaviour than in Fig. iv.43: The average flow of the protons is twice as large as that of the  $\Lambda$ , presented as a triangle. This result has been experimentally observed at AGS

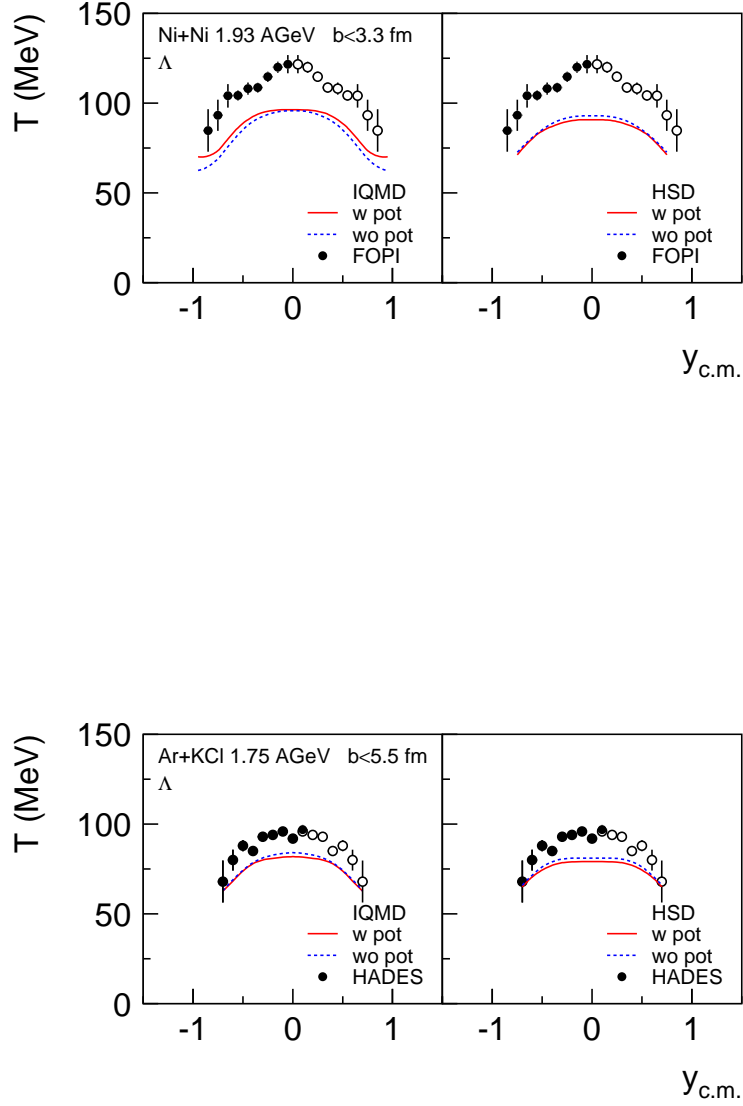


FIG. iv.41: Inverse slope parameter  $T$  of the  $\Lambda$  spectra as a function of rapidity. We compare the FOPI data for central Ni+Ni collisions [110] at 1.93 A GeV and preliminary results for Ar+KCl at 1.75 A GeV [113] from the HADES collaboration with results of the IQMD and HSD transport models. The theoretical predictions were selected according the impact-parameter filter given by the experiment:  $b < 3.3$  fm and  $b < 6.0$  fm for Ni+Ni and Ar+KCl, respectively.

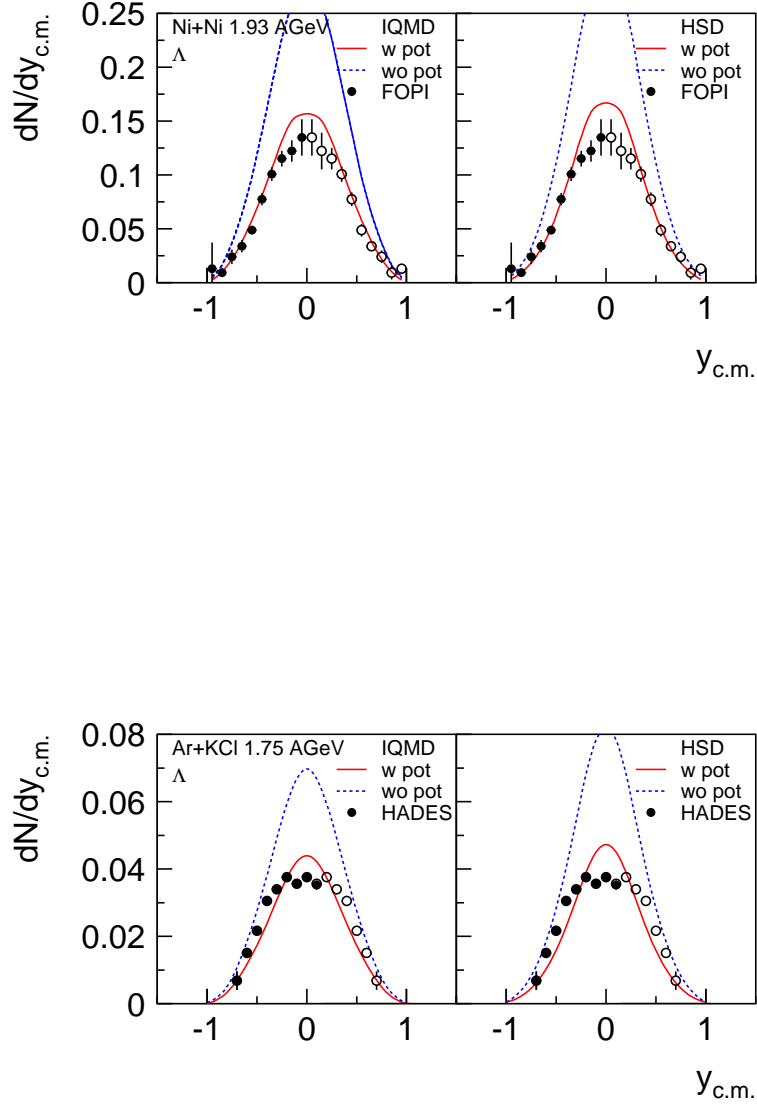


FIG. iv.42:  $\Lambda$  rapidity distribution,  $dN_{\Lambda}/dy_{c.m.}$ , for data Ni+Ni at 1.93 A GeV and Ar+KCl at 1.75 A GeV compared with theoretical results of IQMD and HSD.

energies [126].

In order to understand this result one has to realize that the  $\Lambda$  are produced in the high density zone. The average density for the production of a  $K^+ \Lambda$  pair is around  $2\rho_0$  - in the case of central Ni+Ni at 1.93 A GeV as well as for central Au+Au at 1.5 A GeV (see for example Fig. vi.6). If one calculates  $p_x^{dir}$  only for those nucleons which in the course of the



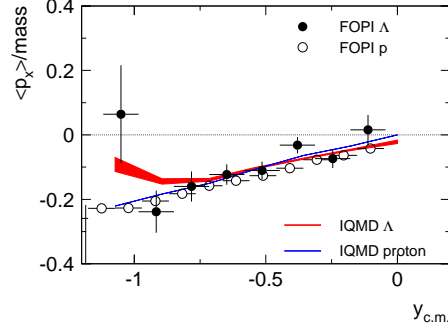


FIG. iv.43: In-plane flow of  $\Lambda$ 's and protons for  $p_t/m_0 > 0.5$  as measured by the FOPI Collaboration [122] in comparison with IQMD calculations.

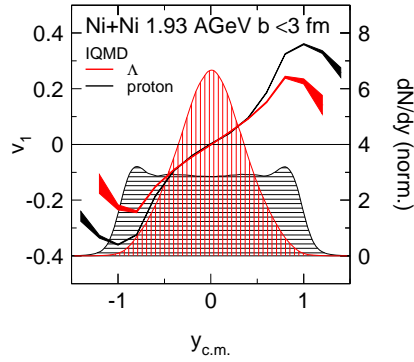


FIG. iv.44: Rapidity distribution and in-plane flow,  $v_1$ , of  $\Lambda$  and p as a function of the rapidity.

reaction have passed a density larger than twice the ground state density,  $p_x^{dir}$  is reduced by a factor of almost two (green dashed dotted line) and comes close to the value for the  $\Lambda$ . The  $p_x^{dir}$  of those nucleons which have participated in the creation of  $K^+$  is finally very close to that of the  $\Lambda$ .

This allows for several conclusions:

- The observed large in-plane flow of protons (which is in first order  $\propto (-dV/dx)t$  where  $V$  is the potential (which is a function of the density) and  $t$  is the passing time of the nuclei) is predominantly caused by nucleons close to the surface of the interaction zone where the density gradient is large but the maximal density, reached during the collision, is well below  $2\rho_0$ .
- In the interior of the interaction zone the density gradients are moderate and lead to a moderate  $p_x^{dir}$
- The  $\Lambda$  carry about the same in-plane flow as the surrounding nucleons. Since most of the

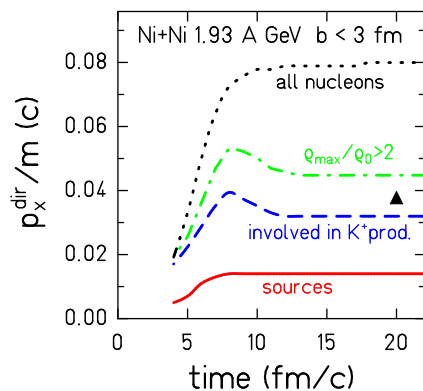


FIG. iv.45: The final average hyperon in-plane flow as compared to that of the sources and of different classes of nucleons. The full triangle corresponds to the value of the  $\Lambda$ .

hyperons are produced as heaviest particle in a three-body phase space decay, the energy of a hyperon directly after its production is rather low. High  $p_t$   $\Lambda$  obtain dominantly their energy from rescattering with high-energetic nucleons and thus adapt to their kinematical properties.

d) Nucleons with a large  $p_t$  come, as the  $\Lambda$ , from the high density zone.

This explains why a cut in  $p_t$  yields similar in-plane flow of the  $\Lambda$  and protons, Fig. iv.43 whereas the in-plane flow is different by a factor of two when we average over all  $p_t$ , as shown in Fig. iv.45.

## V. PRODUCTION OF $K^-$ MESONS

### A. Subthreshold $K^-$ production

Already in the first experiments, it has been observed that close to threshold the  $K^+$  and  $K^-$  yields behave completely different as compared to the extrapolation from the elementary production cross sections  $NN \rightarrow NK^+\Lambda$  and  $NN \rightarrow NNK^+K^-$ . This observation can be seen in Fig. v.1, left, which shows the multiplicity of  $K^+$  and  $K^-$  mesons per participating nucleon  $A_{\text{part}}$  in nucleon-nucleon and in heavy-ion collisions as a function of the energy above threshold in the NN system,  $\sqrt{s} - \sqrt{s_{\text{thres}}}$ . Whereas in heavy-ion reactions the  $K^-$  and the  $K^+$  yields are very similar around their respective thresholds, the elementary cross sections show order of magnitude differences.

The origin of this observation is a new  $K^-$  production mechanism in heavy-ion reactions which is absent in nucleon-nucleon collisions: The  $K^-$  meson contains a  $s$  quark which can

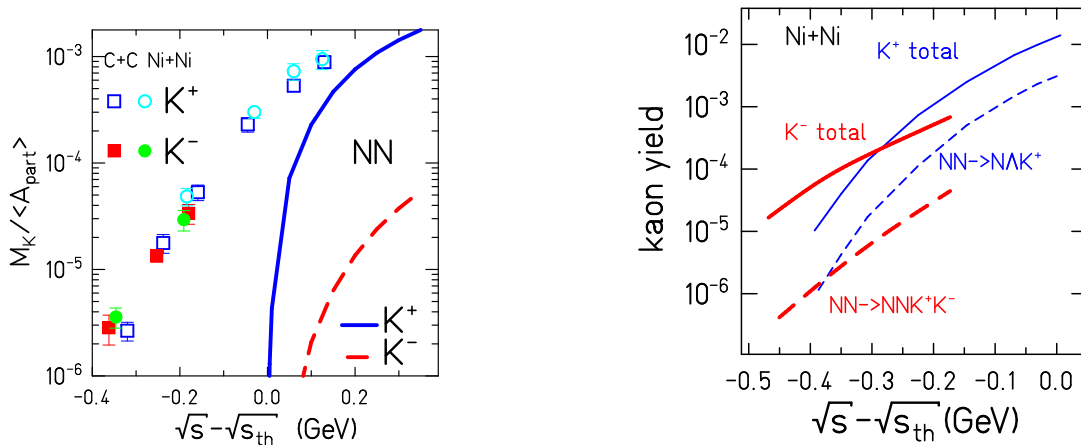


FIG. v.1: Right: Comparison of the production of  $K^+$  and  $K^-$  in heavy-ion reactions in comparison with the production in elementary collisions. Left: Excitation function of the  $K^+$  yield in  $NN \rightarrow NK^+\Lambda$  collisions and of the  $K^-$  yield in  $NN \rightarrow NNK^+K^-$  collisions as compared to the total production of  $K^+$  and  $K^-$  mesons in heavy-ion collisions.

be exchanged with a baryon. This is in contrast to the  $K^+$  whose  $\bar{s}$  does not find a baryonic exchange partner. The only possible inelastic reaction is the charge exchange  $K^+ \leftrightarrow K^0$ . Close to threshold the production of  $s$  and  $\bar{s}$  quarks is dominated by the reaction with the lowest threshold. This is the baryonic reaction  $BB(\Delta) \rightarrow NK^+ Y$  (with  $Y$  being  $\Lambda$  or  $\Sigma$ ) as discussed in Section IV. In heavy-ion collisions the strange baryon can transfer its strange quark to a  $K^-$  and at threshold energies, indeed, most of the observed  $K^-$  mesons are not directly produced, but produced by secondary interactions  $BY \rightarrow NNK^-$  or  $\Lambda(\Sigma)\pi \rightarrow K^- N$ . This new production mechanism, only occurring in heavy-ion collisions, links the  $K^-$  to the  $K^+$  production. The contribution of  $NN \rightarrow NNK^+K^-$  to the  $K^-$  yield in central Au+Au reactions at 1.5 A GeV is even more marginal than that of  $NN \rightarrow NK^+\Lambda$  for the

$K^+$  yield, as shown in Fig. v.1, right.

Hence, there are two dominant mechanisms for the production of strange mesons in heavy-ion collisions: The strangeness production via e.g.  $BB \rightarrow N K^+ + \Lambda(\Sigma)$ , which has been discussed in Section IV and the strangeness exchange reactions  $\Lambda(\Sigma)\pi \rightarrow K^- N$  and  $B\Lambda(\Sigma) \rightarrow K^- NN$  discussed here.

### B. Dynamics of $K^-$ production and emission

For the exchange of strangeness two channels are important:  $\pi Y \rightarrow K^- N$  and  $BY \rightarrow NNK^-$ . The latter process becomes important if B is a  $\Delta$  because there the less kinetic energy is needed to overcome the threshold, yet this cross section is unknown. Following Randrup and Ko [94], we apply an isospin factor to the corresponding NN channel ( $\sigma(N\Delta) = 0.75\sigma(NN) = 0.6 \text{ mb} (E - E_{\text{thres}})$ ), with energies measured in GeV in the hyperon rest frame). The  $\Lambda(\Sigma)\pi \rightarrow K^- N$  cross section can be obtained by detailed balance from the measured  $K^- N \rightarrow \Lambda(\Sigma)\pi$  cross section. Being influenced by the  $\Lambda(1405)$  resonance, the exothermic reaction  $K^- N \rightarrow \Lambda(\Sigma)\pi$  is very strong at low relative momenta whereas the inverse cross section goes to zero there. From the magnitude of the cross sections alone the following reaction scenario emerges: Some of the strange baryons from the primary reaction  $BB \rightarrow N\Lambda K^+$  create in a second reaction a  $K^-$  meson which has a high chance to be reabsorbed quickly by the inverse process  $NK^- \rightarrow \Lambda\pi$ . This situation causes a completely different dynamics as compared to  $K^+$  mesons.

Using these cross sections we calculate the time evolution of the production and absorption of  $K^-$  mesons in the different channels as displayed in Fig. v.2, left. At early times, a dominance of the Y ( $\Lambda, \Sigma$ ) B channel is observed, but most of these early produced  $K^-$  mesons are reabsorbed. Later, when the  $\Delta$  are disintegrated the  $\Lambda(\Sigma)\pi$  channel becomes dominant. By this time the system is less dense and the survival chance of the  $K^-$  mesons has therefore increased. Counting the net number of  $K^-$  mesons which are present in the system as a function of time, one observes that the  $BY \rightarrow NK\Lambda(\Sigma)$  reaction contributes finally less than 50% to the surviving  $K^-$  mesons as can be seen in Fig. v.2, right.

The radial profile of the production points of all  $K^-$  mesons and of the surviving ones is seen in Fig. v.3, left, which displays also the radial profile of the last collision points of the  $K^-$ . These correspond to the production points if the surviving  $K^-$  does not rescatter or to the point of the last elastic collision. The survival probability is obviously depending on the production point. Only about 20% of all produced  $K^-$  survive in Au+Au collisions at 1.5 A GeV. In C+C collisions at the same incident energy this fraction reaches 47%.

The surviving  $K^-$  mesons are produced late or/and close to the surface of the reaction zone. The consequence of both is that the surviving  $K^-$  mesons are produced at low densities. This is detailed on the right hand side of Fig. v.3 showing the density at the points at which the surviving  $K^-$  have been produced and where they had their last collision. The

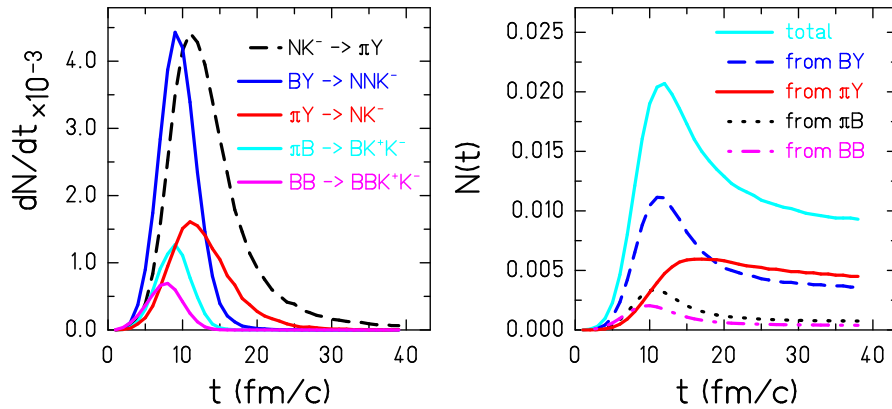


FIG. v.2: Contribution of the different channels to the  $K^-$  yield as a function of creation time of the  $K^-$  (full lines) for central ( $b = 0$ ) Au+Au collisions at 1.5 A GeV . On the left side we display the rate  $dN/dt$ , on the right side the yield  $N(t)$ .

surviving  $K^-$  mesons produced in the interior have a high probability to suffer from elastic  $K^- N$  collisions. Therefore, for the majority of the  $K^-$  mesons the last interaction takes place at less than  $0.5 \rho_0$ . Surprisingly, the  $K^-$  in C+C reactions come from higher densities than those in Au+Au collisions where the  $K^-$  interact still with the expanding fireball, as can be seen in Fig. v.3, right. This observation is not influenced by the  $K^-$  potential as seen in the next section. Therefore, the observed  $K^-$  are neither sensitive to nuclear properties nor to the  $K^- N$  potential at densities higher than  $0.5 \rho_0$  in strong contrast to the  $K^+$ . It is important to note that the total  $K^-$  yield is linked to the total  $K^+$  yield because when more strange baryons are produced more secondary reactions take place in which  $K^-$  mesons are created. This relation has been shown in [127] and has been studied in detail by applying the law of mass action in [128]. There it has been shown that the  $K^-$  production via strangeness exchange seems to be dominant also at AGS energies.

### C. Influence of the $K^- N$ potential

The nuclear matter calculations presented in section II have shown that in cold matter  $K^-$  mesons can hardly be considered as quasi particles because the width of their spectral function is too large. Calculation at finite temperature, however, indicate that with increasing temperature the  $K^-$  regains its quasi-particle properties. Dealing with reactions in which inverse slope parameters of more than 80 MeV are observed we here treat the  $K^-$  meson as a quasi particle. Whereas the theories differ little on the increase of the  $K^+$  mass as a function of the density, there are substantial differences between the different theories for the  $K^-$  pole mass at zero temperature as a function of the density, as shown in section II.

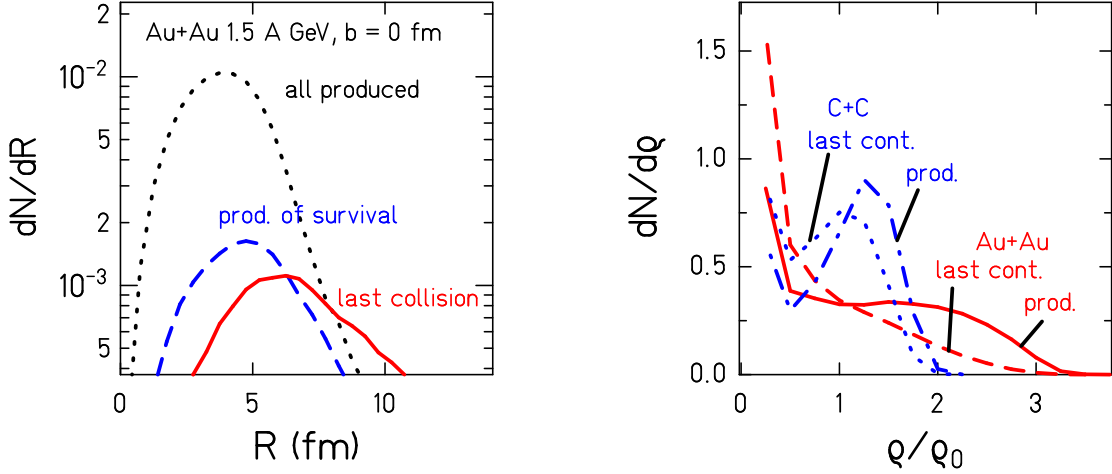


FIG. v.3: Left: Radial profile of the production points for all produced  $K^-$  mesons (dotted line) and of those which are not reabsorbed (dashed line). For those which survive the radial profile of their last interaction point (full line) is displayed as well. Right: Distribution of the density at creation and at the point where the surviving  $K^-$  have their last interaction for Au+Au and C+C collisions at 1.5 A GeV .

These differences are due to details of the calculation, due to a different pion dressing and due to different channels which have been included. A similar uncertainty is also expected for the  $K^-$  masses at finite temperature.

In the IQMD approach the mass, or more precise  $\omega(\mathbf{k} = 0)$ , is given by the mean field calculation of Ref. [82, 129] (see Eq. 60). It is expected that the attractive  $K^-$  N interaction increases the  $K^-$  yield in heavy-ion reactions as compared to an inactive  $K^-$  N interaction because the  $K^-$  becomes "lighter" in matter ( $\omega(\mathbf{k} = 0) < m_0$ ). The situation is becoming more complex if we include both, the attractive  $K^-$  N and the repulsive  $K^+$  N interaction, as seen in Fig. v.4. Then, we have almost the same  $K^-$  multiplicity as if none is active (dashed and solid lines in Fig. v.4). The gain of the yield by a smaller  $K^-$  mass (dotted line) is almost completely compensated by the loss of the number of  $\Lambda$  (dash-dotted line) due to a smaller production cross section if the  $K^+$  becomes heavier. This might appear astonishing as the density dependence of the  $K^+$  N potential is rather weak, while that of the  $K^-$  N interaction is rather strong and less cancellation is expected. The cancellation occurs, however, because the  $K^+$  production occurs at high densities (Fig. iv.11.) whereas the surviving  $K^-$  are created at densities at or below  $\rho_0$ , as shown before.

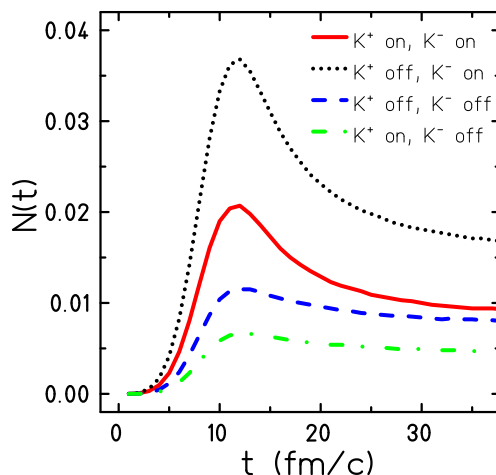


FIG. v.4: Time evolution of the  $K^-$  yield in central Au+Au collisions at 1.5 A GeV for different options of the KN-potentials.

#### D. Uncertainties in the input quantities

Besides the little-known density dependence of the  $K^- N$  potential a second, even less controlled source of uncertainty is the lack of knowledge of the essential elementary cross sections. E.g. the cross section of the  $\Delta\Lambda(\Sigma) \rightarrow NNK^-$  channel is not known at all. Depending on the life time of the  $\Delta$  in matter it may be as important as the  $\pi\Lambda(\Sigma)$  channel (see Fig. v.2) in heavy-ion collisions. It is also nontrivial to extrapolate the measured free  $K^- N \rightarrow \Lambda(\Sigma) + \pi$  cross section to a nuclear environment. Calculations have shown that the  $\Lambda(1405)$  resonance disappears in matter [20–23] but the details, especially the density dependence of the disappearance, depend on the  $K^- N$  interaction. As can be seen from Fig. v.3, there is a broad distribution of densities, which ranges from almost zero to 1.5 (2)  $\rho_0$  in C+C (Au+Au) collisions, to which the emitted  $K^-$  mesons are sensitive. Detailed information on the properties of the  $\Lambda(1405)$  at these densities and hence its role for the  $K^-$  production and annihilation cross sections is not available. Experiments like  $pA \rightarrow X K^-$  could in principle elucidate this question but the few available data are not at all sufficient. Therefore, the two essential input quantities, the  $K^- N$  potential and the  $K^- N \rightarrow \Lambda\pi$  cross section, are much less known than the corresponding quantities for the  $K^+$ .

Besides these uncertainties directly related to the production of the  $K^-$  the dominance of the hyperon induced channels link the production of  $K^-$  directly to the yield of the hyperons. Since these hyperons are dominantly produced together with a positive kaon, there is a direct link between the yield of  $K^+$  and  $K^-$ . Thus, all uncertainties related to the production of  $K^+$  - like the unknown cross section of the production via the  $N\Delta$  channel, see Fig. iii.7 - are inherited by the  $K^-$ . This effects the absolute yield of the  $K^-$  but does not effect the relative  $K^+ / K^-$  ratio.

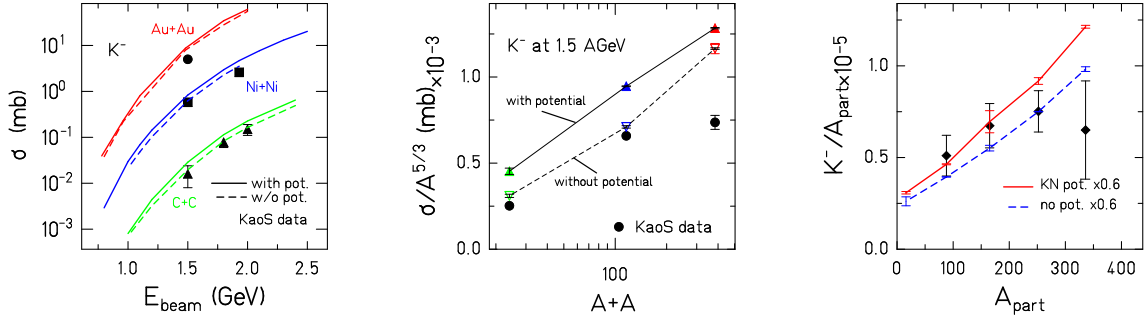


FIG. v.5: Left: Excitation function of the inclusive  $K^-$  cross section with and without the KN potential. The lines refer to IQMD calculations and the symbols to the experimental results of the KaoS Collaboration [109]. Middle:  $K^-$  cross section divided by  $A^{5/3}$  as a function of the system size in theory and experiment. The line are to guide the eye. Right:  $K^- / A_{\text{part}}$  versus  $A_{\text{part}}$  for Au+Au collisions at 1.5 A GeV (right) as compared with IQMD calculations. The IQMD yields are multiplied with the factor which is indicated in the figure.

### E. $K^-$ multiplicity

The excitation function of the  $K^-$  cross section in heavy-ion reactions is shown in Fig. v.5 (left), including and excluding the KN interaction and compared to the results of the KaoS collaboration [109]. As already seen in Fig. v.4, for Au+Au reactions the combined influence of both KN potentials is small. It increases for lighter systems because there the density at the production point of the  $K^-$  is higher (see Fig. v.3) and that of the  $K^+$  lower. Then the  $K^+$  N potential hardly lowers the  $K^+$  yield but the stronger density dependence of the  $K^-$  mass makes it more probable that a  $K^-$  can be produced. The form of the excitation function is well reproduced but the calculations have the tendency to over-predict slightly the yield. This tendency is also visible in the middle part of Fig. v.5 which shows the theoretical and experimental inclusive cross section divided by  $A^{5/3}$  as a function of the system size for 1.5 A GeV. The experimental trend that the  $K^-$  yield increases stronger than the system size is reproduced by the calculations. This tendency is also visible in the centrality dependence of the  $K^-$  yield in Au+Au reactions at 1.5 A GeV (right).

### F. Are data compatible with a strong $K^-$ potential?

One of the essential questions in  $K^-$  physics is the depth of the  $K^-$  N interaction. As discussed in Section II many efforts have been made to determine this potential but a definite answer is not at hand yet. Therefore, it is interesting to explore how the results of simulations of heavy-ion reactions depend on the potential depth and whether the existing data limit the strength. For this purpose we simulate the reaction - keeping the (well established)  $K^+$  N



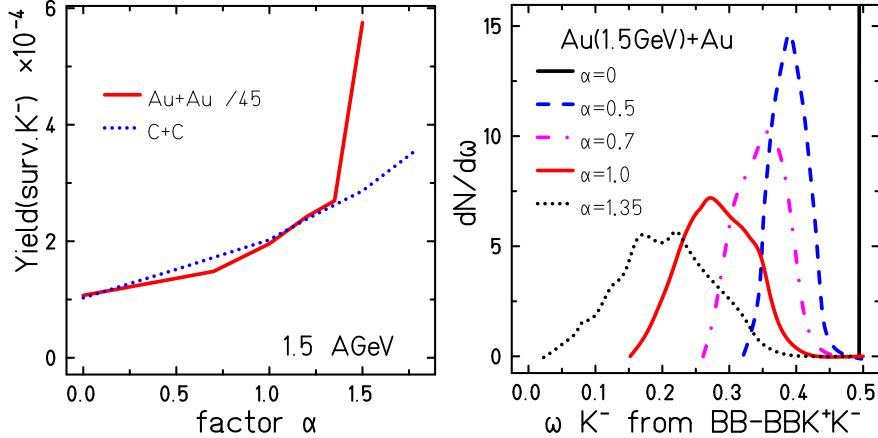


FIG. v.6: Left:  $K^-$  multiplicity as a function of the strength of the  $K^-$  N potential. Right:  $\omega(\mathbf{k} = \mathbf{0})$  distribution as a function of the strength of the  $K^-$  N potential.

potential at its standard value - with a variety of  $K^-$  N potentials. They are obtained by multiplying the potential constants by a factor  $\alpha$  as it is shown in Eq. 68.

In Fig. v.6, left, the calculated  $K^-$  yield in Au+Au and C+C systems for different values of  $\alpha$  is presented. Below  $\alpha = 1.25$  the yield increases moderately and in the same way for Au+Au as for C+C. Above  $\alpha = 1.25$  we observe a very sudden and strong increase of the yield in Au+Au reactions whereas the increase in the C+C system is continuous. Figure v.6, right, shows the origin of the different behavior of the Au+Au and C+C systems above  $\alpha = 1.25$ . It displays the  $\omega(\mathbf{k} = \mathbf{0})$  distribution as a function of the strength of the potential. Already in our standard parameterization ( $\alpha = 1$ ) we observe in Au+Au reactions small values of  $\omega(\mathbf{k} = \mathbf{0})$ . This fraction increases with the strength of the potential and a larger and larger fraction of the  $K^-$  has a very small mass. Above  $\alpha = 1.25$  we find that in some of the production reactions  $\omega(\mathbf{k} = \mathbf{0}) = 0$ . This means a very low threshold in this reaction and hence a large yield. In C+C systems where the density is lower  $\omega(\mathbf{k} = \mathbf{0})$  remains large.

Thus the measurable ratio of the  $K^-$  yield in Au+Au and C+C systems is relatively independent of acceptance cuts and detector response, but is quite sensitive to the depth of the potential. The fact that the yield ratio is reproduced in our simulations (see Fig. v.5) therefore allows for the conclusion that  $\alpha$  has to be smaller than 1.25. The strong  $K^-$  potentials which has been discussed in section II and which are a prerequisite for the existence of a  $K^-$  condensate, are not compatible with heavy ion data.

### G. $K^-$ spectra

The  $K^-$  spectrum at production is a convolution of the momentum distributions of the  $\Lambda(\Sigma)$  and of the  $\pi$  or baryon, respectively, weighted with the production cross section. Figure v.7 shows the various channels which contribute to the  $K^-$  spectra. The sum is

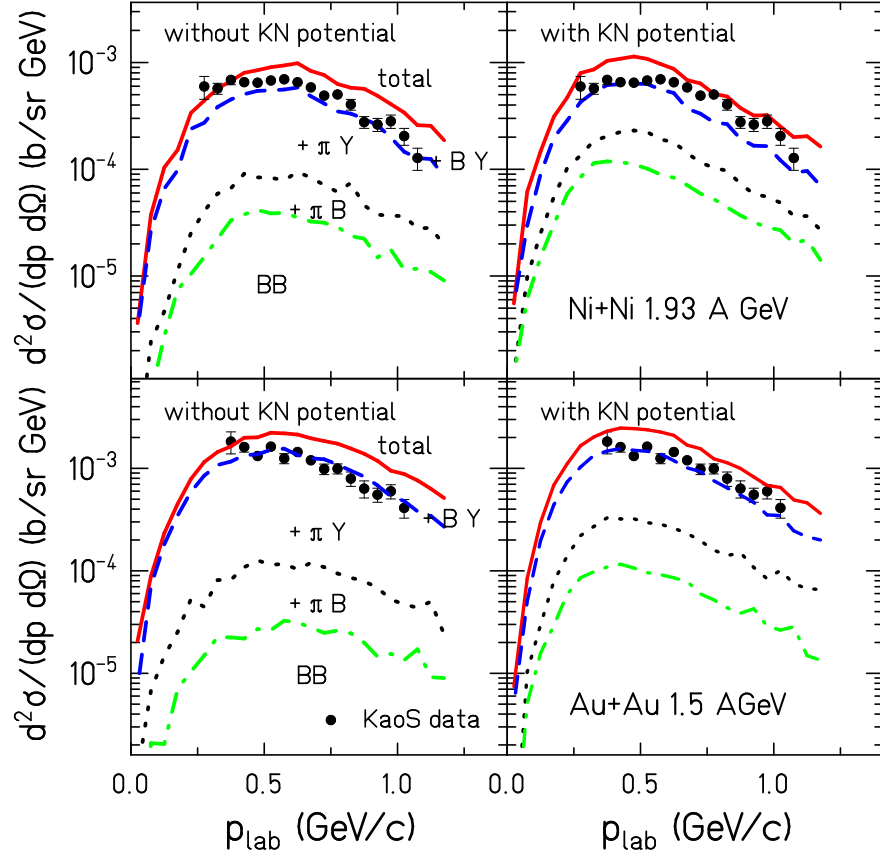


FIG. v.7: Contribution of various channels to the production of  $K^-$  in inclusive Ni+Ni (top) and Au+Au (bottom) collisions at  $\theta_{\text{lab}} = 40^\circ$  with (right) and without (left) KN potential. The respective contributions are cumulative. Hence each line represents the sum of the channels below.

compared to the experimental data of the KaoS Collaboration [109]. As the  $K^-$  momentum distribution in the different channels does not differ substantially, the form of the spectra does not allow for conclusions on the production mechanism. On the left hand side we have switched off both KN potentials in the calculation. As expected from Fig. v.4, the KN potential changes the yield only marginally. The calculation reproduces quite well the form of the spectra but over-predicts slightly the yield, as already seen in Fig. v.5.

The slope of the surviving  $K^-$  at production is around 8 MeV higher for Au+Au than for the C+C reactions at 1.5 A GeV as shown in Fig. v.8. This is due to the large fraction of  $N\Delta$  collisions in the strangeness-production process in Au+Au which produces  $\Lambda$  with a higher energy. After production the shape of the  $K^-$  spectra may be modified in several ways:

(i) The absorption cross section is strongly momentum dependent. Therefore, the slope of the surviving  $K^-$  differ if reabsorption becomes important. The influence of this effect

is still small for the C+C system but it becomes an important contribution to the change of the slope in Au+Au reactions. Figure v.8 illustrates the absorption process showing the  $K^-$  spectra at the initial production, the distribution of the absorbed ones and that of the surviving ones. The corresponding slopes are given in the figure.

(ii) Elastic rescattering of the  $K^-$  with the surrounding nucleons, which have a larger inverse slope parameter, increases the  $K^-$  slope. This is seen on the left hand side of Fig. v.9 which shows a more than twenty percent increase of the slope of those  $K^-$  which had at least two rescattering collisions, independent of the system.

(iii) The potential interaction reduces the  $K^-$  momentum (opposite to the  $K^+$  case) when it approaches the surface of the system because energy is needed to bring the  $K^-$  mass to its free value and this energy is partially taken from the kinetic energy of the  $K^-$ . This leads to an enhancement at small momenta in the c.m. system and to a change of the high-momentum slope, as demonstrated on the right hand side of Fig. v.9, where we have selected  $K^-$  which do not rescatter in order to separate this change from that due to rescattering.

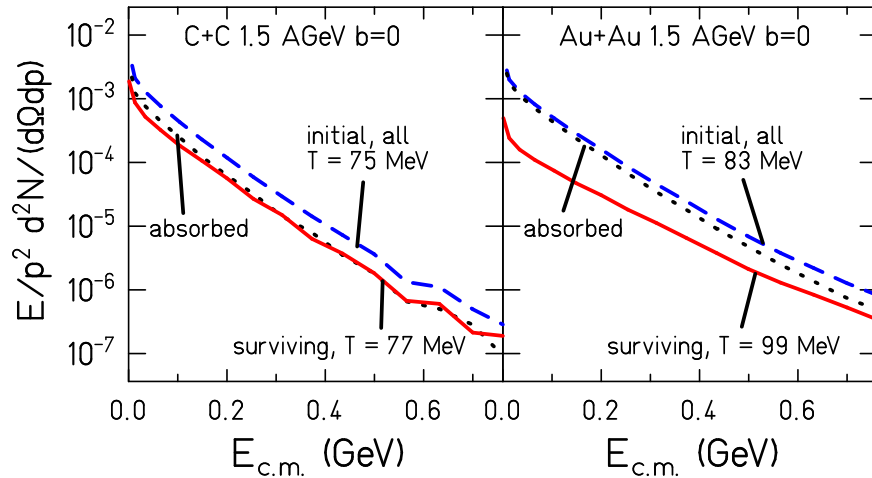


FIG. v.8: Spectral form of  $K^-$  in central collision of C+C (left) and Au+Au (right, yields are divided by 100) at 1.5 A GeV .

Because the distribution of the number of elastic rescatterings is different for the different systems, shown in Fig. v.10, the change of the slope of the  $K^-$  spectra due to rescattering is different in Au+Au as compared to C+C collisions.

Figure v.11 (top) compares the spectra, which have been measured by the KaoS Collaboration [109], with IQMD (upper part) and HSD calculations [69] (lower part). Both theories reproduce the slope of all three systems quite well although they use quite a different potential: IQMD employs a mean field potential (Eq. 60) whereas in HSD different versions of a G-matrix approach are used (for details see [69]). Both approaches use also a different description of the in-medium modification of the  $K^-$  cross section. IQMD (HSD)

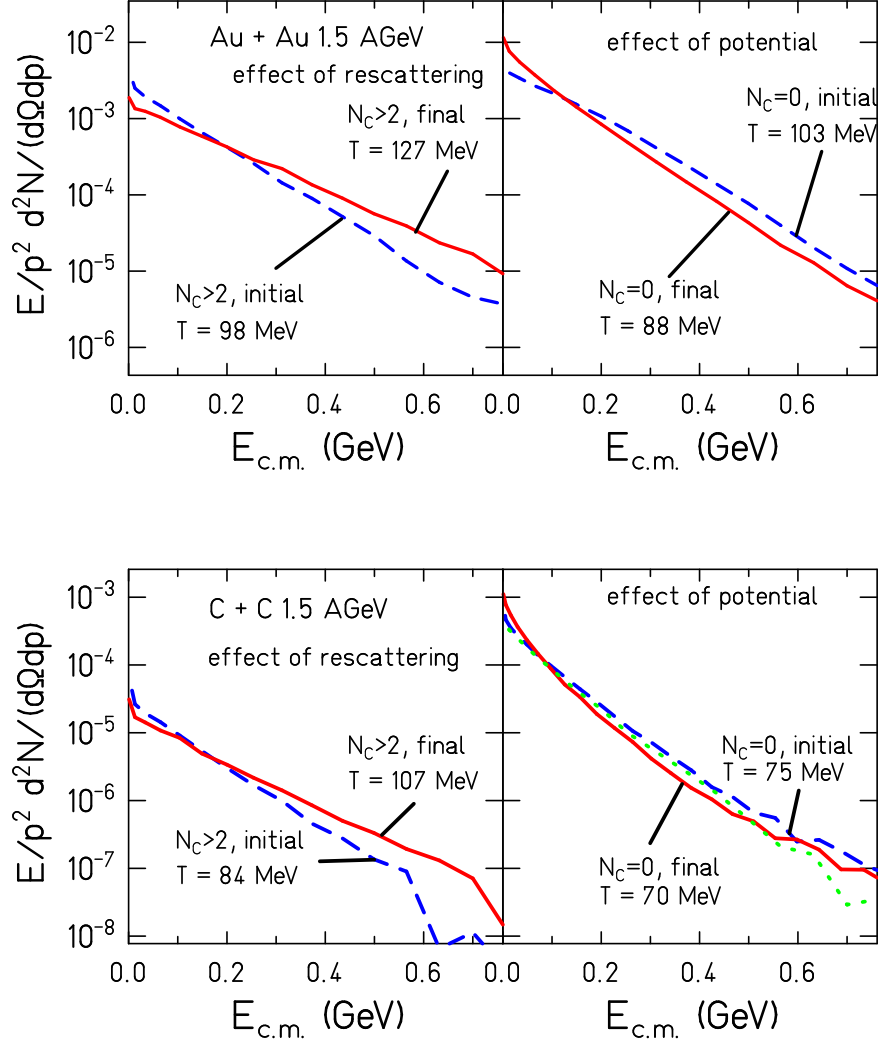


FIG. v.9: Influence of elastic rescattering and of the KN potential on the  $K^-$  spectrum for central Au+Au (top) and C+C (bottom) collisions at 1.5 A GeV. Left: Influence of the rescattering of  $K^-$  by selecting kaons which have scattered twice or more, showing their initial and final distribution. Right: Influence of the KN potential on the spectral shape demonstrated by selecting kaons which never rescattered ( $N_C = 0$ ) and comparing the initial and final spectra.

calculation have the tendency to overpredict (underpredict) slightly the yield. Calculations using the same potential and the same  $K^-$  cross section are not available.

The HADES Collaboration has recently measured  $K^-$  spectra as a function of  $m_t - m_0$  for different rapidity intervals for the reaction Ar+KCl at 1.75 A GeV [134]. Their results are compared with IQMD calculations with and without KN potential in Fig. v.12. As the other HADES spectra in this report, this spectrum is normalized to the  $K^0$  yield because an absolute normalization is not available. All  $K^-$  spectra have an exponential form at high

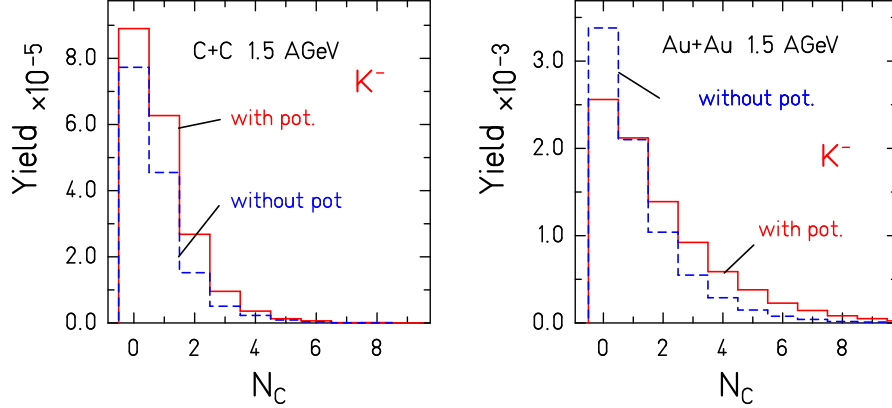


FIG. v.10: Distribution of the number of elastic collisions of  $K^-$  in IQMD simulations of C+C and Au+Au collisions.

momenta if plotted as  $(E/p^2)(d\sigma/dp)$  or as  $(1/m_t^2)d^2M/(dm_t dy)$ .

As shown in Fig. v.12, the inverse slope parameter of the  $K^-$  changes if a KN potential is employed, as could already be inferred from Fig. v.9. The HADES collaboration has parameterized the measured inverse slope parameter  $T$  as a function of the rapidity by  $T(y) = T_0/\cosh(y)$  with  $T_0 = 69 \pm 2$ . Such a form is expected if the emission is isotropic in the center-of-mass system. IQMD calculation, including (excluding)  $K^-$  N potential yields 80 (62) MeV.

The KaoS Collaboration has measured centrality-selected spectra for the Ni+Ni and Au+Au systems [109], which are displayed and compared to IQMD calculations in Fig. v.13. Except for the peripheral Ni+Ni data the slopes are reproduced but the calculation overpredicts the data for the most central collisions. For mid-central events the calculation reproduce the data quantitatively.

Similarly as has been observed for the system-size dependence, due to rescattering and absorption the theoretical inverse slope parameters of the surviving  $K^-$  mesons vary for heavy systems with centrality as well. This is summarized in Fig. v.14 for Au+Au at 1.5 A GeV and compared to the KaoS data [109]. The slope of the  $K^-$  spectra at the moment of their production is determined by the elementary production process and quite independent of the centrality. Selecting only those  $K^-$  mesons which survive the heavy-ion reaction, an inverse slope parameter which increases with centrality, can be observed (Fig. v.8) due to the momentum dependence of the absorption cross section. Elastic  $K^-$  collisions increase the slope even further until finally the potential interaction with the nucleons leads to a reduction. The final slope is in good agreement with experiment.

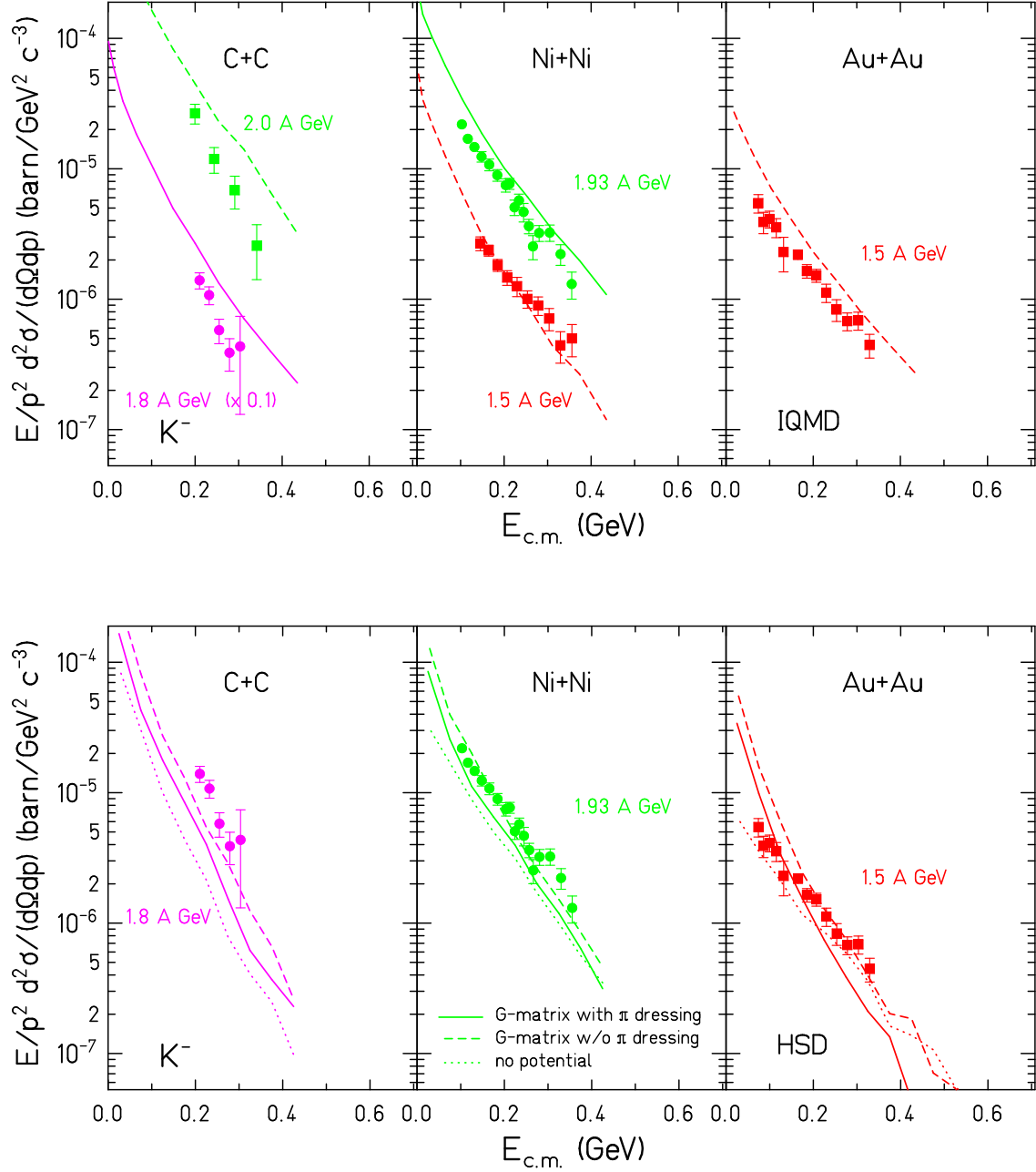


FIG. v.11: Measured (symbols) and calculated (lines) inclusive invariant cross sections of  $K^-$  mesons at mid-rapidity as a function of the kinetic energy  $E_{c.m.}$  for Au+Au (right), Ni+Ni (middle) and C+C (left) reactions at various beam energies. On the top we display IQMD at the bottom HSD calculations. The mid-rapidity condition is a selection of  $\theta_{c.m.} = 90^\circ \pm 10^\circ$  both for the data and the calculations. The data are from the KaoS Collaboration [109].

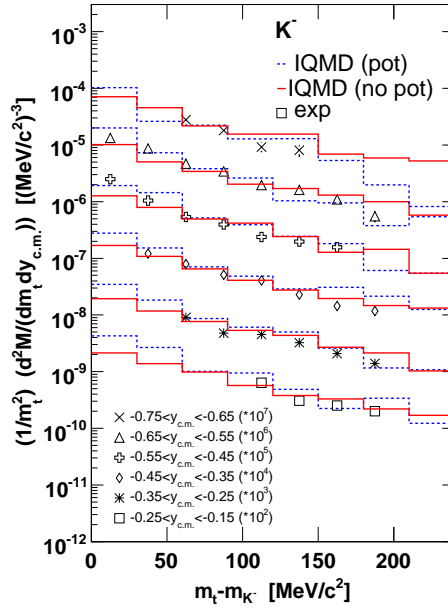


FIG. v.12:  $K^-$  transverse mass spectrum for semi-central collisions of Ar+KCl at 1.75 A GeV measured by the HADES Collaboration [134] as compared with IQMD calculations with active and inactive KN potential. The spectra are normalized to  $K^0$  spectra.

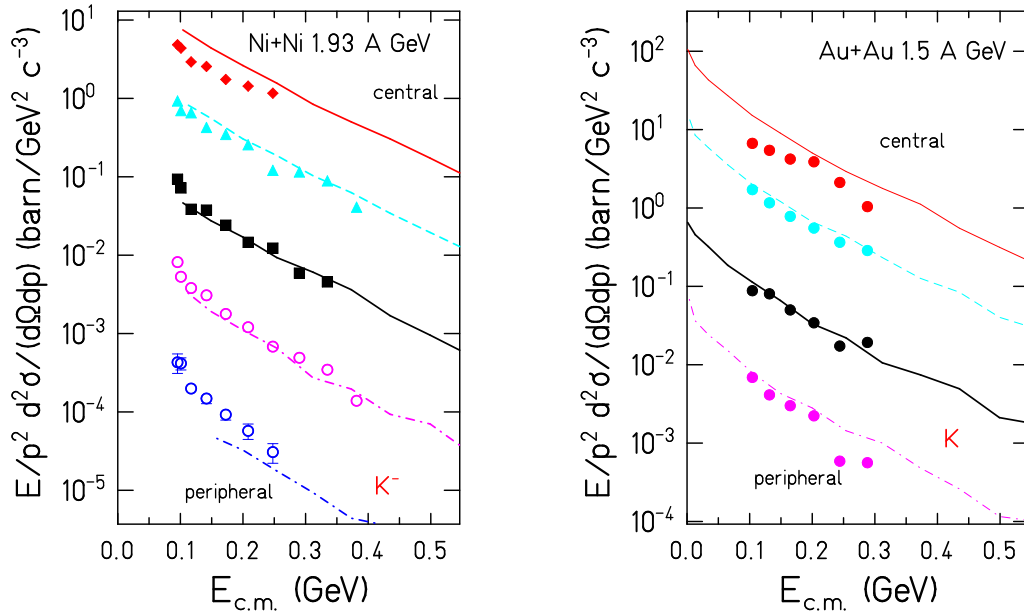


FIG. v.13: Centrality selected energy spectra for Ni+Ni at 1.93 A GeV and Au+Au at 1.5 A GeV measured at  $\theta_{lab} = 40^\circ$  by the KaoS Collaboration [109] as compared with IQMD calculations.

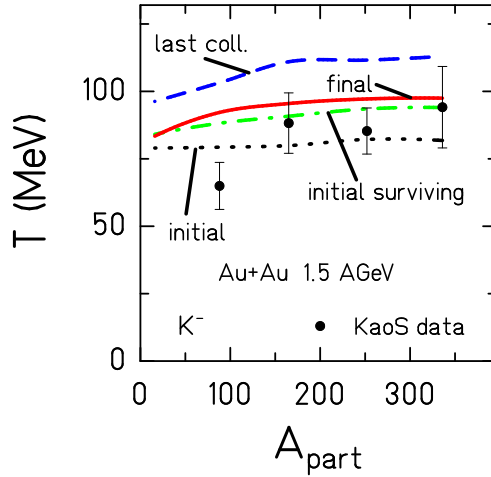


FIG. v.14: Centrality dependence of the inverse slope parameters of the  $K^-$  spectra showing the influence of the different effects and compared to the data of the KaoS Collaboration [109]. The final curve includes in addition the  $K^-$  N potential interaction after the last collision.

## H. Rapidity distribution

As for the  $K^+$  mesons, the measured spectra are extrapolated to small  $p_t$  momenta in order to obtain rapidity density distributions. The result for 1.93 A GeV Ni+Ni is shown in Fig. v.15 and compared with theory, separately for central and peripheral collisions. Both theories, HSD as well as IQMD, show that the  $K^-$  N potential has no influence on the form of the distribution but it enhances the total yield considerably. The HSD [69] calculation reproduces the 1.93 A GeV Ni+Ni data whereas the IQMD calculation overestimates the yield by a roughly a factor of 1.5.

## I. Polar distributions

Similar as for the  $K^+$  mesons, the polar distribution of the  $K^-$  is rather flat at the moment of their production if averaged over their momenta. The distribution is also flat if one selects only those  $K^-$  mesons which survive. Thus, the observed anisotropy is due to the interactions of the  $K^-$  with the system. Elastic rescattering of the surviving  $K^-$  brings the polar distribution closer to that of the scattering partners and therefore leads to an enhancement in forward and in backward direction. It is independent of the strength of the KN potential as can be seen comparing the left and the middle parts of Fig. v.16 which show calculations for  $b < 5.9$  fm Au+Au reactions at 1.5 A GeV . Choosing the surviving  $K^-$  which did not rescatter ( right panel), one selects those with the shortest path through the matter. This path depends on the geometry and therefore, by selecting those particles,



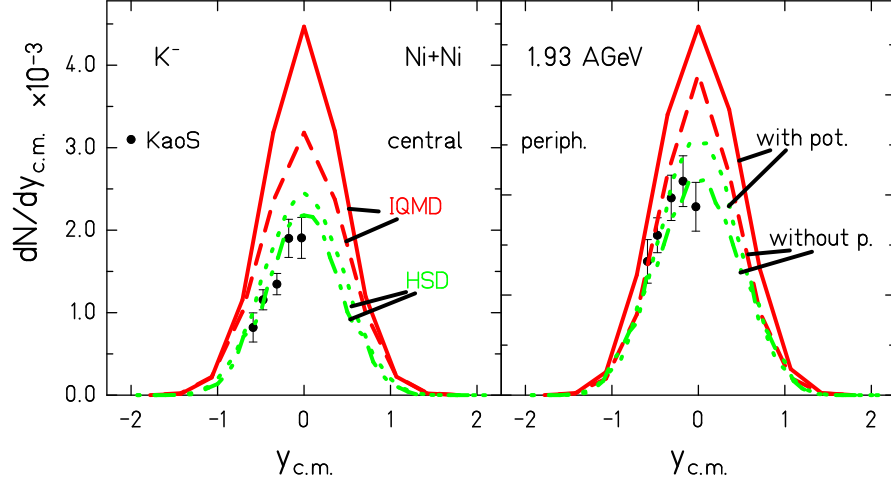


FIG. v.15: The rapidity distribution of  $K^-$  mesons for central ( $b \leq 4.5$  fm, left) and peripheral ( $b = 4.5 - 7.5$  fm, right) Ni+Ni reactions at 1.93 A GeV . The results from the KaoS Collaboration [131] are compared with IQMD (red solid and dashed lines) and HSD [69] (green dotted and dashed-dotted) calculations. The solid and dotted lines correspond to the calculations including the  $K^+$  and  $K^-$  potential, while the dashes and dash-dotted lines show the results without KN potential. Both calculations use different  $K^-$  potentials (see text).

one creates an anisotropy already at production. Again, the potential has no influence on the distribution.

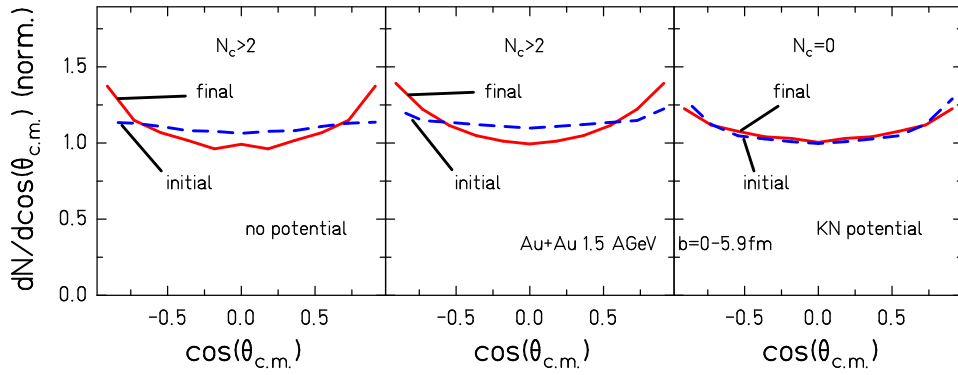


FIG. v.16: Influence of rescattering and of the KN potential on the polar distribution of surviving  $K^-$  for Au+Au reaction at 1.5 A GeV. The distribution marked 'initial' is that of surviving  $K^-$  .

Figure v.17 confronts IQMD and HSD [69] calculations with experiment. On the left (right) hand side, we display the results for peripheral (semi-central) collisions. The upper figure shows Au+Au collisions at 1.5 A GeV , the lower figure Ni+Ni collisions at 1.93 A GeV

. For central collisions, data and theory agree and both theoretical approaches confirm that the KN potential is without any influence on the distribution for heavy systems, as discussed before. For the lighter Ni+Ni system we observe a small influence of the potential in central collisions. For peripheral reactions the potential is more influential but the present error bars are too large in order to draw firm conclusion from the comparison of theory and experiment, may be with the exception of the Ni data.

## J. Azimuthal distribution

### 1. In-plane flow $p_x(y)$ and $v_1$

The in-plane flow of  $K^-$  mesons is, similar to the inverse slope parameter of the spectrum, a sensitive probe for the different processes which the  $K^-$  suffer from creation to observation. The left hand side of Fig. v.18 displays the in-plane flow as a function of the rapidity  $y_{c.m.}$ . Already at production a small in-plane flow can be observed. Absorption modifies this flow substantially. Those  $K^-$  which flow with the nucleons have, due to geometry, a much higher probability to get absorbed. Therefore, the surviving  $K^-$  mesons show initially an anti-flow. Subsequent elastic collisions bring the distribution closer to that of the baryons. In contradiction to the repulsive  $K^+ N$  interaction, the attractive  $K^- N$  interaction pulls the  $K^-$  also towards the baryons. The influence of the rescattering collisions is less important than that of the potential, see Fig. v.18, right.

In Fig. v.19, IQMD and HSD predictions for  $v_1$  as a function of rapidity are shown for Ni+Ni collisions at 1.93 A GeV . The calculations are filtered by the FOPI acceptance. Without the  $K^- N$  potential,  $v_1$  (defined in Eq. 84) of the  $K^-$  is positive and opposite to that of the nucleons. The attractive  $\bar{K}N$  potential pushes the  $K^-$  closer to the nucleons. Consequently the flow of the  $K^-$  changes sign and becomes negative.

### 2. Out-of-plane flow $v_2$

IQMD and HSD predictions for  $v_2$  (defined in Eq. 84) as a function of rapidity for Ni+Ni collisions at 1.93 A GeV within the FOPI acceptance are displayed in Fig. v.20. Error bars for the model predictions are rather large, but there is a tendency of an in-plane enhancement of the elliptic flow ,  $v_2 > 0$ , at large rapidities which is reduced if an attractive  $\bar{K}N$  potential. Closer to mid-rapidity there is no influence of the potential on the elliptic flow.

The azimuthal distribution of  $dn/d\phi$  has been measured by the KaoS Collaboration [119] and is presented in Fig. v.21 in comparison with IQMD calculations. The calculations show no visible influence of the  $\bar{K}N$  potential and the error bars of the data are too large to verify whether the distribution is as flat as theory predicts or whether a small in-plane enhancement ( $v_2 > 0$ ) is observed.

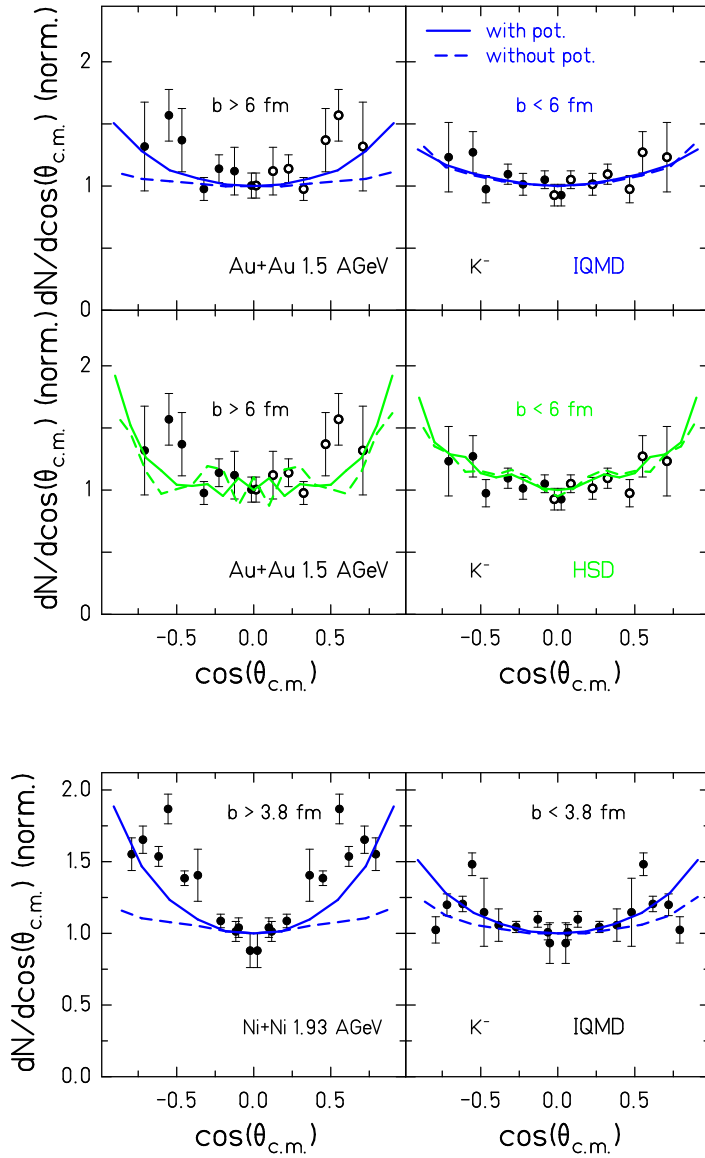


FIG. v.17: The measured polar angle distribution of  $K^-$  mesons for Au+Au at 1.5 A GeV (upper part) and for Ni+Ni at 1.93 A GeV (lower part) for two impact parameter ranges are compared to IQMD and HSD [69] (only for Au+Au) calculations. The  $K^-$  N potential in both approaches is different (see text). The data are from the KaoS Collaboration [109]. The solid (dashed) lines refer to calculations with (without) KN potential. The distributions are normalized to unity for  $\cos \theta_{c.m.} = 0$ .

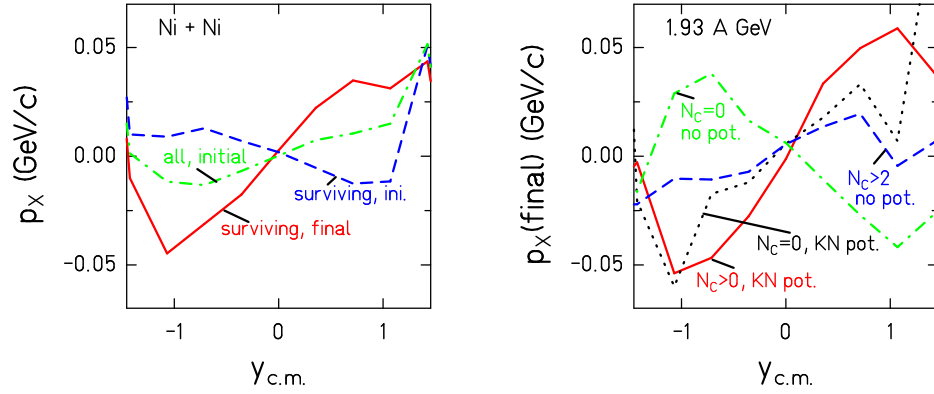


FIG. v.18: In-plane flow  $\langle p_x \rangle (y_{c.m.})$  of  $K^-$  in Ni+Ni reactions at 1.93 A GeV. Left: Influence of the absorption cross section on the in-plane flow. Right: Influence of potential and rescattering collisions on the in-plane flow.

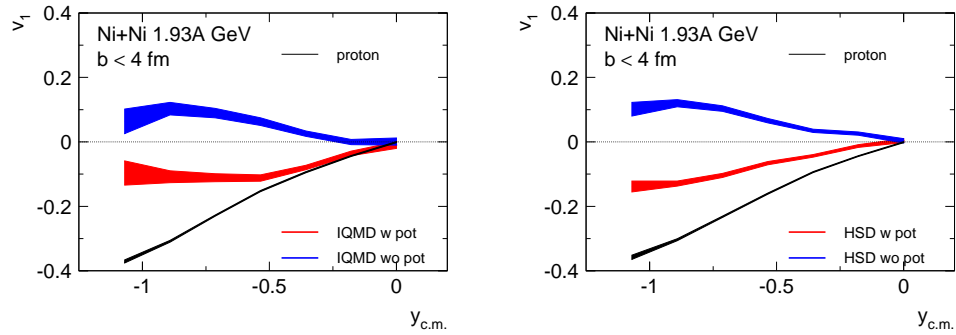


FIG. v.19: IQMD (left) and HSD (right) predictions of  $v_1$  as a function of the rapidity for central Ni+Ni collisions at 1.93 A GeV with and without KN-potential. The results of IQMD predictions are filtered for the acceptance of the new time-of-flight barrel of the FOPI detector.

The differential  $v_2(p_t)$  for the heavier Au+Au system at 1.5 A GeV, measured by the KaoS Collaboration [121] and presented in Fig. v.22, shows a strong  $p_t$  dependence which is not reproduced by the model. Non-central collisions are selected by excluding the 20% most central collisions. This corresponds to impact parameters larger than 6.4 fm. The difference between the calculations including and excluding a  $K^-$  N potential is small. The reason for this small effect is likely the late emission of the  $K^-$ . Then the spectators are gone and cannot absorb the  $K^-$  emitted in the reaction plane. A relation between emission time and out-of-plane enhancement can be seen from Fig. v.23. Early (0-8 fm/c) emitted  $K^-$  exhibit indeed an out-of-plane enhancement evidencing the absorption in the spectator matter. In

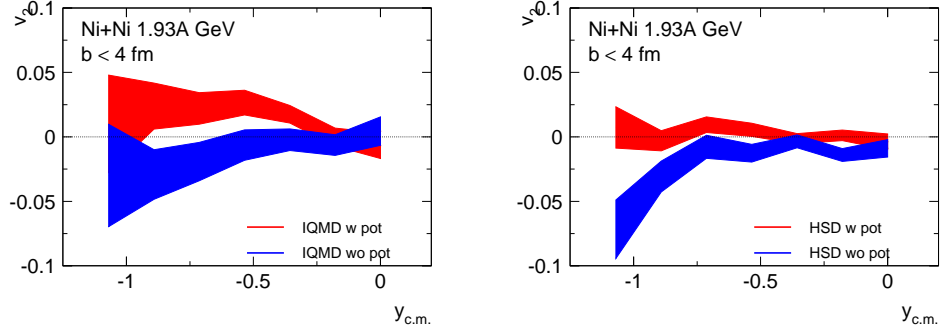


FIG. v.20: IQMD and HSD predictions for  $v_2$  as a function of rapidity for central collisions of Ni+Ni at 1.93 A GeV . The results are filtered with the FOPI acceptance filter.

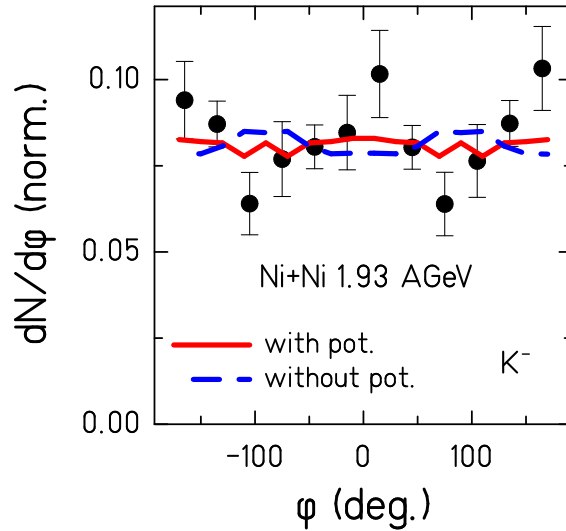


FIG. v.21: Azimuthal distribution of  $dn/d\phi$  for Ni+Ni reactions at 1.93 A GeV from the KaoS Collaboration [119] as compared with IQMD calculations with and without KN potential. The data are obtained for impact parameters between 3.8 fm and 6.5 fm, at rapidities of  $0.3 < y/y_{beam} < 0.7$  and for momenta between 0.2 and 0.8 GeV/c.

the model calculations the bulk of the  $K^-$  are emitted after 8 fm/c which results in a rather flat distribution. One might then speculate whether the observed positive  $v_2$  values for low- $p_t$   $K^-$  indicate an earlier emission than in the model calculations. HSD including off-shell propagation of  $K^-$  and a G-Matrix approach for the  $K^-$  spectral function [69] predicts a stronger transverse momentum dependence for  $v_2$ . The details of the distributions in particular the change of sign at low  $p_t$  is not described, however.

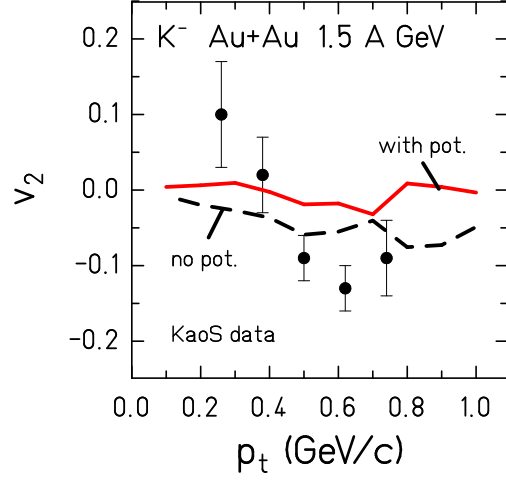


FIG. v.22: Experimental  $v_2(p_t)$  distribution measured by the KaoS Collaboration [121] for non-central Au+Au reactions at 1.5 A GeV as compared with IQMD calculations with and without KN potential.

In conclusion,  $v_2$  appears to be rather insensitive to the KN potential and does not change much as a function of the rapidity. The in-plane flow  $\langle p_x(y) \rangle$  or  $v_1(y)$  is, on the contrary, quite sensitive to the potential but also to the reabsorption cross section.

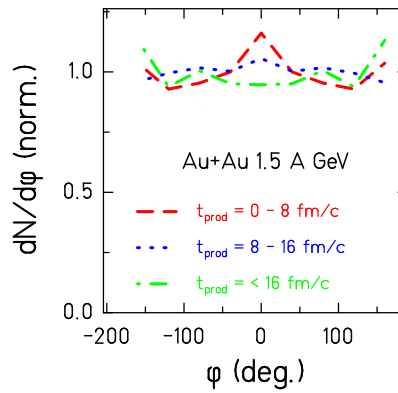


FIG. v.23: Azimuthal distribution selected according to emission time

## VI. DISCUSSION AND SUMMARY

### A. Differences and similarities of $K^+$ and $K^-$ emission

Having demonstrated the quite different production mechanisms for the anti-strange (Section IV) and strange (Section V) mesons we now confront the meson observables directly. In Fig. vi.1 we display the experimental excitation function of the multiplicity per projectile nucleon for  $K^+$  and  $K^-$  as well as that of  $\pi$  observed in inclusive collisions of C+C (dashed lines) and Au+Au (full lines). For both, the  $K^+$  and  $K^-$  mesons, the multiplicity per projectile nucleon is larger for the heavy system than for the light one while for pions the situation is just opposite. Pions can be absorbed in large systems, while the production of  $K^+$  increases with density and hence the yield rises for heavier systems where higher densities are reached. In spite of strong absorption, the  $K^-$  yield in the heavy system is also higher than in the light one. This is again an experimental verification that the  $K^+$  and  $K^-$  production are tied together because the  $K^-$  are produced in a strangeness-exchange reaction with the hyperon which has been created together with the  $K^+$ .

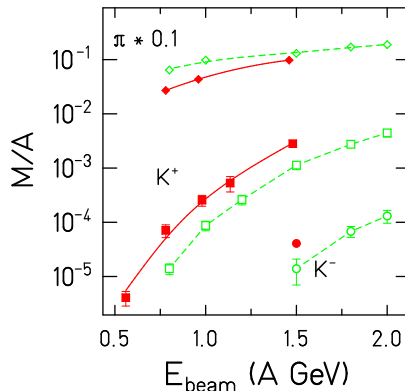


FIG. vi.1: Multiplicity per  $A$  for  $K^+$ ,  $K^-$  and pions (sum of all three species). The dashed (green) lines connect the results for C+C, the full (red) lines those of Au+Au. Data are from Ref. [109].

The rise of the  $K^+$  and  $K^-$  yields as a function of  $E_{\text{beam}}$  reflects a typical threshold behavior. Yet, in contrast to the production in elementary processes, the shape of these two excitation functions are very similar (see Fig. v.1). Again, this testifies how closely both are connected. Consequently we see only the weak rise of the  $K^-/K^+$  ratio with  $E_{\text{beam}}$  shown in Fig. vi.2. Even more interesting, the rise is about the same for all systems. Also IQMD calculation exhibit a rather soft rise and a rather small variation for the different collisions systems. Including the KN potential (thick lines) the calculations over-predict this ratio due to a over-prediction of the  $K^-$  yield, whereas without KN potential (thin lines) theory under-predicts this ratio. As shown in Ref. [127, 128], the yield of pions determines the

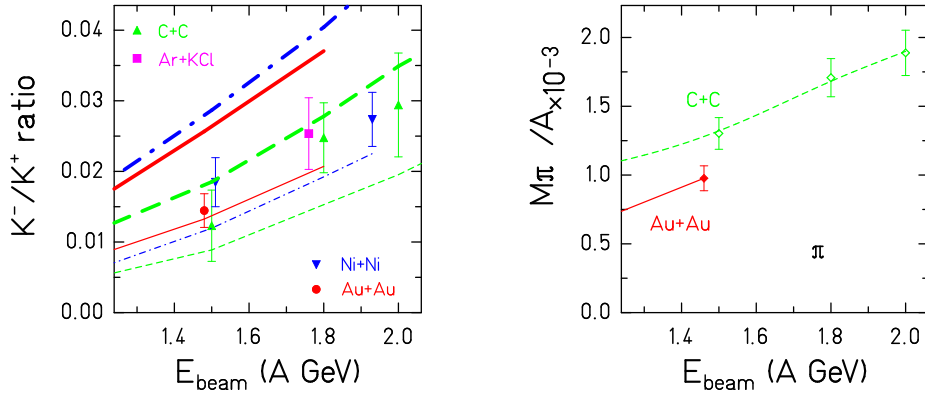


FIG. vi.2: Left: Excitation function of the  $K^- / K^+$  ratio for inclusive collisions of various systems together with IQMD calculations. The experimental data are from the KaoS Collaboration [109] and the Ar+KCl result from the HADES Collaboration [111] with statistical and systematic errors added in quadrature. Thick (thin) lines mark calculations including (excluding) the KN potential. The full, dashed and dashed-dotted lines refer to Au+Au, Ni+Ni and C+C, respectively. Right: Excitation function of  $\pi$  per projectile nucleon.

$K^- / K^+$  ratio, if the strangeness-exchange channel reaches equilibrium. Indeed, the pion excitation function rises in a very similar way, as demonstrated in the right panel. Although in the IQMD only about 60% of the  $K^-$  are produced via the  $Y + \pi = K^- + N$  channels and the rest dominated BY (see Fig. v.2) this trend is not modified. Nevertheless it should be noted that for the 40% remaining channels there is a strong contribution of  $\Delta Y$  reactions. The reacting  $\Delta$  stem mostly from  $N\pi \rightarrow \Delta$  reactions and thus also reflect a dependence on the pion yield.

The multiplicities per projectile or target nucleon  $A$ ,  $M/A$ , and per participating nucleons,  $M/A_{\text{part}}$ , are summarized in Fig. vi.3. On the left hand side, we display these multiplicities for inclusive symmetric reactions as a function of the system size ( $A + A$ ), on the right hand side as a function of the (geometrically determined) participant number,  $A_{\text{part}}$  (taking the values determined by the KaoS Collaboration). As in the previous figures, the Au+Au data are marked by red symbols, Ni+Ni data by blue symbols and C+C by green ones. Both kaon multiplicities rise with system size as well as with centrality. At the same beam energy (1.5 A GeV) the increase with  $A$  is similar for both kaon species (Fig. vi.3, top left). IQMD calculations confirm these findings as we have shown in earlier sections. As a consequence, the ratio  $K^+ / K^-$  is about constant, both as a function of  $A + A$  as well as with  $A_{\text{part}}$ , as seen in the bottom panels. For pions clearly a different behavior is seen. While the multiplicities per  $A$  for inclusive collisions decreases with  $A$ , the centrality dependence is roughly constant as has been found already at the BEVALAC [1]. The system-size dependence can be understood by absorption. At these low incident energies, the multiplicity per  $A$  in heavy-ion



collisions is much lower than that in elementary NN collisions [132]. With increasing beam energy, this difference vanishes and finally at SPS energies the pion multiplicities per  $A$  in heavy-ion collisions exceeds those observed in elementary NN collisions.

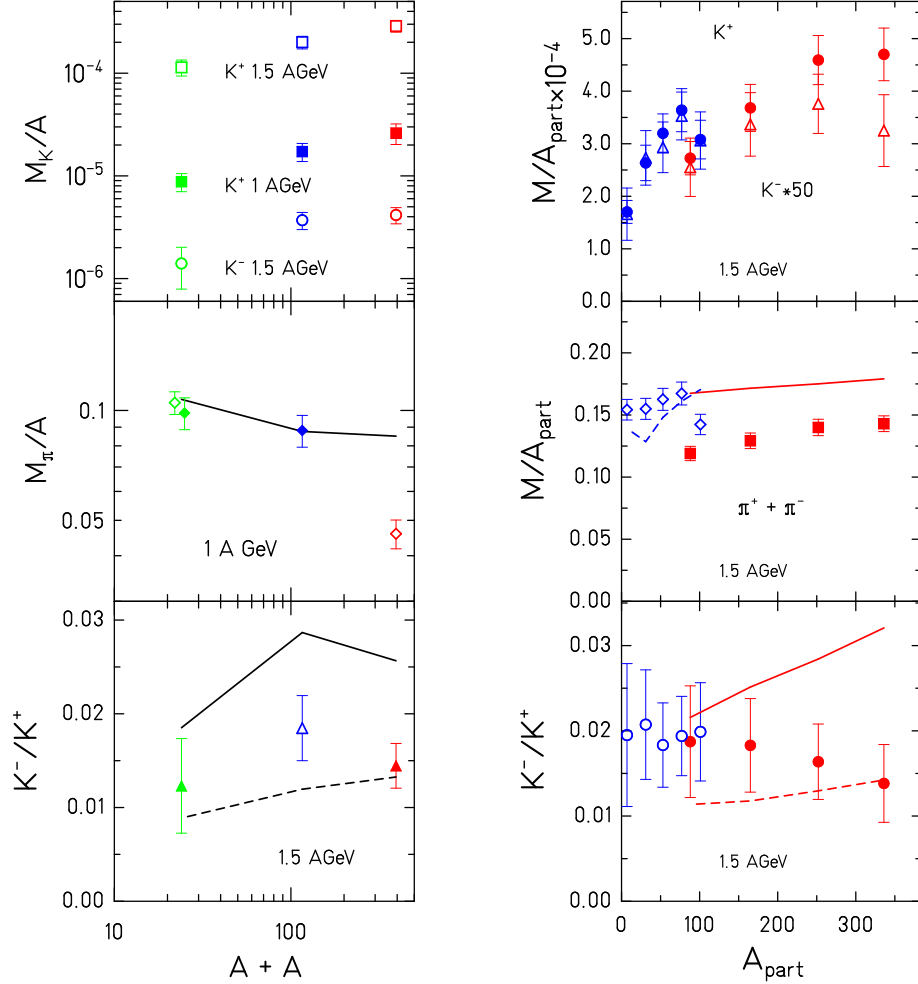


FIG. vi.3: Dependence of the multiplicities of  $K^+$ ,  $K^-$ ,  $\pi$  multiplicity per participating nucleon and of the  $K^-/K^+$  ratio on the system size (for inclusive symmetric reactions at the same beam energy), left, and as a function of the participant number, right. The green symbols refer to C+C collisions, the blue ones to Ni+Ni and the red ones to Au+Au. IQMD calculations including (excluding) the KN potential are given by full (dashed) lines. The data are from Ref. [98, 99, 102, 109].

It has been observed by the KaoS collaboration that the slopes of the  $K^+$  and  $K^-$  spectra show a very systematic behavior: Fitting the mid-rapidity spectra by a function of the form  $Ed^3\sigma/dp^3 \propto \exp(-E/T)$ , the observed inverse slope parameters of the  $K^+$  spectra are always about 15-20 MeV higher than those of the  $K^-$  [109] independent of the system size and independently of the beam energy. This seemingly simple correlation has, however, a

quite complicated origin, if one follows the IQMD calculations.

The elementary production of  $K^+$  mesons follows the three-body phase-space and the energy of the  $K^+$  therefore depends (apart from the beam energy) on the relative contribution of the (on-the-average more energetic)  $\Delta$  N collisions. Even though the three-body phase space distribution does not have an exponential slope, after averaging over the different channels and different c.m.-energies the spectra have an exponential form,  $E d^3N/dp^3 \propto \exp(-E/T)$  (Fig. iv.15). Immediately after production in central Au+Au collisions the inverse slope parameter is  $T = 79(65)$  MeV for central Au+Au (C+C) reactions at 1.5 A GeV (see Fig. iv.15, Fig. iv.17). As seen there, the KN potential does not change the slope considerably. Rescattering on the contrary changes the slope considerably but for C+C collisions the number of rescatterings is small and therefore we observe a final slope of about 80 MeV. In the Au+Au case, on the contrary, rescattering is very important and increases  $T$  to 98 MeV and the strong repulsive  $K^+$  N potential shifts it further up to 110 MeV.

For the  $K^-$  the inverse slope parameter at production (averaged over all production channels) in central Au+Au collisions at 1.5 A GeV is 83 (75) MeV for Au+Au (C+C) (Fig. v.8) and therefore even higher than that for the  $K^+$ . For C+C the influence of absorption on the spectra is negligible and also the potential interaction is weak. It lowers slightly the inverse slope parameter whereas elastic rescattering has the opposite effect (see Fig. v.9). At the end, all effects nearly compensate and the final slope is close to that at production. For Au+Au the situation is different. The strongly momentum-dependent rescattering cross section has the consequence that those  $K^-$  mesons, which are registered finally in the detector, have an initial inverse slope parameter of 99 MeV. Rescattering increases this value but the attractive  $K^-$  N interaction reduces it again and both effects together cancel each other resulting in an inverse slope parameter of 98 MeV. For  $K^-$  mesons the changes of inverse slope parameter due to rescattering and due to the potential compensate partially, whereas for the  $K^+$  they add and the final inverse slope parameter of  $K^+$  is higher than that of the final  $K^-$  slope, as observed experimentally.

The left part of Fig. vi.4 shows this influence of the KN potential on the inverse slope parameter  $T$  of  $K^+$  and of  $K^-$  in IQMD calculations for Au+Au at various centralities at the end of the reaction. The KN potential is the primary reason that  $T(K^+) > T(K^-)$ . Whereas the  $K^-$  N interaction lowers the inverse slope parameter of the  $K^-$  the  $K^+$  N interaction increase the inverse slope parameter of the  $K^+$ . The IQMD results including KN potential are confronted to experimental results from the KaoS Collaboration for Au+Au at 1.5 A GeV [109] in the middle and right panel of Fig. vi.4. The middle part shows the experimental centrality dependence of the inverse slope parameter for Au+Au and Ni+Ni and the right part the data obtained for inclusive reactions at various incident energies. Thus in experiments we see as well  $T(K^+) > T(K^-)$  another piece of evidence for the importance of rescattering and of the KN potential for the dynamics of strange mesons in matter.

It has been argued [133] that the multiplicities of all hadrons observed at SIS energies

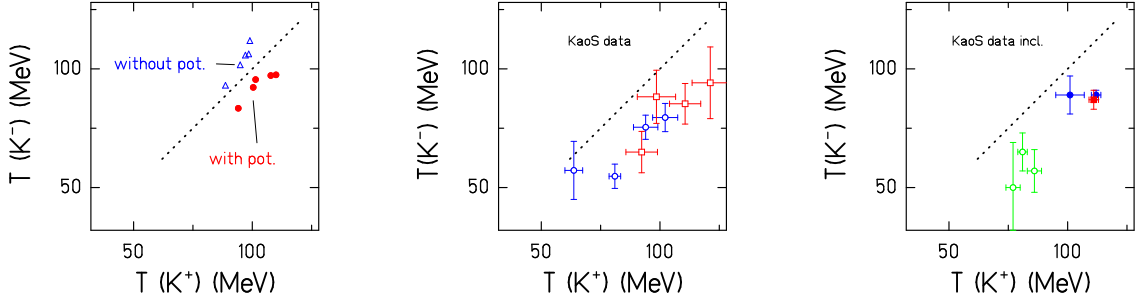


FIG. vi.4: Relation between the inverse slope parameter  $T(K^-)$  versus  $T(K^+)$ . The color code is green for C+C, blue for Ni+Ni and red for Au+Au. Left: IQMD calculations for Au+Au collisions at 1.5 A GeV for different centralities with and without KN potential. Middle: Experimental results for Au+Au collisions at 1.5 A GeV and for Ni+Ni at 1.93 A GeV for various centralities. Right: Data from inclusive collisions of C+C, Ni+Ni and Au+Au at several incident energies. The experimental results are from Ref. [109]

fit very well into the systematics which is expected in statistical model calculations. For this analysis, only the multiplicities of  $K^-$  and  $K^+$  have been used. We have already seen that the different slopes of the  $K^+$  and  $K^-$  spectra do not support the assumption that the system has reached a global equilibrium assuming a unique freeze out. They depend in a complicated way on the dynamics of the system. It is nevertheless interesting to see how these slopes fit into those observed for other particles. This point is approached in two steps. First, the more general question of global equilibration is discussed. If the particles were distributed according to phase space

$$\frac{E dN}{4\pi p^2 dp} = \frac{dN}{dy m_t dm_t d\phi} = \frac{V}{(2\pi)^3} E \exp(-E/T) \quad (85)$$

we expect for the rapidity distribution [135]

$$\frac{dn}{dy} = \frac{V}{(2\pi)^2} T^3 \left( \frac{m^2}{T^2} + \frac{m}{T} \frac{2}{\cosh y} + \frac{2}{(\cosh y)^2} \right) \exp -\frac{m}{T} \cosh y \quad (86)$$

where  $m_t = \sqrt{p_t^2 + m^2}$  is the transverse energy with respect to the direction chosen to calculate  $\langle y^2 \rangle$ . The averaged squared rapidity  $\langle y^2 \rangle$  depends on the mass of the particle  $m$  and on the temperature of the system  $T$ . It turns out that  $\langle y^2 \rangle$  is quite different when comparing the longitudinal and the transverse direction and also different for the various particles. With help of Eq. (86) we determine the inverse slope parameters  $T_{long/trans}$  from  $\langle y_{trans/long}^2 \rangle$ . They are shown in Fig. vi.5, left in longitudinal direction and right in transverse direction. The values of the inverse slope parameter in longitudinal direction exceed those in transverse direction and the values are different for all particles. A

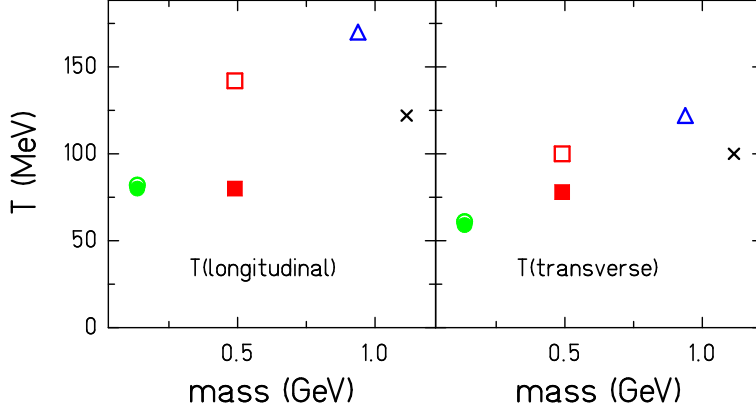


FIG. vi.5: Transverse and longitudinal temperatures for different hadrons in simulations of  $b=0$  Au+Au reactions at 1.5 A GeV . We have converted the calculated  $\langle y_t^2 \rangle$  with help of Eq. (86) into a temperature.  $K^+$  and  $K^-$  are marked by open (full) squares.

global equilibrium is not established in heavy-ion reactions in this energy domain, even in the most central reactions of the largest system. This is not too astonishing because the reaction is fast and a communication between particles in different space regions is almost impossible. In both figures, two particles, the  $K^-$  and the  $\Lambda$  do not follow the general trends. This again is not astonishing from the discussion before: Different particles see different regions of the phase space and separate from the system at different times. Now, the  $\pi$ , the  $K^+$  mesons and possibly the protons lie on a rising line. This trend could be interpreted as resulting from a kinetic freeze out at around  $T = 60 - 70$  MeV and a radial flow component. In most data such a trend is seen and generally interpreted as collective flow. However, the slope of  $\Lambda$  and  $K^-$  cannot be interpreted in such a model.

The question whether the system approaches a local equilibrium will be addressed now. Rescattering brings the slope of particles close to the local temperature. The  $K^+$  mesons and to a much smaller extent also the  $K^-$  mesons have elastic collisions with the surrounding nucleons (only 17% of the  $K^+$  and 30% of the  $K^-$  do not rescatter in central Au+Au reactions at 1.5 A GeV ). It is interesting to investigate whether there are sufficient collisions to bring the  $K^+$  and the  $K^-$  mesons to a local equilibrium with their environment.

In order to address this question we first study when the kaons have their last contact with the system. In Fig. vi.6 (left) we see that the distribution of the last contact time is rather wide with an average value of around 12 fm/c for the  $K^+$  mesons and 15 fm/c for the  $K^-$  mesons. Figure vi.6 (right) shows the density distribution of the system at the time when the kaons had their last contact (solid lines). In the case of  $K^+$  mesons, the average density is around  $1.5 \rho_0$  whereas, as expected, for  $K^-$  mesons the density is much lower.

Now we study the question whether the kaons are in equilibrium with their environment

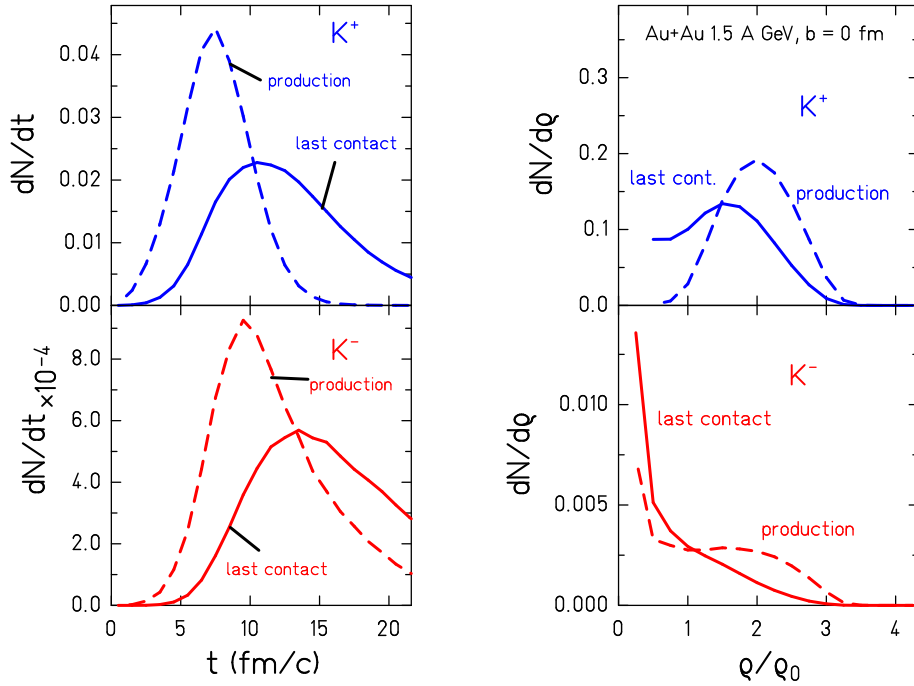


FIG. vi.6: Left: Time profiles for production and last contact for  $K^+$  (top) and for  $K^-$  (bottom) mesons in central Au+Au collisions at 1.5 A GeV . Right: The corresponding distributions of the densities at the production point evidencing a huge difference for the two mesons.

after their last contact. Figure vi.7 shows the inverse slope parameter  $T$  of the spectra as a function of time (i) for nucleons whose distance from the center of the reaction is closer than 7 fm (dashed-dotted) at that time (and which are therefore in the vicinity of the  $K^+$ ) and (ii) for all nucleons (dotted). These slopes are confronted with the slopes of the spectra of those kaons which have their last contact at time  $t$ . We display the slopes which the kaons have immediately after the last contact as well as that of the final spectra of those kaons which had their last contact at  $t$ . Both differ due to the potential interaction between kaons and nucleons. These two kaon slopes differ only for early emission where the density and hence the KN potential is still strong. Yet, they become very similar at later times. The later the  $K^+$  mesons are emitted the closer is their (last contact) inverse slope parameter to that of the surrounding protons (dash-dotted line) as shown in Fig. vi.7 left. The majority of  $K^+$  mesons is emitted earlier, as can be seen from Fig. vi.6, where the  $K^+$  slope differs from the proton slope.

The  $K^-$  mesons come closer to a local equilibrium as can be seen in Fig. vi.7, right. From 10 fm/c on, the slopes of  $K^-$  mesons (at last contact) and of protons are identical. Because most of the  $K^-$  mesons are emitted after 10 fm/c (see Fig. vi.6) their slope is a measure of the local temperature and therefore, even a larger  $K^-$  N elastic scattering cross

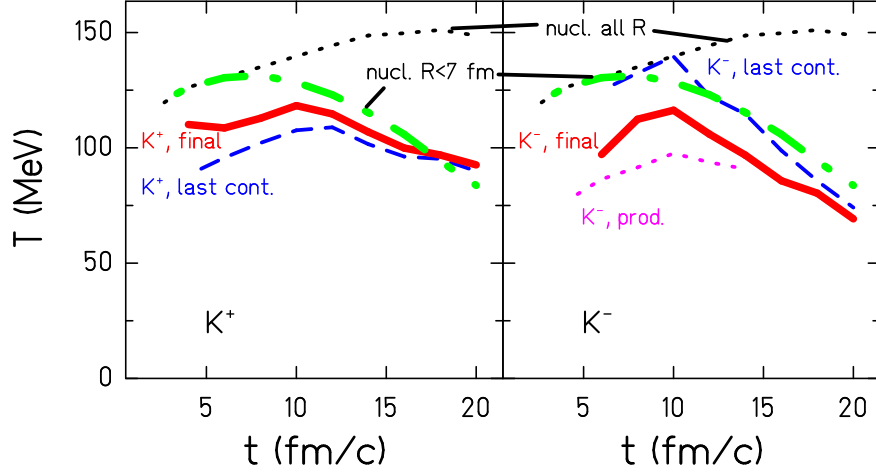


FIG. vi.7: The inverse slope parameters obtained in IQMD calculations as a function of time of last contact for  $K^+$  (left) and for  $K^-$  (right).

section would not change the slope of the kaons. In other words, the slopes are insensitive to rescattering cross section as soon as they are larger than a minimal value. The finally observed slope (full line) is, however, different, because the KN potential changes the slope considerably after the last contact.

### B. Sensitivity of the observables on properties of the system

So far we have shown how the strange meson spectra are modified by the interaction with the medium. Now we would like to address the question: what information do strange mesons carry on properties of the medium? Figure vi.6 (left) shows the time profile for the production and the last collision. The surviving  $K^-$  mesons are produced about 4 fm/c later than the  $K^+$  mesons. This is understandable because the  $\Lambda$  (together with the  $K^+$ ) has to be produced before it can create a  $K^-$  via strangeness exchange.

A drastic difference between the two species is seen when studying the densities at which they have their last contact as shown in Fig. vi.6. The results for  $K^+$  mesons are shown in top panel, those for  $K^-$  in the bottom panel. The  $K^+$  production occurs at around twice normal nuclear matter density and since their number does not change, the  $K^+$  multiplicity measures the system properties at that density. KN rescattering changes their momentum distribution but their last contact is still well above  $\rho_0$ . The  $K^+$  momentum distribution is therefore sensitive to system properties at that density. This makes them an ideal probe for the high-density phase of the reaction. In particular, this fact allows for studying the nuclear equation of state, as will be discussed in the next section.

The  $K^-$  mesons, in contrast, are produced at lower densities and their number is changing due to the  $K^- N \rightarrow \Lambda\pi$  channel. They cannot serve as a probe for high densities but may be sensitive to system properties like the KN potentials at densities below  $\rho = 0.5 \rho_0$ . They are, however, useful to study the absorption cross section  $K^- N \rightarrow Y\pi$  in the medium because its momentum dependence considerably influences the slope of the spectra. It may be possible that without this absorption the local equilibrium, discussed in Section VI.A, is not obtained. One can envisage that high-precision measurement allow to study the behavior of the  $\Lambda(1405)$  in the medium, a question which is highly debated (see Section II).

Thus, the information contained in the spectra of  $K^+$  and  $K^-$  mesons is sensitive to quite different phases and phase space regions of the reaction.

Since the elementary production cross section for  $K^+$  and  $K^-$  mesons have been measured (with the exception of those with a  $\Delta$  in the entrance channel) heavy-ion collisions can help to identify the influence of the medium on the  $K^+$  and  $K^-$  observables. As has been discussed in detail in the previous chapters this interaction with the medium is a very complicated process and very different for  $K^+$  and  $K^-$  even if the  $\Delta$  cross sections were known. This interaction depends on the potential interaction between the kaons and the hadronic matter as well as on in-medium modifications of the involved cross section due to, for example, the dissolution of the  $\Lambda(1405)$  in nuclear matter, as predicted by theory. Presently, it is fair to say that transport calculations which have been developed before the large body of kaon data became available do describe the ensemble of the data (with the exception of the  $p_t$  dependence of  $v_2$ ).

We have seen that almost all of the observables are sensitive to more than one of these unknown or only vaguely known quantities, however with different sensitivity. For this reason we have summarized in Tab. III to which parameters (KN potential, elastic rescattering,  $K^-$  absorption cross section) the different  $K^+$  and  $K^-$  observables are sensitive to and where the main uncertainties are. The most promising observable for further studies is the kaon spectra at low momentum. It depends on the KN potential but is relatively independent of the rescattering cross section. Precision experiments should be able to determine these potentials experimentally. Especially the experimental determination of the  $K^0N$  potential, which is not perturbed by Coulomb interactions, should be within reach.

### C. The nuclear equation of state (EoS)

The understanding of the global properties of infinite nuclear matter is certainly one of the most challenging questions in nuclear physics. Especially the change in the behavior of matter with density is a key property which is relevant also outside of the nuclear physics domain. It plays a major role in the understanding of astrophysical phenomena, e.g. the structure of neutron stars. Indeed, these are expected to have densities around  $2 \rho_0$  to  $5 \rho_0$

observable	KN pot	resc	abs	comments
$K^+$ yield	+	-	-	uncertainties in input
$K^-$ yield	-	+	+	many uncertainties in input, including those of $K^+$
$K^-$ yield (C/Au)	+	-	-	limits the strength of the $K^-$ potential
$K^+ / K^-$ production ratio	-	+	+	same, only the input of $K^+$ cancels
$K^+$ , $K^-$ difference in slopes	+	+	+	mostly potential, also caused by rescattering $K^+$ , absorption of $K^-$
$K^+$ , $K^-$ ratio	+	+	+	also caused by rescattering $K^+$ , absorption of $K^-$
$K^{0,+,-}$ at low momenta	++	+	-	difficult to measure
$v_2$ of $K^+$	+	+	-	contribution of rescattering dilutes the signal
$v_2$ of $K^-$	-	+	-	governed by emission time of $K^-$
$v_{1,2}(p_t)$ of $K^+$	+	+	-	sensitive to potential in HSD
$v_{1,2}(p_t)$ of $K^-$	+	-	+	sensitive to potential in HSD
angular distr. of $K^+$	-	+	-	not sensitive to KN potential
angular distr. of $K^-$	-	+	-	not sensitive to KN potential

TABLE III: Summary of sensitivities of various kaon observables to the different aspects of kaon physics.

just those reached in relativistic heavy-ion collisions. [136]

Theoretical approaches like the Brückner-Hartree-Fock approach [137] are available for densities moderately above and below normal nuclear matter density. This has recently been reviewed by Baldo and Maieron [138]. It agrees well with other approaches like variational calculations and Greens function Monte-Carlo calculations [139] up to densities around  $2\rho_0$ . At higher densities (for  $a/r_0 \approx 1$ ), where  $a$  is the range of the short-range repulsive nuclear force and  $r_0$  is the internuclear distance, other many body diagrams become important. At  $\rho_0$  this value is  $a/r_0 \approx 0.3$  and for densities reached in heavy-ion collision, as discussed here, this approach therefore comes to the limit of its validity. Of course, by introducing phenomenological three-body potentials one may extend the validity of these approaches but they limit also their predictive power.

Many attempts have been made to determine the EoS from experiments using heavy nuclei. However, the extraction of this relation is hampered by several facts:

1. The nuclear binding energies are about  $-8 A$  MeV while the one in the Weizsäcker mass formula for infinite matter is  $-16 A$  MeV. This difference shows that the properties of nuclei are strongly influenced by surface effect and also by the Coulomb force.

2. In heavy-ion reactions nuclei become compressed *and* excited. Excitations and compression cannot be varied separately. Excited nuclear matter consists also of baryonic resonances and of mesons. This means that only a hadronic equation of state at  $T > 0$  is



accessible via experiment. Transport models do describe these excitations, yet they also indicate that in these collisions equilibrium - at least a global one - is not reached. The EoS has therefore to be extracted indirectly.

Three experimental observables have been studied to extract information on the nuclear EoS: (i) the strength distribution of giant isoscalar monopole resonances [140], (ii) the in-plane side-wards flow of nucleons in semi-central heavy-ion reactions at energies between 100  $A$  MeV and 400  $A$  MeV [64] and (iii) the production of  $K^+$  mesons in heavy-ion reactions at energies around 1  $A$  GeV suggested in Ref. [141] and recently studied in Ref. [142].

(i) The study of monopole vibrations [140] has been very successful. Giant monopole resonances are sensitive to the energy which is necessary to change the density of a cold nucleus close to the equilibrium density  $\rho_0$  which limits the information to a very small density range. The vibration frequency depends directly on the force which counteracts any deviation from the equilibrium and therefore to the potential energy. These calculations allow for the determination of the compression modulus

$$K = -V \frac{dp}{dV} = 9\rho^2 \frac{d^2 E/A(\rho, T)}{(d\rho)^2} \Big|_{\rho=\rho_0}$$

which measures the curvature of  $E/A(\rho, T)$  at the equilibrium point. The values found for the volume compressibility in different non-relativistic and relativistic approaches are around  $K = 240$  MeV [143–147], close to what has been dubbed “soft equation of state”. Very recently this value has been questioned because the influence of the surface compressibility may have been underestimated [148]. This may cause an uncertainty of 30%.

(ii) In semi-central heavy-ion collisions the overlap zone of projectile and target becomes considerably compressed. The transverse pressure on the baryons outside of the interaction region causes an in-plane flow which is expected to be proportional to the transverse pressure. This effect can only be observed if the beam energy is large as compared to the Fermi energy, i.e. at well above 100  $A$  MeV. The in-plane flow is one of the few observables which depend on the density profile at the surface of the nuclei during the interaction being directly proportional to the density gradient. It’s sensitivity to the EOS is weak. As shown recently [81] the tiny variation of the in-plane flow with the EOS cannot be consistently calculated in the transport theories, putting doubts on previous conclusions [149].

(iii) The most promising method for the study of nuclear matter properties at high densities is the kaon production in - mainly central - heavy-ion collisions. Here, the yield of  $K^+$  depends sensitively on the density and the energetic condition during the interaction.

As mentioned before,  $K^+$  production below the NN threshold requires several (inelastic) collisions as the energy in first-chance collisions is not sufficient. Due to strangeness conservation together with a  $K^+$  also a  $\Lambda$  has to be created. Hence the threshold is 671 MeV in the center of mass. The most effective way to accumulate energy is the conversion of a nucleon into a  $\Delta$  and to produce in a subsequent collision a  $K^+$  meson via  $\Delta N \rightarrow NK^+\Lambda$ . Two effects influence the yield of produced  $K^+$  with the density reached in the collision and

give thus access to the stiffness of the EoS. For a soft EoS less energy is needed to compress matter and hence (i) more energy is available for the  $K^+$  production and (ii) the density which can be reached in these reactions is higher. The latter effect is the most important one as a higher density leads to a smaller mean free path and therefore the probability that the  $\Delta$  has a collision before it decays is higher. Hence, the  $K^+$  yield increases.

The influence of the density reached in these collisions is illustrated in Fig. vi.8 showing

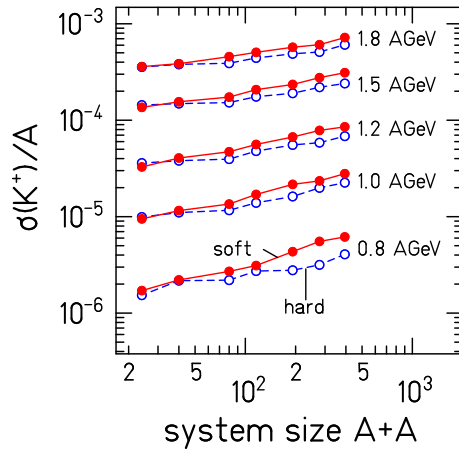


FIG. vi.8: Cross section of  $K^+$  mesons per mass number  $A$  as a function of system size  $A + A$  for several beam energies demonstrating the influence of the stiffness of the EoS on the  $K^+$  yield.

the yield of  $K^+$  per mass number  $A$  as a function of the system size  $A + A$  for different beam energies. The full (red) line represents the calculations with the standard soft ( $K = 200$  MeV) EoS, whereas the dashed (blue) line is the result for a hard ( $K = 380$  MeV) EoS. A hard EoS requires more energy to compress hadronic matter and therefore the kaon yield is lower for heavy systems. Lighter systems do not stop that much and therefore their density during the interaction depends only little on the stiffness of the EoS. The difference in yield for the heavy system is strongest at the lowest beam energy. At beam energies  $> 2 A$  GeV  $K^+$  production by first-chance NN collisions dominates and the sensitivity on the EoS is lost.

It was found that the most sensitive observable for the stiffness of EoS so far is the double ratio [102] of the  $K^+$  production in a heavy and a light system

$$(M_{K^+ / A})_{Au+Au} / (M_{K^+ / A})_{C+C}. \quad (87)$$

This ratio is plotted in Fig. vi.9 as a function of the beam energy for a soft (bold red) and a hard (thin blue) EoS together with the data from the KaoS Collaboration [102]. The calculations by Fuchs et al. [150–152] are also shown as dotted lines. This figure elucidates again that the sensitivity on the EoS is highest at the lowest beam energies and

demonstrates that only a soft EoS is compatible with the experimental data of the KaoS Collaboration [102, 151].

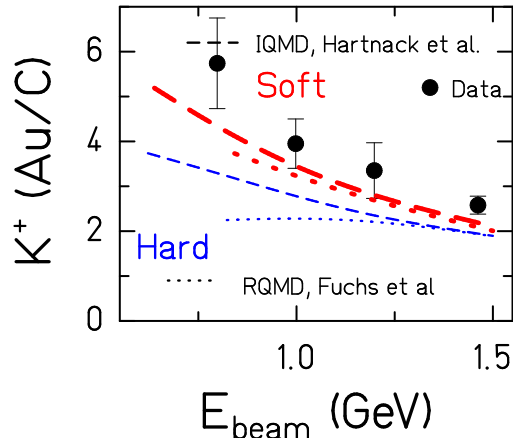


FIG. vi.9: Comparison of the experimental  $K^+$  excitation functions [102] of the double ratio  $(M_{K^+}/A)_{Au+Au}/(M_{K^+}/A)_{C+C}$  (the  $K^+$  multiplicities per mass number  $A$ ) obtained in Au+Au divided by the one in C+C with RQMD [151] (dotted) and with IQMD calculations [142] (dashed). We compare the results of a soft (bold red) with a hard (thin blue) EoS.

Using the ratio of yields many uncertainties in the theoretical approaches cancel because they act in the same way in both systems, as shown in Ref. [142]. Figure vi.10 displays some examples. From top to bottom we show calculations with different  $N\Delta \rightarrow K^+$  NN cross sections, with and without KN potential and for different life times of the  $\Delta$  resonance. None of these uncertainties is able to weaken our previous conclusion that only a soft EoS is compatible with the observed excitation function of the  $K^+$  yield.

For a more quantitative extraction of the compression modulus  $K$ , Fig. vi.11 exhibits the double ratio obtained in IQMD calculations as a function of  $K$  for the two options, with and without the KN potential. On top (bottom) the results for a beam energy of 1 (0.8) A GeV are shown. Again, a compression modulus of less than 250 MeV is required to reproduce the data. Instead of varying the size of the system one can also vary the centrality and this will give an independent observable. Because more central collisions yield a higher compression we expect that the  $K^+$  yield per participant as a function of the centrality depends as well on the EoS. This is indeed observed in the simulations and displayed in Fig. vi.12, top, showing the dependence of the  $K^+$  multiplicity per participant as a function of the participant number  $A_{\text{part}}$  for a hard EoS as well as for a soft EoS with various options: Different  $N\Delta \rightarrow K^+$  YN cross sections with and without KN potentials. These choices modify only little the slope of the curves. In contrast, the calculation with a hard EoS exhibits a drastic decrease of the slope demonstrating the sensitivity on the stiffness of the EoS. It shows as well that the momentum dependence of the interaction (mdi) does not influence the result.

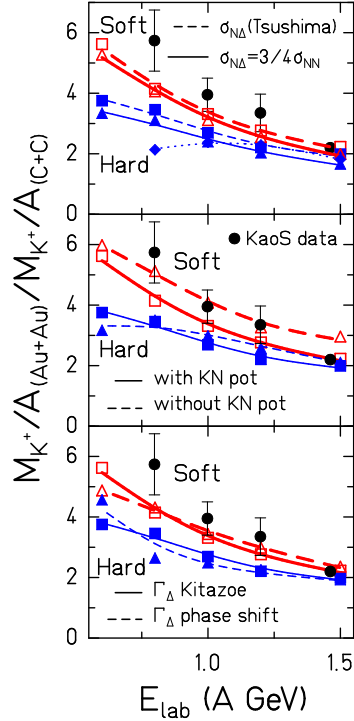


FIG. vi.10: Comparison of the measured excitation function of the ratio of the  $K^+$  multiplicities per mass number  $A$  obtained in Au+Au and in C+C reactions (Ref. [102]) with various assumptions on the physical input. The use of a hard EoS is denoted by thin (blue) lines, a soft EoS by thick (red) lines. The energies of the calculations are given by the symbols, the lines are drawn to guide the eye. On top, two different versions of the  $N\Delta \rightarrow K^+\Lambda N$  cross sections are used. One is based on isospin arguments [94], the other is determined by a relativistic tree level calculation [91, 93]. Middle: IQMD calculations with and without  $KN$  potential are compared. Bottom: The influence of different options for the life time of  $\Delta$  in matter.

On a logarithmic scale  $M/A_{\text{part}}$  exhibits an almost linear increase with  $A_{\text{part}}$ . The curves can therefore be characterized by  $M/A_{\text{part}} \propto A_{\text{part}}^\alpha$  with a characteristic slope parameter  $\alpha$ . The bottom part of Fig. vi.12 shows for the standard  $N\Delta \rightarrow K^+ NN$  cross section and including the  $KN$  potential the slope parameter  $\alpha$  as a function of the compression modulus  $K$ . Also for this observable the data of the KaoS Collaboration [109] are only compatible with values of  $K$  around 200 MeV. Thus two rather independent observables point towards a rather low compression modulus.

## VII. SUMMARY

This report is a comprehensive analysis of strangeness production in p+A and A+A collisions by comparing the recent available experimental data on the production of three kaon

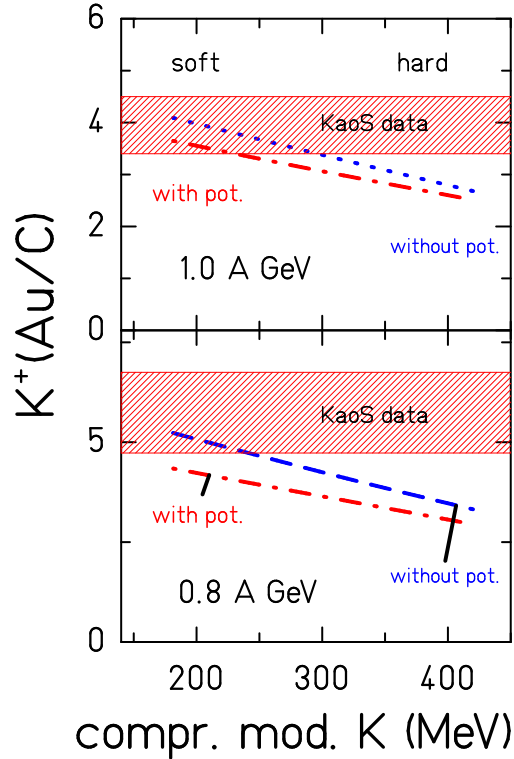


FIG. vi.11: The double ratio  $[M/A(\text{Au}+\text{Au})]/[M/A(\text{C}+\text{C})]$  calculated within the IQMD model (with and without KN potential) as a function of  $K$  at both 0.8 (top) and at 1.0 A GeV (bottom). The experimental values are given as band and allow to estimate upper limits for the compressibility modulus  $K$  as described in the text.

species,  $K^+$ ,  $K^0$ ,  $K^-$ , and of  $\Lambda$  hyperons with results from one and in some cases from two transport theories. With the exception of  $v_1(p_t)$  of  $K^+$ ,  $v_2(p_t)$  of  $K^-$  mesons the multitude of the available experimental data are simultaneously reproduced by the two transport approaches. Consequently, one can conclude that the physics of strangeness production close to threshold in p+A and A+A collisions is qualitatively and for most of the observables also quantitatively understood. This is a remarkable result in view of the fact that experimental data for several of the essential elementary cross sections are not available and that hence this input to the transport models is based on theory only.

This agreement establishes the following scenario for strangeness production in heavy ion reactions at these sub-threshold energies: Close to threshold the most important process in which strange particles are produced is the associate strangeness production via the  $\Delta N \rightarrow Y K^{+0}N$  channel. In this reaction a sufficient  $\sqrt{s}$  value can be more easily obtained than in NN collisions. Hence, the creation of  $K^+$  mesons occurs preferably via multi-step interactions. The production of  $K^+$  in nucleus nucleus collisions is therefore right from the

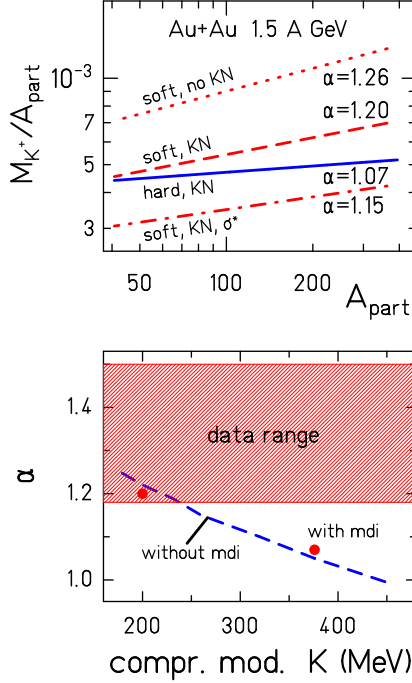


FIG. vi.12: Dependence of the  $K^+$  scaling on the nuclear equation of state. We present this dependence in form of  $M_{K^+} = A_{part}^\alpha$ . On the top the dependence of  $M_{K^+}/A_{part}$  as a function of  $A_{part}$  is shown for different options: A “hard” EoS with KN potential (solid line), the other three lines show a “soft” EoS, without KN potential and  $\sigma(N\Delta)$  from Tsushima [91, 93] (dotted line), with KN potential and the same parametrization of the cross section (dashed line) and with KN potential and  $\sigma(N\Delta) = 3/4\sigma(NN)$ . On the bottom the exponent  $\alpha$  is shown as a function of the compression modulus  $K$  for calculations with momentum-dependent interactions (mdi) and for static interactions ( $t_4 = 0$ , dashed line, see Eq. 57).

beginning different than that in elementary collisions.

In contrast,  $K^-$  are produced dominantly in secondary collisions where a strange baryon transfers its strange quark to a meson, i.e. via strangeness exchange.  $K^-$  production is therefore closely connected to the  $K^+$  production as strange baryons are created together with  $K^+$ . This is again in contrary to elementary reactions in which this strangeness-exchange channel is absent and where  $K^-$  are exclusively produced in  $N N \rightarrow N N K^- K^+$  reactions. This channel contributes only very moderately to the  $K^-$  yield in heavy-ion reactions at these energies.

The  $K^+$  rescatter after being produced. Rescattering becomes more important if the nuclei are larger. Already in C+C reactions a  $K^+$  rescatters on the average more than once. This rescattering is visible in the spectra. At production,  $K^+$  mesons have in the average a much smaller kinetic energy than the nucleons of the surrounding matter. Rescattering increases therefore the inverse slope parameter of the  $K^+$  spectra. It causes also finite  $v_1$  and

$v_2$  values. The latter, however, are strongly modified by the potential interaction between  $K^+$  and the surrounding nucleons. This potential interaction modifies also the spectra, mainly at low transverse momentum but also, in a very moderate way, at higher momenta where it is responsible for a further increase of the inverse slope parameter. Only for the small fraction of  $K^+$  which stay in collisional contact with the nuclear system until very late times the slope of the  $K^+$  and that of the nucleons come close to each other (but, as said, this  $K^+$  slope is still modified by the  $K^+$  nucleus potential interaction which acts when the  $K^+$  leave the nuclear environment). Generally the inverse slope parameter of the  $K^+$  spectra is smaller than that of the surrounding nucleons and much smaller than that of all nucleons. (Nucleons do not come to a global thermal equilibrium.) Most of the  $K^+$  are emitted early and are not in equilibrium with their environment. It remains for the moment an open question, which deserves a further investigation, why nevertheless the multiplicity of strange particles is well described in statistical models.

$\Lambda$ 's are produced in association with  $K^+$  mesons. They serve as a cross check for the  $K^+$  production as far as their multiplicity is concerned. They rescatter with the nuclear environment with a large but not very well known cross section which modifies the slope considerably. Rescattering is also the reason for the considerable in-plane flow which is as large as that for the surrounding nucleons. For the  $\Lambda$  the two available data sets cannot be reconciled if compared with IQMD and HSD calculations. So further investigations are necessary.

The  $K^-$  meson is more difficult to describe than  $K^+$  and  $\Lambda$ . First of all, in cold nuclear matter it is far away from being a quasi particle, i.e. from a particle with a small width. The only available calculation indicates that for the temperatures which are of importance for heavy-ion collisions it becomes close to a quasi-particle. This is understandable because at high temperatures the Pauli blocking of the intermediate states is less important. Second, it is produced in secondary collisions. For one channel,  $Y \pi \rightarrow K^- N$ , the cross section can be obtained by detailed balance from the measured inverse cross section provided that it is not modified in the medium. This is a very strong assumption because it was predicted that the  $\Lambda(1405)$  resonance disappears already at low densities. For the other cross section,  $Y N \rightarrow K^- N N$  little information is available. Third, there is a strong debate of the strength of the  $K^-$  nucleus potential where measurements of kaonic atoms and those from kaonic clusters are difficult to reconcile.

The cross section of the reaction  $K^- N \rightarrow \Lambda\pi$  is rather large, hence in heavy systems a large number of the produced  $K^-$  becomes absorbed before escaping from the expanding system whereas in light systems like C+C this is of less importance. Due to the large momentum dependence of this cross section reabsorption modifies strongly the slope of the surviving  $K^-$ . This explains the large difference of the slope of heavy systems as compared to that of light ones. As a consequence of the large reabsorption cross section most of the surviving  $K^-$  are produced close to the nuclear surface. Consequently, both, the yield of  $K^-$  and their spectral shape, are not clean observables for the  $K^-$  nucleus potential.

As for the  $K^+$ , the  $K^-$  nucleus interaction modifies the slope at low transverse momentum considerably but only slightly the slope of the  $K^-$  spectra at intermediate and large transverse momentum. Because the  $K^-$  potential is attractive the change of the momentum spectrum at low transverse momentum has an opposite curvature than that for the  $K^+$  which are repelled by a repulsive  $K^+$  nucleus potential. Experimentally the low transverse momentum region is not easily accessible but this is the only observable which allows to determine the  $K$ -nucleus potential.

The comparison between calculations and data show clearly that a  $K^-$  condensate is not within reach in the beam energy domain of our studies. It would be signaled by a drastic change of the ratio of  $K^-$  multiplicities in a light and a heavy system as a function of the beam energy because in light and heavy systems quite different densities are reached. This has experimentally not been observed.

Using the free cross section and a standard mean field approach for the  $K^-$  nucleus interaction a reasonable description of all  $K^-$  observables can be obtained. The little known cross sections limit the predictive power of transport calculations for  $K^-$  observables.

To make progress in understanding the strength of the  $K^+$  and  $K^-$  nucleus interaction in the nuclear medium it is necessary to reach a consistent description of all sensitive observables in a heavy ion reaction, i.e. directed flow [118], spectra at low transverse momenta [112], ratios of  $K^-$  and  $K^+$  spectra [114]. None of the observables is exclusively sensitive to the depth of the  $K^+$  and  $K^-$  nucleus as a function of density. Also  $K^0$  spectra at very low momenta, as measured by the HADES collaboration, [112] do not depend exclusively on the  $K^+$  nucleon potential but in addition on the  $K^+$  nucleon rescattering cross section. Hence, spectra of different projectile target combinations are necessary to establish this potential unambiguously.

Because  $K^+$  mesons are created during the dense phase of the collision, several  $K^+$  observables turn out to be sensitive to the hadronic equation of state. These data together with the model calculations clearly point towards a rather soft equation of state. Only values of the compression modulus  $K$  at nuclear ground state density below 250 MeV are compatible with the heavy-ion collision data which are sensitive to densities of around twice normal nuclear matter density. These values agree with the one found in the analysis of giant monopole vibrations which test, however, only densities very close to the ground state density.

In summary, employing the experimental free scattering cross section and theoretical model predictions for cross sections where experimental data are not available, theory agrees with experiment if a repulsive  $K^+$  and an attractive  $K^-$  nucleon potential in medium are employed. Transport calculations can reveal the complicated processes which are at the origin of multiplicities, spectral slopes and angular distributions of kaons observed in proton-nucleus and heavy ion reactions.

Acknowledgement: We would like to thank Dr. Ch. Fuchs, Dr. L. Tolos and Dr. H. Wolter for a careful reading of the manuscript as well as Dr. A. Förster and Dr. A. Schmah for



discussions. This work was supported by the Helmholtz International Center for FAIR within the framework of the LOEWE program (Landesoffensive zur Entwicklung Wissenschaftlich-Ökonomischer Exzellenz) launched by the State of Hesse.

---

- [1] J. W. Harris *et al.* Phys. Rev. Lett. **47**, 229 (1981)
- [2] S. Schnetzer *et al.* Phys. Rev. C **40**, 640 (1989) [Erratum-ibid. C **41**, 1320 (1990)]
- [3] C. Hartnack, R. K. Puri, J. Aichelin, J. Konopka, S. A. Bass, H. Stöcker and W. Greiner Eur. Phys. J. A **1**, 151 (1998) [arXiv:nucl-th/9811015]
- [4] W. Cassing and E. L. Bratkovskaya, Phys. Rept. **308**, 65 (1999).
- [5] C. Fuchs Prog. Part. Nucl. Phys. **53**, 113 (2004) [arXiv:nucl-th/0312052]
- [6] F. Dohrmann Int. J. Mod. Phys. E **15**, 761 (2006)
- [7] N. Kaiser, P. B. Siegel and W. Weise Phys. Lett. B **362**, 23 (1995) [arXiv:nucl-th/9507036]
- [8] N. Kaiser, T. Waas and W. Weise Nucl. Phys. A **612**, 297 (1997) [arXiv:hep-ph/9607459]
- [9] J. A. Oller, E. Oset and A. Ramos Prog. Part. Nucl. Phys. **45**, 157 (2000) [arXiv:hep-ph/0002193]
- [10] J. Schaffner-Bielich J. Phys. G **27**, 337 (2001) [arXiv:nucl-th/0009083]
- [11] L. Tolos, D. Cabrera, A. Ramos and A. Polls Phys. Lett. B **632**, 219 (2006) [arXiv:hep-ph/0503009]
- [12] M. Nikipelov *et al.* Phys. Lett. B **540**, 207 (2002) [arXiv:nucl-ex/0202021]
- [13] C. B. Dover, J. Huefner and R. H. Lemmer Annals Phys. **66**, 248 (1971)
- [14] M. Lutz Phys. Lett. B **426**, 12 (1998) [arXiv:nucl-th/9709073]
- [15] M. Lutz, A. Steiner and W. Weise Nucl. Phys. A **574**, 755 (1994)
- [16] A. D. Martin Nucl. Phys. B **179**, 33 (1981)
- [17] C. B. Dover and G. E. Walker Phys. Rept. **89**, 1 (1982)
- [18] M. Lutz, nucl-th/0212021
- [19] A. Baca, C. Garcia-Recio and J. Nieves Nucl. Phys. A **673**, 335 (2000) [arXiv:nucl-th/0001060]
- [20] V. Koch Phys. Lett. B **337**, 7 (1994) [arXiv:nucl-th/9406030]
- [21] T. Waas, N. Kaiser and W. Weise Phys. Lett. B **365**, 12 (1996)
- [22] T. Waas, N. Kaiser and W. Weise Phys. Lett. B **379**, 34 (1996)
- [23] T. Waas and W. Weise Nucl. Phys. A **625**, 287 (1997)
- [24] D. B. Kaplan and A. E. Nelson Phys. Lett. B **175**, 57 (1986)
- [25] A. E. Nelson and D. B. Kaplan, Phys. Lett. B **192**, 193 (1987).
- [26] C. M. Ko and G. Q. Li, J. Phys. G **22** (1996) 1673 [arXiv:nucl-th/9611027].
- [27] C. H. Lee, H. Jung, D. P. Min and M. Rho, Phys. Lett. B **326** (1994) 14 [arXiv:hep-ph/9401245].
- [28] N. Kaiser, P. B. Siegel and W. Weise, Nucl. Phys. A **594**, 325 (1995) [arXiv:nucl-th/9505043].

- [29] S. J. Dong and K. F. Liu, Nucl. Phys. Proc. Suppl. **42**, 322 (1995) [arXiv:hep-lat/9412059].
- [30] M. Fukugita, Y. Kuramashi, M. Okawa and A. Ukawa, Phys. Rev. D **51** (1995) 5319 [arXiv:hep-lat/9408002].
- [31] R. K. Bhaduri, *Models of the Nucleon* (Addison-Wesley, Reading, MA, 1988).
- [32] C. L. Korpa and M. F. M. Lutz, Acta Phys. Hung. A **22** (2005) 21 [arXiv:nucl-th/0404088].
- [33] E. Oset and A. Ramos, Nucl. Phys. A **635** (1998) 99 [arXiv:nucl-th/9711022].
- [34] A. Ramos and E. Oset, Nucl. Phys. A **671**, 481 (2000) [arXiv:nucl-th/9906016].
- [35] L. Tolos, A. Ramos and A. Polls, Phys. Rev. C **65**, 054907 (2002) [arXiv:nucl-th/0202057].
- [36] E. Friedman, A. Gal and C. J. Batty, Phys. Lett. B **308**, 6 (1993).
- [37] E. Oset and A. Ramos, Nucl. Phys. A **679**, 616 (2001) [arXiv:nucl-th/0005046].
- [38] A. Rios, A. Polls, A. Ramos and I. Vidana, Phys. Rev. C **72**, 024316 (2005) [arXiv:nucl-th/0503074].
- [39] L. Tolos, A. Ramos, A. Polls and T. T. S. Kuo, Nucl. Phys. A **690**, 547 (2001) [arXiv:nucl-th/0007042].
- [40] M. F. M. Lutz and C. L. Korpa, Nucl. Phys. A **700**, 309 (2002) [arXiv:nucl-th/0105067].
- [41] L. Tolos, A. Ramos and E. Oset, Phys. Rev. C **74**, 015203 (2006) [arXiv:nucl-th/0603033].
- [42] A. Mueller- Groeling, K. Holinde and J. Speth, Nucl. Phys. A **513**, 557 (1990).
- [43] E. Friedman, A. Gal and C. J. Batty, Nucl. Phys. A **579**, 518 (1994).
- [44] E. Friedman, A. Gal and J. Mares, Phys. Rev. C **60**, 024314 (1999) [arXiv:nucl-th/9804072].
- [45] A. Cieply, E. Friedman, A. Gal and J. Mares, Nucl. Phys. A **696**, 173 (2001) [arXiv:nucl-th/0104087].
- [46] N. Barnea and E. Friedman, Phys. Rev. C **75**, 022202 (2007) [arXiv:nucl-th/0611020].
- [47] Y. Akaishi and T. Yamazaki, Phys. Rev. C **65**, 044005 (2002).
- [48] T. Suzuki *et al.*, Nucl. Phys. A **754**, 375 (2005) [arXiv:nucl-ex/0501013].
- [49] M. Agnello *et al.* [FINUDA Collaboration], Nucl. Phys. A **775**, 35 (2006).
- [50] E. Oset and H. Toki, Phys. Rev. C **74**, 015207 (2006) [arXiv:nucl-th/0509048].
- [51] T. Yamazaki and Y. Akaishi, Phys. Lett. B **535**, 70 (2002).
- [52] A. Dote, H. Horiuchi, Y. Akaishi and T. Yamazaki, Phys. Rev. C **70**, 044313 (2004) [arXiv:nucl-th/0309062].
- [53] A. Ramos, V. K. Magas, E. Oset and H. Toki, arXiv:nucl-th/0702019.
- [54] V. K. Magas, E. Oset and A. Ramos, Phys. Rev. C **77** (2008) 065210 [arXiv:0801.4504 [nucl-th]].
- [55] V. K. Magas, E. Oset and A. Ramos, arXiv:0901.1086 [nucl-th].
- [56] H. J. Schulze, A. Lejeune, J. Cugnon, M. Baldo and U. Lombardo, Phys. Lett. B **355**, 21 (1995).
- [57] H. J. Schulze, M. Baldo, U. Lombardo, J. Cugnon and A. Lejeune, Phys. Rev. C **57**, 704 (1998).
- [58] I. Vidana, A. Polls, A. Ramos, M. Hjorth-Jensen and V. G. J. Stoks, Phys. Rev. C **61**, 025802

- (2000) [arXiv:nucl-th/9909019].
- [59] T. A. Rijken, V. G. J. Stoks and Y. Yamamoto, Phys. Rev. C **59**, 21 (1999) [arXiv:nucl-th/9807082].
- [60] C. Hartnack *et al.*, Nucl. Phys. A **495**, 303C (1989).
- [61] Ch. Hartnack, PhD thesis, GSI-Report 93-5 (1993)
- [62] Christoph Hartnack, nucl-th/0507002
- [63] S. A. Bass, C. Hartnack, H. Stöcker and W. Greiner, Phys. Rev. C **51**, 3343 (1995) [arXiv:nucl-th/9501002].
- [64] H. Stöcker and W. Greiner, Phys. Rept. **137**, 277 (1986).
- [65] W. Cassing, V. Metag, U. Mosel and K. Niita, Phys. Rept. **188**, 363 (1990).
- [66] J. Aichelin, Phys. Rept. **202**, 233 (1991).
- [67] S. A. Bass *et al.*, Prog. Part. Nucl. Phys. **41**, 255 (1998) [Prog. Part. Nucl. Phys. **41**, 225 (1998)] [arXiv:nucl-th/9803035].
- [68] W. Cassing, E. L. Bratkovskaya, U. Mosel, S. Teis and A. Sibirtsev, Nucl. Phys. A **614**, 415 (1997) [arXiv:nucl-th/9609050].
- [69] W. Cassing, L. Tolos, E. L. Bratkovskaya and A. Ramos, Nucl. Phys. A **727**, 59 (2003) [arXiv:nucl-th/0304006].
- [70] A. Mishra, E. L. Bratkovskaya, J. Schaffner-Bielich, S. Schramm and H. Stöcker, Phys. Rev. C **70**, 044904 (2004) [arXiv:nucl-th/0402062].
- [71] J. P. Jeukenne, A. Lejeune and C. Mahaux, Phys. Rept. **25**, 83 (1976).
- [72] L. G. Arnold *et al.*, Phys. Rev. C **25**, 936 (1982).
- [73] G. Passatore, Nucl. Phys. **A95**, 694 (1967).
- [74] S. Hama, B. C. Clark, E. D. Cooper, H. S. Sherif and R. L. Mercer, Phys. Rev. C **41**, 2737 (1990).
- [75] J. Aichelin, A. Rosenhauer, G. Peilert, H. Stöcker and W. Greiner, Phys. Rev. Lett. **58**, 1926 (1987).
- [76] G. F. Bertsch and S. Das Gupta, Phys. Rept. **160**, 189 (1988).
- [77] C. Hartnack and J. Aichelin, Phys. Rev. C **49**, 2801 (1994).
- [78] B. A. Li, L. W. Chen and C. M. Ko, Phys. Rept. **464**, 113 (2008) [arXiv:0804.3580 [nucl-th]].
- [79] C. Hartnack, J. Aichelin, H. Stöcker and W. Greiner, Mod. Phys. Lett. A **9**, 1151 (1994).
- [80] G. Stoicea *et al.* [FOPI Collaboration], Phys. Rev. Lett. **92**, 072303 (2004) [arXiv:nucl-ex/0401041].
- [81] A. Andronic *et al.* [FOPI Collaboration], Phys. Lett. B **612**, 173 (2005) [arXiv:nucl-ex/0411024].
- [82] J. Schaffner, J. Bondorf and I. N. Mishustin, Nucl. Phys. A **625**, 325 (1997) [arXiv:nucl-th/9607058].
- [83] L. Tolos, D. Cabrera and A. Ramos Phys. Rev. C **78**, 045205 (2008) [arXiv:0807.2947 [nucl-th]]

- [84] P. Danielewicz and G. F. Bertsch, Nucl. Phys. A **533**, 712 (1991).
- [85] S. A. Bass, J. Phys. G **28**, 1543 (2002) [arXiv:nucl-th/0112046].
- [86] M. Bleicher, UFTP Frankfurt, private communication.
- [87] G. Hartnack, L. Sehn, J. Jaenicke, H. Stöcker and J. Aichelin, Nucl. Phys. A **580**, 643 (1994).
- [88] B.R. Martin, G. Shaw; "Particle physics", John Wiley and Sons, Chichester (England) 2nd ed. (1997), Chapt. 6.1.1 Charmonium
- [89] W. J. Hogan, P. A. Piroué and A. J. S. Smith, Phys. Rev. **166**, 1472 (1968).
- [90] A. Sibirtsev, Phys. Lett. B **359**, 29 (1995).
- [91] K. Tsushima, A. Sibirtsev and A. W. Thomas, Phys. Rev. C **59**, 369 (1999) [Erratum-ibid. C **61**, 029903 (2000)] [arXiv:nucl-th/9801063].
- [92] J. T. Balewski *et al.*, Phys. Lett. B **420**, 211 (1998) [arXiv:nucl-ex/9803003].
- [93] K. Tsushima, S. W. Huang and A. Faessler, Phys. Lett. B **337**, 245 (1994) [arXiv:nucl-th/9407021].
- [94] J. Randrup and C. M. Ko, Nucl. Phys. A **343**, 519 (1980) [Erratum-ibid. A **411**, 537 (1983)].
- [95] A. A. Sibirtsev, W. Cassing and C. M. Ko, Z. Phys. A **358**, 101 (1997) [arXiv:nucl-th/9612040].
- [96] C. Amsler *et al.* (Particle Data Group), Phys. Lett. B **667**, 1 (2008) and 2009 partial update for the 2010 edition and references therein
- [97] A. Wagner *et al.*, Phys. Rev. Lett. **85**, 18 (2000) [arXiv:nucl-ex/0005004].
- [98] R. Averbeck, R. Holzmann, V. Metag and R. S. Simon, Phys. Rev. C **67**, 024903 (2003) [arXiv:nucl-ex/0012007].
- [99] W. Reisdorf *et al.* [FOPI Collaboration], Nucl. Phys. A **781**, 459 (2007) [arXiv:nucl-ex/0610025].
- [100] T. Schuck, Diplomarbeit, University of Frankfurt, 2003.
- [101] H. Oeschler, J. Phys. G **28**, 1787 (2002) [arXiv:nucl-ex/0202003].
- [102] C. Sturm *et al.* [KAOS Collaboration], Phys. Rev. Lett. **86**, 39 (2001) [arXiv:nucl-ex/0011001]; C. Sturm, PhD thesis, TH Darmstadt, 2001.
- [103] B. Hong *et al.* [FOPI Collaboration], Phys. Rev. C **57**, 244 (1998) [Erratum-ibid. C **58**, 603 (1998 PHRVA,C58,603.1998)] [arXiv:nucl-ex/9707001].
- [104] M. Büscher *et al.*, Phys. Rev. C **65**, 014603 (2002) [arXiv:nucl-ex/0107011].
- [105] M. Büscher and M. Nekipelov [ANKE collaboration], arXiv:nucl-ex/0207002.
- [106] M. Büscher, private communication.
- [107] W. Scheinast *et al.* [KaoS Collaboration], Phys. Rev. Lett. **96** (2006) 072301 [arXiv:nucl-ex/0512028].
- [108] E. E. Kolomeitsev *et al.*, J. Phys. G **31**, S741 (2005) [arXiv:nucl-th/0412037].
- [109] A. Förster *et al.*, Phys. Rev. C **75**, 024906 (2007) [arXiv:nucl-ex/0701014].
- [110] M. Merschmeyer *et al.*, Phys. Rev. C **76**, 024906 (2007).
- [111] A. Schmah and L. Fabbietti, arXiv:0911.0300 [nucl-ex].

- [112] G. Agakishiev *et al.*, Phys. Rev. C **82** (2010) 044907 [arXiv:1004.3881 [nucl-ex]].
- [113] G. Agakishiev *et al.* [HADES Collaboration], arXiv:1010.1675 [nucl-ex].
- [114] K. Wisniewski *et al.* [ FOPI Collaboration ], Eur. Phys. J. **A9** (2000) 515-519. [nucl-ex/0101009]. [115]
- [115] D. Best *et al.* [FOPI Collaboration], Nucl. Phys. A **625**, 307 (1997) [arXiv:nucl-ex/9704005].
- [116] A. Förster *et al.* [KaoS Collaboration], Phys. Rev. Lett. **91**, 152301 (2003) [arXiv:nucl-ex/0307017].
- [117] J. Ritman, private communication
- [118] P. Crochet *et al.* [FOPI Collaboration], Phys. Lett. B **486**, 6 (2000) [arXiv:nucl-ex/0006004].
- [119] F. Uhlig *et al.*, Phys. Rev. Lett. **95**, 012301 (2005) [arXiv:nucl-ex/0411021].
- [120] Y. Shin *et al.* [KaoS Collaboration], Phys. Rev. Lett. **81**, 1576 (1998) [arXiv:nucl-ex/9807003].
- [121] M. Ploskon [KaoS Collaboration], Nucl. Phys. A **749**, 170 (2005) and PhD Thesis, University of Frankfurt, 2005 .
- [122] J. L. Ritman *et al.* [FOPI Collaboration], Z. Phys. A **352**, 355 (1995) [arXiv:nucl-ex/9506002].
- [123] G. Alexander, U. Karshon, A. Shapira, G. Yekutieli, R. Engelmann, H. Filthuth and W. Lughofer, Phys. Rev. **173**, 1452 (1968).
- [124] K. J. Anderson, N. M. Gelfand, J. Keren and T. H. Tan, Phys. Rev. D **11**, 473 (1975) [Erratum-ibid. D **11**, 3359 (1975)].
- [125] C. David, C. Hartnack and J. Aichelin, Nucl. Phys. A **650**, 358 (1999) [arXiv:nucl-th/9805017].
- [126] P. Chung *et al.*, Phys. Rev. Lett. **86**, 2533 (2001) [arXiv:nucl-ex/0101002].
- [127] H. Oeschler, J. Phys. G **27**, 257 (2001) [arXiv:nucl-ex/0011007].
- [128] J. Cleymans, A. Förster, H. Oeschler, K. Redlich and F. Uhlig, Phys. Lett. B **603**, 146 (2004) [arXiv:hep-ph/0406108].
- [129] J. Schaffner, A. Gal, I. N. Mishustin, H. Stöcker and W. Greiner, Phys. Lett. B **334**, 268 (1994).
- [130] J. Schaffner-Bielich, V. Koch and M. Effenberger, Nucl. Phys. A **669**, 153 (2000) [arXiv:nucl-th/9907095].
- [131] M. Menzel *et al.* [KaoS Collaboration], Phys. Lett. B **495**, 26 (2000) [arXiv:nucl-ex/0010013]; M. Menzel, Ph.D. Thesis, Universität Marburg, 2000.
- [132] C. Müntz *et al.* [KaoS Collaboration], Z. Phys. A **352**, 175 (1995); C. Müntz *et al.*, Z. Phys. A **357**, 399 (1997).
- [133] J. Cleymans, H. Oeschler and K. Redlich, Phys. Rev. C **59**, 1663 (1999) [arXiv:nucl-th/9809027].
- [134] G. Agakishiev *et al.* [HADES Collaboration], Phys. Rev. C **80**, 025209 (2009) [arXiv:0902.3487 [nucl-ex]], A. Schmah, Ph.D.thesis, Darmstadt University of Technology, 2008.
- [135] E. Schnedermann, J. Sollfrank and U. W. Heinz, Phys. Rev. C **48** (1993) 2462

- [arXiv:nucl-th/9307020].
- [136] J. Aichelin and J. Schaffner-Bielich, *Relativistic Heavy Ion Physics (Landolt-Börnstein: Numerical Data and Functional Relationships in Science and Technology - New Series / Elementary Particles, Nuclei and Atoms)*, Springer, Heidelberg, 2010 arXiv:0812.1341 [nucl-th].
- [137] P. Ring and P. Schuck, *The Nuclear Many Body Problem*, Springer, Heidelberg
- [138] M. Baldo and C. Maieron, *J. Phys. G* **34**, R243 (2007) [arXiv:nucl-th/0703004].
- [139] C. Fuchs and H. H. Wolter, *Eur. Phys. J. A* **30** (2006) 5 [arXiv:nucl-th/0511070].
- [140] D. H. Youngblood, H. L. Clark and Y. W. Lui, *Phys. Rev. Lett.* **82**, 691 (1999).
- [141] J. Aichelin and C. M. Ko, *Phys. Rev. Lett.* **55**, 2661 (1985).
- [142] C. Hartnack, H. Oeschler and J. Aichelin, *Phys. Rev. Lett.* **96**, 012302 (2006) [arXiv:nucl-th/0506087].
- [143] J. Piekarewicz, *Phys. Rev. C* **69**, 041301 (2004) [arXiv:nucl-th/0312020] and references therein.
- [144] B. K. Agrawal, S. Shlomo and V. K. Au, *Phys. Rev. C* **68**, 031304 (2003) [arXiv:nucl-th/0308042].
- [145] G. Colo and G. N. Van, arXiv:nucl-th/0309002.
- [146] G. Colo, N. Van Giai, J. Meyer, K. Bennaceur and P. Bonche, *Phys. Rev. C* **70**, 024307 (2004) [arXiv:nucl-th/0403086].
- [147] D. Vretenar, T. Niksic and P. Ring, *Phys. Rev. C* **68**, 024310 (2003) [arXiv:nucl-th/0302070].
- [148] M. M. Sharma, *Nucl. Phys. A* **816**, 65 (2009) [arXiv:0811.2729 [nucl-th]].
- [149] P. Danielewicz, R. Lacey and W. G. Lynch, *Science* **298**, 1592 (2002) [arXiv:nucl-th/0208016].
- [150] C. Fuchs, D. S. Kosov, A. Faessler, Z. S. Wang and T. Waindzoeh, *Phys. Lett. B* **434**, 245 (1998) [arXiv:nucl-th/9801048].
- [151] C. Fuchs, A. Faessler, E. Zabrodin and Y. M. Zheng, *Phys. Rev. Lett.* **86**, 1974 (2001) [arXiv:nucl-th/0011102].
- [152] C. Fuchs, A. Faessler, S. El-Basaouny and E. Zabrodin, *J. Phys. G* **28**, 1615 (2002) [arXiv:nucl-th/0103036].